LONDON'S GLOBAL UNIVERSITY

Manipulation of Fischer Tropsch Catalysts for Controlled Selectivity: Investigating the role of a Manganese Dopant

Jay Morgan Pritchard

Department of Chemistry

University College London

Primary Supervisor: Prof. Andrew Beale

Secondary Supervisor: Prof. Gopinathan Sankar

Industrial Supervisor: Dr James Paterson

Thesis submitted for the degree of Doctor of Philosophy

2022

I, Jay Pritchard confirm that the work presented in my thesis is my own. Where information has been derived from other sources, I confirm that this has been indicated in the thesis.

Abstract

Cobalt-based Fischer-Tropsch (FT) catalysts are widely used to convert syngas to long-chain hydrocarbons. Recently, significant increases in alcohol selectivity have been reported with high manganese doping. In this work, commercially relevant catalyst extrusions have been studied by synchrotron X-ray Diffraction Computed Tomography (XRD-CT) during catalyst activation and operation to understand the evolution of crystalline phases of cobalt nanoparticles supported on TiO_2 with various manganese doping levels (up to 10 wt. %). Data processing pipelines have been developed to assist in the Rietveld refinement of large quantities of diffraction data to provide quantitative metrics for the spatially and temporally resolved diffraction results. A high pressure cell and testing methodology have been developed to conduct *operando* studies at relevant pressures (25 bar) and temperatures on an imaging beamline, with the potential to operate multiple samples simultaneously to maximise runtime and operation utilisation while removing inter-run variability.

Since a large proportion of the Mn dopant tends to be highly disperse, a series of model catalyst systems were developed to evaluate different catalyst-dopant interactions and doping levels. A modified salt-mediated hydrothermal synthesis was used to produce Co_3O_4 nanoparticles which either comprised a Co-Mn spinel solid solution, manganese surface coated Co_3O_4 particles or physical mixtures of Co_3O_4 and Mn_3O_4. These systems were produced with various Co:Mn ratios to correspond to the commercially relevant extrusions, before being supported on TiO_2. The resulting catalysts were characterised via XRD and STEM and tested for FT activity and selectivity to understand what type of interaction, and what ratios of Co:Mn, are required to produce significant quantities of alcohol products under typical FT conditions. The % Mn requirements for alcohol selectivity in the commercially relevant catalysts correspond to the model systems where the cobalt and manganese were closely interacting. The development of the model systems also provides effective reference materials for comparison of characterisation results with the commercial catalyst samples.

Impact Statement

Fischer-Tropsch catalysis is of interest industrially due to the technology being highly adaptable and therefore can provide an alternative and potentially renewable source of hydrocarbons. In this work, a series of industrially relevant cobalt Fischer-Tropsch catalysts were studied. The catalysts studied display remarkably high alcohol selectivity, which is unusual for Fischer-Tropsch catalysts. The study of these catalysts provides insight into a technology for renewable organic alcohol production. Organic alcohols are chemicals with a variety of applications, including detergent feedstocks, cosmetics & solvents.

The focus of the study of the catalyst series was via X-Ray Diffraction Computed Tomography (XRD-CT). The developments made in the XRD-CT experimental setup discussed in this work are not limited to the catalyst series studied, and rather are applicable to the wider field of catalysis or functional materials in general. In these studies, the simultaneous study of catalyst samples via the use of multi-sample reactors, as well as the use of high pressure testing cells to study samples under industrially relevant conditions, exemplify the advantages of spatially resolved techniques, and highlight further potential of XRD-CT as a characterisation tool in the *in situ* and *operando* study of heterogeneous catalysts. During processing of the large volume of diffraction data collecting during XRD-CT measurements, processing pipelines were developed to allow for the automated Rietveld refinement of the spatially resolved diffraction data. This allows for quantitative mapping of phase weights, as well as the mapping of other refined metrics, which represents a more complete representation of the collected data in comparison to the typical mapping of single peak areas.

To further study the effect of high levels of manganese as a dopant for alcohol selective Fischer-Tropsch, a series of model catalyst systems were developed. To be able to prepare a variety of model catalyst samples with varying manganese and cobalt interactions and loadings, a salt-mediated Co_3O_4 nanoparticle synthesis was used. This synthetic method was further developed to co-incorporate manganese into the synthesis to result in a cobalt-manganese mixed spinel oxide. The synthesis allows for the cobalt and manganese levels to be tuned to produce a desired ratio.

Cobalt-Manganese mixed oxides are not only of interest in Fischer-Tropsch catalysis, but as catalysts in other reactions such as CO_2 hydrogenation & CO_2 to methanol. Additionally,

cobalt-manganese mixed oxides are commonly used materials in the development of battery & supercapacitor electrodes.

Acknowledgements

I would like to sincerely thank Professor Andrew Beale for providing me with the opportunity to work on this project. Andy's continuous motivation and insight throughout the project has been invaluable, and I will be forever grateful for his support.

I would also like to sincerely thank my industrial supervisor, Dr James Paterson, for his expertise and encouragement throughout the duration of this project. His support and encouragement to keep me on track has been greatly appreciated.

Thank you to the students and staff of the Catalysis Hub based at Harwell. It has been a privilege to work among such kind and talented people. To the team at Finden, thank you for your expertise and company during beamtimes.

Finally, to my wife Estefy for her endless support over the years and the inspiration to push myself to be the best version of myself. Thank you from the bottom of my heart.

Table of contents

Abstract 1
Impact Statement 2
Acknowledgements 4
Table of contents 5
List of Figures 8
List of tables 13
Chapter 1 General Introduction 14
1.1 Commercial Fischer Tropsch 18
1.2 Catalyst Doping 18
1.3 Scope of work 19
1.4 References 22
Chapter 2 Literature review 24
2.1 Effect of Mn doping on Co FT catalysts 25
2.2 Alcohol selective FT catalysts 30
2.3 Model Catalyst Systems 35
2.4 In Situ study of catalysts by CT methods 36
2.5 In Situ X-ray Diffraction of Cobalt FT Catalysts 39
2.6 References 40
Chapter 3 Methodology 41
3.1 XRD-CT 41
3.1.1 X-Ray Diffraction 41
3.1.2 Synchrotron X-ray Sources 43
3.1.3 Computed Tomography 45
3.1.4 Rietveld Refinement 46
3.2 Additional Characterisation Techniques 48
3.2.1 X-ray Fluorescence 48
3.2.2 Electron Microscopy 49
3.2.3 Energy dispersive X-ray spectroscopy 50
3.2.4 X-ray Photoelectron Spectroscopy 51
3.2.5 Diffuse Reflectance Infrared Fourier Transform Spectroscopy 51
3.3 References 53
Chapter 4 - Ambient pressure XRD-CT study of Mn doped catalyst extrusion series 54
4.1 Introduction 54
4.2 Experimental 55
4.2.1 Catalyst Series 55
4.2.2 Setup for *In Situ* X-ray Diffraction Computed Tomography 55
4.2.3 In Situ XRD-CT during Catalyst Activation and Fischer-Tropsch 57
4.2.4 Rietveld Refinement Processing Pipeline 59
4.3 Results and Discussion 62

4.3.1 Reconstructed Data 62
4.3.2 In situ reduction 69
4.3.3 Fischer-Tropsch Testing 83
4.4 Conclusions 89
4.5 References 91
Chapter 5 - High pressure XRD-CT study of Mn doped catalyst extrusion series 92
5.1 Introduction 92
5.2 Experimental 93
5.2.1 Catalyst samples 93
5.2.2 XRD-CT measurement 93
5.2.3 Reactor design 94
5.2.4 In Situ XRD-CT during reduction and Fischer-Tropsch 96
5.2.5 Data Processing 97
5.3 Results & Discussion 99
5.3.1 Reactor Design 99
5.3.2 Data processing 99
5.3.3 In situ reduction 106
5.3.4 In situ Fischer-Tropsch synthesis 112
5.4 Conclusion 119
5.5 References 120
Chapter 6 - Manganese doped model catalyst systems for alcohol selective Fischer-Tropsch 121
6.1 Introduction 121
6.2 Experimental 123
6.2.1 Catalyst Synthesis 123
6.2.2 Characterisation 124
6.2.3 Catalyst Testing 126
6.3 Results & Discussion 126
6.3.1 Synthesis & Characterisation 126
6.3.2 Catalytic Testing 140
6.3.3 Activity comparison 147
6.3.4 DRIFTS CO Absorption 149
6.4 Conclusions 156
6.5 References 158
Chapter 7 - Summary and Conclusions 159
7.1 Further work 165
7.2 References 166
Author Contribution Statement 167
Chapter 8 Appendices 168
Appendix for Chapter 4 – Ambient pressure XRD-CT study of Mn doped catalyst extrusion series 168

Example Input parameter file for Rietveld refinement in Topas 6.....171
Data Processing Code for XRD-CT.....174
Appendix for Chapter 5 – High pressure XRD-CT study of Mn doped catalyst extrusion series 177
Appendix for Chapter 6 – Manganese doped model catalyst systems for alcohol selective Fischer-Tropsch 180

List of Figures

Figure 1-1 A) ideal weight % vs carbon number chain with varying alpha B) ideal ln(wt. %/n) vs carbon number with varying alpha. 16
Figure 2-1 STEM-EELS (Co = red, Mn = blue, Ti = green) of calcined 7.5 wt.% Co, 2.5 wt.% Mn / TiO_2 catalyst. Reproduced from Morales et al. with permission from Elsevier, J. Catal., 2005, 230, 301 – 308. 25
Figure 2-2 A & B) effect of pressure on Fischer-Tropsch selectivity. C) CO desorption temperature vs Mn/Co ratio as measured by TPD. Reproduced from Johnson et al. with permission from ACS Publications, ACS Catal., 2015, 5, 5888 – 5903. 28
Figure 2-3 Alcohol and Olefin selectivity with increasing manganese doping on 10 % Co/TiO_2. Reproduced from Paterson et al. with permission from Wiley-VCH, ChemCatChem 2018, 10, 5154 – 5163. 30
Figure 2-4 Alcohol group selectivity and CO conversion measurements against temperature. Reproduced from Xiang et al. with permission from ACS Publications, J. Am. Chem. Soc. 2013, 135, 7114 – 7117. 32
Figure 2-5 CO conversion and selectivity for a) Co/CeSi catalyst b) Co/CeMnSi catalyst. Reproduced from Ribeiro et al. with permission from Springer, Top. Catal. 2014, 57, 550 – 560. 34
Figure 2-6 Transitions observed in a gamma alumina supported Ni catalyst precursor during thermal activation via XRD-CT. The heatmaps on the left correspond to the spatially resolved peak intensities from the diffraction patterns right. Reproduced from Jacques et al. with permission from Wiley-VCH, Angew. Chem. Int. Ed. 2011, 50, 10148 – 10152. 37
Figure 2-7 XRD-CT intensity maps for cobalt species during reduction and Fischer-Tropsch of 10% Co/Al_2O_3. Reproduced from Senecal et al. with permission from ACS Publications, ACS Catal. 2017, 7, 2284 – 2293. 37
Figure 3-1 Illustration of conditions of Bragg diffraction, where d is the lattice spacing, θ is the angle between incident beam and lattice planes, and $2.d.\sin\theta / \lambda$ is an integer. Blue circles represent atoms/ions, grey lines the relevant lattice planes, and red lines the incident and reflected X-rays. .. 42
Figure 3-2 Illustration of Synchrotron components, including (1) LINAC (2) Booster Ring (3) Storage Ring (4) Beamlines (5) Front End (6) Optics Hutch (7) Experimental Hutch (8) Control Cabin (9) RF cavities (10) Control building. Reproduced from diamond.ac.uk.[4] 44
Figure 3-3 - Ray diagram of TEM electromagnetic lenses and apertures for the collection of a transmission image. 49
Figure 4-1 Experimental setup at ESRF ID15A showing a) quartz 2-walled reactor b) heat guns c) gas lines d) rotation stage and e) beamline source. 56
Figure 4-2 Reaction temperature profile and gas compositions during H_2 activation (light blue) and FT reaction (light orange). 58
Figure 4-3 Arrangement of cropped extrusion CTs as a function of time originating from the sinograms (top left) to create a reconstructed 2D intensity distribution (top right) and from which a stacked array as a function of time and % Mn is created and shown below. Note the data in the figure are scaled to a common intensity and the scalebar on the right indicates the scaled relative diffraction intensities for the pixels in thermograms on the left. 60
Figure 4-4 Example of the application of selection criteria for A) total summed diffraction contribution (showing selection of both catalyst extrusion and quartz capillary wall) B) Minimum peak maximum showing selection of both catalyst extrusion and reconstruction artefacts) and C) Both criteria combined (showing selection of only catalyst extrusion). The selection filter decides which voxels to perform sequential Rietveld refinement. The axis units for each image are voxel co-ordinates 61
Figure 4-5 A) Example of total diffraction contribution sinogram prior to reconstruction B) reconstructed CT showing quartz reactor tube (light blue circle), catalyst trilobed extrusions and thermocouple. For both images, the x & y axis are voxel coordinates, with arbitrary intensity

heatmap scale. Note the thermocouple is the light blue object at the bottom left hand side of the right hand figure 62
Figure 4-6 Example diffractogram from 80 x 80 µm voxel of undoped catalyst at start of reduction. Indexing lines are included for the anatase (red), rutile (blue) and Co_3O_4 (green) phases 63
Figure 4-7 summed diffraction pattern for each catalyst extrusion prior to activation, with excluded regions highlighted (pink) due to contribution from thermocouple reconstruction artefacts 64
Figure 4-7 Comparison of the summed diffraction patterns of each catalyst extrusion between 4.5° – 6° 2θ, with the $Co_{(3-x)}Mn_xO_4$ (511) & (440) peaks highlighted (blue) 64
Figure 4-8 Reference Lattice Parameter from Meera et al.[11] and lattice parameters of catalyst extrusion series with varying Mn content 65
Figure 4-9 Maps of refined lattice parameter of $Co_{(3-x)}Mn_{(x)}O_4$ for each catalyst extrusion. 66
Figure 4-11 A-E Maps of refined crystallite size of $Co_{(3-x)}Mn_{(x)}O_4$ phase for A) 0 %, B) 0.5 %, C) 1 %, D) 5 % & E) 10 % in nanometres. Note each map has a different heatmap scale to allow for visualisation of the spatial distribution within each extrusion. 67
Figure 4-12 Maps of cobalt phase wt. % progressing throughout temperature ramp (100 – 350 °C, 1.4 °C/min) and dwell (2h) of catalyst activation, with wt. % loadings generated by Rietveld refinement of each individual voxel. 69
Figure 4-13 Refined phase wt. % during catalyst activation for 0, 1, 5, 10 % cobalt phase on the primary axis, with temperature profile on the secondary axis. 70
Figure 4-14 Rietveld refined phase intensity and wt. % of TiO_2 anatase and Co_3O_4 in the 0 % Mn catalyst extrusion. Axis for each heatmaps display voxel co-ordinates. 72
Figure 4-15 Co_3O_4 and CoO wt. % heatmaps of the undoped extrusion during scan 6 (t = 1.5 – 1.8 h, temp = 240 – 268 °C). 73
Figure 4-16 Co (HCP) and Co (FCC) wt. % heatmaps of undoped extrusion at the end of reduction, scan 15. 73
Figure 4-17 An example of radial batching, with the cropped extrusion (left) being filtered into groups of voxels (right) where the division of each voxel is dependent on the distance of the voxel to the exterior of the extrusion. 74
Figure 4-18 Radial distribution of spinel oxide before reduction for each catalyst extrusion, from the exterior (blue) to the interior (yellow) of the extrusion. The colour scheme of radial depth groups in this figure and following figures correspond to the colour schemes of layers shown in Figure 4-17. . 74
Figure 4-19 Radial distribution of Co phases in 0 % Mn extrusion at varying points during reduction, A) Co_3O_4 , B) CoO , C) Co FCC + Co HCP. 75
Figure 4-20 Radial distribution of spinel oxide A) at end of reduction for each catalyst extrusion, B) for the final 3 scans of the 5 % Mn extrusion. 76
Figure 4-21 Radial distribution of $Co_{(1-x)}Mn_{(x)}O$ for each catalyst extrusion at end of reduction. 77
Figure 4-22 Diffraction around $Co_{(1-x)}Mn_{(x)}O$ 220 reflection for each catalyst extrusion in scan 6 (t = 1.5 – 1.8 h, temp = 240 – 268 °C) with markings for the CoO 220 reflection (green dashed line) and MnO 220 reflection (orange dashed line). 78
Figure 4-23 Evolution of $Co_{(1-x)}Mn_{(x)}O$ 220 peak in 10% Mn catalyst during reduction from scans 6 - 15, with for nominal peak positions for CoO (green dashed line) and MnO (orange dashed line). 79
Figure 4-24 Radial $Co_{(1-x)}Mn_{(x)}O$ lattice parameter at end of reduction for 5 and 10 % Mn catalyst extrusions. 80
Figure 4-25 Radial distribution of cobalt metal (combined FCC and HCP) at end of reduction for each catalyst extrusion. 81
Figure 4-26 Summed diffraction patterns of 5 % Mn extrusion at beginning and end of pseudo-FT conditions (comparison of diffraction patterns for remaining extrusions included in Figure 8-4 through Figure 8-7). 84
Figure 4-27 Heatmaps of subtracted difference of FCC and HCP cobalt metal wt. % for start vs end of pseudo-FT conditions for each catalyst extrusion. 85

Figure 4-28 Radially grouped subtracted difference of A) FCC and B) HCP cobalt metal wt. % for start vs end of pseudo-FT conditions for each catalyst extrusion. 86
Figure 4-29 Calculated FCC crystallite size for 0.5, 5 & 10 % Mn extrusions at start and end of pseudo-FT conditions. 0 & 1 % Mn extrusions were excluded from spatial crystallite size refinement of the Co FCC phase due to the overlapping of the exclusion area required by the thermocouple reconstruction artefacts overlapping with the 111 reflection of Co FCC. 87
Figure 4-30 Calculated HCP crystallite size for each extrusion at start and end of pseudo-FT conditions. 88
Figure 5-1 Illustration of high pressure testing cell. 94
Figure 5-2 Left – Inner quartz tube of reactor cell, with catalyst extrusions loaded individually within quartz capillarties. Right - Insulated reactor mounted on beamline stage, with heating guns. 95
Figure 5-3 Reaction profile during catalyst activation and FTS, showing reactor temperature over time with corresponding gas composition of 20 % H_2/He during activation (light blue) and 5% CO/ 10% H_2 / He during FTS (orange) 97
Figure 5-4 Illustration of equivalent sinograms measured with & without coverage of external reactor wall. Heatmap scale bar represents normalised relative summed diffraction intensity 100
Figure 5-5 Comparison on CT reconstruction A) without, B) with stitching of wide-scan translation steps, and C) reactor diffraction contribution around 3.7° 2θ 100
Figure 5-6 Example diffractogram of reactor contribution. 101
Figure 5-7 A) Reconstructed CT and B) diffraction pattern, from sinogram minus the blank scan. 103
Figure 5-8 Example diffraction pattern from single reconstructed voxel with 2θ regions containing reactor contribution highlighted (blue regions). The reactor contribution is reconstructed as a doublet, and includes negative values between the peak maximums 105
Figure 5-9 Heatmaps of refined wt. % loadings for oxide phases during catalyst activation. For each group of heatmaps, the vertical stacking corresponds to subsequent scans measured, and the horizontal stacking corresponds to increasing manganese content for 0, 0.5, 1, 1.5, 2, 3, 5 & 10 % Mn. 106
Figure 5-10 Visualisation of reconstruction artefact from reactor tube weld, with heatmap intensity representing normalised diffraction intensity at 3.7° 2θ 107
Figure 5-11 Heatmaps of refined wt. % loadings for cobalt metallic phases during catalyst activation 108
Figure 5-12 Radially batched Rwp for each catalyst extrusion at end of reduction, before filtering out high Rwp voxels. 110
Figure 5-13 Radially batched refined wt. % of Cobalt HCP and Cobalt FCC for each catalyst extrusion, with Rwp filtering set to 15 %. 111
Figure 5-14 Heatmaps of refined wt. % of $Co_{(1-x)}Mn_{(x)}O$ at t = 1, 18 & 36 hours, for each catalyst extrusion. 112
Figure 5-15 Radially grouped change in $Co_{(1-x)}Mn_{(x)}O$ wt. % loading between t = 1 h & t = 36 h, for each catalyst extrusion. 113
Figure 5-16 Heatmaps of refined wt. % of A) FCC cobalt and B) HCP cobalt at t = 1, 18 & 36 hours, for each catalyst extrusion. 114
Figure 5-17 Radially grouped change in metal loading between end of reduction and start of FT, for FCC & HCP. 115
Figure 5-18 Radially grouped change in A) FCC cobalt and B) HCP cobalt wt. % loading between t = 1 h & t = 36 h, for each catalyst extrusion. 116
Figure 5-19 Summed diffraction pattern of 5 % Mn catalyst at t = 1 h & t = 36 h. 117
Figure 6-1 Diffraction pattern of synthesised JP25, with Co_3O_4 reflections indexed. 127
Figure 6-2 Diffraction patterns of synthesised mixed-oxide particle series JP25 (Co_3O_4) , JP26 (100:30 Co:Mn) & JP27 (100:10 Co:Mn), with reflections indexed for Co_3O_4. 128
Figure 6-3 Lattice Parameter of $Co_{(3-x)}Mn_{(x)}O_4$ for varying x from reference literature adapted from Meera et al.[8], and synthesised mixed oxide nanoparticle series with varying Mn doping. 129

Figure 6-4 Diffractograms of Mn surface coated Co_3O_4 particles, with Co_3O_4 reflections indexed (red). 130
Figure 6-5 Diffraction pattern of synthesised sample JP23, Mn_3O_4, with reflections of tetragonal spinel indexed (red). 131
Figure 6-6 STEM imaging of JP25, Co_3O_4. 132
Figure 6-7 STEM images and Co, Mn elemental maps of a) JP25-D (100:1), b) JP25-C (100:5), c) JP25-B 100:10 surface doped Co:Mn, and d) JP11 100:50 mixed oxide Co:Mn particles. 133
Figure 6-8 Ti and Co EDX maps of TiO_2 supported Co_3O_4 reference particles JP25. 134
Figure 6-9 XANES Spectra of Mn K-edge for 1, 3 & 5 % Mn Mixed oxide catalyst series, and 3 % physical mixture catalyst. 136
Figure 6-10 XANES Spectra of Mn K-edge for 3% Mn mixed oxide, surface doped & physical mixture catalysts. 136
Figure 6-11 XPS spectra of JP25 (Co_3O_4), JP26 (100:30 mixed oxide) & JP27 (100:10 mixed oxide) at the Co 2p region. 137
Figure 6-12 XPS spectra of JP23 (Mn_3O_4), JP26 (100:30 mixed oxide) & JP27 (100:10 mixed oxide) at the Mn 2p region. 138
Figure 6-13 Summary of catalytic testing results of surface doped model catalysts at 240 °C. 141
Figure 6-14 Summary of catalytic testing results of mixed-oxide model catalysts at 240 °C. 142
Figure 6-15 Summary of catalytic testing results of physical mixture model catalysts at 230 °C. 143
Figure 6-16 Paraffin : Olefin : Alcohol selectivities for each catalyst series tested. 144
Figure 6-17 Alcohol selectivity (primary axis) and outlet H_2:CO (secondary axis) for each catalyst series tested. 145
Figure 6-18 Alcohol selectivity, CO_2 selectivity (primary axis) and H_2:CO consumption (secondary axis) for each catalyst series tested. 146
Figure 6-19 Activity of each catalyst series tested per g cobalt at 240 °C (*230 °C). 147
Figure 6-20 Activity profile of physical mixture model catalysts throughout testing, with temperature increases from 220 – 230 °C (green dashed line) for each catalyst, and temperature increase from 230 – 240 °C (orange dashed line) for 0 and 1 % Mn catalysts only. 148
Figure 6-21 DRIFTS spectra for CO absorption on supported mixed oxide catalyst series. 149
Figure 6-22 DRIFTS spectra with baseline correction and gas phase CO subtraction of supported mixed oxide catalyst series. 150
Figure 6-23 DRIFTS spectrum with baseline correction and gas phase CO subtraction of CO absorption on P25 TiO_2. 151
Figure 6-24 Normalised DRIFTS spectra of normalised CO absorption on unsupported mixed oxide model particles. 152
Figure 6-25 Normalised DRIFTS spectra with baseline correction and gas phase CO subtraction of normalised CO absorption on supported surface doped catalyst series. 153
Figure 6-26 Normalised DRIFTS spectra with baseline correction and gas phase CO subtraction of supported 3 % Mn catalysts with varying interaction methods. 154
Figure 8-1 – CT Example of reconstruction artefact caused by outer casing of thermocouple. Large grain size leading to incorrect reconstruction, with diffraction contribution from 310 Stainless steel fcc structure overlapping with internal reactor volume, including regions containing catalyst extrusion. 168
Figure 8-2 - Example diffraction pattern of catalyst extrusion voxel (red) and corresponding diffraction pattern of reactor diffraction contribution artefact (blue). 168
Figure 8-3 Example Rietveld refinement fit in Topas 6 for single voxel of 10% Mn extrusion at end of reduction. 169
Figure 8-4 – Summed X-ray diffraction patterns of 0% Mn catalyst at start (red) & end (blue) of FT conditions. 169
Figure 8-5 – Summed X-ray diffraction patterns of 0.5% Mn catalyst at start (red) & end (blue) of FT conditions. 170

Figure 8-6 - Summed X-ray diffraction patterns of 1% Mn catalyst at start (red) & end (blue) of FT conditions. 170
Figure 8-7 - Summed X-ray diffraction patterns of 10% Mn catalyst at start (red) & end (blue) of FT conditions. 171
Figure 8-8 Example input parameter file used for Rietveld refinements in Topas 6. 171
Figure 8-9 Refinement and refkey script. This script was used to process the cropped CT array of extrusion diffraction data for Rietveld refinement. The cropped array contains a series of 23x23 crops with increasing manganese & scan number on the axes. The doping level and scan number of each crop is identified, to correlate it with a specific input parameter file. The input parameter file for the refinement is shared for each voxel within a CT crop. Prior to a voxel being refined, selection criteria is applied to ensure diffraction contribution from the catalyst is present in that voxel, and that empty space is not being refined. The RefKey is a map of which voxels were refined, such that the output data can be spatially reconstructed. 174
Figure 8-10 Import Refined Parameters Script. This script is designed to rearrange the imported bulk results of a refined dataset into a 2D array. The refined data and refinement key are used to remap each refined voxel to their 2D coordinate. The 3rd dimension of the array are the various Rietveld refinement parameters exported from the input parameter files at the end of each refinement. .. 175
Figure 8-11 Radial Batching - This script filters each extrusion from the refinement key, and for each voxel gives a corresponding integer value for radial depth, from 1 at the catalyst exterior up to 4 at the catalyst interior.The refined values are then squeezed into a single average at each radial depth value, for each extrusion within the dataset. 176
Figure 8-12 - Example Rietveld refinement fit for single voxel of 10% Mn extrusion at end of reduction. 177
Figure 8-13 Summed diffraction pattern for 0 % Mn catalyst at t = 1 h & t = 36 h. 178
Figure 8-14 Summed diffraction pattern for 0.5 % Mn catalyst at t = 1 h & t = 36 h. 178
Figure 8-15 Summed diffraction pattern for 1 % Mn catalyst at t = 1 h & t = 36 h. 178
Figure 8-16 Summed diffraction pattern for 1.5 % Mn catalyst at t = 1 h & t = 36 h. 179
Figure 8-17 Summed diffraction pattern for 2 % Mn catalyst at t = 1 h & t = 36 h. 179
Figure 8-18 Summed diffraction pattern for 3 % Mn catalyst at t = 1 h & t = 36 h. 179
Figure 8-19 Summed diffraction pattern for 10 % Mn catalyst at t = 1 h & t = 36 h. 180
Figure 8-20 - EDX spectrum of JP11, 100:50 mixed oxide nanoparticles. 180
Figure 8-21 - EDX Layered Image of JP17-1, supported Co_3O_4 dispersed in P25 TiO_2. 181

List of tables

Table 2-1 Alcohol selectivities of cobalt-manganese oxide extrusions recorded at 220 °C. Values reproduced from Keyser et al. with permission from Elsevier, Appl. Catal. A 171, 1998, 99 – 107..... 33
Table 4-1 - Scans collected during catalyst activation with corresponding time and temperature ranges..... 59
Table 4-2 Cobalt oxide and metal phase % in refined extrusions post reduction, including HCP : FCC ratio and crystallite size. 71
Table 4-3 Rietveld refined Co(1-x)Mn(x)O phase wt. % at start and end of pseudo-FT conditions for each catalyst extrusion. 84
Table 5-1 XRD-CT scans collected during catalyst activation, with corresponding time and temperature ranges..... 96
Table 6-1 — Synthesis details of mixed spinel nanoparticles 124
Table 6-2 — Synthesis details of surface coated nanoparticles..... 124
Table 6-3 – Rietveld refined parameters of mixed spinel nanoparticles..... 128
Table 6-4 – Rietveld refined parameters of surface coated nanoparticles. 130
Table 6-5 — Rietveld refined parameters for surface coated particles supported on TiO_2..... 131
Table 6-6 — Elemental XRF analysis results of tested supported catalyst series 134
Table 6-7 – Relative Quantification of Co and Mn phases by fitting of XPS results. 139

Chapter 1 General Introduction

The Fischer-Tropsch (FT) process is the reaction of syngas (hydrogen and carbon monoxide) into long-chain hydrocarbons using a catalyst. The technology allows for the synthesis of high purity fuels and feedstock chemicals, traditionally derived from crude oil refinement, from gasified coal or natural gas[1,2] Interest in the technology is currently high due to the increase in natural gas sourced from shale fracking,[3] as well as the expected long-term increase in crude oil prices.[4] Additionally, incentives have made it economically viable to use the FT reaction to process methane (via syngas) sourced from waste and renewable sources, such as landfills and biomass sources, into carbon neutral fuels and feedstocks.[5]

The stoichiometry of the FT reaction is as shown in Equation 1-1, dependant on the final product:

$$nCO + (2n+1)H_2 \rightarrow C_nH_{2n+2} + nH_2O \quad (1.1.1)$$

$$nCO + 2nH_2 \rightarrow C_nH_{2n} + nH_2O \quad (1.1.2)$$

$$nCO + 2nH_2 \rightarrow C_nH_{2n+1}OH + (n-1)H_2O \quad (1.1.3)$$

$$nCO + (2n-2)H_2 \rightarrow C_{n-1}H_{2n-1}CO_2H + (n-2)H_2O \quad (1.1.4)$$

Equation 1-1 Stoichiometry of the Fischer-Tropsch reaction producing alkanes (1.1.1), alkenes (1.1.2), alcohols (1.1.3) & carboxylic acids (1.1.4).

An additional competing reaction also occurs between the produced H_2O, and the feed CO called the water gas shift (WGS) reaction, shown in Equation 1-2:

$$CO + H_2O \leftrightarrow H_2 + CO_2$$

Equation 1-2 Water Gas Shift equilibrium.

As the WGS reaction consumes the feed CO but produces H_2, the rate of this reaction can have an effect on the ratio of H_2:CO present during the reaction.

The syngas feed for the FT process is typically generated by either steam methane reforming (SMR), partial oxidation of methane or coal gasification. The method used for the production of syngas varies the H_2:CO produced, and so the WGS can be used to tune the ratio to the desired region.

There are two main catalyst systems used in commercial Fischer-Tropsch: cobalt-based and iron-based.[6] Both catalyst systems are typically supported on porous oxide supports, along with any dopants or promotors, however their operational conditions and product streams are different.[7][8] Traditionally, cobalt systems are more expensive, are more stable, run at a lower temperature and are focused on product streams that require high chain growth. Iron systems on the other hand favour olefin production, are more WGS active, and have lower methane selectivity.

In addition to cobalt and iron, nickel and ruthenium are also FT active but have not found commercial application. For nickel, this is largely due to its high methane selectivity. Ruthenium has been found to be highly active for FT compared to Co and Fe, however its high cost prohibits its use in industrial scale FT.

The Fischer-Tropsch reaction has a wide range of products. A distribution of carbon chain lengths are produced, with functional groups including alkenes, alcohols and acids, although the majority of product formed during cobalt Fischer-Tropsch are linear alkanes, and then alkenes, with only a small amount of alcohols and acids typically produced. Cobalt FT catalysts have been shown to be effective for selectivity towards high value middle distillates and waxes.[9][10]

The distribution of carbon chain lengths can be described by the Anderson-Schulz-Flory (ASF) distribution, as shown by Equation 1-3.[11] In this model, α is the probability of chain growth and is assumed to be independent of chain length. W_n is the weight fraction of a hydrocarbon with chain length *n*, and is dependent on α. Figure 1-1 A illustrates the effect of α on the carbon number distribution of the reaction with an ideal distribution, and Figure 1-1 B shows the linear relationship of ln(wt. % /*n*) of the ideal distribution with carbon number.

$$W_n = n\,\alpha^{n-1}\,(1-\alpha)^2$$

Equation 1-3 The Anderson-Schulz-Flory Distribution.

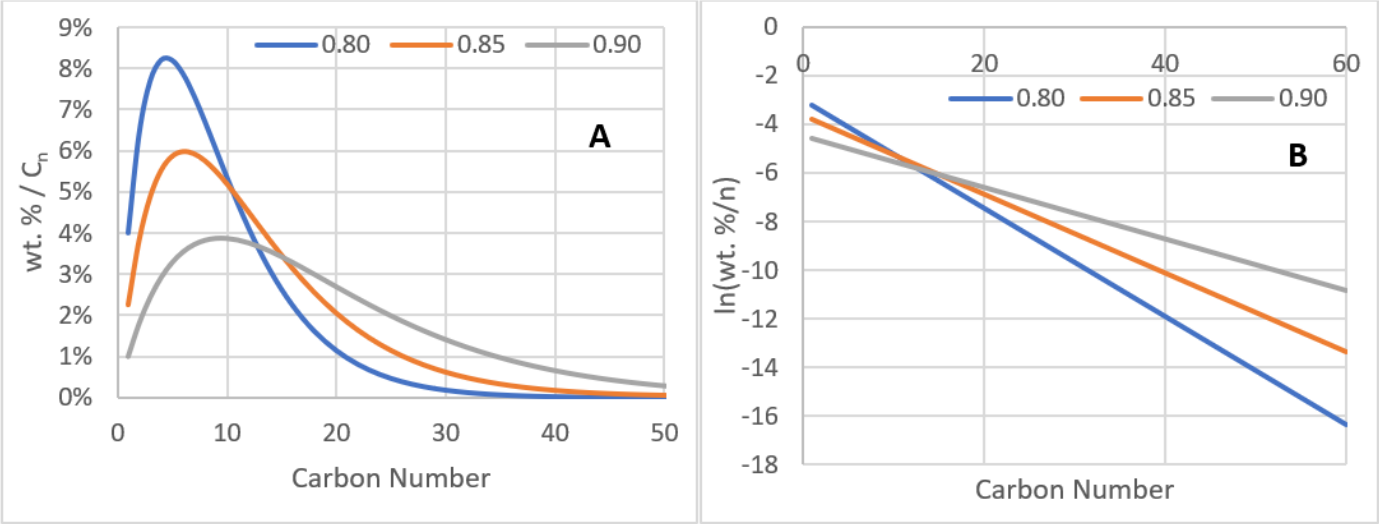

Figure 1-1 A) ideal weight % vs carbon number chain with varying alpha B) ideal ln(wt. %/n) vs carbon number with varying alpha.

Typically, catalyst design and process conditions are optimised to adjust α to maximise the productivity within the desired carbon number region. In addition to this, catalysts have been designed to influence the selectivity towards different functional groups[12] however efforts to do so can be challenging for multiple reasons. First, due to the complexity of both the reaction and the catalysts, the reaction mechanism is not understood well enough to be able to accurately predict the potential multitude of effects that changes in the catalyst will have on the reaction.[13] Second, due to the temperature and pressure requirements, it is not trivial to study the catalyst while it is under reaction conditions, or even in its active form. This means that if a catalyst is developed that is found to have favourable performance or selectivity, it can be challenging to understand why.

There are several suggested pathways for the mechanism of the Fischer-Tropsch reaction. A common suggested mechanism for the chain growth is via CO insertion[14] as shown in Equation 1-4. Here, a chemisorbed CO molecule is inserted between a carbon chain and the active cobalt surface.

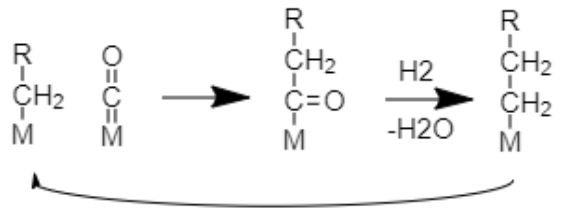

Equation 1-4 Simplified mechanism of CO insertion.

An alternative mechanism is CO dissociative carbide insertion, shown in Equation 1-5. Here, the CO is broken down on the surface of the catalyst, and reduced by H_2 prior to the insertion of the carbon into the growth chain. This mechanism gained traction due to the measurement of carbon covered surfaces which were oxygen deficient.[15]

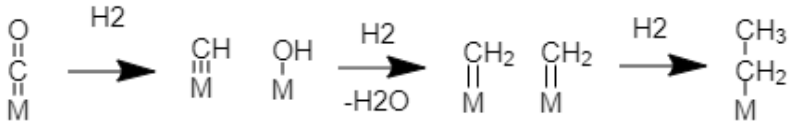

Equation 1-5 Simplified mechanism of CO dissociation and CH_2 insertion.

A key difference between the mechanisms is that the CO bond is present in the carbon chain for the CO insertion mechanism, whereas it is broken prior to insertion in the dissociative mechanism.

A significant proportion of publications on the development of Fischer-Tropsch catalysts do not discuss the selectivity of the catalyst towards oxygenate functional groups. This is likely due to the facilities required to accurately analyse liquid and wax FT products in comparison to the gas products, as well as the oxygenates typically being a minor component of the product distribution. A common metric used for the selectivity performance of a catalyst is C_5+ selectivity, which notes the percentage of carbon products with a chain length of C_5 and over. This is common as the value of products below C_5 is relatively low, and it is easy to infer the C_5+ selectivity by measuring only the gas phase products for C_1 to C_4, and assuming that the unmeasured remaining products are C_5+ . To accurately measure the alcohol selectivity is more challenging, as you would need to analyse the gas, liquid organic, wax and aqueous phases of your products. This challenge leads to relatively few publications that discuss product distributions beyond gas phase selectivity, C_5+ selectivity and ASF alpha. There is value in tailoring your reaction towards alcohol production though, as they are common feedstock chemicals in products such as detergents, plasticisers, fuel additives and solvents.

1.1 Commercial Fischer Tropsch

Since its discovery in 1925 by Franz Fischer and Hans Tropsch, the FT process has historically had sporadic commercial application. Utilisation of the reaction has been traditionally limited due to unfavourable economics compared to traditionally derived hydrocarbons, however exceptions have occurred in countries with limited oil reserves but significant coal reserves. For instance, Sasol has operated FT facilities in South Africa since the 1950s, producing liquid hydrocarbons from gasified coal and more recently natural gas.[16]

Modern utilisation of the FT process is limited to a small number of facilities, however growth has recently been driven due to the potential renewable scope of the reaction. While modern large scale FT facilities such as Pearl GTL in Qatar, and Shell MDS in Malaysia[17] produce liquid hydrocarbons from natural gas, recent investment in FT technology has centred around it's potential to produce more renewable hydrocarbons. The ability of the FT process to produce traditionally non-renewable products from methane derived from renewable or carbon neutral sources has resulted in an uptick in small scale commercial projects with various feedstocks.

For example in 2017, a reference plant operated in Oklahoma by ENVIA Energy, a joint venture involving Waste Management and FT technology from Velocys, produced 200 barrels per day of FT product from a feedstock of captured landfill methane blended with natural gas.[18] Additionally, in 2022 Fulcrum BioEnergy, with technology collaboration from BP and Johnson Matthey, commissioned a FT facility producing an estimated 11 million gallons of aviation fuel, diesel and petrol per year from gasified municipal waste.[19]

1.2 Catalyst Doping

Cobalt FT catalysts are frequently doped to alter their characteristics to be more favourable during operation. The addition of a dopant will typically aim to improve the catalyst activity, selectivity, longevity, or operability. For instance, platinum is commonly added to cobalt FT catalysts as it improves the reducibility of the catalyst, which means that catalyst activation can occur at a lower temperature and typically increases cobalt dispersion and therefor activity.[20] Reducing at a lower temperature can improve the characteristics of the activated

catalyst, such as improved surface area and limiting strong metal-support interaction (SMSI) on some supports. Lower reduction temperatures can also have implications on the specifications required for the reactor as catalyst reduction typically occurs at a much higher temperature than the catalyst is operated at.[21]

Another example of a dopant used in FT catalysts is an organic matrix combustion synthesis, where an organic fuel is added along with the cobalt salts during catalyst synthesis. The combustion of the fuel during calcination causes rapid oxidation of the cobalt, leading to more disperse oxide with higher surface area and a more active and stable catalyst.[22] While the dopant itself is not present in the active catalyst, it alters the synthesis of the catalyst such that the resulting structure is more favourable for the reaction.

Manganese was reported in relation to cobalt FT catalysis as early as the 1930s.[23] The investigation of manganese in modern day catalyst studies is extensive, and it has found it to have many effects on FT catalysis, including as an electronic promoter, stabiliser, water-gas shift promotor, reduction promotor, increasing cobalt dispersion and promoting favourable selectivity for chain growth and minimising methane selectivity.[24][25]

Recently, Paterson *et al*. have reported the effect of high manganese doping levels on significant increases in alcohol selectivity.[26] While alcohols typically form a minor part of the Fischer-Tropsch product stream, <3 %, the authors report selectivities of 30 % and beyond with the addition of manganese dopant at ratios of 3:10 Mn:Co and higher. The production of alcohols at such significant quantities would allow them to be separated into their own product stream on a commercial scale, whereas at typical selectivities they would be hydrogenated.

1.3 Scope of work

The aim of this project is to study the relationship of manganese oxide doping levels on titania supported cobalt Fischer-Tropsch catalyst extrusions, and its dramatic effect on long chain alcohol selectivity. Previous experimental results[26] on equivalent catalysts have shown that increasing manganese doping within a series of cobalt catalysts beyond 3 wt. % Mn loading drastically increases the alcohol selectivity by an order of magnitude, from <2.5 % alcohols

for 1 wt. % Mn loading, to >20 % alcohols for 3 wt. % Mn loading. Two approaches were used in this work to investigate the project's aim. Firstly, the catalyst extrusion series reported[26] by Paterson *et al*. were supplied by the project's sponsor, BP, and studied extensively by *in situ* XRD-CT during catalyst activation and FTS. Secondly, a variety of model catalyst systems were developed and tested to represent various Mn % loadings and Co-Mn interactions.

The reason for this significant and sudden increase in selectivity is not immediately apparent, and due to the complexity of characterising oxide supported catalysts *in situ*, it is not trivial to deduce which structures are present in the activated catalyst during reaction that may be responsible for the selectivity changes observed. The addition of the dopant also affects multiple characteristics of the catalyst, as well as influencing other operational metrics such as conversion.

Computed Tomography (CT) allows the reconstruction of an x-ray image across the measurement plane from the associated sinogram, collected via a series of translations and rotations. While traditionally the technique is used to reconstruct x-ray absorption contrast images, such as in the medical field, the reconstruction technique can also be applied to techniques relevant to material characterisation, such as x-ray diffraction (XRD) and x-ray fluorescence (XRF).[27][28][29]

X-Ray Diffraction Computed Tomography (XRD-CT) can be used to construct 2D planar images of catalyst samples, where each voxel within the image contains an x-ray diffractogram that represents the diffraction contribution from that point in space. This allows the technique to be used to spatially resolve the crystalline structures present within catalyst samples. As x-rays are highly transmissible and the technique is spatially resolved, this allows XRD-CT to be highly applicable to *in situ* and *operando* studies which can provide insight into a catalysts' crystalline phases under operational conditions.

In this work, *in situ* XRD-CT was used extensively to study the series of cobalt Fischer-Tropsch catalysts with varying manganese loadings. Both the experimental setup and processing pipeline were developed to attempt to maximise the potential of the measurement and to provide maximum insight into the catalyst series. This allows insight into which species are present during reaction, and their abundance and stability, and so their potential role in the observed changes in reaction metrics.

XRD-CT experiments were conducted during catalyst activation and reaction at atmospheric conditions. Subsequently, a high pressure cell was developed and commissioned to study the catalysts under representative FTS conditions, at 25 Bar pressure.

Additionally, model catalyst systems were developed and studied to investigate the relationship between specific manganese doping interactions on cobalt FT catalysts and alcohol selectivity. A series of catalysts with varying loading levels and orientations were developed to produce isolated cobalt-manganese environments, which were then characterised and tested for catalytic performance and alcohol selectivity. The use of model catalyst systems in this manner allows for a reduction in the complexity of the synthesised catalyst compared to traditionally synthesised catalyst systems.

1.4 References

1. F. Fischer and H. Tropsch, *Berichte der Deutschen Chemischen Gesellschaft (A and B Series)*, 1926, **59**, 830–831.
2. F Fischer, H Tropsch - US Patent 1,746,464, 1930
3. Natural gas supply, disposition and prices, US Energy Information Administration Forecast 2017 https://www.eia.gov/outlooks/aeo/data/browser/#/?id=13-aeo2017&cases=ref2017~ref_no_cpp&sourcekey=0 accessed 18th January 2019
4. Petroleum product prices, US Energy Information Administration Forecast 2017 https://www.eia.gov/outlooks/aeo/data/browser/#/?id=12-aeo2017&cases=ref2017~ref_no_cpp&sourcekey=0 accessed 18th January 2019
5. Renewable Fuel Standard Program, US Environmental Protection Agency, https://www.epa.gov/renewable-fuel-standard-program/renewable-identification-numbers-rins-under-renewable-fuel-standard accessed 18th January 2019
6. M. E. Dry, *Catalysis Today,* 2002, **71**, 227–241.
7. B. H. Davis, *Industrial & Engineering Chemistry Research*, 2007, **46**, 8938–8945.
8. M. Luo, S. Bao, R. S. Keogh, A. Sarkar, G. Jacobs, B. H. Davis, "Fischer Tropsch Synthesis: A Comparison of Iron and Cobalt Catalysts", AIChE 2006.
9. A. Y. Khodakov, W. Chu and P. Fongarland, *Chemical Reviews*, 2007, **107**, 1692–1744.
10. E. Iglesia, S. C. Reyes, R. J. Madon and S. L. Soled, *Advances in Catalysis*, 1993, 221–302.
11. H. Schulz, K. Beck and E. Erich, *Fuel Processing Technology*, 1988, **18**, 293–304.
12. G. Bezemer, P. Radstake, U. Falke, H. Oosterbeek, H. Kuipers, A. Vandillen and K. DeJong, *Journal of Catalysis*, 2006, **237**, 152–161.
13. A. A. Adesina, *Applied Catalysis A*: General, 1996, **138**, 345–367.
14. G. Blyholder, D. Shihabi, W. Wyatt and R. Bartlett, *Journal of Catalysis*, 1976, **43**, 122–130.
15. P. M. Maitlis, *Pure and Applied Chemistry*, 1989, **61**, 1747–1754.
16. Commercial use of Fischer-Tropsch synthesis - http://netl.doe.gov/research/Coal/energy-systems/gasification/gasifipedia/sasol accessed September 2022
17. https://www.shell.com.my/business-customers/shell-middle-distillate-synthesis/about-smds.html accessed September 2022
18. https://www.velocys.com/technology/ accessed March 2022
19. https://www.fulcrum-bioenergy.com/sierra-biofuels accessed July 2022
20. G. Jacobs, J. A. Chaney, P. M. Patterson, T. K. Das, J. C. Maillot and B. H. Davis, *Journal of Synchrotron Radiation*, 2004, **11**, 414–422.
21. S. Vada, A. Hoff, E. AdnaneS, D. Schanke and A. Holmen, *Topics in Catalysis*, 1995, **2**, 155–162.
22. P. Moreau, D. Leonarduzzi,, L. Barrio, H. Becker, and H. Robota, 25th North American Catalysis Society Meeting. NAM, 2017.
23. D. Smith, C. O. Hawk, and P L. Golden, *Journal of the American Chemical Society*, 1930, **52.8**, 3221-3232.
24. T. E. Feltes, L. Espinosa-Alonso, E. de Smit, L. D'Souza, R. J. Meyer, B. M. Weckhuysen, and J. R. Regalbuto, *Journal of Catalysis* 2010, **270.1**, 95-102.
25. F. Morales, E. de Smit, F. M. de Groot, T. Visser and B. M. Weckhuysen, *Journal of Catalysis*, 2007, **246.1**, 91-99.
26. J. Paterson, M. Peacock, R. Purves, R. Partington, K. Sullivan, G. Sunley and J. Wilson, *ChemCatChem,* 2018*,* **10.22**, 5154-5163.
27. T. M. Buzug, "Computed tomography." Springer handbook of medical technology, 311-342.
28. R. Collins, *Journal of Microscopy,* 1989, **156**, Pt 2.
29. G. Harding, J. Kosanetzky, and U. Neitzel, *Medical Physics,* 1987*,* **14.4**, 515-525.

30. R. Partington, J. Clarkson, J. Paterson, K. Sullivan, and J. Wilson, *Journal of Analytical Science and Technology*, 2020, **11.1**, 1-20.

Chapter 2 Literature review

Promoters or dopants are introduced to catalysts for a variety of reasons. Platinum for example, is a common promoter added to cobalt FT catalysts to improve the reducibility of the cobalt, and so increasing the catalyst activity or lowering the parameters required for the reduction.[1] Alternatively, a promoter may be added to vary the reaction during the synthesis of the catalyst. For example, Girardon *et al*.[2] introduced ruthenium nitrosyl nitrate in combination with cobalt acetate during synthesis, which lead to a decrease in the decomposition temperature of the salts, and a higher dispersion of the cobalt in the synthesised catalyst. In both examples, the researchers were trying to maximise the potential for cobalt to perform as a catalyst, however some dopants are used to change the selectivity or stability of a catalyst. For instance, Xiong *et al*.[3] found that the addition of zirconium to an alumina supported cobalt catalyst lowered the amount of cobalt aluminate species formed during reaction. This limited the catalyst deactivation during the FT reaction, as a common deactivation mechanism for supported catalysts is the formation of cobalt-support mixed oxides.

The mechanism by which a promoter or dopant affects a catalyst is not always trivial to determine, and can require intricate examination. For instance, Bertole *et al*. [4] studied the effects of rhenium on various supported cobalt FT catalysts by measuring $^{12}CO \rightarrow {}^{13}CO$ isotope transients in reaction steady state measurements. They found that while rhenium does benefit the catalyst's methane selectivity via improved reducibility, it doesn't take part in the catalysis itself as any Re/Co mixed alloys will be depleted of Re at the surfaces.

2.1 Effect of Mn doping on Co FT catalysts

This project focuses on the addition of manganese as a dopant to titania supported cobalt FT catalysts. While manganese is a widely studied dopant in FT catalysts, with benefits ranging from methane selectivity,[5] % C5+ selectivity,[6] and olefin selectivity,[7] its potential in the promotion of alcohol selectivity is not widely realised.

Morales *et al.* [8] found that the addition of 2 wt. % Mn to their 7.5 wt. % Co/TiO_2 catalysts had desirable effects on the catalyst. This includes slightly increased activity, decreased methane selectivity and increased ASF α. These observations held for the pressures tested at, 1, 4, 8 and 18 bar. They also observed a decrease in the reducibility of the catalyst, however they do not discuss the reaction selectivity beyond methane and C5+ selectivity. The authors' hypothesis for the observed effects of manganese doping involves a lower capacity of the catalyst to chemisorb hydrogen, which may reduce the rate of chain termination, therefore increasing chain growth probability. The focus of this publication was to investigate how the doped Mn interacts with the cobalt phase. Through Scanning Transmission Electron Microscopy – Electron Energy Loss Spectroscopy, (STEM-EELS) the authors observed MnO particles preferentially around cobalt sites as shown in Figure 2-1, rather than the manganese forming mixed spinel oxides with the cobalt. They suggested that this proximity could allow the MnO to act as a co-catalyst to the cobalt after the reduction of the catalyst, by providing additional CO insertion sites for chain growth and increasing reaction rate.

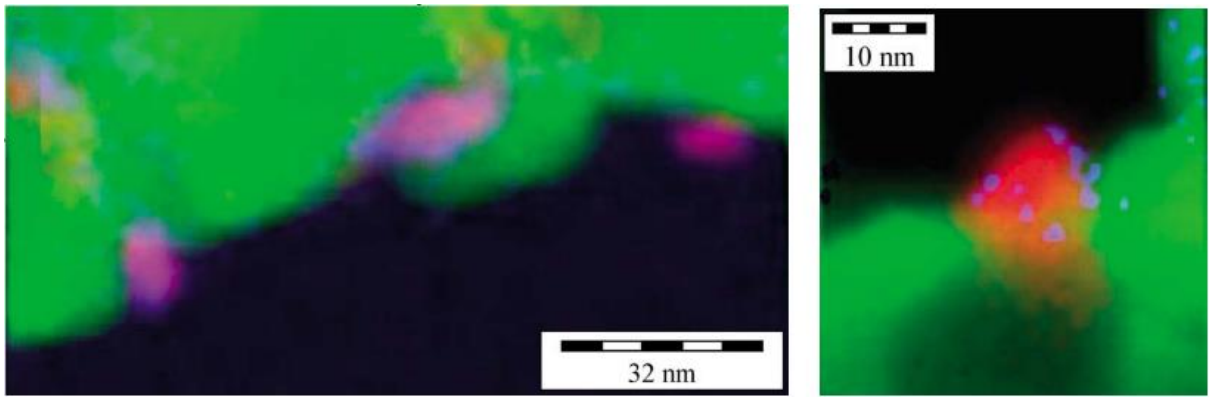

Figure 2-1 STEM-EELS (Co = red, Mn = blue, Ti = green) of calcined 7.5 wt.% Co, 2.5 wt.% Mn / TiO_2 catalyst. Reproduced from Morales et al. with permission from Elsevier, Journal of Catalysis., 2005, 230, 301 – 308.

In additional work published by Morales *et al*,[9] the effect of the manganese oxide promotor on the CO and H_2 adsorption properties was investigated. The authors used Diffuse

Reflectance Infrared Fourier Transform Spectroscopy (DRIFTS) to observe that increases in manganese doping beyond 2.15 % (or just over 0.3:1 Mn:Co by weight) significantly hinder the catalyst's ability to chemisorb hydrogen. They suggest that this reduced hydrogen availability is responsible for an observed increase in the formation of olefins, as well as an improvement in C5+ selectivity.

The DRIFTS experiments studying the dopants effect on CO adsorption showed a strong correlation between the amount of manganese doped, and the strength of the adsorbed CO bond. They suggest that the dopant is withdrawing electron density from the active cobalt, which in turn reduces electron back donation into the CO π^* orbital. This relatively strengthened CO bond is less prone to CO dissociation and hydrogenation, and the authors suggest that this electronic promotion by the manganese is responsible for the observed decrease in methane selectivity. They also note that the increased Mn doping led to an increase in the reaction CO_2 selectivity at high levels, suggesting the MnO was acting as a catalyst for the WGS reaction.

Zhou *et al*. [10] investigated the potential of an unsupported, 20 wt. % Co/MnO_x catalyst for an olefin selective Fischer-Tropsch synthesis. By changing the solvent used for the synthesis from water to 1,4-Butanediol (BDO), the authors introduce a change in the final structure and performance of the catalyst. Via DRIFTS experiments, the authors observe that the addition of BDO to the catalyst synthesis leads to a system that prefers linearly adsorbed CO over bridged CO, likely due to an increase in electron density of the cobalt. This suggests a reduced interaction between the cobalt and manganese dopant in the BDO catalyst, relative to the H_2O-synthesised catalyst. This effect could lead to an increase in the rate of CO dissociation, as well as a reduction in the rate of hydrogenation, which they suggest is responsible for the observed increase in reaction rate, and olefin selectivity, between the catalysts. Similarly, the reduction profile of the BDO catalyst follows a more similar profile to a reference Co_3O_4 than the H_2O catalyst, who's reduction profile is less well defined. This also suggests reduced interaction between the cobalt and manganese species in the BDO catalyst.

Research published by Treviño *et al*. [11] have noted the ability of MnO to provide stable sites for terminal oxygenate intermediates while studying manganese oxide doping on zeolite supported ruthenium catalysts. The authors discuss the use of the catalyst in higher oxygenate formation. They demonstrate the ability of MnO to adsorb terminal CO with FTIR

spectra, with which they also show that physical mixtures of supported MnO and supported Rh do not behave in the same way as Rh and MnO supported in proximity. This gives rationale for the increased oxygenate production they observe with the MnO doping, as the MnO site is able to facilitate CO insertion into a growing alkyl chain from the Rh site, and stabilize the terminal oxygenate intermediate before the chain is hydrogenated into its final product

Johnson *et al*. [12] investigated the effect of Mn promotion on the performance of a Co/SiO_2 catalyst. The dopant was added in unison with the cobalt precursor during a typical IWI synthesis, where manganese acetate was added along with the cobalt nitrate solution precursor to a support prior to calcination, with a Mn:Co ratio up to 0.5:1. The authors characterised the resulting catalysts extensively, including STEM-EDX elemental maps showing the distribution of the doped manganese oxide in relation to the cobalt species. The elemental maps show a clear preference for the manganese species to sit adjacent to the cobalt, similar to observations made by Morales *et al*.[8] They also observed a decrease in hydrogen chemisorption with increasing Mn, as well as a decrease in cobalt reducibility. Particle size measurements taken by TEM did not appear to show any dependence with doping levels, with the exception of a slight increase in mean crystallite diameter at 0.5:1 Mn:Co from ~10 to ~12 nm.

X-ray absorption spectra were also collected for the catalyst series for the passivated catalysts, the reduced catalysts, and the reduced catalysts after 6 h of syngas exposure. The results for the Mn K-edge indicate an initial oxidation state of the Mn between that expected for Mn_2O_3 and MnO_2, however after reduction there was a shift towards that expected of MnO for all the samples. Exposure to syngas had little effect on the Mn state. There was a definite trend in cobalt reducibility however, with Co(0) levels in the reference catalyst at 55 %, decreasing for each catalyst in the series down to only 23 % Co(0) for the 0.5:1 Mn

The authors also studied the temperature at which CO is desorbed from the catalysts, noting that the desorption temperature reached a plateau of 460 °C at 0.1:1 Mn:Co and did not increase with increasing manganese doping. These observations are mirrored by the observed trend in product selectivity, where the addition of Mn has a favourable effect on the methane

and C5+ selectivity up to 0.1:1 Mn:Co, however between 0.1 and 0.5, little change is observed as shown in Figure 2-2.

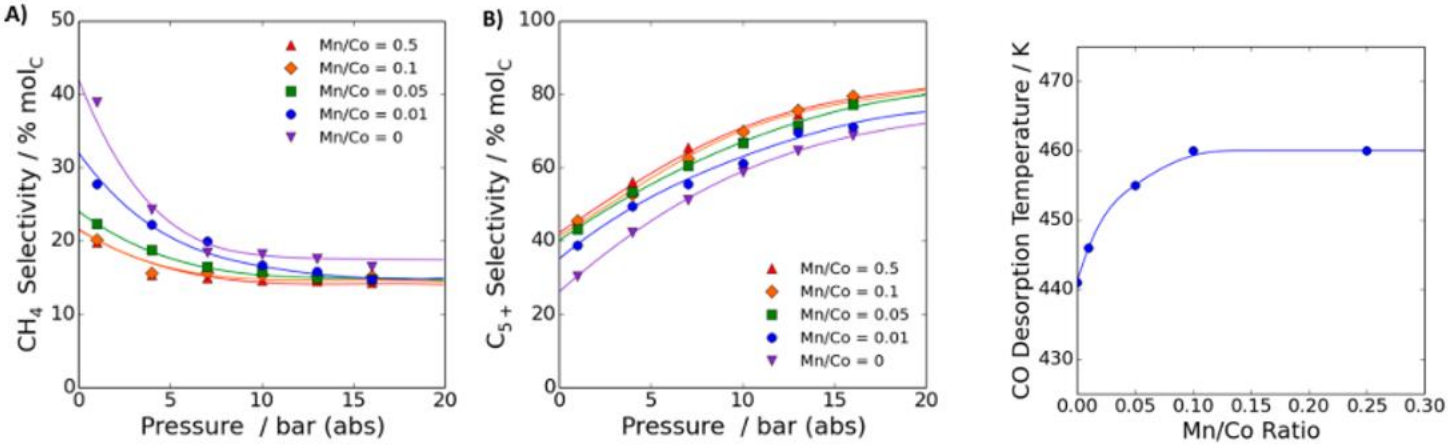

Figure 2-2 A & B) effect of pressure on Fischer-Tropsch selectivity. C) CO desorption temperature vs Mn/Co ratio as measured by TPD. Reproduced from Johnson et al. with permission from ACS Publications, ACS Catalysis., 2015, 5, 5888 – 5903.

Regarding catalyst activity, the authors found that the addition of 0.01 Mn:Co increased the catalyst activity by roughly 50 % in terms of CO consumptions rates per unit of cobalt. Increasing the dopant ratio to 0.05:1 returned an activity similar to that of the unpromoted catalyst, and further increases in dopant continued to reduce the activity. If however you compare the CO consumption against the available catalyst sites, as determined by H_2 chemisorption post reduction, the addition of the dopant increases the TOF per catalyst site up to 0.1:1, similar to the changes observed in the selectivity and CO desorption temperatures.

Johnson *et al.* hypothesise that the observed plateau could be due to the Mn forming a metal alloy with the active Co, with preferential placement on the surface of the nanoparticle due to Mn's lower surface free energy. This is supported by the amount of Mn required to form a monolayer on the surface of the nanoparticles being roughly 0.1:1. The authors note that while these observations are consistent, they found no evidence of metallic Mn and XANES spectra showed the Mn to be in a mixture of +2 and +3 oxidation state in the reduced catalyst. The manganese being present in the oxide form is also consistent with studies on similar systems by Morales *et al.*[8] discussed prior.

While the authors do not report the effect of the dopant on the selectivity of different functional groups, they do hypothesise the observed effect on activity and chain growth. They attribute an increase in CO adsorbates with increasing Mn doping as being a potential factor for two reasons. First, they note that increased CO surface coverage would favour chain growth due to the reduced coverage of H_2 available for chain termination. Second, the carbonyl stretching frequencies of adsorbed intermediates as measured by IR spectroscopy are weakened. This would allow for an Increase in the rate of CO disproportionation and therefore chain growth. This hypothesis is compatible with that proposed by Morales *et al.* [9], where they suggest a reduction in the ability of the catalyst to adsorb H_2 is responsible for a decreased chain termination rate, however Morales *et al*. suggested the observed rate change was potentially due to adjacent MnO_2 particles providing additional sites for CO insertion.

An additional effect of the weakened carbonyl stretches observed by Johnson *et al*., is a potential increase in the chance of the carbonyl bond to be reduced to form a terminal alcohol during chain termination, however the authors do not discuss the effect these observations may have on functional group selectivity.

In Summary, Johnson *et al*. extensively study the manganese doped Co/SiO_2 catalysts, and their observations of preferential manganese sites adjacent to active cobalt species, and the effect on the adsorption of CO and H_2 provide insight into the potential cause of the observed effects of manganese on alcohol selectivity, albeit on a different catalyst support than this project.

2.2 Alcohol selective FT catalysts

Paterson *et al.*[13] report the performance of Mn-doped Co-FT catalysts with manganese loadings ranging from 0 – 10 wt. % on 10 wt. % Co/TiO_2. The authors found increasing the Mn doping led to a trend of decreasing Co_3O_4 crystallite size in the synthesised catalyst as measured by both XRD and H_2 Chemisorption. While addition of 1 % Mn was reported to have roughly double the CO conversion versus the undoped catalyst, as predicted by the decreased crystallite size, the 5 % Mn catalyst reportedly has less than half the activity of the undoped catalyst.

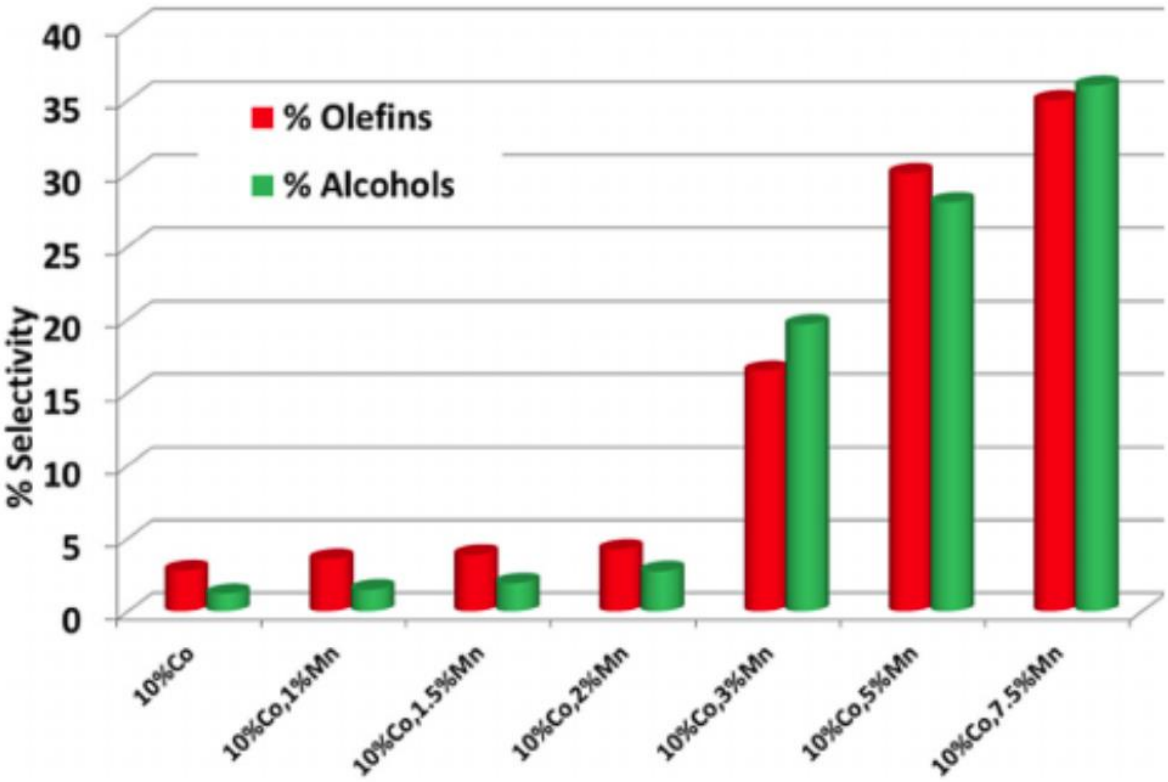

Figure 2-3 Alcohol and Olefin selectivity with increasing manganese doping on 10 % Co/TiO_2. Reproduced from Paterson et al. with permission from Wiley-VCH, ChemCatChem 2018, 10, 5154 – 5163.

Figure 2-3 shows the reported selectivity towards olefins and alcohols for each doping level studied by Paterson *et al*. While relatively minor increases are observed in alcohol selectivity up to 2 % Mn, which displays ~2.5 % alcohols, a significant increase is observed at higher manganese loadings. The 3 % Mn catalyst displays an alcohol selectivity of almost 20 %, while the higher loadings of 5 and 10 % Mn are reported to have ~27 and ~35 % alcohol selectivity.

The trend observed with the alcohol selectivity with increasing manganese is parallel to the olefin selectivity, which increases in a similar order of magnitude.

Meanwhile they observe that the changes in activity and selectivity are not observed in catalysts prepared by combining physical mixtures of supported Co and Mn on TiO_2, and only in catalysts prepared with co-impregnation of the synthesis salts.

The observed effects of the addition of manganese during the catalyst synthesis suggest both a structural and an electronic effect on the resulting catalyst. The increased dispersion of the cobalt oxide in the calcined catalyst shows that the addition of manganese is having an effect during the calcination stage of the catalyst synthesis, and the increase in surface area as measured by H_2 chemisorption shows that this increased dispersion persists throughout reduction. The significant increases observed in olefin and alcohol selectivity show that the manganese is also involved in a modification of the cobalt, with a close interaction required as backed up by the lack of selectivity changes within the physical mixture systems reported.

To understand how the effect of Mn loading affects the catalyst during operation at different positions of the bed, Paterson *et al*. conducted *in situ* XRD on the 1 and 5 % Mn extrusions with varying H_2:CO ratios to represent different bed positions. The formation of bulk cobalt carbide was measured on the 5 % Mn extrusion under FT conditions of 10 bar, H_2:CO of 1.4. As the ratio of H_2:CO decreases towards the outlet of the reactor during FTS, this ratio represents a typical ratio around the middle of the catalyst bed. Study of the 1 % Mn however under the same *in situ* experiment found that even with a H_2:CO ratio as low as 0.6, the 1 % Mn did not indicate any presence of CoC_2 by XRD.

Pei *et al*. [14] demonstrate the ability of Co-CoC_2 catalysts to produce long chain alcohols during Fischer-Tropsch synthesis. They report a reference Co catalyst achieving 7.5 % alcohol selectivity, while the Co-CoC_2 equivalent catalyst achieved a significantly higher selectivity of 38.4 %. This comes at the significant expense of % C5+ selectivity however, which in the reference catalyst is 74.3 %, decreasing to 36 % in the Co-CoC_2 catalyst They suggest that the cause for this increased alcohol production is explained by DFT calculations they performed showing the increase in activation energy for the dissociation of CO over the CoC_2 sites in comparison to the Co sites. This favours the retention of the CO bonds via non-dissociative adsorption, increasing the selectivity towards oxygenates as final products. This effect would

have to occur at the Co-CoC_2 interface to allow for the alcohol group to be added during the chain growth.

Given this, the formation of surface or bulk CoC_2 on the catalyst extrusions reported by Paterson *et al*.[13] is a potential mechanism by which the presented alcohol selectivity is achieved with the high % Mn loadings. The consumption of active cobalt metal to a carbide phase would also be consistent with the observed drop in activity that is associated with the increased alcohol selectivity.

Xiang *et al*. [15] discuss the use of their CoCuMn core-shell catalysts for the selective synthesis of long-chain terminal alcohols during Fischer-Tropsch. The catalyst particles contained predominantly a Co core, with a Cu and Mn mixed shell. A reference sample with a Co core and Cu shell was also included. Through Atom Probe Tomography (APT), the authors map the elements within a particle, showing a strong CuMn shell and Co core with slight amounts of Cu and Mn scattered throughout. They also see minimal presence of oxygen atoms on the surface of the particle, significantly below stoichiometric quantities for the corresponding metal oxides. The authors observe that the addition of Mn to the catalyst significantly increases both terminal alcohol selectivity and CO conversion as shown in Figure 2-4.

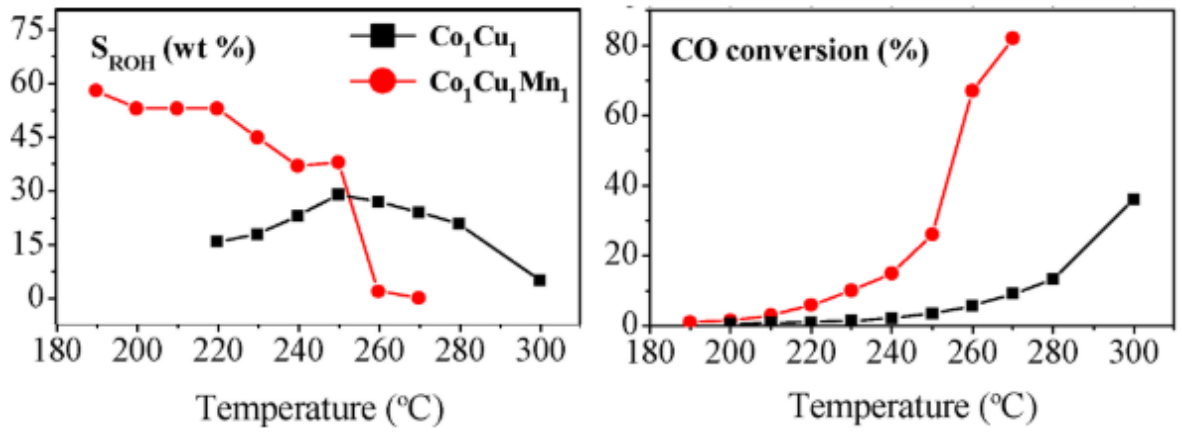

Figure 2-4 Alcohol group selectivity and CO conversion measurements against temperature. Reproduced from Xiang et al. with permission from ACS Publications, Journal of the American Chemical Society. 2013, 135, 7114 – 7117.

While the alcohol selectivity is high, it decreases with increasing temperature and conversion, dropping to almost 0 % at conversions above 60 %. This makes the yields below 10 % at its highest at 250 °C. The authors do not put forward a hypothesis for the dependence of Mn on alcohol selectivity or the activity increase, though they do note that the particles they

measure via APT may be subject to reconstruction during the reaction. Although the recorded selectivity is high at lower temperatures, the lack of conversion leads to the productivity to remain low (<5 %) throughout the temperature range.

Chaumette *et al*. [16] studied the mechanistic route for alcohol insertion and hydrocarbon chain growth in doped cobalt systems. Their aim was to design tests that simulate the mechanistic steps and correlate the results to the catalyst reaction performance. They report a correlation between higher alcohol selectivity and the disproportionation of acetaldehyde during temperature programmed desorption (TPD) measurements, in tandem with hydrocarbon selectivity with CO disproportionation. The authors doped a Co catalyst with Cu, Mo, Ru and an unspecified promotor to vary the catalysts ability to disproportionate acetaldehyde and found strong correlation between these results, and the catalysts' alcohol selectivity.

Keyser *et al.*[7] synthesised mixed oxide extrusions of cobalt and manganese via coprecipitation with ammonium hydroxide. The authors tested the extrusions under FT conditions, including measuring the alcohol selectivity up to C_6, however at H_2:CO ratios of 1:1 and 2:1. Table 2-1 shows the selectivities recorded in a fixed bed reactor for two Co:Mn ratios under differing operating conditions.

Table 2-1 Alcohol selectivities of cobalt-manganese oxide extrusions recorded at 220 °C. Values reproduced from Keyser et al. with permission from Elsevier, Applied Catalysis A 171, 1998, 99 – 107.

Co:Mn	**1:1**	**1:1**	**1:3**	**1:3**
H_2:CO	1:1	1:1	2:1	2:1
GHSV (1/h)	222	222	75	75
PRESSURE (Bar)	6	21	21	21
TIME ON STREAM (TOS)	507	641	293	1366
BED LENGTH (m)	0.25	0.25	1	1
%CO CONVERSION	14.0	18.0	66.0	33.3
%C_1OH	1.98	1.33	1.85	0.55
%C_2OH	3.81	2.29	4.43	1.14
%C_3OH	2.59	1.33	2.40	0.44
%C_4OH	0.35	0.43	4.49	1.00
%C_5OH	0.12	0.07	2.66	1.16
%C_6OH	0.07	0.04	1.68	1.11
%C_4-C_6OH AVERAGE	0.18	0.18	2.94	1.09

A significant difference in C_4-C_6 alcohol selectivity was recorded between the 1:1 and 1:3 doping ratios, however the reported operating conditions differ significantly in the reported data. It was observed that as the 1:3 catalyst deactivated, the average C_4-C_6 selectivity dropped significantly from 2.94 % to 1.09 %. The authors do not discuss the potential active species present during FT reaction after the initial reduction at 350 °C under 100 GHSV of pure hydrogen.

Ribeiro *et al*. [17] report the effect of various support dopants in Ce/Si mixed oxide supported Co FT catalysts, including with manganese. Cobalt was loaded onto the $CeO_2.SiO_2$ and the modified 10 % $MnOx/CeO_2.SiO_2$ to 15 wt. % via incipient impregnation, in the same step as the addition of the manganese in the modified support. The resulting catalysts were reduced and tested under FT conditions at 18.3 bar, 220 °C. Both catalysts discussed show promising n-alcohol selectivity as shown in Figure 2-5, with selectivity increasing as the reaction proceeds up to 300 h on stream, however the authors do not define the n-alcohol selectivity other than as $C_{2+}OH$. Ribeiro *et al*. hypothesise that the increase in alcohol selectivity over time is due to a reduction in the catalyst's ability to hydrogenate the functional group, though have no determination as to the effect Mn doping is having on the catalyst to cause this.

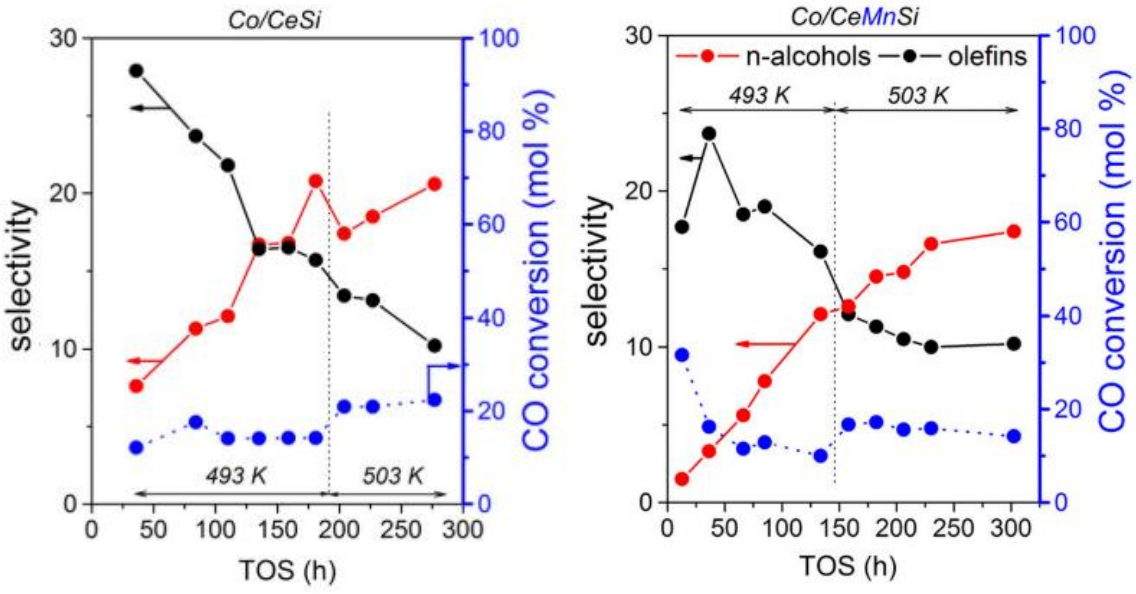

Figure 2-5 CO conversion and selectivity for a) Co/CeSi catalyst b) Co/CeMnSi catalyst. Reproduced from Ribeiro et al. with permission from Springer, Topics in Catalysis 2014, 57, 550 – 560.

2.3 Model Catalyst Systems

One of the difficulties in studying supported catalysts is that there can be a wide range of environments and species within the sample. This can lead to challenges in both synthesising specific catalyst environments, as well as characterising them. A way to simplify this, is to study model catalyst systems. This involves synthesising active or precursor particles separate to the catalyst support, allowing you to modify and characterise your active component prior to supporting. It can also allow you to effectively tune specific variables, such as crystallite size or wt. % loading, without impacting other characteristics of the catalyst which may be sensitive to alterations of traditional synthesis methods such as incipient wetness impregnation (IWI).

Werner *et al*. [18] synthesised model catalysts while studying the effect of Mn doping on CH_4 and C5+ selectivity of cobalt FT catalysts. The authors synthesise nanoparticles of Co and Co-Mn (10:1 Co:Mn) by a polyol reduction of metal acetylacetonates. High resolution STEM-EDS showed homogenous distribution of Mn in the doped nanoparticles. The supported particles were compared to traditionally synthesised catalyst equivalents. Catalytic testing found that the model samples performed comparably to the traditionally synthesised IWI catalysts in regards to turnover frequency (TOF) and selectivity, however the rate per gram of cobalt of the model systems was <20 % that of the traditional catalysts. The authors attribute this to significant sintering of the model particles during calcination once supported due to the small particle size distribution, (2-12 nm) leading to a loss of available surface area and lower activity.

Prieto *et al*.[19] utilised model Co/ITQ-2 catalysts to study the effect of cobalt particle size in FT synthesis. The authors tuned a reverse micellar synthesis to load Co_3O_4 particles with varying crystallite size distributions (ranging 6 – 12 nm) onto the zeolite support, as well as a commercial Co_3O_4 nanopowder (125 nm). The produced catalysts were used to study the dependence of TOF with Co particle size, and the authors were able to confirm an increase between 5.6 – 10.4 nm, with TOF stabilising above. The authors also used FTIR to study the absorption of CO on the surface of the catalysts, and observed reconstruction of the metal surface under ambient pressure FT condition, associated with the CO dissociation irrespective

of metal particle size. The authors also observe a restructuring of the catalyst by CO-FTIR under ambient FT conditions, occurring across the particle sizes studied.

2.4 In Situ study of catalysts by CT methods

In recent years, advances in synchrotrons have allowed for traditional X-ray based analytical techniques to be combined with computed tomography, to introduce a spatial factor to measurements and resulting in 2D or 3D images. For example, with X-ray Diffraction Computed Tomography (XRD-CT) it is possible to generate a 2D or 3D map of a samples crystalline structure, providing insight into spatial effects and inhomogeneity that would otherwise be unknown.

Jacques *et al*. [20] have demonstrated the ability of XRD-CT as a technique to track the evolution of chemical structures of a supported catalyst. In the study, an alumina supported nickel catalyst is measured during *in situ* calcination from the catalyst precursor. Figure 2-6 illustrates the precursor transitioning to the final catalyst via several intermediate steps. The authors identify 9 separate crystalline phases during the thermal activation by XRD-CT. Given the CT technique allows reconstruction of the collected diffraction contribution, the crystalline phases (and their mean crystallite size) can be spatially resolved within the cross section of the catalyst pellet.

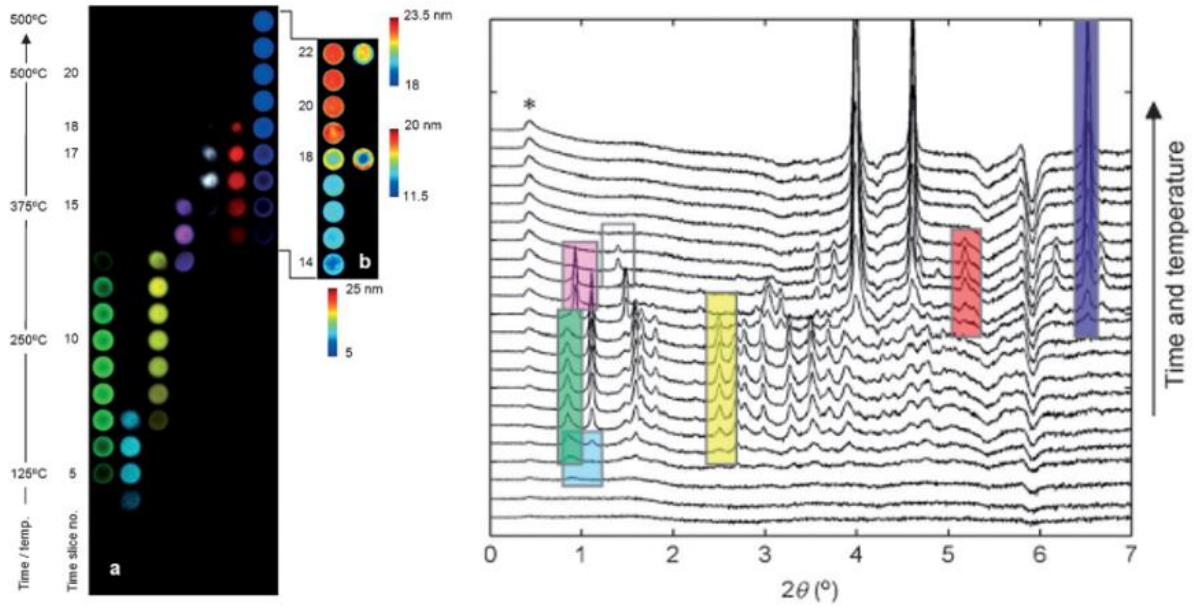

Figure 2-6 Transitions observed in a gamma alumina supported Ni catalyst precursor during thermal activation via XRD-CT. The heatmaps on the left correspond to the spatially resolved peak intensities from the diffraction patterns right. Reproduced from Jacques et al. with permission from Wiley-VCH, Angewandte Chemie International Edition 2011, 50, 10148 – 10152.

Senecal *et al.* [21] have studied a Co/Al_2O_3 Fischer-Tropsch catalyst by *in situ* XRD-CT. Utilising the technique, the chemical structure of a catalyst pellet has been mapped, allowing the tracking of the catalyst phases during reduction and reaction conditions. The authors conducted the reduction and reaction at atmospheric conditions in a 4 mm diameter quartz tubular reactor. By measuring the composition over the reduction, they are able to track the peak intensity of the diffracted cobalt phases and indicate the relative levels of active cobalt metal present. This is also mapped onto the catalyst pellet and shows not only a heatmap of the cobalt species, but also the distribution of crystallite sizes.

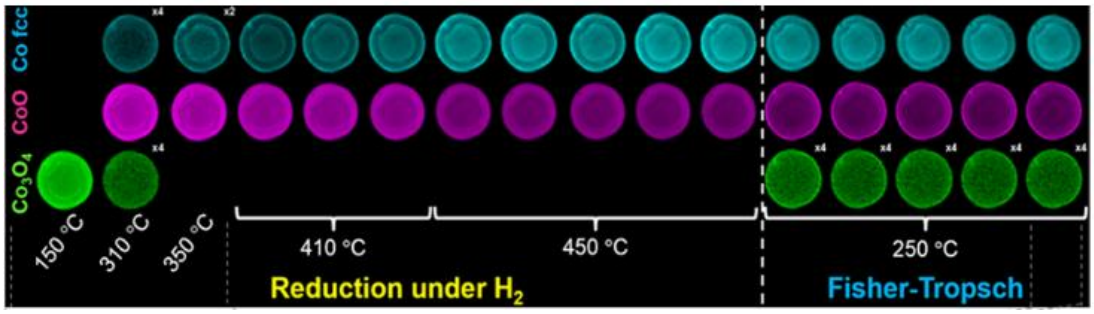

Figure 2-7 XRD-CT intensity maps for cobalt species during reduction and Fischer-Tropsch of 10% Co/Al_2O_3. Reproduced from Senecal et al. with permission from ACS Publications, ACS Catalysis 2017, 7, 2284 – 2293.

As shown in Figure 2-7, the authors were able to observe the initial formation of CoO from Co_3O_4 during the early stage of the reduction, followed by the evolution of cobalt metal from CoO as the reduction temperature increases to 450 °C. They also observed the re-oxidation of cobalt species to CoO and Co_3O_4 during FT reaction. The spatial dimension of the measurement also allowed the authors to observe a dependence of Co_3O_4 crystallite size and reducibility.

Additionally, the spatially resolved technique allowed the authors to observe inhomogeneity within the catalyst pellet, with the cobalt species showing a slight transition in intensity as a function of pellet depth, suggesting an egg-shell, egg-yolk preferential distribution.

In this work, the relative quantification of the crystalline phases containing cobalt was achieved via Bragg peak fitting using a Gaussian function. For each phase, a single peak was fitted and intensity used as a basis for the ratio of total cobalt phases.

Another technique the authors utilised was Pair Distribution Function CT (PDF-CT). An advantage of PDF-CT is that its sample sensitivity is independent to crystallite size, unlike XRD. This means that PDF-CT is able to map the crystallite size distribution of the sample more accurately, and to observe smaller crystallite sizes. The authors used the technique to map the cobalt species crystallite size distribution and observed that the smaller Co particles were likely to be oxidised during the FT reaction, leading to an increase in the average Co crystallite size. The technique allowed the authors to determine that the increase in average crystallite size (as seen by XRD) was due to this preferential oxidation of smaller particles, rather than from the sintering of multiple smaller particles to single larger particles.

2.5 In Situ X-ray Diffraction of Cobalt FT Catalysts

Karaca *et al*. [22] report using *in situ* XRD to study the evolution of cobalt within a FT catalyst operating under realistic FT conditions (20 bar, H_2/CO = 2, T = 493 K). The alumina supported catalysts were loaded with 25 wt.% Co and 0.1 wt.% Pt, prepared via a two-step IWI co-impregnation. The synthesised catalysts were studied by *in situ* XRD loaded in a 1 mm quartz capillary. The authors identify cobalt sintering within a short reaction timeframe, 3-5 h, as well as the formation of cobalt carbide beyond 8 h, both of which they identify as responsible for deactivation due to a decrease in active cobalt sites. The small diameter of the reaction cell used allow the authors to operate under representative FT pressures, while obtaining good quality results with observations made in relevant time frames.

Paterson *et al*.[23] compare the evolution of cobalt phases during typical H_2 activation versus a sequential H_2-CO-H_2 activation on Co/TiO_2 by *in situ* XRD. Using an *in situ* setup with a high-powered lab diffractometer, they observe the preferential formation of the cobalt HCP via the H_2-CO-H_2 treatment, as well as an associated decrease in methane selectivity and improvement in C5+ selectivity. Additionally, Paterson *et al*.[24] also report on the effect of water dosing during catalyst activation on the progression of cobalt phases as measured by *in situ* XRD. They see a delay in reduction of CoO during activation with H_2O dosing, proportional to the amount being dosed. In the resulting activated catalyst, sintering is observed with increasing H_2O dosing. The experiment provides insight into the effect of bed position during catalyst reduction, due to the H_2O partial pressure increasing with bed position towards the reactor outlet during catalyst activation.

2.6 References

1. S. Vada, A. Hoff, E. AdnaneS, D. Schanke and A. Holmen, *Topics in Catalysis*, 1995, **2**, 155–162.
2. J. S. Girardon, A. Constant-Griboval, L. Gengembre, P. A. Chernavskii, and A. Y. Khodakov, *Catalysis Today,* 2005*,* **106.1-4**, 161-165.
3. H. Xiong, Y. Zhang, K. Liew, and J. Li, *Journal of Molecular Catalysis A: Chemical,* 2005*,* **231.1-2,** 145-151.
4. C. J. Bertole, C. A. Mims, and G. Kiss, *Journal of Catalysis*, 2004, **221.1**. 191-203.
5. T. E. Feltes, L. Espinosa-Alonso, E. de Smit, L. D'Souza, R. J. Meyer, B. M. Weckhuysen, and J. R. Regalbuto, *Journal of Catalysis* 2010, **270.1**, 95-102.
6. G. Bezemer, P. Radstake, U. Falke, H. Oosterbeek, H. Kuipers, A. Vandillen and K. DeJong, *Journal of Catalysis*, 2006, **237**, 152–161.
7. M. J. Keyser, R. C. Everson, and R. L. Espinoza, *Applied Catalysis A: General*, 1998, **171.1**, 99-107.
8. F. Morales, F. M. F. De Groot, O. L. J. Gijzeman, A. Mens, O. Stephan and B. M. Weckhuysen, *Journal of Catalysis*, 2005, **230.2**, 301–308.
9. F. Morales, E. de Smit, F. M. de Groot, T. Visser and B. M. Weckhuysen, *Journal of Catalysis*, 2007, **246.1**, 91-99.
10. W. G. Zhou, J. Y. Liu, X. Wu, J. F. Chen, and Y. Zhang, *Catalysis Communications*, 2015, **60**, 76-81.
11. H. Treviño, T. Hyeon, and W. M. Sachtler, *Journal of Catalysis*, 1997, **170.2**, 236-243.
12. G. R. Johnson, S. Werner, and A. T. Bell, *ACS Catalysis,* 2015, **5.10**, 5888-5903.
13. J. Paterson, M. Peacock, R. Purves, R. Partington, K. Sullivan, G. Sunley and J. Wilson, *ChemCatChem,* 2018*,* **10.22**, 5154-5163.
14. Y. P. Pei et al. *ACS Catalysis,* 2015, **5.6**, 3620-3624.
15. Y. Xiang, V. Chitry, P. Liddicoat, P. Felfer, J. Cairney, S. Ringer and N. Kruse, *Journal of the American Chemical Society*, 2013, **135.19**, 7114-7117.
16. P. Chaumette, P. Courty, A. Kiennemann and B. Ernst, *Topics in Catalysis,* 1995, **2.1**, 117-126.
17. M. C. Ribeiro, M. K. Gnanamani, I. R. Azevedo, R. C. Rabelo-Neto, G. Jacobs, B. H. Davis and F. B. Noronha, *Topics in Catalysis*, 2014, **57.6**, 550-560.
18. S. Werner, G. R. Johnson, A. T. Bell, *ChemCatChem*, 2014, **6.10**, 2881-2888.
19. G. Prieto, A. Martínez, P. Concepción, and R. Moreno-Tost, *Journal of Catalysis*, 2009, **266.1**, 129-144.
20. S. Jacques, S. et al. *Angewandte Chemie International Edition*, 2011, **50.43**, 10148-10152.
21. P. Senecal et al, *ACS Catalysis*, 2017, **7.4**, 2284-2293.
22. H. Karaca et al., *Chemical Communications*, 2010, **46.5**, 788-790.
23. J. Paterson, M. Peacock, E. Ferguson, R. Purves, and M. Ojeda, *ChemCatChem*, 2017, **9.18**, 3463-3469
24. J. Paterson, M. Peacock, E. Ferguson, M. Ojeda, and J. Clarkson, *Applied Catalysis A: General*, 2017, **546**, 103-110.

Chapter 3 Methodology

3.1 XRD-CT

3.1.1 X-Ray Diffraction

X-ray diffraction is a valuable technique, used extensively within this work, for use in the study of crystalline materials. XRD is useful not only in the identification of crystal structures, but also for determining properties of the material such as crystallite size, lattice parameters, site occupancy, strain & preferred orientation. As such, it is frequently used in the characterisation of heterogeneous catalysts. [1] [2]

XRD works on the basis that as X-rays pass through a structure, they interact with electron density within the material. Elastic scattering occurs during this interaction, whereby the energy of the incident X-rays and scattered x-rays are equal. As X-rays pass through an atom, the interaction of the X-ray with electron density causes secondary X-ray emissions in a spherical wave. The interaction between these scattered X-rays in most directions will be destructive, however if the scatters are arranged symmetrically, i.e in phase, they will interact constructively. Within crystallography, this happens only in certain directions and is dependent on the X-ray wavelength and the d-spacing between the places within the crystal structure. The directions in which constructive scattering occurs is defined by Bragg's law, shown in Equation 3-1.

$$n.\lambda = 2.d.\mathrm{Sin}\theta$$

Equation 3-1 Bragg's Law.

In Bragg's law, d represents the distance between two planes within a lattice, λ is the wavelength of the incident X-rays, and θ is the angle between the incident X-rays and the lattice plane. As θ is the angle between the incident X-rays and the plane of diffraction, the angle of diffraction is twice this value, 2θ. Additionally, as the angle of diffraction is dependent on the wavelength of the X-rays, a monochromatic incident beam must be used. To produce constructive interference of scattered X-rays, or reflections, Bragg's equation must resolve n as an integer.

Figure 3-1 shows a visual representation of the conditions required for constructive interference, where 2.d.sinθ/λ is an integer, and therefore the diffracted waves interact constructively.

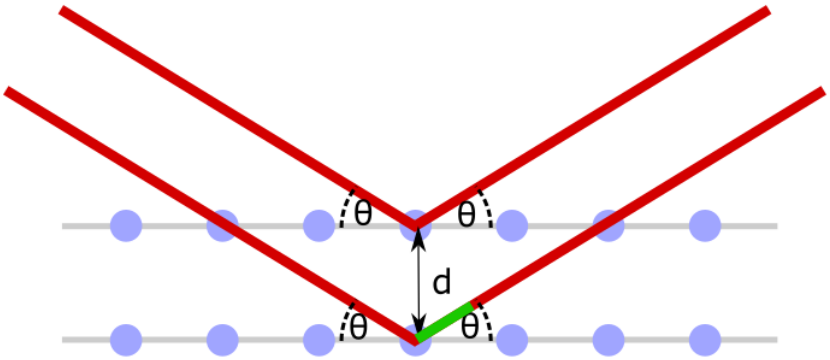

Figure 3-1 Illustration of conditions of Bragg diffraction, where d is the lattice spacing, θ is the angle between incident beam and lattice planes, and 2.d.sin θ/ λ is an integer. Blue circles represent atoms/ions, grey lines the relevant lattice planes, and red lines the incident and reflected X-rays.

For a single crystal, X-ray diffraction results in the production of scattered beams of X-rays, producing a diffraction pattern of spots on a 2-dimensional detector. During powder XRD measurements, the crystals present within the sample are not uniformly oriented, and so instead produce diffracted X-rays in the shape of cones, which are detected as diffraction rings on a 2-dimensional detector.

For analysis of the collected diffraction data, 2D detector results are integrated to generate a plot of measured count intensity vs 2θ. The value of 2θ would typically be calibrated using a known standard, such as CeO_2 in this work, for a specific X-ray wavelength and detector configuration. The diffraction peak positions, and to a lesser extent relative intensities, can be used for the identification of crystalline phases present within the sample measured. Each crystallographic structure has a corresponding fingerprint of diffracting lattice planes determined by the crystal structure, with d-spacings and lattice parameters dependent on the elements that comprise the structure.

Additionally, the shape of the peaks are also relevant to the sample studied. While there are significant instrumental contributions to peak shape, the instrument contribution can be deconvoluted through measurement of a known standard. This means that peak broadening

measured can be correlated to sample parameters such as strain and particle size, both of which contribute to peak broadening.

In this work, XRD measurements were taken largely at ID15A ESRF using a synchrotron X-ray source. Additional X-ray Diffraction measurements supporting catalyst synthesis were taken on a Rigaku Miniflex 10-70° 2θ 1.54 Å Cu source, measured at 3°/min. For measurements on the Rigaku Miniflex, roughly 100 mg of each of the measured materials was finely ground and flattened on a sample holder for analysis. Rietveld refinements were conducted using Topas 6.[3]

3.1.2 Synchrotron X-ray Sources

The vast majority of the XRD measurements collected in this project used a synchrotron X-ray source, specifically the ID15A beamline at the European Synchrotron Radiation Facility (ESRF). Synchrotrons are large central facilities, and use of the beamlines is highly contested with limited availability. X-rays produced from a synchrotron radiation source have a very high flux, be polarised, parallel and are energy tuneable. The dimensions of the cross section of the X-ray beam can also be varied. This makes synchrotron X-ray sources highly useful for the collection of XRD data for experiments where the spatial or temporal resolution of the measurement is important, as the brilliance of the X-rays allows for rapid measurement while still generating high quality results. Additionally, the high energy and high flux X-rays are able to transmit through materials when conventional X-ray sources may not be sufficient.

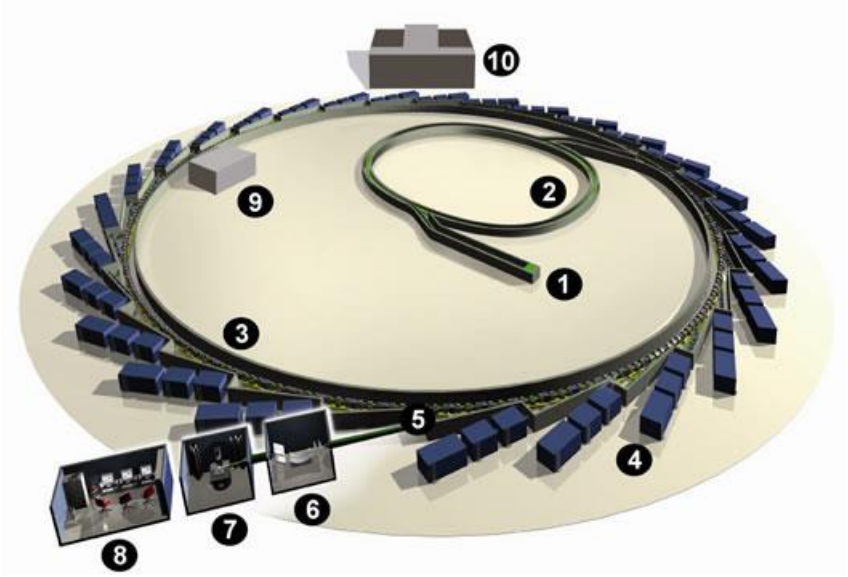

Figure 3-2 Illustration of Synchrotron components, including (1) LINAC (2) Booster Ring (3) Storage Ring (4) Beamlines (5) Front End (6) Optics Hutch (7) Experimental Hutch (8) Control Cabin (9) RF cavities (10) Control building. Reproduced from diamond.ac.uk.[4]

Synchrotrons are typically electron (or alternatively positron) particle accelerators, comprising of a linear accelerator, a smaller booster ring and a larger storage ring. Electrons are produced in an electron gun, before being accelerated under vacuum in a linear accelerator into a booster ring. The electrons are bunched within the booster ring and are further accelerated to relativistic velocities. The accelerated electrons are then injected into the larger storage ring. The storage ring may contain an order of 1000 bunches of electrons simultaneously.[5] The storage ring is a polygon, rather than a ring, with each straight edge connected with bending magnets to bend the electron stream as it passes.

When the accelerated electrons undergo radial acceleration at relativistic speeds within the magnetic fields, they emit X-ray radiation. The X-rays produced are utilised at beamline facilities within synchrotrons for a variety of purposes. The storage ring electrons are interacted with to produce X-rays in two main ways. Firstly, via the bending magnets (BM) that maintain the orbit of the electrons around the storage ring at the corners of the polygon. BMs generate a relatively wide spectrum of X-rays.[6] Secondly, via insertion devices (ID) that manipulate the trajectory of the electron beam back and forth, but return it to its original vector. Insertion devices can be a wiggler or an undulator, but they are both periodic arrays of magnetic fields. A wiggler ID works by bending the electron beam back and forth in a stronger magnetic field typically than a BM. This produces harder X-rays, however still with a similar broad spectrum as a BM. An undulator works similarly by oscillating the electron

beam, however they use a greater number of weaker magnets that create coherent radiation with dependent on the distance between the magnets. This distance can be adjusted to fine-tune the wavelength of the created X-rays.

ID15A at ESRF, the beamline used in this work, utilised a U22 undulator insertion device at the point the experimental work was conducted, prior to upgrades conducted at the beamline in 2020.[7]

Between the ID and sample stage are a series of X-ray optics designed to manipulate the X-ray beam to the desired parameters. These include attenuators to control X-ray flux, vertical and horizontal transfocators that collimate the beam, monochromators to control the energy range of the X-rays, and finally the focusing mirrors and beam slits.[14]

In this work, a 90 / 95 keV monochromatic X-ray pencil beam of 40 x 40 µm was used for XRD-CT measurements. The high flux and energy make synchrotron X-rays valuable for XRD-CT measurements due to the high intensity of the diffraction and high transmissibility of the X-rays through the reactor and sample mediums. Additionally, the 40 x 40 µm beam allows for high spatial resolution, and the rapid acquisition of measurements allowing CT measurements to be taken in a reasonable timeframe. A Pilatus 2M 2D detector was used to measure X-ray diffraction images during XRD-CT measurements.

3.1.3 Computed Tomography

Tomography is the sectional imaging of an object by a penetrating wave, with the image being on the same plane of measurement as the wave. Computed tomography is the algorithmic reconstruction of a tomographic image.

Tomographic data is collected by measuring typically transmittance across a series of 1 dimensional line scans of a subject, with rotations of the subject in between. This generates a 2D array of data, translation steps vs rotation angle, with each pixel containing a measurement. This array is referred to as a sinogram.

A collected sinogram can be algorithmically reconstructed into a real space 2D image, representing a 2D cross section across the plane of translation and rotation. In this work, collected sinograms were reconstructed into real space images using Filtered Back Projection (FBP).[8]

FBP is the combination of back projection and ramp filtering. Back projection is the manner in which the image is reconstructed, where at each line scan is projected across the 2D array at the angle it was measured. This generated an approximation of the original image due to the constructive interaction at regions where the subject interferes in some manner with the measurement device.

The generated 2D image through back projection however still contains low intensity contributions from the subject in the space throughout the projection, where there is not as much constructive interaction. The application of a ramp filter allows for the removal of this contribution. This is achieved by identifying where the regions with low frequencies of constructive contribution are and filtering them out, retaining only the areas of contribution with high frequency of constructive interaction.

In this work, XRD-CT is used extensively to study the crystalline phases within catalysts during operation within a reaction cell. In these experiments, the collected data per step within a line scan is a 2D diffraction image, rather than the absorption value that may be traditionally collected during a CT measurement. The 2D diffraction images collected are integrated into a diffractogram with 2048 intensity values at 2048 2θ values.

For the purposes of the tomography, this equates to collecting 2048 simultaneous sinograms, where each sinogram represents the diffraction contribution at a value of 2θ. This means that for each XRD-CT measurement, 2048 separate FBP reconstructions are required to generate a real space image for each 2θ value. The reconstructed images can then be recombined, to form a 3D array, where two dimensions are the spatial dimensions of the measurement plane, and the third dimension is a diffraction pattern, representing the diffraction contribution for that reconstructed pixel.

Given that the XRD measurements are acquired with an X-ray beam with a vertical height component, the reconstructed images have a vertical component corresponding to the X-ray beam. Due to this, the reconstructed pixels of the CT image are referred to as voxels rather than pixels, as they represent a 3D volume.

3.1.4 Rietveld Refinement

The Rietveld refinement is a method for modelling a calculated diffraction profile to a measured diffraction profile [9]. It does this while considering both structural and instrumental

parameters. To do this however, a reasonable initial approximation of the model is required due to the wide variety of potentially modelled parameters which can cause the model to be mis-fit.

There are three main components of the peaks within a diffraction profile, the peak position, the peak intensity, and the peak shape. Each component is a function of multiple parameters, from both the sample studied as well as the components in an instrument used for the measurement. Rietveld refinements consider both the structural and instrumental components of a modelled profile to allow for representative modelling of the collected diffraction pattern. The instrumental parameters are typically pre-determined by fitting of an instrument measured standard or internal reference material, and then fixed to allow the fitting of the modelled phases profile to the experimental results.

This is achieved by generating a non-linear least squares method to achieve a fit of the calculated profile with the experimental data. The aim is to minimise a function that measures the difference between the calculated and measured data. This is an iterative method whereby fitted variables are adjusted and the modelled pattern refitted to the experimental data. Typically the iterations are applied either until the change in goodness of fit reaches a set minimum threshold, or a set maximum number of iterations is reached.[10][11]

As Rietveld refinements consider a model of the full profile, they are able to manage overlapping reflections effectively, which makes the refinement valuable for the characterisation of the supported catalysts studied in this work where up to six distinct crystalline phases may be present. In this work, Rietveld refinement is used to allow for the production of quantitative phase information of the reconstructed spatially resolved XRD-CT data. This was achieved by manually performing a refinement of the total summed diffraction pattern of a catalyst extrusion within a scan. The parameters fit within this manual refinement were then used as a starting point in automated follow up refinements of each individual spatially resolved diffraction pattern within that extrusion crop. The parameters of the spatially resolved refinements were output to provide representative heatmaps of refinement metrics such as phase intensity, relative phase wt.%, lattice parameters and broadening information.

3.2 Additional Characterisation Techniques

3.2.1 X-ray Fluorescence

X-ray Fluorescence is a technique commonly used for determining the elemental composition of samples. X-ray fluorescence occurs when a sample is bombarded with high energy X-rays, causing the sample to fluoresce secondary X-rays of an energy characteristic to the element from which the fluoresced X-ray is emitted. This characteristic fingerprint can therefore be used for both the determination of elemental composition, as well as the quantification.

The underlying mechanism for which X-ray fluorescence occurs is due to the ability of high energy X-rays to be able to ionise atoms by the removal of core electrons. For this to happen, the energy of the X-ray source must be higher than the ionisation energy of the element. When an atom is ionised by removal of a core electron, it allows an outer shell electron to drop to the available orbital. When this occurs, the electron emits a fluoresced photon, with the energy representing the difference in energy between the two electron orbitals. As the energy difference between the two electron orbitals is dependent on the element, the energy of any emitted photons detected can be used to determine the elements present within a sample studied. Elements can have a number of different spectral energies, depending on which orbitals are involved in the drop.[12]

While X-ray fluorescence measurements can allow for quantitative analysis of elemental composition, consideration must be given to the transmissibility of the secondary emissions. As the energy level of the fluoresced X-ray is similar to orbital energies, the transmissibility of the lower energy X-rays is higher within the sample.

In this work, quantitative XRF elemental analysis was conducted by diluting approximately 0.2 g of sample in 6.5 g of lithium tetraborate / lithium metaborate / lithium bromide at a ratio of 66.67 : 32.83 : 9.5 %. The diluted samples were fused at 1050 °C for 12 mins, and cast into a 32 mm glass bead for analysis.

The use of light elements in the dilution allows for the secondary X-rays emitted to be highly transmissible through the dilution medium, allowing for good intensity data and quantitative comparison at different energies.

3.2.2 Electron Microscopy

Electron Microscopy (EM) is able to provide valuable insight into the morphology and composition of materials at the nanoscale. The maximum resolution of any microscope is dependent on the wavelength used to study the subject. In the case of EM, high energy electrons are used for the imaging, due to the relationship between electron velocity, determined by accelerating voltage, and the electron wavelength as described by the de Broglie relationship.[13] For example, a voltage of 200 kV would provide a wavelength of 2.74 pm, allowing for high resolution microscopy imaging.

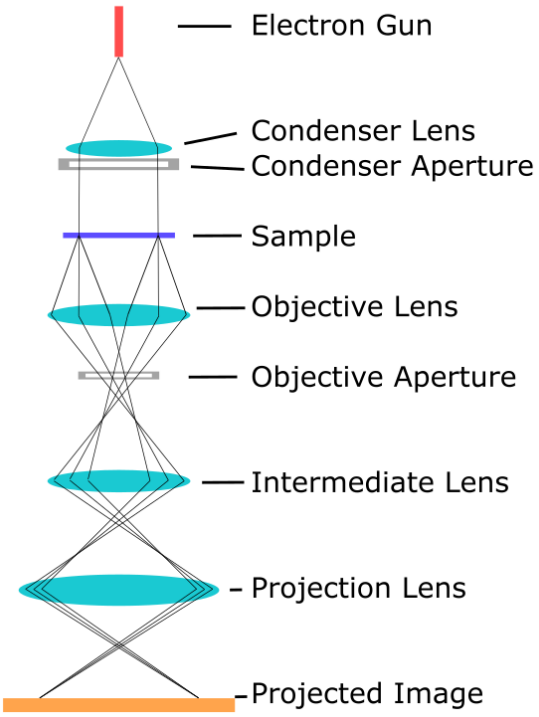

Figure 3-3 - Ray diagram of TEM electromagnetic lenses and apertures for the collection of a transmission image.

Transmission Electron Microscopy (TEM) instruments use an electron gun to generate and accelerate an electron beam. The condenser lens focuses the electron beam onto the sample, illuminating the imaged region, which transmit through the sample and are projected onto the objective lens. The intermediate and projection lens then modify the electron beam for projection onto a detector or fluorescent plate. TEM Instruments require operation under high level vacuum (typically $>10^{-7}$ Pa for high resolution instruments) due to the large path the electron beam travels during imaging (1 - 2 m).

The resulting high resolution contrast image represents the difference in electron densities in the imaging plane, as the proportion of the electron beam diffracted is dependent on the electron density of the measured sample. This makes TEM a useful technique for the determination of nanoparticle size, morphology, as well as variability within samples.

Scanning transmission electron microscopy (STEM) is a variation of TEM. Instead of the electron beam illuminating the entire imaging region as in TEM, in STEM the electron beam is highly focused and scanned across the imaging region. The added value of STEM over TEM is that it allows for techniques such as energy dispersive X-ray spectroscopy (EDX) to be applied to the measured sample.

In this work, TEM imaging was conducted at the Research Complex at Harwell (RCaH) on a JEOL JEM 2100 EM with a 200 kV beam. STEM imaging was conducted on a JEOL ARM200CF at the Electron Physical Sciences Imaging Centre (ePSIC) at the Rutherford Appleton Laboratory. To prepare samples for imaging by TEM and STEM, roughly 10 mg of sample was dispersed in ~ 2 ml of ethanol by sonication. A drop of the suspended sample was added to a holey carbon film on 300 mesh copper sample grid for imaging.

3.2.3 Energy dispersive X-ray spectroscopy

EDX is an analytical technique that allows for the quantification of the elemental composition during the study of a sample by electron microscopy. In EDX measurements, an electron beam excites an electron for the core shell of an atom. The relaxation of an electron from a higher orbital into this core shell, causes the emission of an X-ray. The energy of the emitted X-ray is element specific, as it corresponds to the difference between the energy levels of the two electron orbitals. Measurement of the energies of the emitted X-rays can therefore be used to quantifiably measure the elemental composition of the imaged sample.

Measurement of EDX during STEM where the electron beam is being rastered over the imaged sample allows for the mapping of elemental composition within the sample. This is a valuable technique for determining composition uniformity and dispersion of elements within supported catalysts.

3.2.4 X-ray Photoelectron Spectroscopy

X-ray Photoelectron Spectroscopy (XPS) is a surface sensitive technique that measures the photoelectric effect of X-ray ionised samples from the first few nanometres of surface material. The technique provides valuable insight into the elemental, and chemical, composition on the surface of materials.

During an XPS measurement, the studied sample is exposed to a monochromatic X-ray source. When the incident X-rays ionise an atom, an electron is ejected. The energy of this ejected electron is dependent on the energy of the X-rays, minus the binding energy of the orbital the electron is ejected from. As the binding energy is related to the element of the atom ionised, measuring the energies of ejected photoelectrons allows for identification of the elements present within the surface region of the sample. Additionally, the measured intensities of photoelectrons can be used for quantification of elements present at the sample's surface. Lab scale XPS measurements are typically taken at ultra-high vacuum ($>10^{-7}$ Pa) to minimise interaction of ejected electrons with atmosphere between the sample and the detector.

In this work, XPS measurements were taken by XPS Harwell. For each sample, a monochromatic Al Kα (1486.7 eV) source was used. High resolution scans of the Co & Mn edges were typically taken in 3 sweeps of 300 steps, 0.1eV step size and 239 ms dwell time. XPS spectra were charge corrected using adventitious carbon at 284.8 eV. XPS spectra were plotted and quantified using CasaXPS v2.3.25.

3.2.5 Diffuse Reflectance Infrared Fourier Transform Spectroscopy

The vibrations of molecular bonds can be excited by the interactions of infrared radiation in the 4000 – 400 cm^{-1} range, as they interact with the rotational-vibrational structure of molecules. These vibrations have characteristic frequencies that can be used to identify specific functional groups. The selection rule for Infrared (IR) spectroscopy states that vibrations are only IR active if there is a dipole moment change during the vibration of the molecule.

In catalysis, IR spectroscopy plays a valuable role in determining how molecules interact with the surface of the catalyst. This can provide insight into why certain responses are observed

to variation in the physical, chemical, or electronic structure of the catalyst, as changes in the interaction between the reaction molecules and catalyst surface may be detected.

Diffuse reflectance infrared Fourier transform spectroscopy (DRIFTS) is frequently used to study IR absorption of samples that are strongly absorbing. Rather than measuring a spectrum of transmission in the infrared band, DRIFTS experimental setups use an ellipsoid or paraboloid mirror to direct diffusely reflected IR radiation to the detector.

In this work, *in situ* CO absorption experiments were conducted on reduced model catalysts, to understand how varying manganese doping levels and interactions varied the interaction of gas phase CO with the surface of the catalyst.

DRIFTS CO absorption experiments were conducted on an Agilent Carey 680 Fourier-Transformed Infrared Spectrometer, with a MCT detector and a Harrick Praying Mantis reaction cell. Samples were reduced in 20 ml/min 50 % H_2/He at 400 °C (10 °C/min) for 1 h, and cooled to 30 °C. For CO Absorptions, the sample cell was purged with He and a baseline collected. Sequential measurements were taken every 30 s for 5 min while 10 ml/min of 10 % CO / He was dosed through the cell. For samples supported on P25, the samples were studied undiluted. For the unsupported nanoparticles, the samples were diluted in pre-dried KBr, at a ratio of 10:1 KBr:sample.

3.3 References

1. A. Guinier, X-ray diffraction in crystals, imperfect crystals, and amorphous bodies. Courier Corporation, 1994.
2. Advanced Certificate in Powder Diffraction on the Web http://pd.chem.ucl.ac.uk/pdnn/pdindex.htm
3. A. A. Coelho, *Journal of Applied Crystallography*, 2018, **51.1**, 210-218.
4. https://www.diamond.ac.uk/Science/Machine/Components.html Accessed September 2022
5. P. Suortti, "X-ray, Synchrotron Radiation, and Neutron Diffraction.", 2003, 989-1023.
6. https://www.esrf.fr/about/synchrotron-science/synchrotron.html accessed September 2020
7. https://www.esrf.fr/home/UsersAndScience/Experiments/StructMaterials/ID15A/technical-description.html, Accessed October 2022
8. A. C. Kak and M. Slaney, Principles of computerized tomographic imaging. Society for Industrial and Applied Mathematics, 2001.
9. H. M. Rietveld, *Journal of Applied Crystallography*, 1969, **2.2**, 65-71.
10. E. Prince, "Mathematical aspects of Rietveld refinement." The Rietveld Method (1993): 43-54.
11. A. A. Coelho, J. Evans, I. Evans, A. Kern and S. Parsons, *Powder Diffraction*, 2011, **26.S1**, S22-S25.
12. B. Beckhoff, B. Kanngießer, N. Langhoff, R. Wedell, and H. Wolff, Handbook of practical X-ray fluorescence analysis. Springer Science & Business Media, 2007.
13. R. F. Egerton, *Ultramicroscopy*, 2014, **145**, 85-93.
14. G. B. M. Vaughan et al., *Journal of Synchrotron Radiation*, 2020, **27.2**, 515-528.

Chapter 4 - Ambient pressure XRD-CT study of Mn doped catalyst extrusion series

4.1 Introduction

The major product streams of the Fischer-Tropsch reaction are typically olefinic and paraffinic hydrocarbons.[1] Recently, Paterson *et al*.[2] have reported alcohol selectivities of >30 % under typical FTS operating conditions, during the testing of manganese doped cobalt FT catalysts with >3 % Mn content. The authors hypothesise that the addition of manganese at higher levels of doping is leading to the formation of cobalt carbide during FTS. Following this, the cobalt carbide – cobalt metal interface can then encourage non-dissociative CO activation leading to an increase in alcohol selectivity. This mechanism is reported in Co-CoC_2 catalysts by Pei *et al.*,[3] which have been shown to be selective towards alcohols during FTS.

In this work, equivalent catalyst extrusions have been studied in an effort to understand how the crystalline phases present during FTS are affected by varying manganese levels, and whether any correlation can be found with the displayed alcohol selectivity above 3 % Mn.

Prior to reaction, cobalt FT catalysts are activated under H_2 to reduce the cobalt oxide to the active cobalt metal. As the crystalline phases evolve during this activation step, characterisation of the oxide catalyst can be of limited use as the structures present are not representative of those present during catalysis.[4] The reduced catalyst is highly air sensitive however, as cobalt in its metallic form is oxidised on contact with atmospheric oxygen.[5]

In situ techniques allow for the study of samples during operation, allowing changes to be studied as they happen. In this work, XRD-CT has been used in combination with a multi-sample *in situ* setup to simultaneously study multiple samples from our catalyst series. As XRD-CT is a spatially resolved technique, we are not only able to study multiple samples at once, but we are also able to make insights into the spatial distribution of crystalline phases present within the catalyst extrusions studied.[6]

The catalyst series was studied by XRD-CT during catalyst activation and reaction, at atmospheric conditions. The reconstructed diffraction patterns were Rietveld refined[7] to provide spatially resolved quantitative phase information for each extrusion, allowing significant insight into the evolution of diffracted phases during operation.

4.2 Experimental

4.2.1 Catalyst Series

The commercial catalyst series studied in this project has been supplied by BP, the projects' industrial sponsors. The catalyst series is based on cobalt supported on titania trilobed extrusions, with 10 wt. % Co and 0-10 wt. % Mn. The supplied catalysts are in spinel oxide form prior to activation and reaction. This report focuses on results obtained for catalysts containing 0, 0.5, 1, 5 and 10 wt. % Mn.

The catalysts were synthesised by the simultaneous impregnation of cobalt nitrate hexahydrate and manganese acetate hexahydrate on P25 titania. The resulting mixture was formed into extrusions 1.8 mm trilobed extrusions, before being calcined at 300 °C for 2 h.

4.2.2 Setup for *In Situ* X-ray Diffraction Computed Tomography

XRD-CT experiments have been conducted at ESRF on the ID15A beamline where a 90 keV monochromatic incident beam of 40 x 40 µm was utilised. To collect the required sequence of diffraction patterns that could then be reconstructed into a tomographic image, the reaction cell was translated across the beam by a known number of steps (s) and rotated by s/180°. The translation was repeated until the reaction cell had been scanned 180° in total. The number of translational and rotational steps are determined such that the desired spatial or temporal resolution is achieved. An additional variable is the acquisition time per step, which must be sufficient enough to produce a high signal to noise ratio for each scan collected. This is dependent on the X-ray flux, sample crystallinity, cell transmittance and detector sensitivity. The diffraction patterns were collected with a Pilatus 2M 2D detector, with its response calibrated with an 8 nm CeO_2 standard.

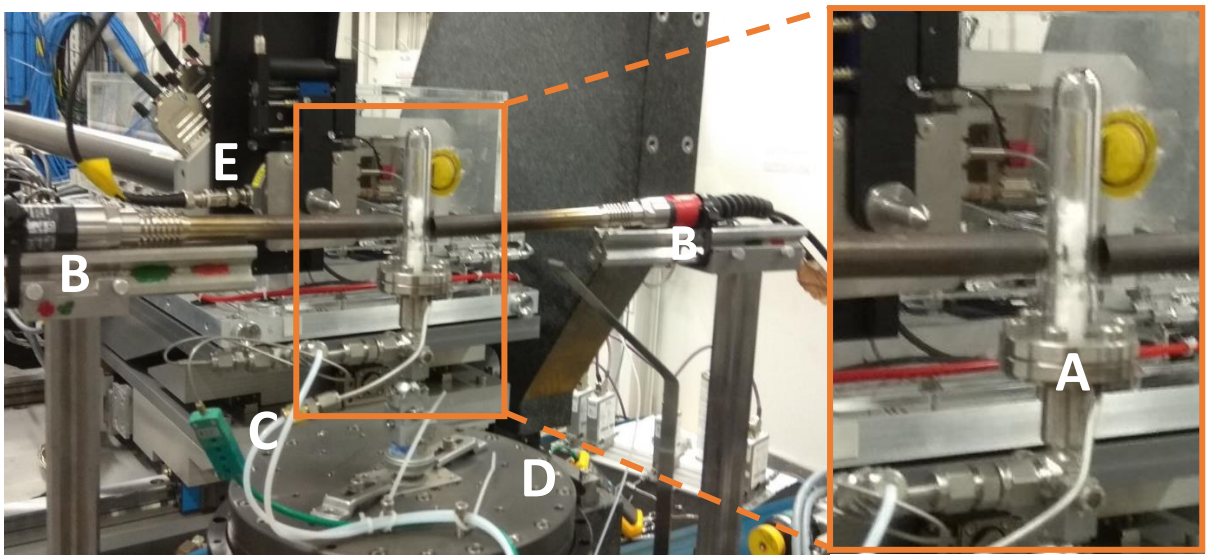

Figure 4-1 Experimental setup at ESRF ID15A showing A) quartz 2-walled reactor B) heat guns C) gas lines D) rotation stage and E) beamline source.

An appropriate reactor setup was required to conduct the XRD-CT measurement, that allowed for the reactor to be rotated 180° during operation. This raised challenges for the setup of both the gas supply and extraction, as well as heating source, as these features should not interfere with the X-ray beam during the measurement. A suitable setup to overcome this restriction is a single-ended tube in tube setup, as shown mounted to the experimental stage of ID15A in Figure 4-1. This allowed the catalyst bed to be held within the beam, and the inlet and outlet gas connections to be below the beam level, which reduced the opportunity for the gas lines to cross the path of the beam during rotation. The reaction gas is flowed up the outer tube and down the inner tube, where the catalyst bed is located. A thermocouple is inserted via the outlet gas line to the X-ray measurement zone, to provide live temperature measurements. The reactor setup was mounted on a goniometer to allow for the vertical alignment of the reaction cell, as well as aligning the rotational axis to be perpendicular to the beamline source.

The reactor was heated during operation via two heat guns, which were mounted perpendicular to the beamline. The heat guns remained static during rotation steps, however they were mounted to the translation stage to ensure their position remained constant relative to the reaction cell. A thermocouple was mounted internally within the reactor in the catalyst bed to ensure representative temperature measurement experienced by the catalyst samples. As the reactor was made of quartz, the heat conductivity between the two reactor walls and the catalyst bed was low, and a large differential was observed between the

required heat gun setpoint (690 °C) at the maximum reactor temperature (350 °C) as measured by the thermocouple within the catalyst bed. The ability to conduct reaction at pressure was also limited due to the reactor material.

Due to the limited time availability on beamlines which are capable of conducting XRD-CT experiments, it was important to optimise the quantity and quality of experimental data gained within the time frame available. As such, a single extrusion of multiple catalysts within the series were loaded into the reactor simultaneously, and the experiment conducted on multiple extrusions at the same time. As well as reducing the number of experiments required for the full series to be studied, this removed the chance of variability between experiments that may influence the results. This comes at the expense of temporal resolution in the CT scans however, as with a single catalyst extrusion, a smaller diameter reactor could be utilised, and scan times would be reduced.

A single ~10 mm long extrusion of each catalyst was loaded into separate 2 mm diameter quartz capillaries and held in place with quartz wool above and below the catalyst. These loaded capillaries were arranged radially within the reaction cell, held in place throughout their length with densely packed quartz wool. The capillaries were loaded so that each loaded extrusion intersected the same horizontal plane, to allow for each extrusion to be measured within a single CT scan. The voids between the capillaries were densely packed with quartz wool to encourage gas flow through the loaded capillaries during operation.

4.2.3 In Situ XRD-CT during Catalyst Activation and Fischer-Tropsch

The catalyst activation was conducted under 100 ml/min (~7000 GHSV) 20%H_2/He flow at 350 °C at atmospheric pressure. The ramp to temperature was at 1.4 °C/min over 3 h, and the activation was held at 350 °C for 2 h.

Post activation, the reaction was cooled to 140 °C before being ramped to reaction conditions of 250 °C at 5 °C/min under 100 ml/min (~7000 GHSV) of 5 %CO/10 %H_2/He, however due to operational complications, the gas flows were not changed until 220 °C. The reaction was held at conditions for 3 h before being cooled to room temperature and decommissioned. Figure

4-2 shows the reaction temperature profile and corresponding gas flow compositions during the experimental work.

For both the catalyst activation and operation under pseudo FTS conditions, the gas velocities used are greatly in excess of those required for the mass of catalyst loaded. This is to ensure that the gas flows through the loaded capillaries within the reaction cell, and not only between them. Additionally, the high flow rates mean each extrusion studied is exposed to gas composition reflecting the typical inlet of a fixed bed reactor throughout the length of the extrusion. The means that the point at which a measurement is taken along the length of the extrusions should not impact the observations made.

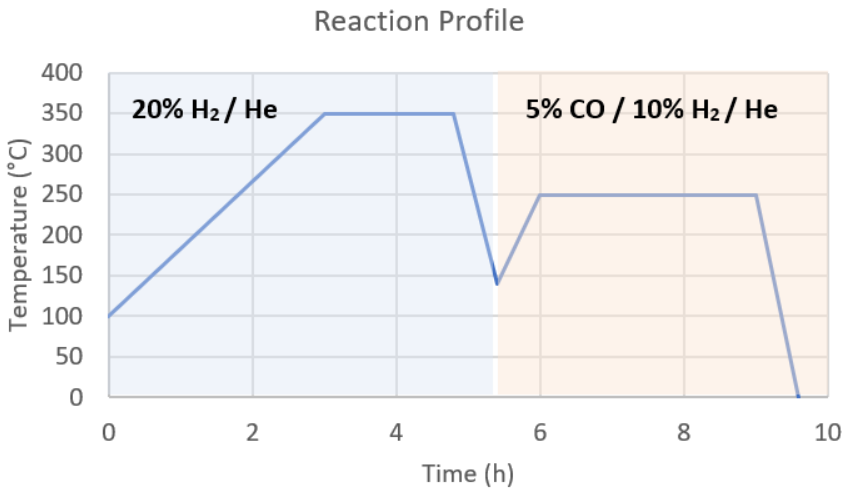

Figure 4-2 Reaction temperature profile and gas compositions during H_2 activation (light blue) and FT reaction (light orange).

During the reduction at operation of the catalyst, XRD-CT scans were conducted with the following parameters: 90 keV monochromatic incident beam 40 x 40 µm in size, 10 ms acquisition time per diffraction pattern, 161 translation steps with 80 µm step size and 161 rotations (1.12°). This yields a reconstructed CT image of 160 x 160 voxels with a spatial resolution of 80 µm and temporal resolution of 20 min between scans.

Table 4-1 shows the scans collected during catalyst activation, with the corresponding nominal time and temperature ranges.

Table 4-1 - Scans collected during catalyst activation with corresponding time and temperature ranges.

Scan Number	Time Start (h)	Time End (h)	Temp Start (°C)	Temp End (°C)
1	0	0.3	100	128
2	0.3	0.6	128	156
3	0.6	0.9	156	184
4	0.9	1.2	184	212
5	1.2	1.5	212	240
6	1.5	1.8	240	268
7	1.8	2.1	268	296
8	2.1	2.4	296	324
9	2.4	2.7	324	350
10	2.7	3.0	350	350
11	3.0	3.3	350	350
12	3.3	3.6	350	350
13	3.6	3.9	350	350
14	3.9	4.2	350	350
15	4.2	4.5	350	350

4.2.4 Rietveld Refinement Processing Pipeline

The quantity of X-ray diffraction patterns collected (~720,000) during this scope of work necessitates the development of an automated pipeline to process the data volume while retaining the spatial resolution of the measurement. The collected sinogram diffraction data was reconstructed into real space images via filtered back projection (FBP). The catalyst extrusions present in the reconstructed image were cropped and ordered by % Mn, with subsequent CTs added to produce an array of % Mn vs time, as illustrated in Figure 4-3. This is an effective method of visualisation of the catalyst extrusions over time, as well as removing the majority of the reconstructed empty space between the catalyst extrusions.

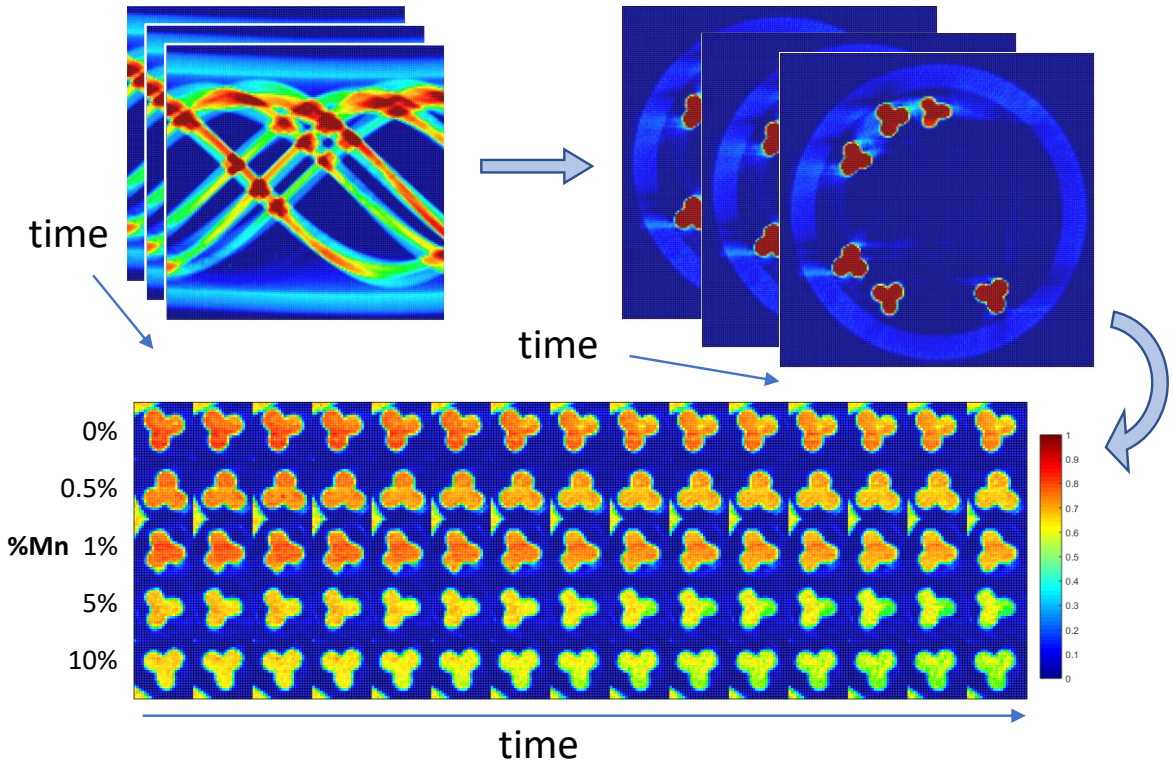

Figure 4-3 Arrangement of cropped extrusion CTs as a function of time originating from the sinograms (top left) to create a reconstructed 2D intensity distribution (top right) and from which a stacked array as a function of time and % Mn is created and shown below. Note the data in the figure are scaled to a common intensity and the scalebar on the right indicates the scaled relative diffraction intensities for the pixels in thermograms on the left.

Each individual extrusion crop had the sum of its diffraction contribution Rietveld refined[7] using Topas 6.[8] This allowed the refinement parameters for each extrusion to be used as a starting point for the individual voxels within the crop of that extrusion, as the samples studied have good uniformity.

Prior to bulk refinement, a selection filter is applied to the crops of each extrusion to identify which voxels contain diffraction contribution of a catalyst extrusion. This includes both a minimum value for total summed contribution within that voxel, and a minimum value for the maximum peak intensity. By tuning the values of these checks, the application of both these selection criteria is effective in selecting voxels that contain diffraction contribution from the catalyst, while excluding false positives that may arise due to broad intensity of the quartz capillary vessels, or sharp peaks from reconstruction artifacts.

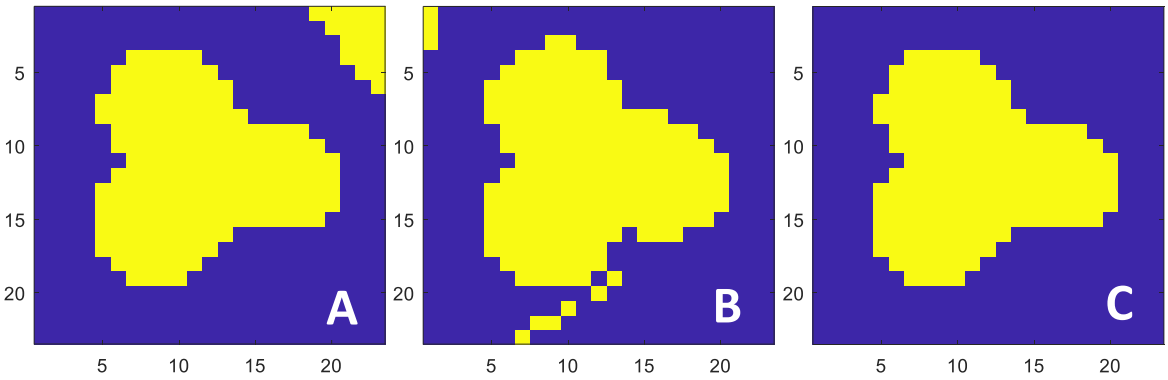

Figure 4-4 Example of the application of selection criteria for A) total summed diffraction contribution (showing selection of both catalyst extrusion and quartz capillary wall) B) Minimum peak maximum showing selection of both catalyst extrusion and reconstruction artefacts) and C) Both criteria combined (showing selection of only catalyst extrusion). The selection filter decides which voxels to perform sequential Rietveld refinement. The axis units for each image are voxel co-ordinates

Figure 4-4 A & B shows the application of each of these selection criteria filters individually, with Figure 4-4 C showing the combined application of both filters. The selection criteria map is then used as a key to determine which voxels contain diffraction contribution from the catalyst extrusions and are therefore Rietveld refined. Subsequently, a filter is passed over the refinement map key to label each refined voxel with a radial depth. This allows the refined parameters to be grouped for evaluation by distance from the edge of the extrusion.

Additionally, post refinement a filter is passed over the refined array to remove any refined voxels with a high Rwp > 15 %. This prevents any voxels which may have passed the selection criteria erroneously from distorting the batched results if the refinement has not achieved a reasonable goodness of fit. (Rwp > 15 %)

The scripts used for each step are included in Figure 8-9, Figure 8-10 & Figure 8-11 in the appendix, in addition to Figure 8-8, an example input parameter file built for the Rietveld refinement in Topas 6.

4.3 Results and Discussion

4.3.1 Reconstructed Data

In Situ XRD-CT was conducted on the Mn doped catalyst series to understand what effect varying levels of Mn has on the evolution and distribution of phases within the catalyst during catalyst activation and FTS at atmospheric pressure.

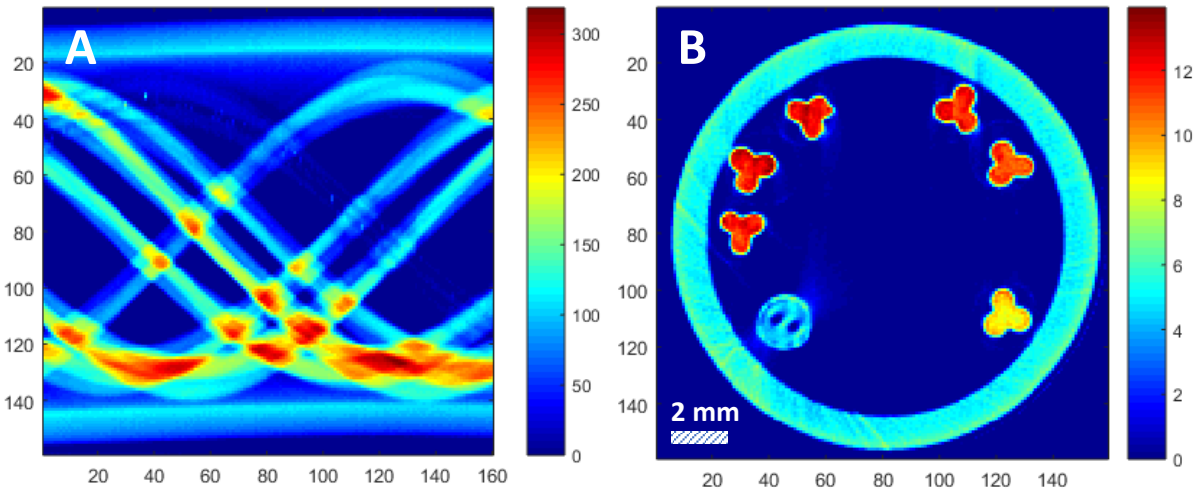

Figure 4-5 A) Example of total diffraction contribution sinogram prior to reconstruction B) reconstructed CT showing quartz reactor tube (light blue circle), catalyst trilobed extrusions and thermocouple. For both images, the x & y axis are voxel coordinates, with arbitrary intensity heatmap scale. Note the thermocouple is the light blue object at the bottom left hand side of the right hand figure

Figure 4-5 shows an example of a A) collected sinogram and B) reconstructed CT image. The trilobed catalyst extrusions are arranged radially around the wall of the inner reactor tube, in an identifiable pattern. The temperature probe thermocouple is also present within the measurement plane.

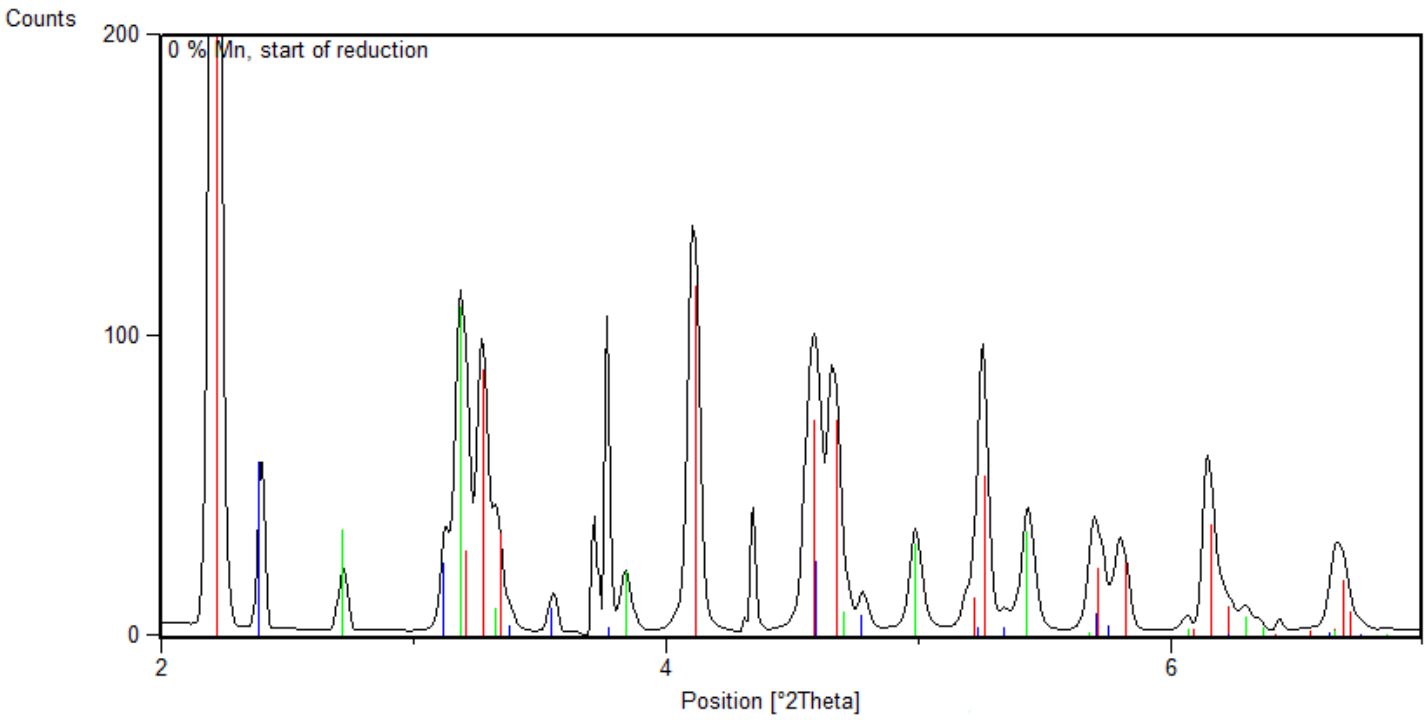

Figure 4-6 Example diffractogram from 80 x 80 µm voxel of undoped catalyst at start of reduction. Indexing lines are included for the anatase (red), rutile (blue) and Co_3O_4 (green) phases

Figure 4-6 shows an example reconstructed voxel of the un-doped catalyst extrusion prior to reduction. The reconstructed diffractogram shows the clear presence of the expected phases, anatase, rutile and Co_3O_4 and appears to have virtually no background contribution. The peaks are clearly separated and defined, with good signal:noise intensity.

Figure 4-7 shows the summed diffraction pattern of each catalyst extrusion tested prior to reduction. The resulting reconstructed contribution of the catalyst extrusions shows good signal intensity, with minimal noise or background. The contribution of the thermocouple has not reconstructed entirely, with some contribution of the stainless-steel outer wall of the thermocouple interfering with the contribution of the catalyst samples. This is likely due to large crystal grain size leading to the diffraction not behaving consistently like a powder diffraction across all the rotation steps. Due to this, the catalyst extrusions show some minor presence of artefacts at from the stainless-steel 310 FCC phase of the thermocouple casing. The effect of these reconstruction artefacts are visualised in the appendix in respect to both the CT image (appendix Figure 8-1) and diffraction pattern (appendix Figure 8-2). For the Rietveld refinements, the location of these artifact peaks have been excluded. Due to their

non-typical peak shape and lack of consistency throughout the measurement plane, they are not suitable for fitting in combination with the catalyst extrusion phases.

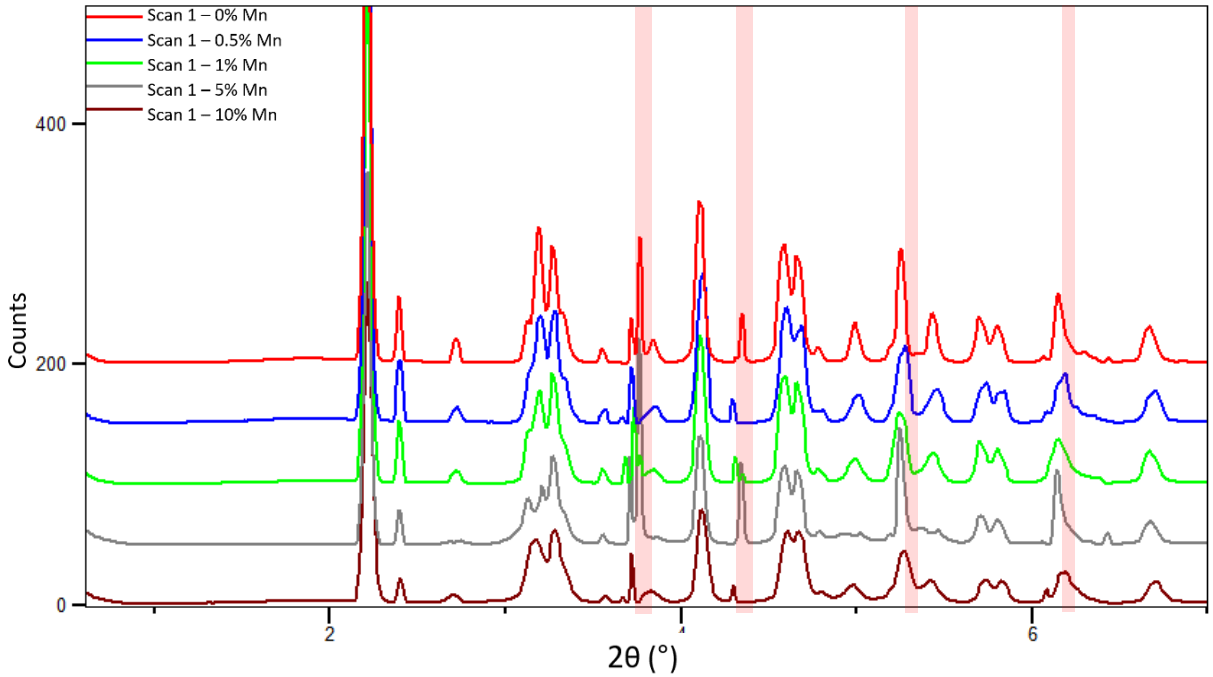

Figure 4-7 summed diffraction pattern for each catalyst extrusion prior to activation, with excluded regions highlighted (pink) due to contribution from thermocouple reconstruction artefacts

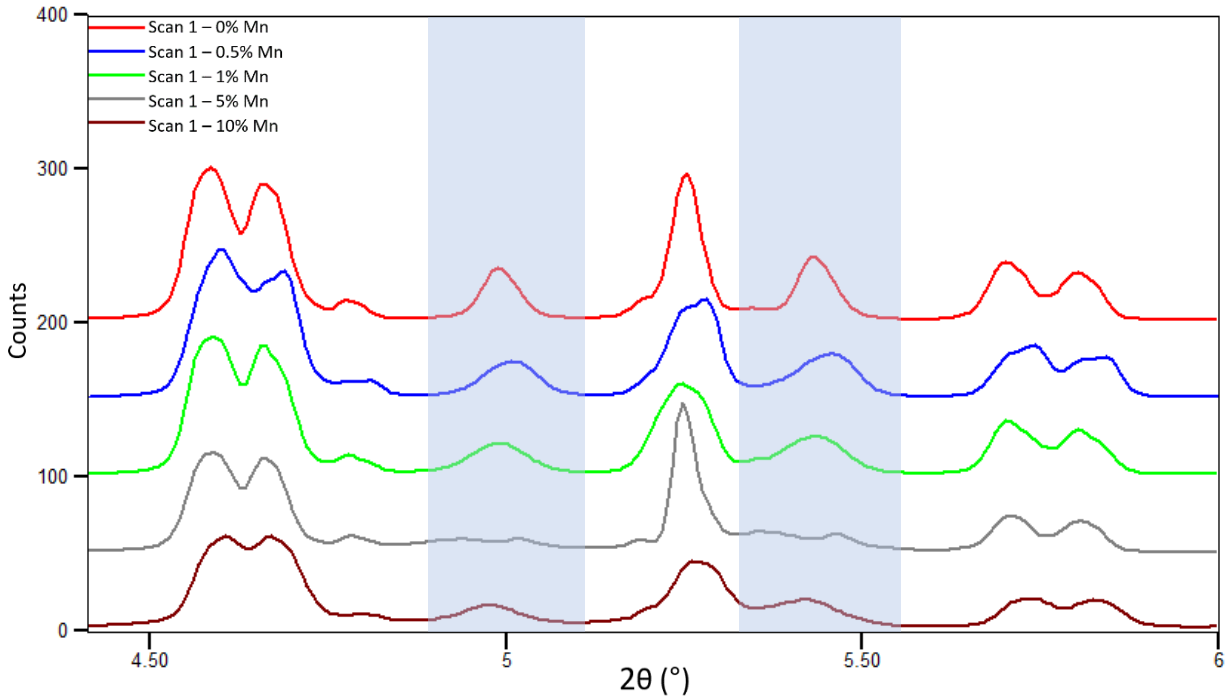

Figure 4-8 Comparison of the summed diffraction patterns of each catalyst extrusion between 4.5° – 6° 2ϑ, with the $Co_{(3-x)}Mn_xO_4$ (511) & (440) peaks highlighted (blue)

Figure 4-8 shows the summed diffraction patterns between 4.5° and 6° 2θ for each catalyst extrusion. Focusing on the highlighted spinel $Co_{(3-x)}Mn_xO_4$ peaks at 5° (511) and 5.4° (440) we

can see that the addition of increasing amounts of manganese to the catalyst leads to a broadening of the spinel peaks. In addition, the peak shape of the anatase and rutile support structure do not appear to be consistent between the samples.

An explanation for the variation in peak width between the samples is due to the 180° rotation of the reactor during the collection of the tomograph. As the catalyst extrusions are arranged radially around the inside wall of the reactor, and not at the centre of rotation, their distance to the detector varies. This distance then changes as the reactor is rotated. Not only does this lead to each extrusion's diffraction contribution varying, causing a broadening of the measured peaks, but also the average distance to the detector will be different for each extrusion, as the reactor is only rotated 180°, rather than a full 360°. The effect of this broadening will of course also be present in the cobalt-manganese phases.

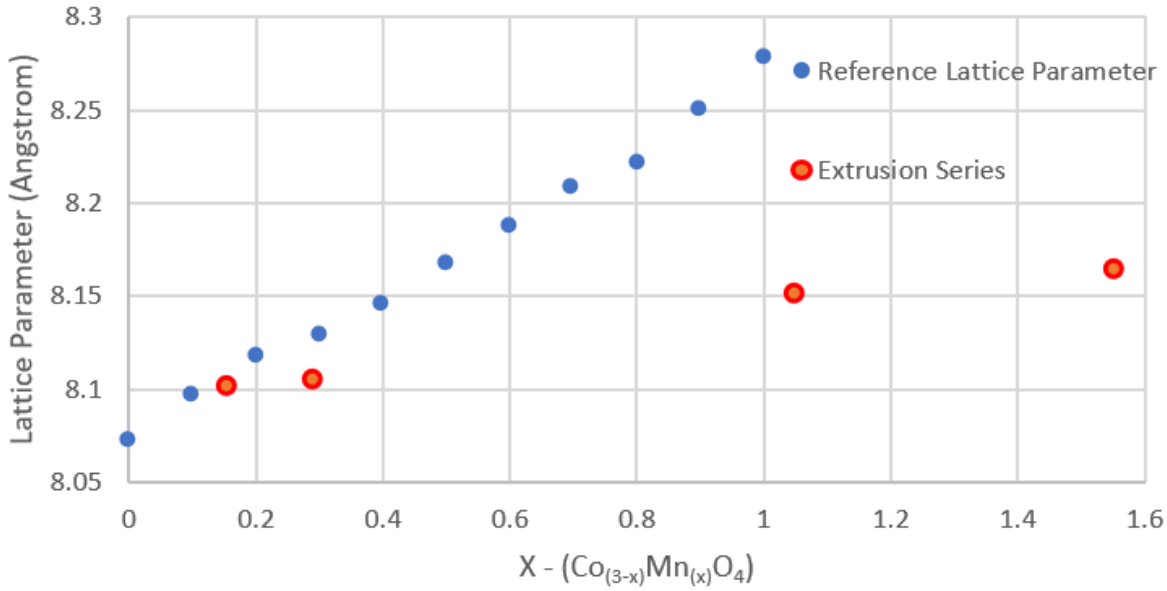

Figure 4-9 Reference Lattice Parameter from Meera et al.[11] and lattice parameters of catalyst extrusion series with varying Mn content

An increase in the lattice parameter is observed in the spinel oxide $Co_{(3-x)}Mn_{(x)}O_4$, with increasing manganese as it is incorporated into the spinel structure. As the catalyst series was synthesised via simultaneous deposition of mixed cobalt and manganese salts, the resulting samples are expected to have Co and Mn distributed throughout the catalyst, with the expectation that they will form mixed oxides upon calcination. While Mn_3O_4 typically take the form of the tetragonal spinel with space group $I4_1/amd$[9] the Co_3O_4 exists as cubic spinel with space group Fd-3m.[10] In the collected diffraction patterns in this work, only the presence of

the cubic spinel structure is observed. Figure 4-9 plots the bulk refined lattice parameter for the spinel oxide phase for each doped extrusion. In addition, a reference plot is included showing the expected lattice parameter for varying values of X, between 0.1 – 1.[11]

The lattice parameter expansion observed within the catalyst extrusion series is considerably less than the expected expansion assuming homogenous distribution of the Co and Mn. This suggests that while a proportion of the manganese is forming mixed oxide species with the cobalt, a significant proportion is unaccounted for within the diffraction pattern. An explanation for this would be that the manganese is highly distributed over the surface of the supporting titania, with a domain size too small to detect by diffraction. This would not be unreasonable at the % Mn loadings of these catalysts, as highly disperse MnO_2 has been reported on TiO_2 via IWI synthesis requiring loadings of 6 % for detection of MnO_2 by XRD. [12]

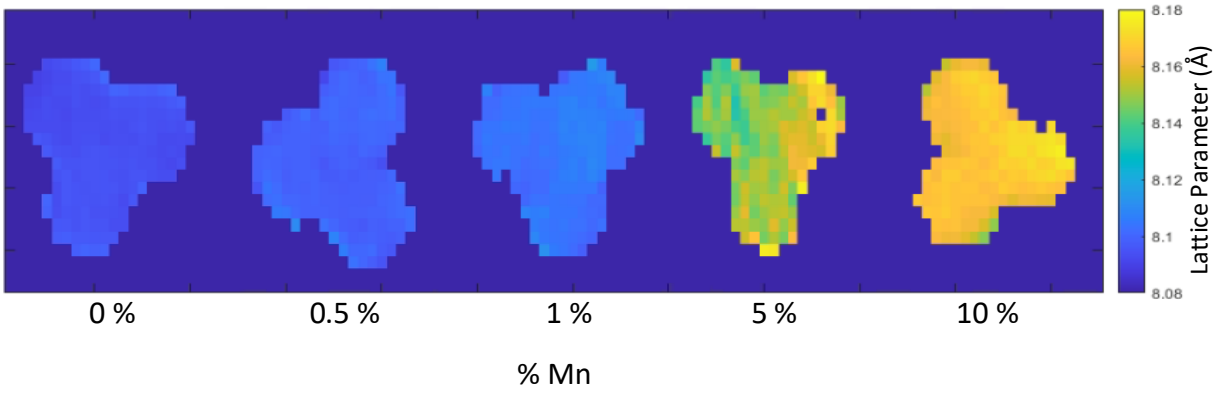

Figure 4-10 Maps of refined lattice parameter of $Co_{(3-x)}Mn_{(x)}O_4$ for each catalyst extrusion.

Figure 4-10 shows the spatially resolved heatmap of the refined lattice parameter for the spinel mixed oxide phase for each catalyst extrusion. From the heatmaps, we can see little variance in lattice parameter across the depth of the extrusions. An exception is seen in the 5 % Mn extrusion where one lobe of the trilobe appears to show a higher lattice parameter, potentially suggesting an increase in manganese content within the structure relative to cobalt.

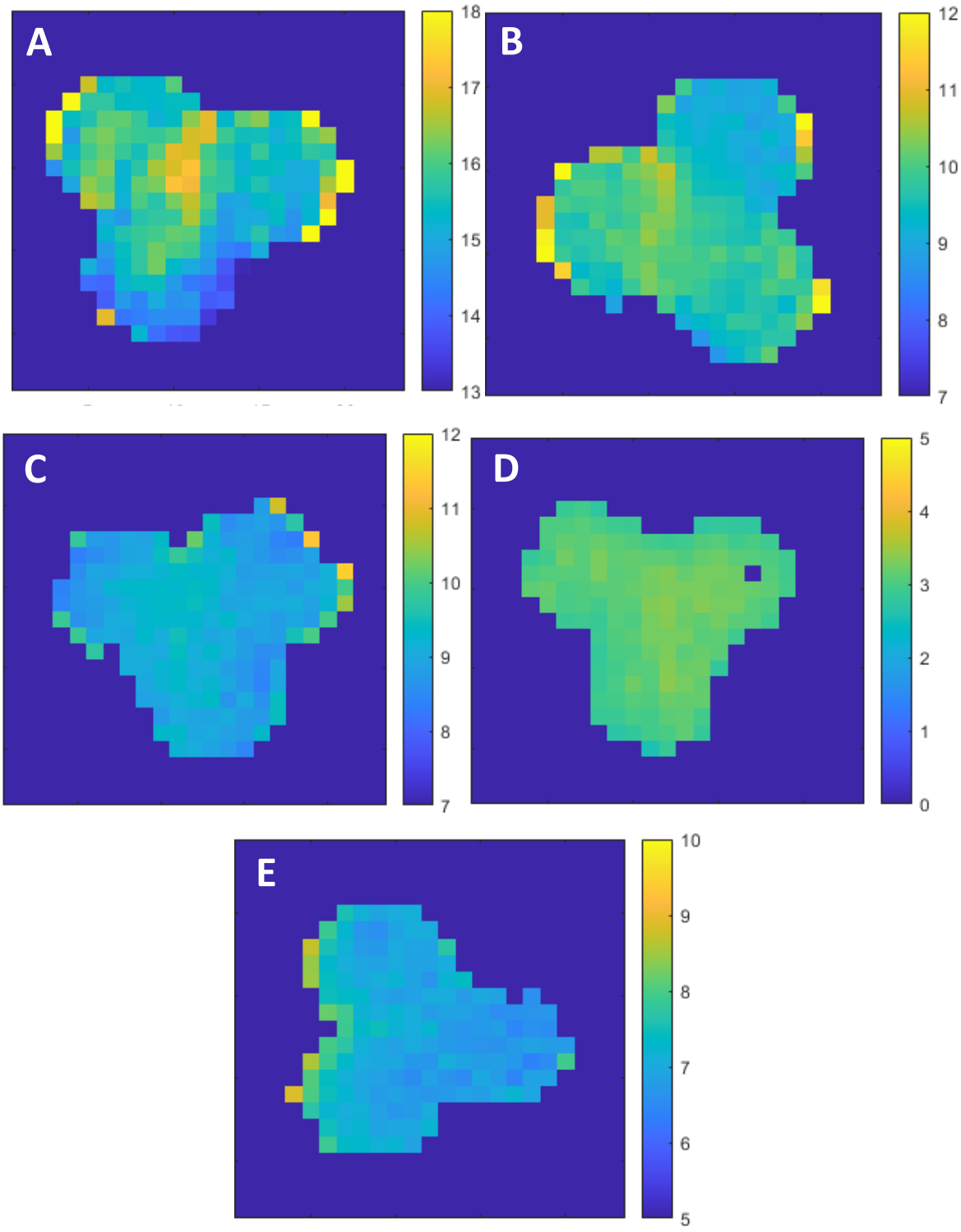

Figure 4-11 A-E Maps of refined crystallite size of $Co_{(3-x)}Mn_{(x)}O_4$ phase for A) 0 %, B) 0.5 %, C) 1 %, D) 5 % & E) 10 % in nanometres. Note each map has a different heatmap scale to allow for visualisation of the spatial distribution within each extrusion.

The refined $Co_{(3-x)}Mn_{(x)}O_4$ crystallite size parameter from the Rietveld refinement of each catalysts extrusion at the start of reduction is shown in Figure 4-11. The scales of the heatmaps vary between each extrusion to allow for effective visualisation within the spatially

resolved refinements. Between the extrusions, a significant decrease in measured crystallite size is observed with increasing Mn levels. This is clear to see in the increased peak broadening of the spinel reflections as shown in Figure 4-8. The undoped sample shows the most inhomogeneity in crystallite size in Figure 4-11, with a large region within the body of the extrusion displaying up to 17 – 18 nm compared to the typical size of 15 – 16 nm throughout the rest of the extrusion. While the 0.5 % Mn extrusion shows some variation in one of the lobes of the trilobe compared to the remaining two, the rest of the catalyst series appear comparatively homogeneous in regards to crystallite size.

Across the range of doping levels, some voxels at the exterior of the extrusion display higher crystallite size. This doesn't appear consistent however, with only individual or small clusters of voxels standing out. Beyond these standouts, the exteriors of the extrusions do not display on average higher crystallite size in comparison to the interior regions.

Consideration must be given to the fact that addition of manganese to form a mixed spinel oxide will not form a disperse phase with a consistent repeating structure. Variations in the levels of manganese between oxide particles within the sample will lead to variations in lattice parameters, and an apparent broadening of the reflections. Additionally, there is the potential for the formation of polycrystalline particles, where multiple regions of different crystal orientations are present. In this case, the calculated crystallite size is more representative of the grain size within the polycrystalline particles, and not representative of the overall particle size. Overall, this means that the fitted crystallite size broadening is not necessarily representative of the supported particle size in the oxide phases beyond the undoped sample.

4.3.2 In situ reduction

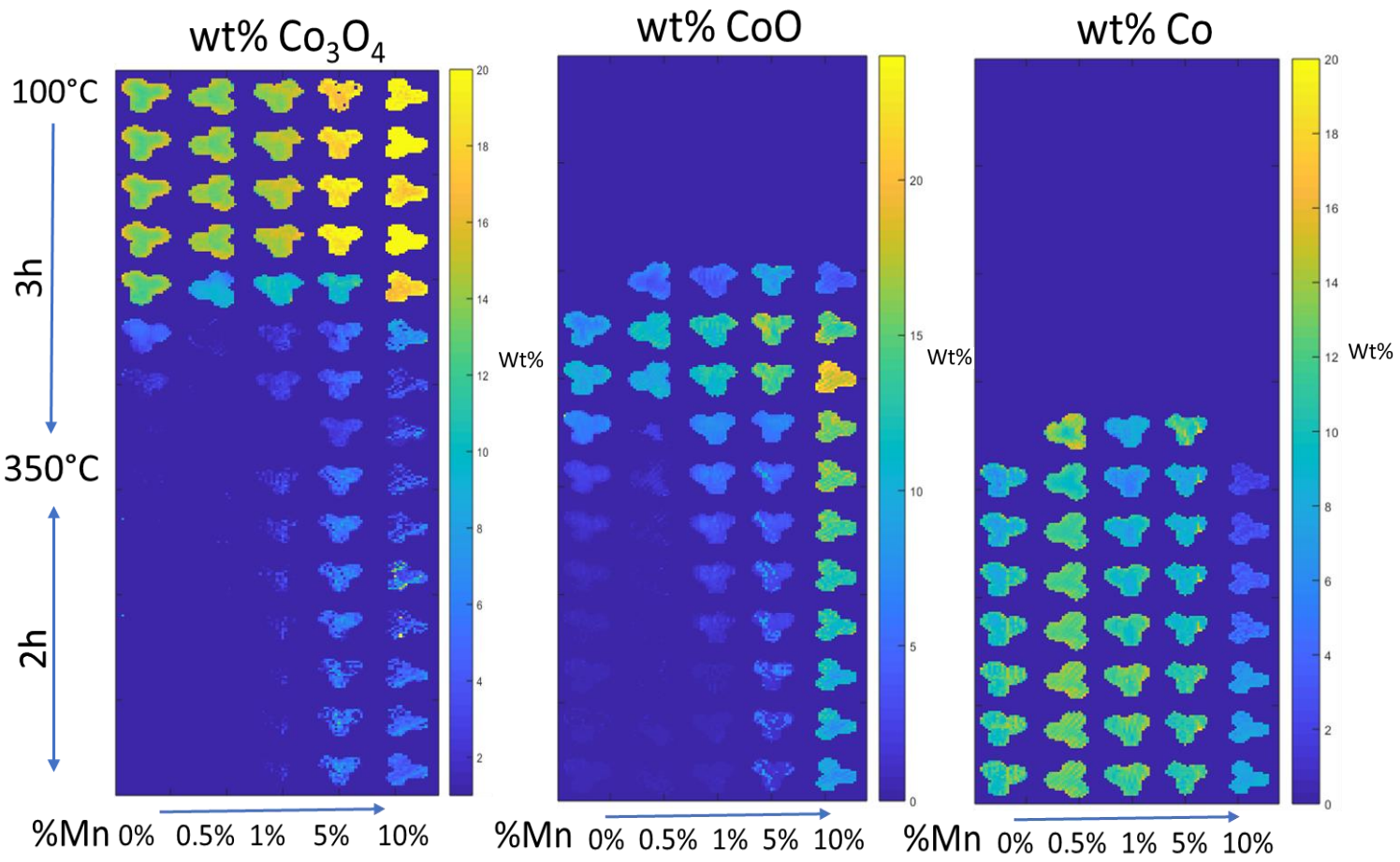

Figure 4-12 Maps of cobalt phase wt. % progressing throughout temperature ramp (100 – 350 °C, 1.4 °C/min) and dwell (2h) of catalyst activation, with wt. % loadings generated by Rietveld refinement of each individual voxel.

The individual reconstructed voxels were Rietveld refined to produce heatmaps of various refined parameters such as lattice parameters and weight %. Figure 4-12 shows the heatmaps of phase weight % of each cobalt phase present during catalyst activation. The undoped catalyst exhibits a delayed reduction relative to the 0.5 – 5 wt. % Mn doped samples for both the reduction to CoO, and to the cobalt metal phases. A similar reduction profile is seen in the 10 % Mn sample, however the reduction of Co from $Co_{(1-x)}Mn_{(x)}O$ to Co metal phases in this catalyst is hindered, with reduction still appearing to continue in the final scan. With the exception of the 10 % Mn sample, the catalysts appear to be effectively reduced within the measured parameters, with the wt. % of cobalt metal phases appearing ~9 – 12 wt. % and the wt. % of $Co_{(1-x)}Mn_{(x)}O$ appearing below 2 % in all other samples in the final scan. However, for

the 5 and 10 % sample, a detectable amount of spinel oxide appears to be present throughout the reduction.

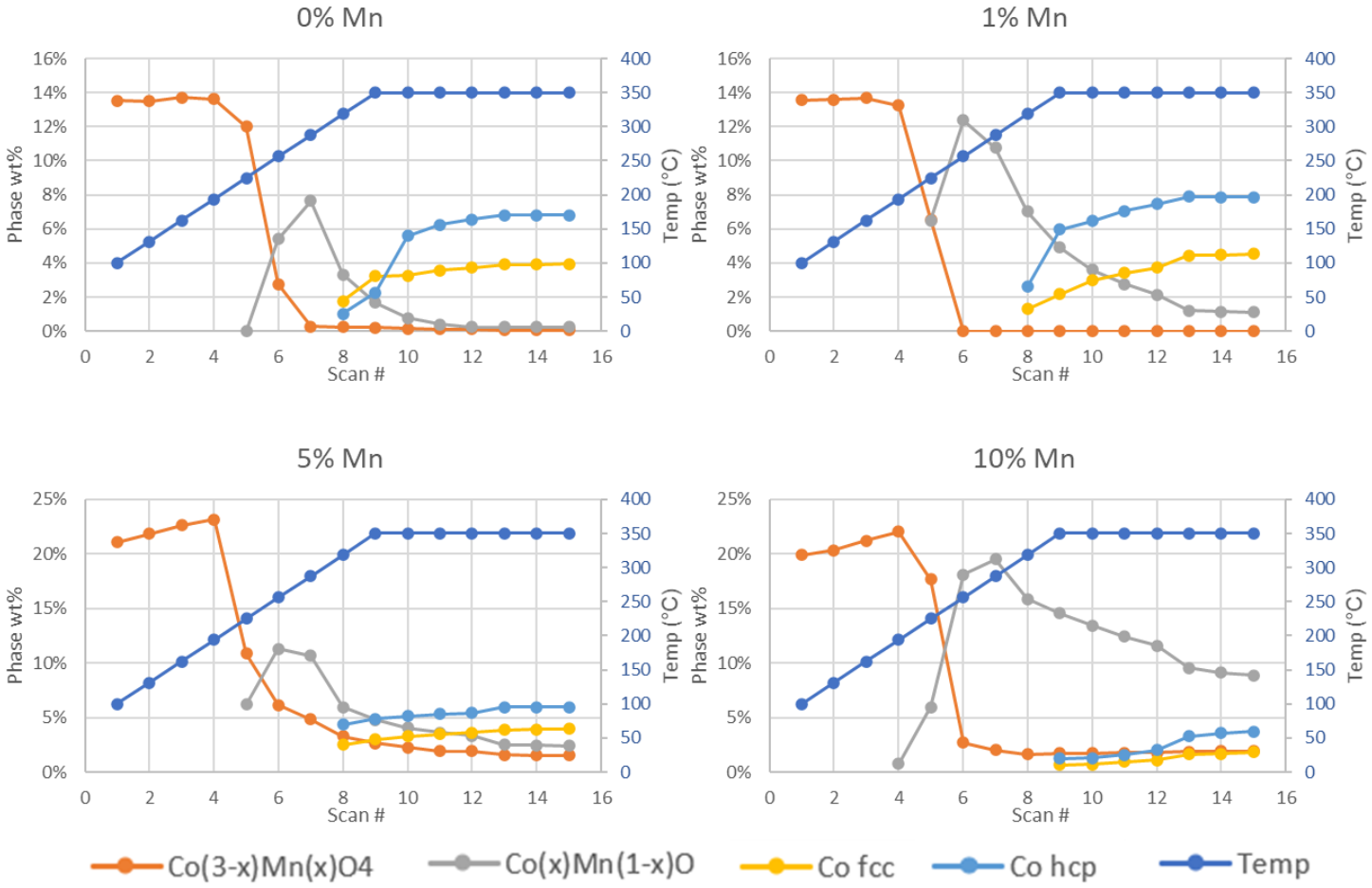

Figure 4-13 Refined phase wt. % during catalyst activation for 0, 1, 5, 10 % cobalt phase on the primary axis, with temperature profile on the secondary axis.

The charts within Figure 4-13 show the average evolution of phases within the catalyst extrusions during catalyst activation. As observed in the previous heatmaps, the 5 and 10 % Mn catalysts appear to contain both spinel oxide and $Co_{(x)}Mn_{(1-x)}O$ within the final scan, with the 10 % Mn catalyst still progressing in its reduction and containing ~8 wt. % $Co_{(x)}Mn_{(1-x)}O$.

For each catalyst, we can see that the predominant cobalt metal phase at the end of reduction is the HCP structure. Table 4-2 shows the wt. % of cobalt metal phases within the reduced catalyst extrusions, and their ratio. However, given the nominal loadings of the catalyst extrusions is 10 wt. % Co, a number of the extrusions appear to have their Co metal loadings overcompensated for.

The accuracy of the cobalt metal weight loadings, in particular the HCP, are reduced across the series due to the increased broadening of the cobalt metal phase which typically overlap with the TiO_2 support structures. This makes accurately quantifying the amount of FCC and HCP present within the reduced samples challenging by X-ray diffraction, as the HCP phase is likely being overestimated due to the overlapping of the significantly more intense anatase and rutile phases.

The lower content of cobalt metal in the high %Mn catalysts is consistent with the remaining oxide content present at the end of reduction.

Table 4-2 Cobalt oxide and metal phase % in refined extrusions post reduction, including HCP : FCC ratio and crystallite size.

% Mn	0	0.5	1	5	10
Wt. % $Co_{(x)}Mn_{(1-x)}O$	0.35	0.0	0.0	1.74	8.06
Wt. % Co FCC	3.94	4.55	4.54	3.98	1.85
Wt. % Co HCP	6.81	8.33	7.88	5.95	3.70
HCP : FCC	1.73	1.83	1.74	1.49	2.00
Size FCC (nm)	8.9	7.8	10.3	9.0	13.6
Size HCP (nm)	3.6	3.9	3.6	4.5	4.4

Figure 4-14 shows the heatmaps of anatase and Co_3O_4 intensity and weight loading of the undoped catalyst extrusion. Within the Co_3O_4 intensity map we can see a haloing, with the scale appearing to be larger around the exterior or the extrusion lobes. This haloing is not correlated with the intensity plot of the anatase support phase. When fit to phase wt. %, this haloing around the exterior of the extrusion is more apparent with the loading averaging ~12 wt. % in the interior of the extrusion, versus ~16 wt. % at the exterior.

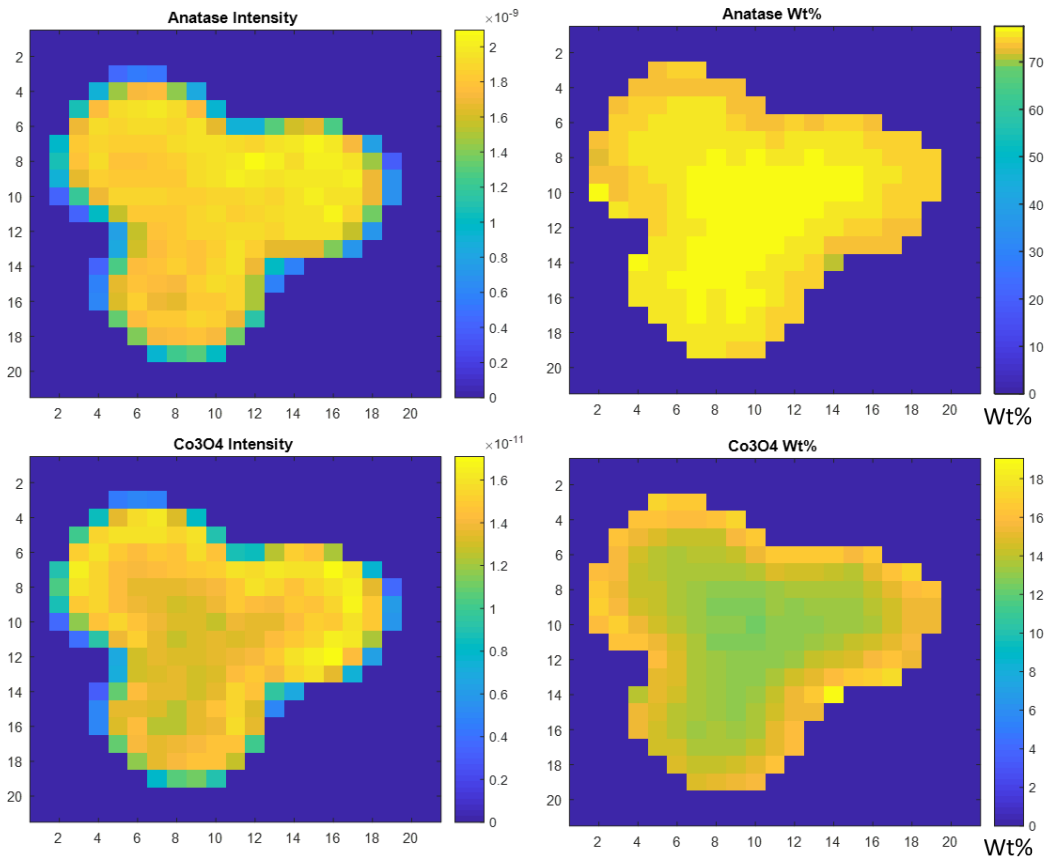

Figure 4-14 Rietveld refined phase intensity and wt. % of TiO_2 anatase and Co_3O_4 in the 0 % Mn catalyst extrusion. Axis for each heatmaps display voxel co-ordinates.

Figure 4-15 shows the heatmaps of cobalt oxide phases present in an intermediate stage of reduction. The gradient of Co_3O_4 within the extrusion has been inverted, with an increase now present within the internal of the extrusion. Meanwhile the CoO distribution is weighted strongly towards the exterior of the extrusion. This clearly shows that the cobalt oxide towards the exterior of the extrusions is being preferentially reduced during activation. This behaviour is not unexpected, and can arise from two possibilities.

Firstly, the exterior of the catalyst extrusion may be easier to reduce due to a variation in catalyst properties. Secondly, due to a gradient in H_2 present within the extrusion. As H_2 is consumed during the reduction of catalyst oxide phases, the partial pressure of H_2 will decrease locally, and be replaced by H_2O. This will cause a gradient of H_2 and H_2O throughout the radius of the extrusions, assuming minimal diffusion from the ends of the extrusions.

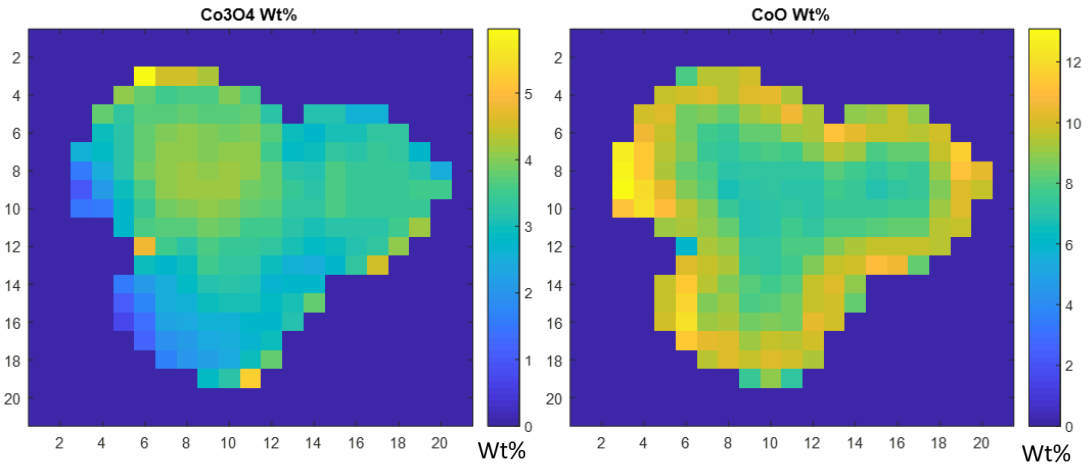

Figure 4-15 Co_3O_4 and CoO wt. % heatmaps of the undoped extrusion during scan 6 (t = 1.5 – 1.8 h, temp = 240 – 268 °C).

The heatmaps of Co metal phases present post reduction are shown in Figure 4-16. While the tendency for increased cobalt loading is still present towards the exterior of the extrusion, the location of higher loadings of HCP the exterior of the extrusion appear to be inverse to the regions of FCC with the highest loading.

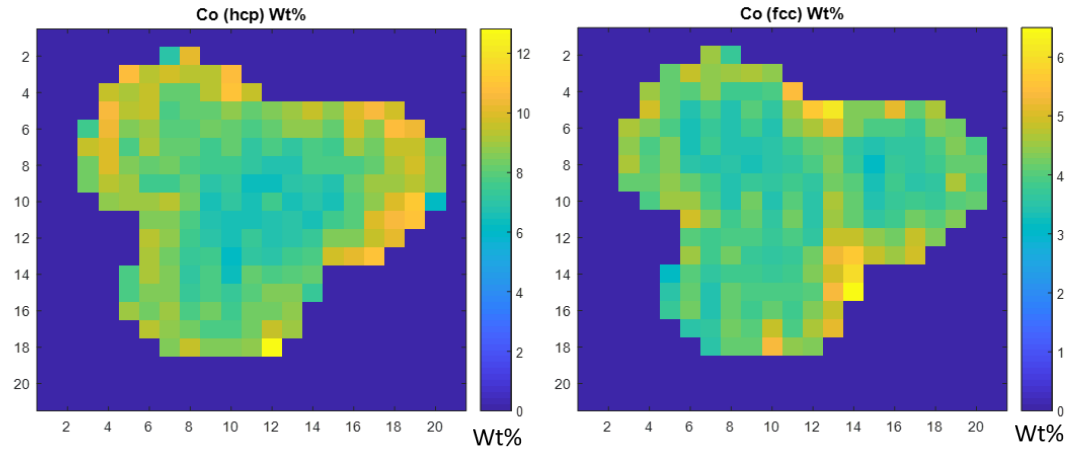

Figure 4-16 Co (HCP) and Co (FCC) wt. % heatmaps of undoped extrusion at the end of reduction, scan 15.

In an effort to compare the radial distributions more numerically between extrusions with varying manganese levels, the catalyst extrusions were subdivided into groups by their radial depth. Figure 4-17 shows an example extrusion with its radial batching map. A function (appendix Figure 8-11) was written to determine the distance of each voxel to the exterior layer of the extrusion, and the voxels were then divided into groups by this radial depth. This allows for refined metrics to be combined between voxels with the same radial depth. Typically, this function splits each catalyst extrusion into 5 layers of depth, however

frequently the 5th most internal layer contain only a small number of voxels. Consequently, any voxels further than 4 voxels from the exterior of the extrusion were grouped within the 4th and final group to prevent low population variability from skewing any observed trends, as well as providing an equal number of subdivisions across the results.

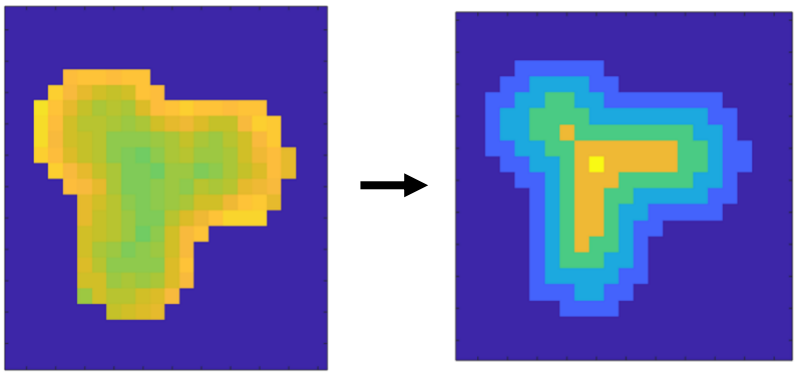

Figure 4-17 An example of radial batching, with the cropped extrusion (left) being filtered into groups of voxels (right) where the division of each voxel is dependent on the distance of the voxel to the exterior of the extrusion.

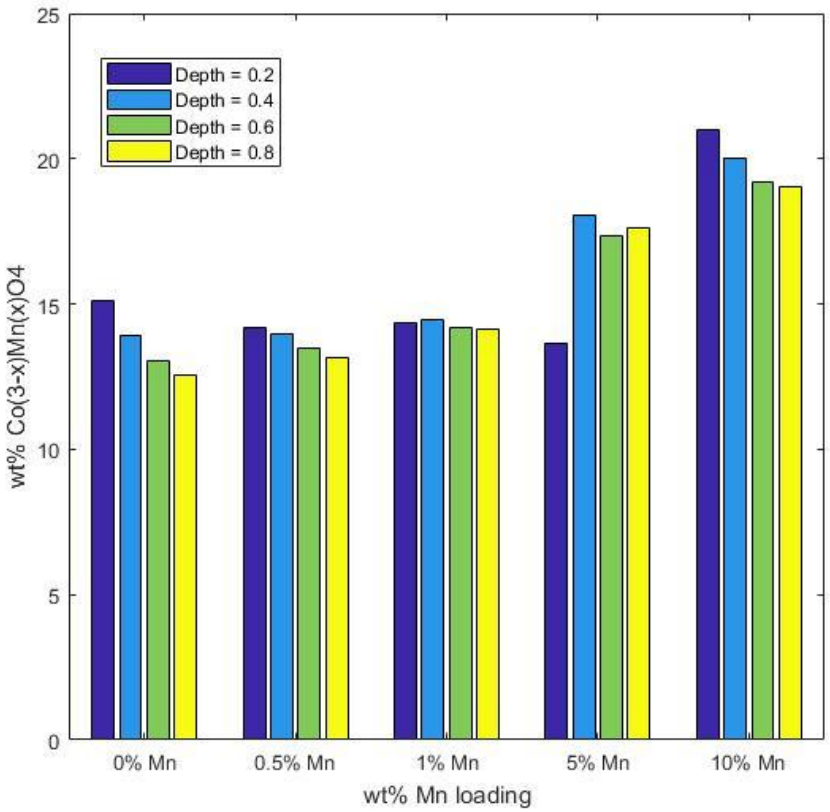

Figure 4-18 Radial distribution of spinel oxide before reduction for each catalyst extrusion, from the exterior (blue) to the interior (yellow) of the extrusion. The colour scheme of radial depth groups in this figure and following figures correspond to the colour schemes of layers shown in Figure 4-17.

Figure 4-18 shows the weight loading of $Co_{(3-x)}Mn_{(x)}O_4$ at varying radial depth for each dopant level. As observed in Figure 4-14 the undoped sample has a significant gradient in Co_3O_4 loading towards the exterior of the extrusion. This trend is reduced within the 0.5 % Mn extrusion, and in the 1 % Mn catalyst no gradient is present. While a gradient is observed in the 10 % Mn sample, the 5 % extrusion shows a significant decrease in Co loading around the exterior of the extrusion compared to the rest of the extrusion depth.

While the gradient throughout the trilobes is reduced by the addition of small amounts of Mn, the 0.5 % and 1 % Mn doped extrusions show a comparable total loading of spinel oxide. As the amount of Mn doping is increased to 5, followed by 10 %, the extrusions show an expected increase in spinel contribution.

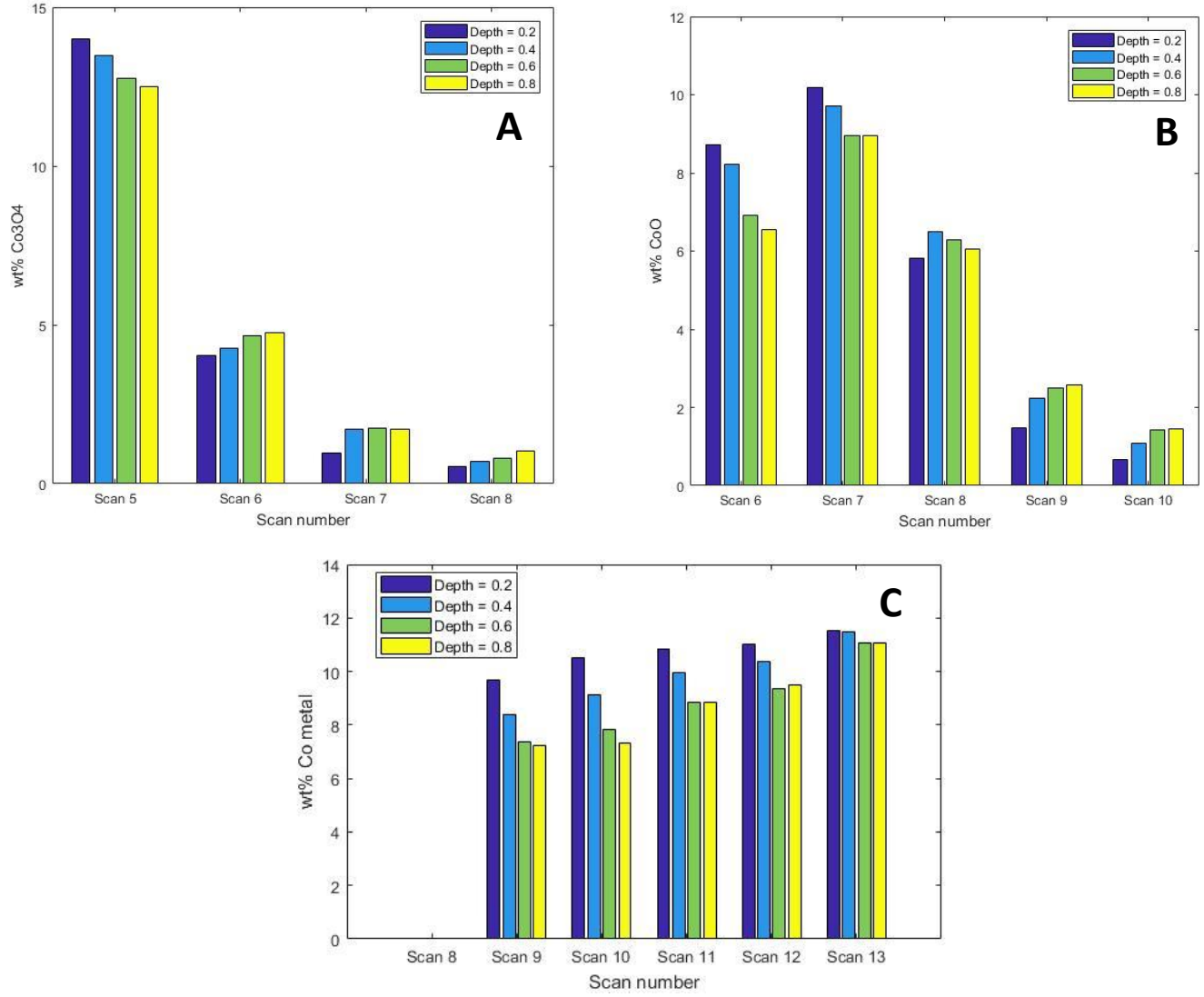

Figure 4-19 Radial distribution of Co phases in 0 % Mn extrusion at varying points during reduction, A) Co_3O_4 , B) CoO , C) Co FCC + Co HCP.

Figure 4-19 shows the radially distributed progression of cobalt phases within the un-doped catalyst extrusion during the reduction process. Between scans 5 & 6 in Figure 4-19 A, an inversion is observed in the radial distribution of Co_3O_4 within the extrusion, with the gradient swapping from increased intensity at the exterior, to increased intensity trending towards the interior. This supports the observations made from the heatmaps in Figure 4-15, suggesting an initial preferential reduction of the Co_3O_4 at the exterior of the extrusion.

The change in distribution of wt. % CoO supports this, with Figure 4-19 B showing the initial distribution skewing heavily towards the exterior layer in scan 6, as the exterior Co_3O_4 is reduced first, with a similar inversion observed over subsequent scans as the CoO is reduced to cobalt metal phases.

The cobalt metal distribution shown in Figure 4-19 C shows the expected initial gradient of higher wt. % towards the exterior of the extrusion initially, and this gradient diminishes as the reduction proceeds, with scan 13 showing only a slight difference in loadings at varying radial depths. This suggests that by the end of the activation, the reduction process is no longer diffusion limited, and that the cobalt has been effectively reduced throughout the depth of the extrusion for the undoped catalyst.

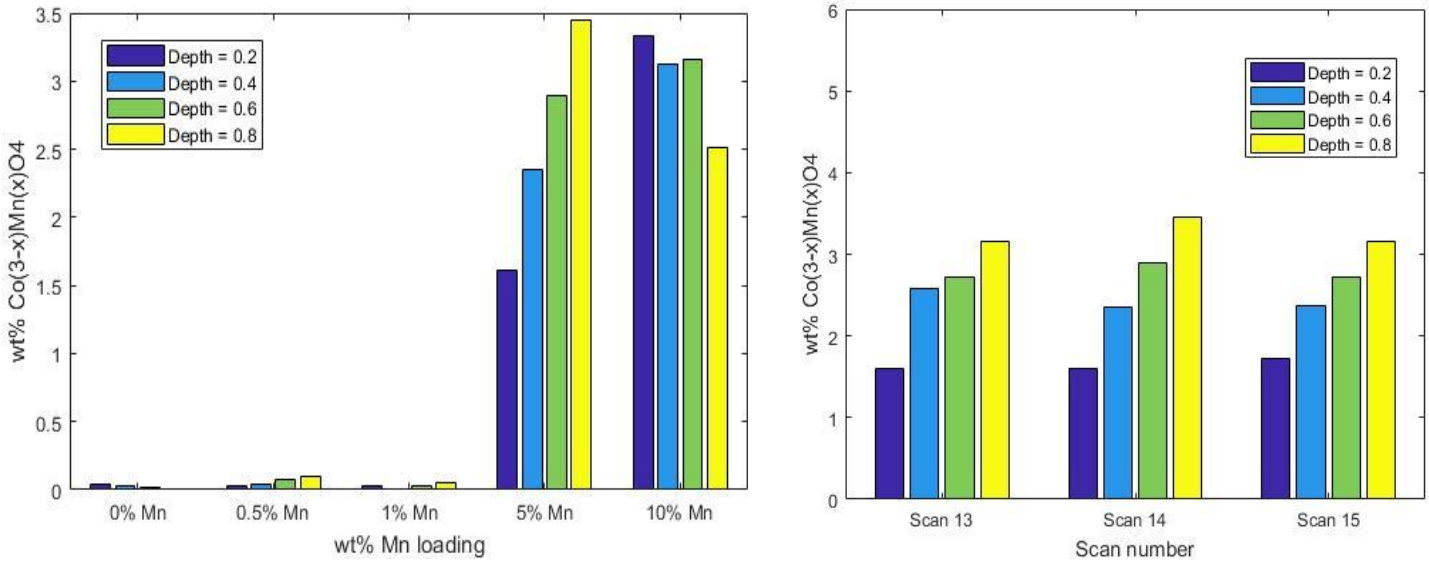

Figure 4-20 Radial distribution of spinel oxide A) at end of reduction for each catalyst extrusion, B) for the final 3 scans of the 5 % Mn extrusion.

Figure 4-20 A shows the radial distribution for spinel oxide for each catalyst extrusion in the final scan, at the end of reduction. For the catalyst extrusions with 0 – 1 % Mn show ~0 %

spinel oxide, the 5 and 10 % Mn catalysts still contain 2 – 3 % spinel oxide post reduction. While the 5 % Mn extrusion shows a clear trend of increasing wt. % spinel towards the interior of the extrusion, this is not the case with the 10 % Mn catalyst which shows an even distribution, with the exception of the far interior which displays a relative drop in $Co_{(3-x)}Mn_{(x)}O_4$ of 22 % compared to the remainder of the extrusion.

The distribution of spinel oxide within the 5 % Mn catalyst hints at the reduction is not H_2 diffusion limited at the end of reduction as the reduction has halted, and we can see from Figure 4-20 B that the distribution remains unchanged for the last 3 scans, or 1 h. The presence of remaining spinel oxide in the 5 and 10 % samples is consistent with the bulk refinements report in Figure 4-13.

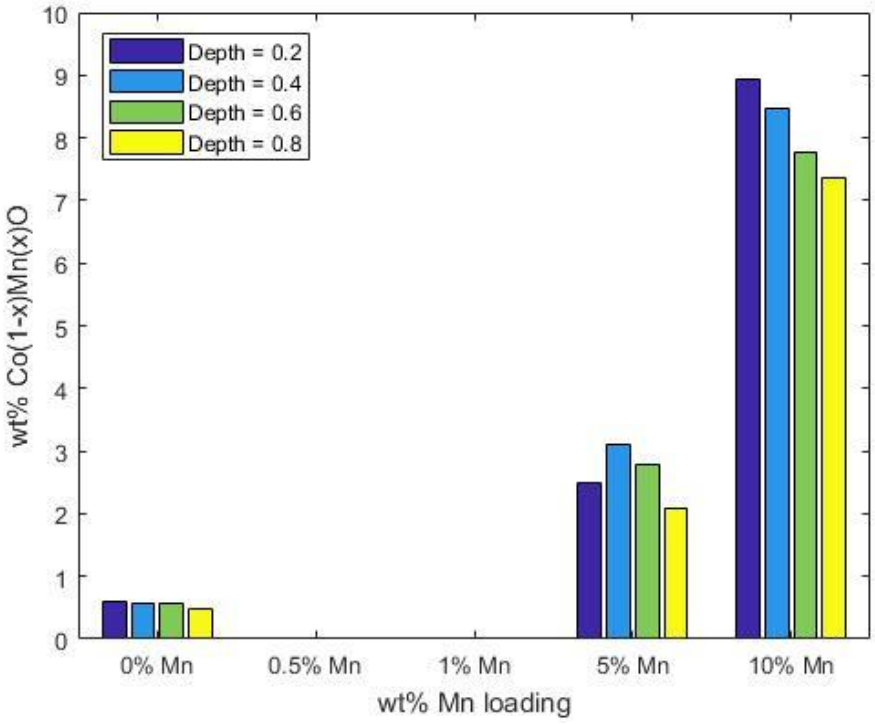

Figure 4-21 Radial distribution of $Co_{(1-x)}Mn_{(x)}O$ for each catalyst extrusion at end of reduction.

Figure 4-21 shows the radial distribution of $Co_{(1-x)}Mn_{(x)}O$ of each catalyst within the series at the end of reduction. While ~0.5 % CoO remains within the undoped extrusion, the 0.5 and 1 % Mn extrusions show no detectable presence of $Co_{(1-x)}Mn_{(x)}O$ by diffraction at any depth. Meanwhile, both the 5 and 10 % Mn catalyst extrusions show a gradient in the intermediate oxide with increasing intensity towards the exterior of the extrusions. While the outer layer of the 5 % Mn extrusion does show a lower loading of $Co_{(1-x)}Mn_{(x)}O$ oxide at the end of

reduction, this is consistent with the initial lower loading of the spinel $Co_{(3-x)}Mn_{(x)}O_4$ at the beginning of reduction, as shown in Figure 4-18. Once this initial variance is factored in, the trend between the 5 and 10 % Mn extrusions is consistent.

While cobalt oxide is expected to reduce to the metallic phases under the reduction conditions, the manganese is expected to remain in the MnO phase.[13] Although the 0.5 and 1 % Mn extrusions have a low loading of Mn, no presence of MnO is detected at the end of reduction by diffraction. Given the high dispersion of the manganese within the cobalt oxide prior to reduction, it is expected that the lack of diffraction of MnO phase at the end of reduction is due to the high dispersion and low overall loading.

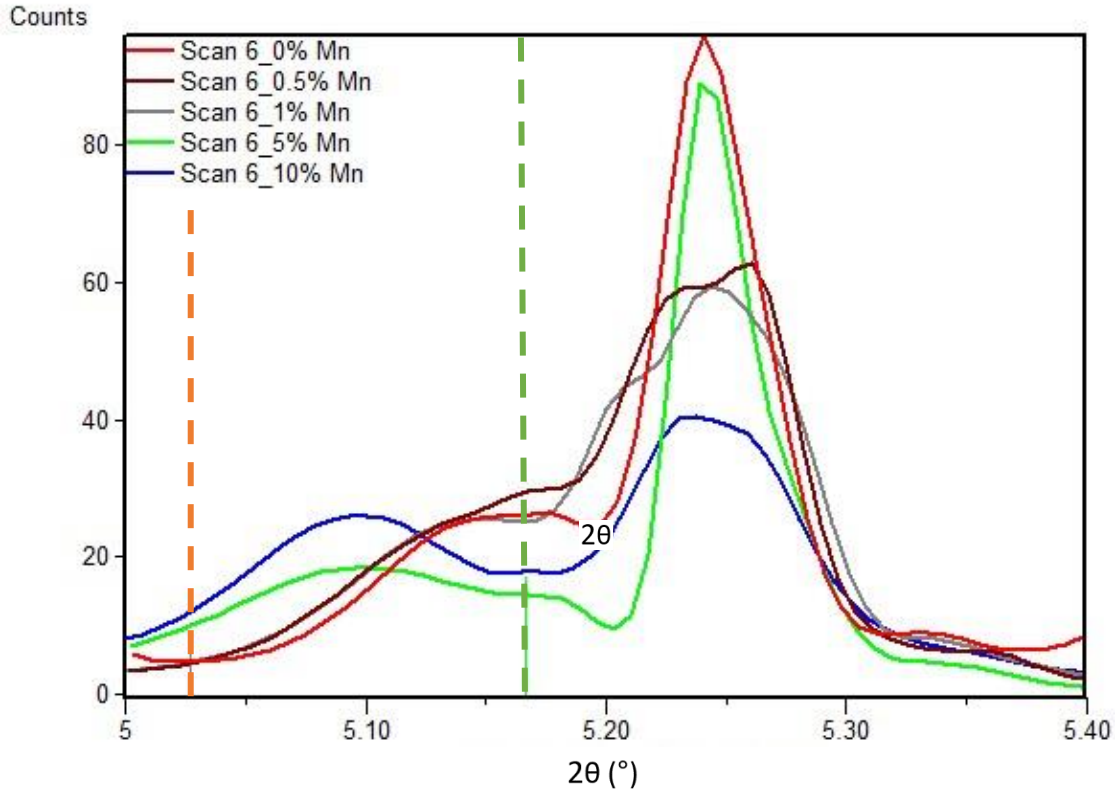

Figure 4-22 Diffraction around $Co_{(1-x)}Mn_{(x)}O$ 220 reflection for each catalyst extrusion in scan 6 (t = 1.5 – 1.8 h, temp = 240 – 268 °C) with markings for the CoO 220 reflection (green dashed line) and MnO 220 reflection (orange dashed line).

Figure 4-22 shows the diffraction data around the region of the cubic $Co_{(1-x)}Mn_{(x)}O$ 220 peak for each catalyst extrusion, taken part way through reduction with scan 6. By scan 6, the spinel oxide is largely reduced for each extrusion, with the exception of the undoped catalyst which still displays distinct peaks for Co_3O_4.

For the catalyst extrusions with 1 % Mn and below, the 220 reflection is positioned at the expected 2θ angle for CoO, around 5.17. Both the 5 and 10% Mn catalysts show a shift in the peak position by 0.07 2θ, with the lattice expanding due to the occupancy of the manganese in the cubic structure. While reflection maxima for both extrusions appear in the same position, they are asymmetric and appear to contain multiple broad contributions between the expected position for CoO (220) and MnO (220) respectively. This suggests that the ratio of manganese to cobalt within the $Co_{(1-x)}Mn_{(x)}O$ phase is not homogeneous, however this is to be expected as the structure is being actively reduced while the measurements are taking place. During this time it is reasonable to expect that even if initially the distribution of cobalt and manganese was homogeneous, with a consistent ratio across the spinel structure, that different regions are reduced to different extents. This would cause the apparent Co:Mn within the intermediate oxides to vary across the sample, leading to a broadening affect in the diffraction patterns of those phases.

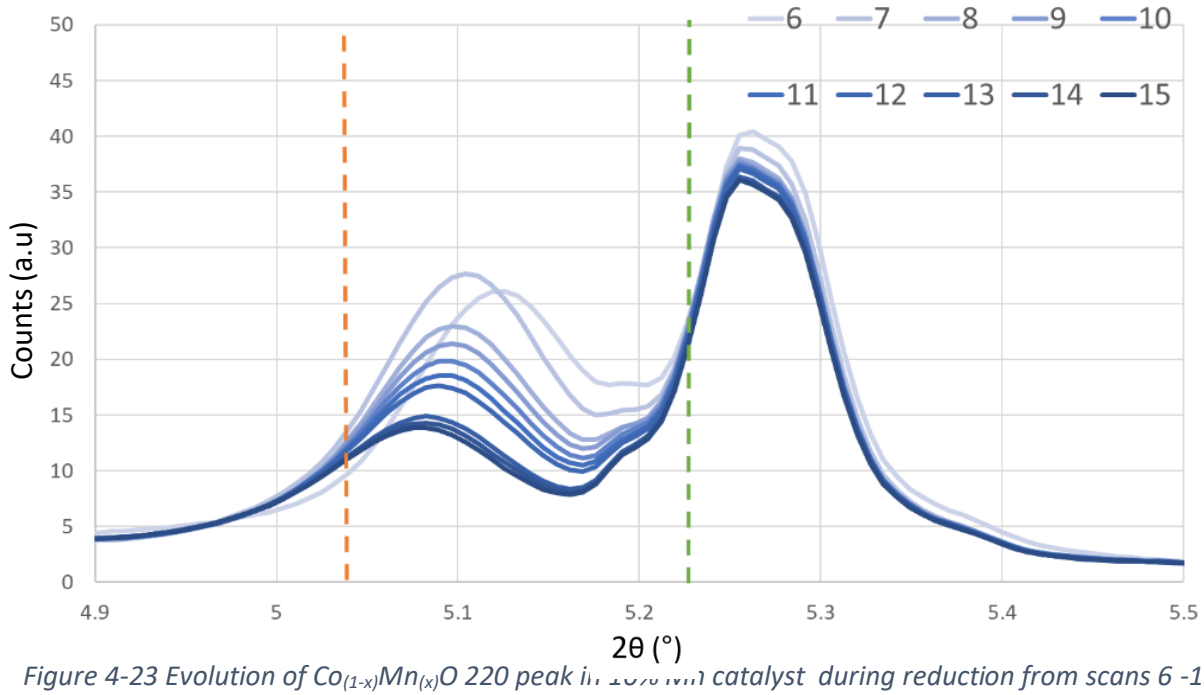

Figure 4-23 Evolution of $Co_{(1-x)}Mn_{(x)}O$ 220 peak in 10% Mn catalyst during reduction from scans 6 -15, with for nominal peak positions for CoO (green dashed line) and MnO (orange dashed line).

Figure 4-23 shows the continuation of the evolution of the cubic $Co_{(1-x)}Mn_{(x)}O$ phase focusing on the 220 reflection. As subsequent scans are taken, the 220 reflection is observed to progressively shift to a lower °2θ value, as the intensity also drops with increasing cobalt reduction to the metallic phases.

The observations made can be explained by a shift in the ratio of cobalt and manganese within the $Co_{(1-x)}Mn_{(x)}O$, as while the cobalt within the phase is reduced to the metal, the manganese remains oxidised and the Co:Mn ratio is depleted. This more Mn enriched structure has a larger lattice parameter, hence the decrease in 2θ position for the 220 reflection.

Towards the end of reduction in scans 13 to 15, the reflection position for $Co_{(1-x)}Mn_{(x)}O$ has generally stabilised but not shifted entirely to the position expected for pure MnO. This suggests that a proportion of the cobalt within the catalyst is not effectively reduced under the reduction conditions used for the experiment, and is trapped in the 2+ mixed-oxide form. This is consistent with the observations made in Figure 4-20 B, which show the reduction of the 2+ oxide phase has halted between scans 13 & 15. Additionally, given that the wt. % of this phase is ~2.5 % at the end of reduction, and it contains both manganese and cobalt, a significant proportion of the 5 % Mn loaded onto this catalyst is unaccounted for, with no other manganese phases identified beyond the two mixed oxides. While the Mn dopant isn't expected to reduce beyond the MnO oxide, no additional phases are detected by diffraction that account for the manganese content.

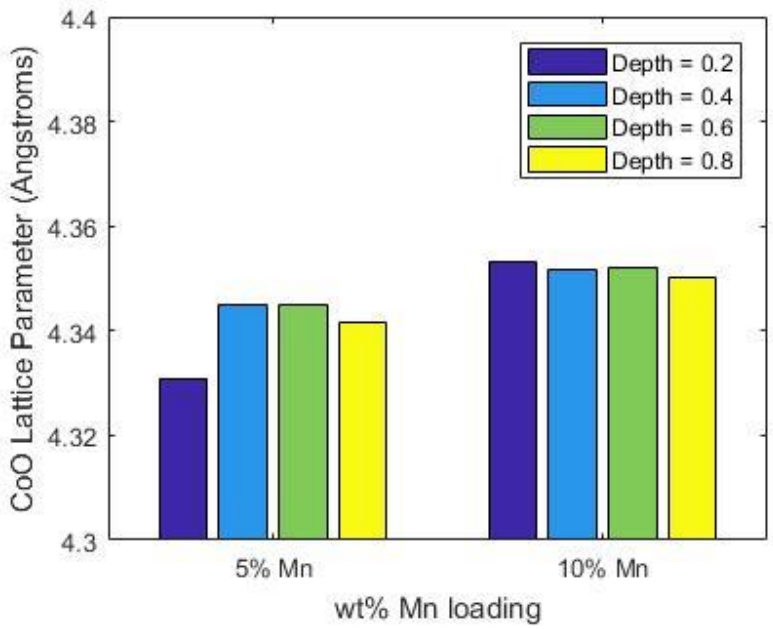

Figure 4-24 Radial $Co_{(1-x)}Mn_{(x)}O$ lattice parameter at end of reduction for 5 and 10 % Mn catalyst extrusions.

Figure 4-24 shows the radially batched $Co_{(1-x)}Mn_{(x)}O$ lattice parameter for the 5 and 10 % manganese catalysts at the end of reduction. While there is a slight negative gradient in lattice

parameter in the 10 % Mn catalyst from the external to the internal of the extrusion, the total variation is from 4.353 Å to 4.350 Å, or an average contraction of the structure by 0.07 %.

There is also minimal variation in the lattice size of the $Co_{(1-x)}Mn_{(x)}O$ in the 5 % Mn catalyst remaining post reduction. However, the catalyst shows a reduced lattice parameter in the exterior of the extrusion compared to the interior. This suggests the $Co_{(1-x)}Mn_{(x)}O$ phase in the exterior has a higher cobalt content, either due to a lower degree of reduction of the $Co_{(1-x)}Mn_{(x)}O$ to cobalt metal, or a decrease in manganese content within the mixed oxide structure. Figure 4-18 and Figure 4-21 show the exterior of the 5 % Mn extrusion to have both lower spinel oxide and $Co_{(1-x)}Mn_{(x)}O$ content than expected by the typical trends observed across the remaining catalyst extrusions.

While the exterior of the catalyst extrusion is subject to higher error, due to the propensity for the voxels to only be partially filled with catalyst extrusion leading to reduced signal intensity, this cannot explain a change in lattice parameter in a specific phase. The change in lattice parameter combined with the variation in wt. % loading suggests that the observations made for the exterior of the 5 % extrusion is real, and not a symptom of overall decreased signal intensity.

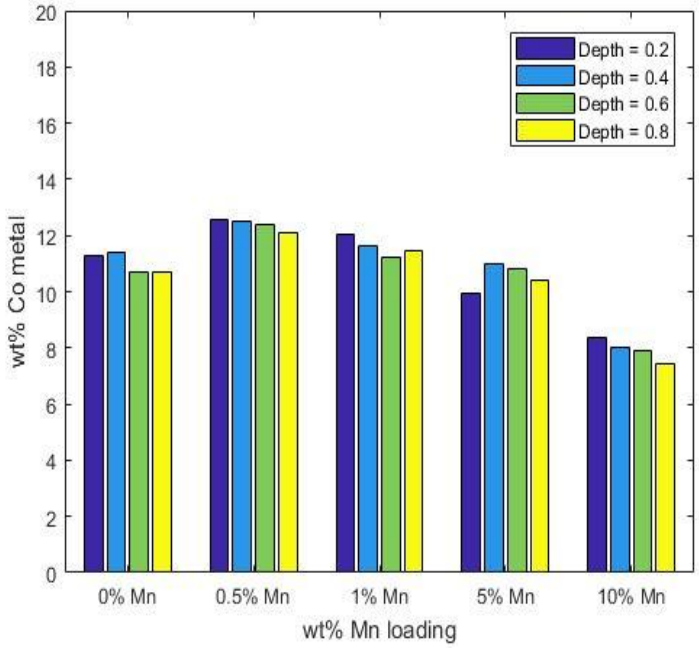

Figure 4-25 Radial distribution of cobalt metal (combined FCC and HCP) at end of reduction for each catalyst extrusion.

Figure 4-25 shows the radial distribution of cobalt metal present in each catalyst extrusion at the end of reduction. In comparison to the undoped sample, we can see that the 0.5 and 1 % Mn catalyst extrusions show a greater extent of reduction throughout the depth of the trilobes, with both showing increased wt. % cobalt metal at all depths. As the % Mn loading is increased to 5 %, a small decrease in final cobalt metal content is observed, which is expected from the observations of cobalt retained within the cobalt spinel and cubic oxides at the end of reduction. The same observation is made for the 10 % extrusion, however the decrease is more significant as expected by the retained presence of $Co_{(1-x)}Mn_{(x)}O$ at the end of reduction. With the exception of the exterior of the 5 % Mn catalyst, each extrusion shows an overall trend of slightly decreasing metal content towards the interior of the catalyst extrusions.

4.3.3 Fischer-Tropsch Testing

After reduction, the catalysts underwent a brief period of operation at pseudo-FT conditions. Cobalt FT catalysts typically evolve over the initial period under FT conditions[14] undergoing partial deactivation before stabilisation of activity and product selectivity occurs. Due to this, it is useful to operate the studied catalysts under FT conditions for a period of time to allow them to overcome this initial change. The structure of the catalyst after this period is then more representative of the active catalyst than post reduction. Due to the limitations of the quartz reaction cell, it was not feasible to operate under the pressures typical for Fischer-Tropsch, and so instead the reaction was conducted at atmospheric pressure. Under these conditions, the catalyst is expected to largely produce methane, and while some evolution of the catalyst may occur due to exposure of syngas, the catalyst will not be exposed to the same conditions expected during typical FTS.

The reaction cell was operated under pseudo-FT conditions for only 3 h, during which 5 scans were measured. For the purposes of comparison, only the first and last scans measured are discussed, to allow for comparison of the changes observed over the brief experimental time. Figure 4-26 shows the summed diffraction pattern of the 5 % Mn extrusion for both the first scan and the last scan prior to decommissioning. When normalised by the major peak of the anatase (101) structure, the summed diffraction patterns overlap very precisely. This includes the regions of the metallic cobalt phases as well as the $Co_{(1-x)}Mn_{(x)}O$ phase. This is consistent throughout the extrusions, (reported in the appendix Figure 8-4 through Figure 8-7) which all show no visual difference in their summed diffraction patters from start to finish of the pseudo-FT conditions.

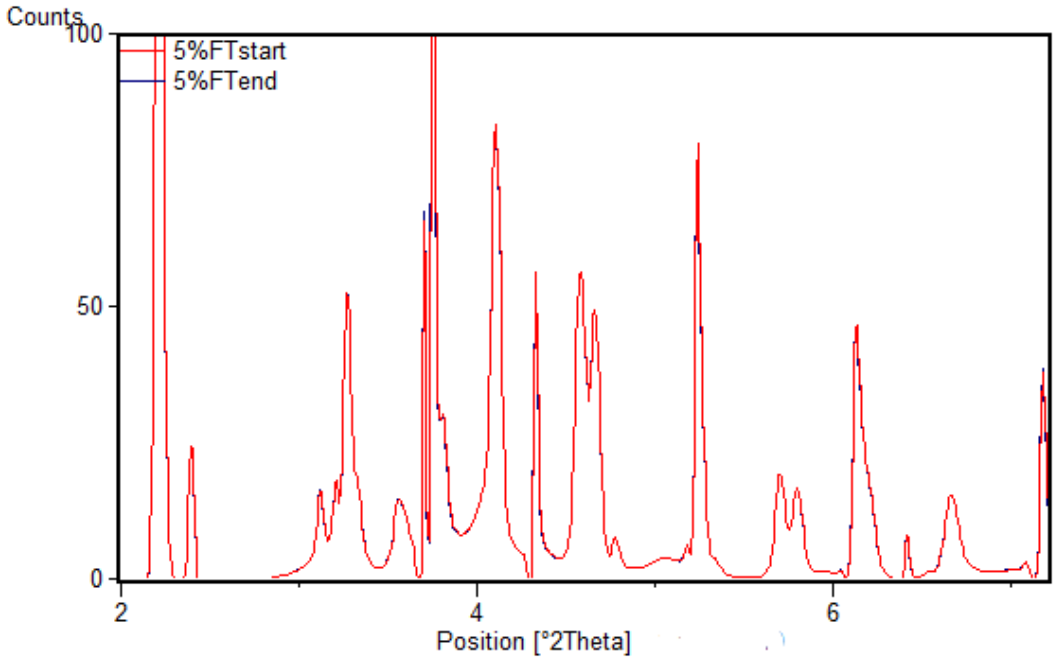

Figure 4-26 Summed diffraction patterns of 5 % Mn extrusion at beginning and end of pseudo-FT conditions (comparison of diffraction patterns for remaining extrusions included in Figure 8-4 through Figure 8-7).

Table 4-3 Rietveld refined Co(1-x)Mn(x)O phase wt. % at start and end of pseudo-FT conditions for each catalyst extrusion.

% Mn		**0**	**0.5**	**1**	**5**	**10**
$Co_{(1-x)}Mn_{(x)}O$	Start	0.35	0.0	0.0	1.74	8.06
Phase wt. %	End	0.35	0.0	0.0	1.72	8.01

Table 4-3 shows the Rietveld refined phase loadings of each catalyst extrusion at the beginning and end of the pseudo-FT conditions. Across the series, no significant change is detected in the wt. % of $Co_{(1-x)}Mn_{(x)}O$. A slight variation appears for the high % Mn samples, which display a very minor decrease, however this change is not large enough to be considered significant.

Beyond the cobalt oxide and metallic phases, no additional phases were detected in the summed diffraction patterns between the start and end of pseudo-FT conditions.

Figure 4-27 shows the difference heatmaps for both FCC and HCP cobalt metal between the start and end of the pseudo-FT conditions. The heatmaps were generated by subtracting the difference of the refined wt. % value for each voxel refined. For the majority of the extrusion crops, little is observable beyond the noise or variability of the refinement. The exception

looks to be the FCC phases of the 0 and 5 % Mn extrusions, which appear to have a slight reduction in FCC loading across the depth of the catalyst extrusions.

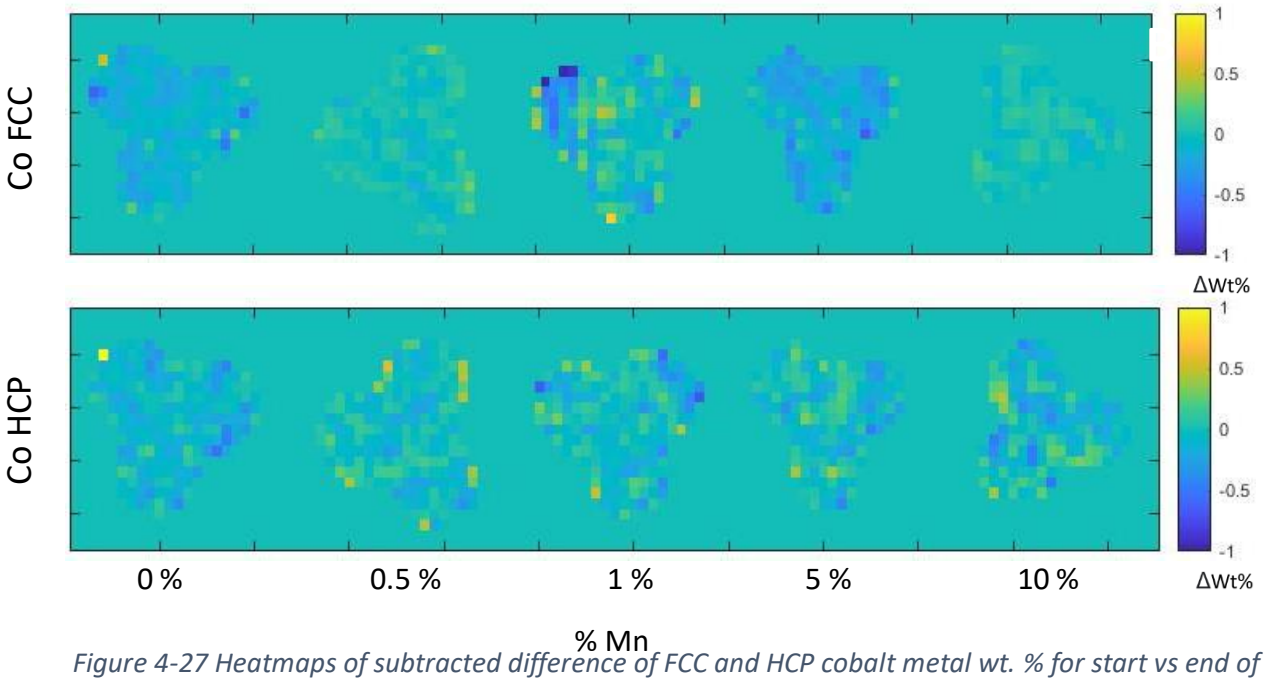

Figure 4-27 Heatmaps of subtracted difference of FCC and HCP cobalt metal wt. % for start vs end of pseudo-FT conditions for each catalyst extrusion.

Figure 4-28 shows the same subtracted refinement metrics, however grouped by radial depth. Visualised in this manner, the decrease in FCC wt. % for the 0 and 5 % Mn catalyst extrusions is a lot clearer with the decrease present across the depth of both extrusions. For the remaining extrusions the FCC wt. % change is minimal, with the exception of the exterior of the 1 % Mn extrusion which appears to show a reduction in loading for the two exterior groups. The heatmap of the 1 % Mn extrusion in Figure 4-27 A shows a cluster of voxels around a section of the exterior which report a significant decrease in FCC cobalt wt. %. These clusters appear to be responsible for the majority of the overall average decrease in FCC cobalt metal in the outer two layers, rather than the shift being consistent throughout the extrusion cross-section.

For the HCP wt. % the majority of change observed is minimal, though overall there is a slight reduction in loading across the catalyst series. The change is more significant in two areas, firstly the 0 % undoped catalyst shows a decrease in HCP loading similar to the decrease in FCC loading observed. The second region that shows significant change is the interior of the 10 % Mn extrusion, where both inner layers show a decrease of 0.1 wt. %. While the change is significant relative to the other observations made, the heatmaps in Figure 4-27 B suggest

that a small number of voxels are responsible for the change rather than a general trend of cobalt oxidation within the interior as a whole.

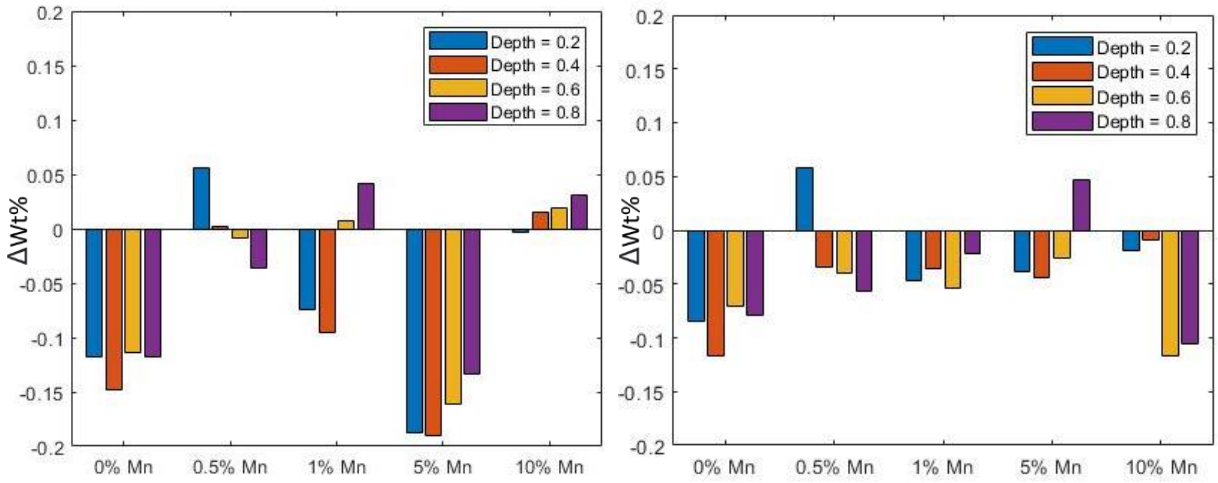

Figure 4-28 Radially grouped subtracted difference of A) FCC and B) HCP cobalt metal wt. % for start vs end of pseudo-FT conditions for each catalyst extrusion.

While the changes observed in the structure of the catalyst during operation under pseudo-FT conditions are minor, the catalysts were operated for a short period of only 3 h and at non-representative pressures. Other than the minor changes observed in the cobalt metal and oxide phases, no other phases were detected by XRD between scans taken during operation under pseudo-FT conditions.

To gain a better understanding of the effect on manganese on the evolution of the active cobalt phases during FTS, the catalysts would need to be operated over longer periods, and under conditions more representative of FTS, i.e. at high pressure.

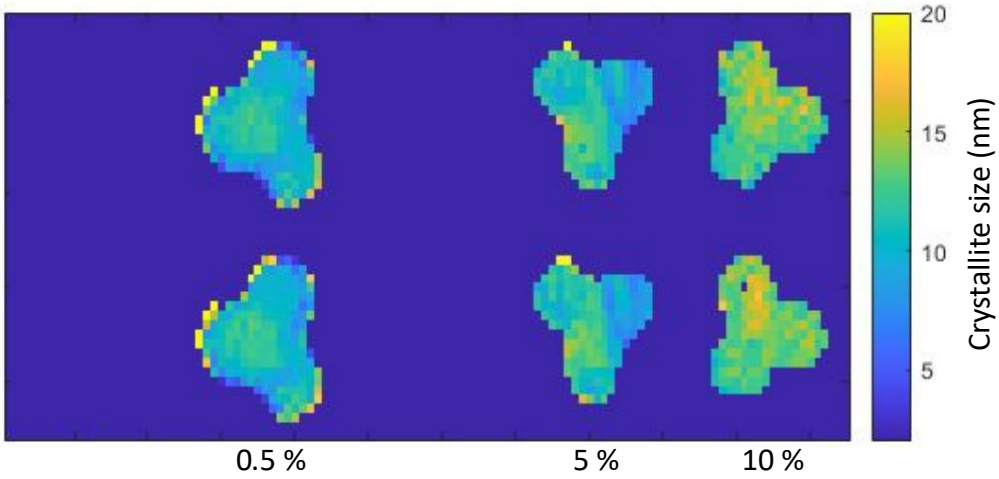

Figure 4-29 Calculated FCC crystallite size for 0.5, 5 & 10 % Mn extrusions at start and end of pseudo-FT conditions. 0 & 1 % Mn extrusions were excluded from spatial crystallite size refinement of the Co FCC phase due to the overlapping of the exclusion area required by the thermocouple reconstruction artefacts overlapping with the 111 reflection of Co FCC.

Figure 4-29 and Figure 4-30 show the crystallite size measured at the start and end of pseudo-FT conditions for cobalt FCC and cobalt HCP respectively. Due to overlapping of the exclusion range of the artefacts from the thermocouple casing and the cobalt FCC peak in the 0 % and 1 % extrusions, fitting of the broadening contribution of this phase wasn't possible. For both extrusions, when the broadening contribution was allowed to be fit during the spatially resolved refinement, the excluded region allowed the phase to diverge during the fit. Due to this, the broadening contribution for the FCC phase was fixed in these extrusions. For the remaining extrusions, the spatially resolved crystallite size corresponds well to the bulk crystallite sizes reported in Table 4-2, with a minor increase observed in the 10 % Mn sample. While minor variations in regions are observed across the extrusions, little variation is observed between the scans taken at the start and end of the pseudo-FT conditions.

For the equivalent heatmaps of cobalt HCP phase shown in Figure 4-30, we can see a much more obvious variation between doping levels. In this case, at higher doping levels we can see an increase in HCP crystallite size from ~3.5 nm to up to 5 – 6 nm. Across the series, we can see striations, lines of variation of fitted crystallite size. This is more significant in some extrusions than others, but given they are parallel within the extrusions these are likely due reconstruction artefacts from the thermocouple casing. The effect is likely minor as the

overall crystallite size change is small, and that the striations are not observed in the weight loading heatmaps. As with the FCC phase, no significant variation is observed between the start and end of the pseudo-FT conditions.

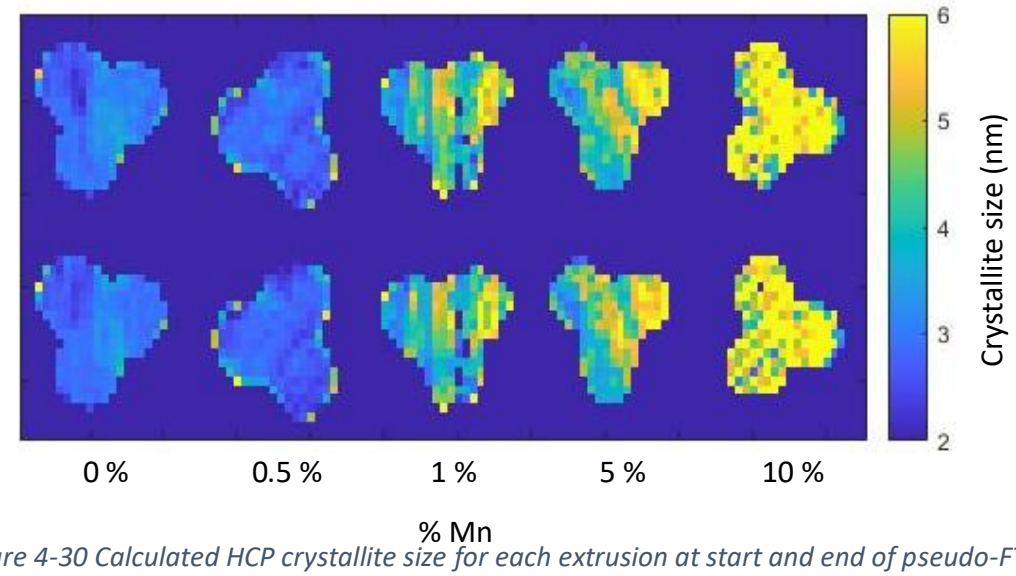

Figure 4-30 Calculated HCP crystallite size for each extrusion at start and end of pseudo-FT conditions.

4.4 Conclusions

A series of manganese doped cobalt FT catalyst extrusions have been extensively studied by XRD-CT. Simultaneous *In situ* study by XRD-CT of the catalysts provided insight into the relationship between manganese loading and the evolution of cobalt phases during H_2 activation. The spatially resolved nature of XRD-CT has allowed insight into the activation of the cobalt phases in relation its location within the catalyst extrusion. The evolution of phases during catalyst activation has been studied as a function of radial depth, providing insight into the preferential reduction of the exterior radius of the extrusions.

Data processing workflows have been developed to allow for the Rietveld refinement of the spatially resolved reconstructed diffraction patterns. This has allowed for quantitative phase information over the cross section of the catalyst extrusions studied.

While the catalyst extrusions were further studied under pseudo FT conditions at atmospheric pressure, the short run time and lack of pressure limited the evolution of phases present within the extrusions during this time. To study the catalyst series under representative operational FT conditions, a high pressure cell will be required in addition to an extended run plan.

Paterson *et al*.[2] report that equivilent catalyst extrusions to ones studied in this work display sudden alcohol selectivity (>30 %) with manganese loadings ≥3 wt. %, and with little alcohol selectivity (<5 %) with doping levels lower than this. In this work, a significant variable in the resulting extrusions post activation is the presence of the intermediate oxide phase $Co_{(1-x)}Mn_{(x)}O$, which is only detected in the extrusions with 5 and 10 % Mn. However, given the limited number of samples examined in this study, specifically around the 2 – 3 % Mn levels reported by Paterson *et al*. as being a selectivity threshold, the correlation of the presence of this phase post activation with reported alcohol selectivity is limited.

While Paterson *et al*.[2] report the formation of cobalt carbides at H_2:CO ratios relevant to typical FT operation, no additional phases formed that could be identified by diffraction during the limited operation under pseudo-FT conditions. Additionally, the experimental parameters used include a higher H_2:CO of 2, which would disfavour the formation of bulk

CoC_2. Given the reports of Pei *et al*.,[3] the potential formation of cobalt carbides during operation is of particular interest in relation to alcohol selectivity.

4.5 References

1. G. P. Van Der Laan and A. A. C. M. Beenackers, *Catalysis Reviews*, 1999, **41(3-4)**, 255-318.
2. J. Paterson, M. Peacock, R. Purves, R. Partington, K. Sullivan, G. Sunley, and J. Wilson, *ChemCatChem*, 2018, ***10*(22)**, 5154-5163.
3. Y. P. Pei et al. *ACS Catalysis,* 2015, **5.6**, 3620-3624.
4. J. Paterson, M. Peacock, E. Ferguson, R. Purves, and M. Ojeda, *ChemCatChem*, 2017, **9.18**, 3463-3469
5. H. G. Tompkin and J. A. Augis, *Oxidation of Metals*, 198*1.* **6(5)**, 355-369.
6. P. Senecal et al., *ACS Catalysis*, 2017, ***7*(4)**, 2284-2293.
7. H. M. Rietveld*, Journal of Applied Crystallography*, 1969, **2.2**, 65-71.
8. A. A. Coelho, *Journal of Applied Crystallography*, 2018, ***51*(1)**, 210-218.
9. B. Boucher, R. Buhl and M. Perrin, *Journal of Physics and Chemistry of Solids*, 1971, ***32*(10)**, 2429-2437.
10. X. Liu and C. T. Prewitt, *Physics and Chemistry of Minerals*, 1980, ***17*(2)**, 168-172.
11. Meera et al, *International Journal of Physical, Chemical & Mathematical Sciences*, 2014, **3,** 1
12. C. L. De Silva, R. K. Garlapalli, and J. P. Trembly, *Journal of Environmental Chemical Engineering*, 2017, **5(1)**, 488-493.
13. O. A. Bulavchenko, T. N. Afonasenko, A. V. Ivanchikova, V. Y. Murzin, A. M. Kremneva, A. A. Saraev and S. V. Tsybulya, *Inorganic Chemistry,* 2021, **60(21)**, 16518-16528.
14. H. Karaca et al., *Chemical Communications*, 2010, ***46*(5)**, 788-790.

Chapter 5 - High pressure XRD-CT study of Mn doped catalyst extrusion series

5.1 Introduction

To best understand how catalyst systems behave during their operation, it is ideal to study them in operational conditions that are as close to representative as possible. This provides confidence that observations made during study are applicable to the catalyst studied while they are undergoing operation. Prior to their operation, cobalt Fischer-Tropsch catalysts undergo a hydrogen activation, to reduce the cobalt oxide phase to the active cobalt metal, which is air sensitive. Following this, the Fischer-Tropsch reaction is conducted at both high temperature (≥200 °C) and pressure (≥20 bar). During operation, the catalysts undergo significant structural change both in the short and long term.[1]

Van Ravenhorst *et al.*[2] report on the formation of cobalt carbide in a Co/TiO_2 catalyst studied in operando conditions over 48 h by XRD & XAS. During the experiment, the authors report the detection of cobalt carbide formation was initially observed by XAS, and subsequently by XRD, however they note that the formation of the carbide did not correlate with a change in product formation. The experiment was operated under a H_2:CO of 1:1, and responsible for the rapid formation of the cobalt carbide. While a H_2:CO of 1:1 is lower than typical of FT operation conditions, the ratio is representative of conditions expected towards the outlet of a fixed catalyst bed during operation, where carbide formation is a more relevant form of deactivation.

Conducting characterisation on a catalyst sample within a reaction cell capable of operating at conditions of high temperature and pressure is challenging. With a brilliant X-ray source and sufficient detector sensitivity, X-ray Diffraction Computed Tomography (XRD-CT) can be used to investigate the crystalline phases of a catalyst during operation,[3] providing the X-ray source and diffraction are brilliant enough to penetrate the reaction cell.

In this work, a high-pressure reaction cell has been designed and commissioned to allow for the simultaneous study of multiple catalyst samples under representative Fischer-Tropsch conditions. Various issues arose due to the complexity of the task of investigating samples

contained within a metal reaction cell, and solutions were explored to overcome these challenges.

5.2 Experimental

5.2.1 Catalyst samples

The commercial catalyst series studied in this project has been supplied by BP, the projects' industrial sponsors. The catalyst series is based on cobalt supported on titania trilobed extrusions, with 10 wt. % Co and 0-10 wt. % Mn. The supplied catalysts are in spinel oxide form prior to activation and reaction. This report focuses on results obtained for catalysts containing the following loadings: 0, 0.5, 1, 1.5, 2, 3, 5, & 10 % manganese.

The catalysts were synthesised by the simultaneous impregnation of cobalt nitrate hexahydrate and manganese acetate hexahydrate on P25 titania. The resulting mixture was formed into extrusions 1.8 mm trilobed extrusions, before being calcined at 300 °C for 2 h.

5.2.2 XRD-CT measurement

XRD-CT experiments have been conducted at ESRF on the ID15A beamline where a 95 keV beam of 40 x 40 µm was utilised. The reactor cell was mounted on a goniometer and aligned to the X-ray beam axis for both perpendicular translation and axis of rotation. To collect the required sequence of diffraction patterns that could then be reconstructed into a tomographic image, the reaction cell was translated across the beam by a known number of steps (s) and rotated by s/180°. The translation was repeated until the reaction cell had been scanned 180° in total. The number of translational and rotational steps are determined such that the desired spatial or temporal resolution is achieved. An additional variable is the acquisition time per step, which must be sufficient to produce a high signal to noise ratio for each scan. This is dependent on the X-ray flux, sample crystallinity, cell transmittance and detector sensitivity. The diffraction patterns were collected with a Pilatus 2D detector.

5.2.3 Reactor design

A pressure reactor was designed and utilised for an operando XRD-CT study. The aim of the reactor developed was to be able to conduct XRD-CT measurements on the reaction cell under operando FT conditions. The reactor cell was also developed so that multiple catalysts could be loaded simultaneously and positions with the same vertical position, such that they would simultaneously overlap with a horizontal cross section.

Figure 5-1 shows an illustration of the design, made from Swagelok tube fittings. The tapered sample holder was made of quartz.

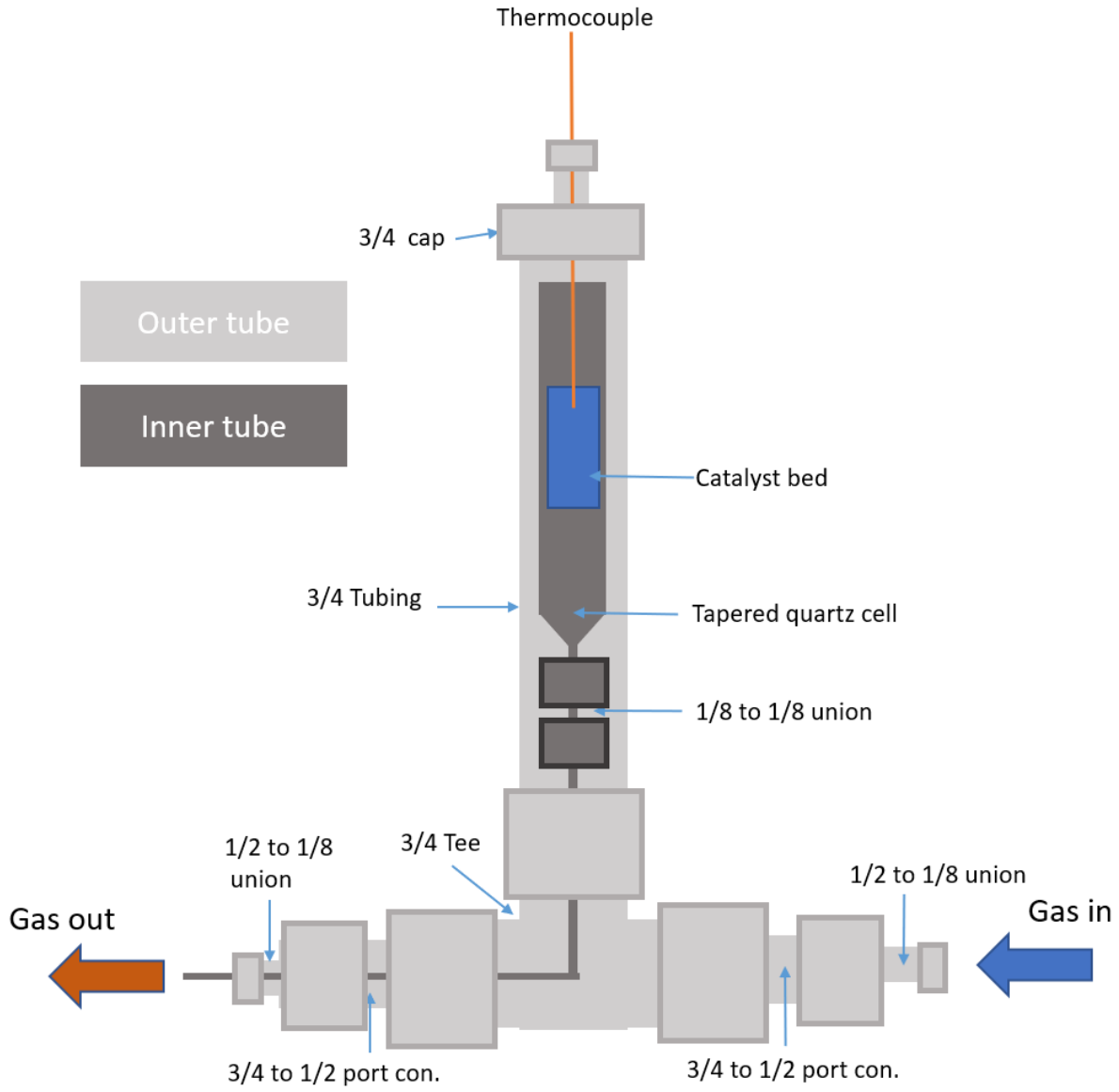

Figure 5-1 Illustration of high pressure testing cell.

The design of the reactor cell allows it to be mounted on a rotation and translation stage via clamping of the ¾" T-union, with X-rays allowed to pass over the sample measurement zone unobstructed by various reactor fittings. The reactor below the catalyst bed was insulated and heated by heater tape to 120 °C throughout operation, while the temperature of the catalyst bed was controlled by two heater guns aligned perpendicular to the X-ray beam. The reactor temperature was measured by a thermocouple inserted via a union in the top of the reaction cell.

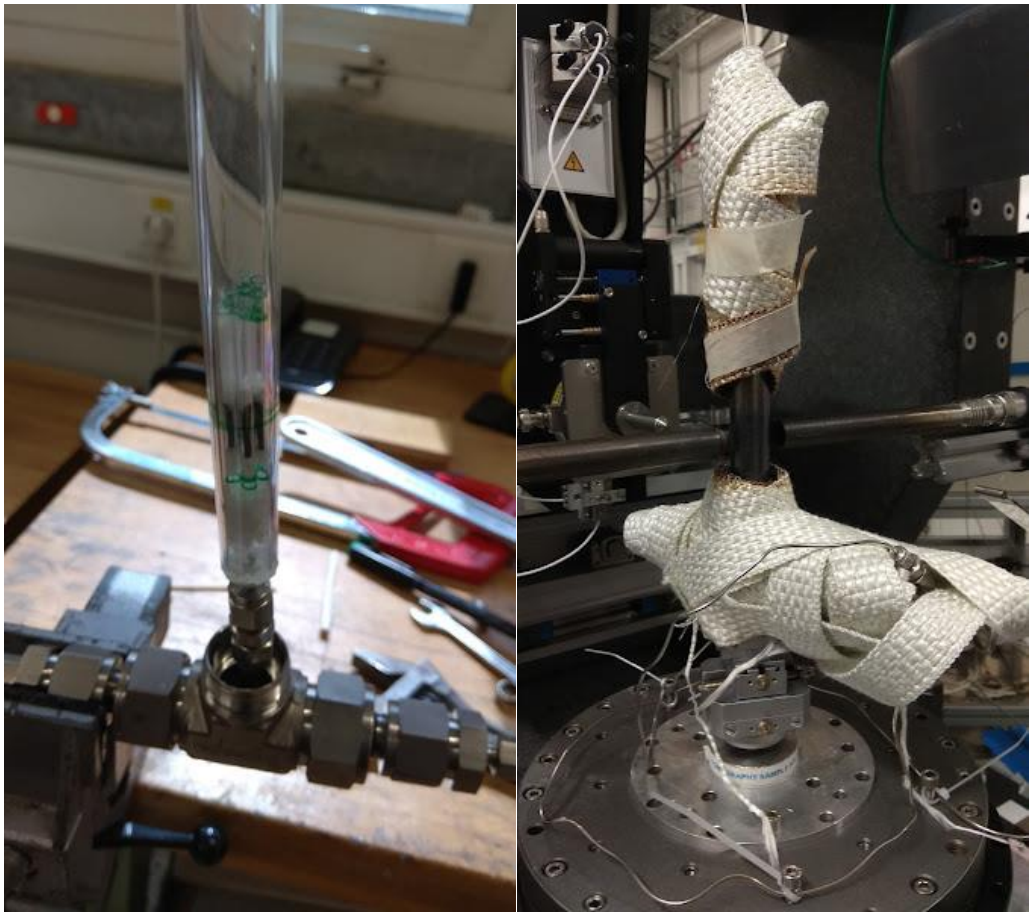

Figure 5-2 Left – Inner quartz tube of reactor cell, with catalyst extrusions loaded individually within quartz capillarties. Right - Insulated reactor mounted on beamline stage, with heating guns.

A single catalyst extrusion of each of the eight catalysts were loaded into the reaction cell, arranged radially with increasing manganese loading. Each extrusion was initially loaded into a 2 mm quartz capillary to allow each loaded capillary to be positioned accurately with each catalyst extrusion being positioned on the same horizontal cross section. Quartz wool was used to fix the positions of the capillaries above and below the measurement zone, so that the capillaries did not move during installation or operation of the reactor cell.

5.2.4 In Situ XRD-CT during reduction and Fischer-Tropsch

The catalyst reduction was conducted under 100 ml/min (~7000 GHSV) 20 % H_2/He flow at 350 °C for 12 h at 10 bar. The ramp to temperature was at 2.1 °C/min over 2 h from 100 °C. Table 5-1 shows the nominal time and temperature ranges for the collected scans reported.

Table 5-1 XRD-CT scans collected during catalyst activation, with corresponding time and temperature ranges

Scan Number	Time Start (h)	Time End (h)	Temp Start (°C)	Temp End (°C)
1	0	0.4	100	150
2	0.4	0.8	150	200
3	0.8	1.2	200	250
4	1.2	1.6	250	300
5	1.6	2	300	350
6	2	2.4	350	350
7	5.6	6	350	350
8	8.6	9	350	350
9	11.6	12	350	350

During the post reduction step, the reaction was cooled to 150 °C before being pressurised to 25 bar and ramped to 250 °C at 5 °C/min under 100 ml/min of 5 % CO/10 % H_2/He. The reaction was held at FTS conditions for 36 h before being decommissioned.

Figure 5-3 shows the reaction profile, including temperature over time with corresponding gas compositions for each testing phase.

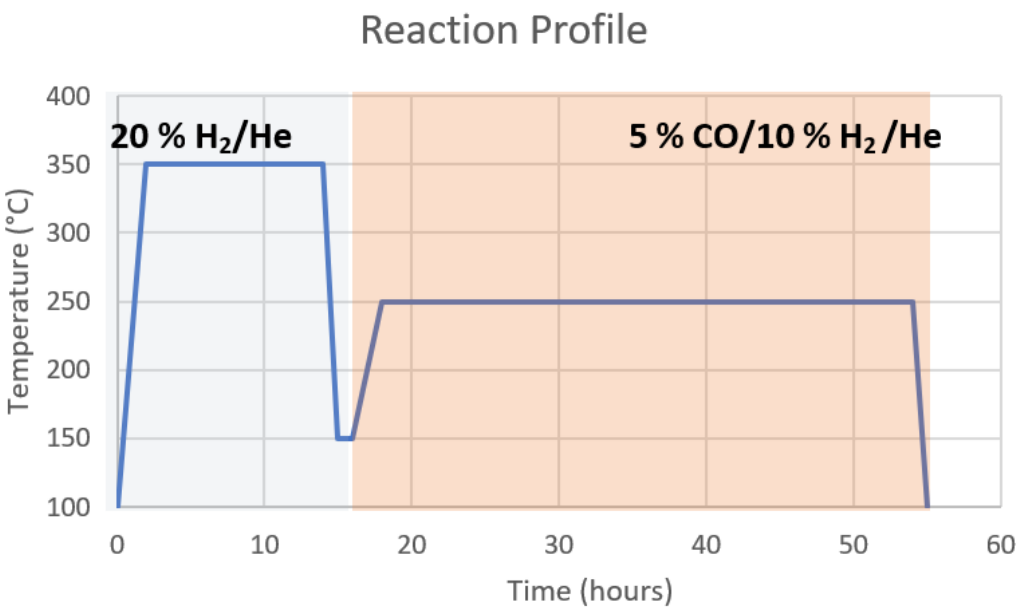

Figure 5-3 Reaction profile during catalyst activation and FTS, showing reactor temperature over time with corresponding gas composition of 20 % H_2/He during activation (light blue) and 5% CO/ 10% H_2 / He during FTS (orange)

During the reduction and operation of the catalyst, XRD-CT scans were conducted with the following parameters: 90 keV monochromatic 40 x 40 µm X-ray beam, 10 ms acquisition time, 181 translation points with 80 µm step size and 181 rotation points. The total scan time was ~30 min. This yields a reconstructed CT image of 180 x 180 voxels with a spatial resolution of 80 µm and temporal resolution between scans of 30 min.

In order to minimise the measurement time of space outside the catalyst bed, the translation of each scan was limited to the edges of the internal quartz tube. A full scan of the total reactor was also taken, so that the edges of the translation measurements can be cropped into each sinogram measurement prior to reconstruction.

5.2.5 Data Processing

To include the outer tube of the reactor in the edges of the collected sinograms, each sinogram was cropped into the full scan prior to reconstruction. This is required to allow the diffraction contribution of the reactor tube to be accurately reconstructed.

The cropped sinogram diffraction data was reconstructed into real space images via filtered back projection (FBP).[4] The catalyst extrusions present in the reconstructed image were

copped and ordered by % Mn, with subsequent CTs added to produce an array of % Mn vs time.

Additionally, each extrusion was sub-divided into groups by radial depth, to allow for easy study of the effect of distance from the perimeter of the extrusion on the evolution of phases during reduction and operation.

Rietveld refinements[5] were conducted using the sum of the diffraction contribution from each individual extrusion crop, using Topas 6,[6] and the resulting fit parameters were used as a basis for the automation of the refinement of each individual voxel within that crop.

5.3 Results & Discussion

5.3.1 Reactor Design

During initial trials of the reactor design, the reactor was scanned by XRD-CT on the ID15A beamline with a Swagelok 3/4" stainless steel outer tube. It was found that during measurements, the Pilatus detector was experiencing hotspots in excess of the levels in which the detector can be safely operated, and therefor triggering the safety shutoff of the beamline. These hotspots were still present with an aluminium attenuator in place blocking 95 % of the X-ray beam intensity, where the safety shutoff of >1 x 10^6 counts per second on individual pixels were still frequently triggering, causing the scanning procedure to abort.

It was determined that the cause of these hotspots was likely due to large crystallite domains of the stainless steel tube causing highly intense single crystal diffraction spots on the detector which was set up for the intensities expected for powder diffraction only.

Alternative 3/4" tubes were examined to see if they exhibited the same issue with tripping the safety shutoffs of the detector, and a carbon steel tube was found to produce good powder diffraction rings with intensities far below the safety limits.

One-sixteenth inch stainless steel gas lines were used for the inlet and outlet of the reactor setup. Due to the pressures and temperatures present during operation, the use of flexible plastic gas lines was not feasible for reasons of safety. While the 1/16" gas lines were coiled slightly to allow for increased flexibility, it was found that the reactor setup could not be reliably rotated 360° without the reactor becoming misaligned and shifting due to the tensions caused by the gas lines. However, an orientation was found where the reactor could be rotated 180° back and forth without the reactor shifting in the goniometer setup. This meant that the collection of CT scans was limited to collecting scans via a total of 180° of rotation rather than a full 360°.

5.3.2 Data processing

The initial step of processing the collected sinograms, prior to reconstruction, was to stitch the reference reactor wide-scan collected as illustrated in Figure 5-4. This involves replacing the centre of the wide-scan with each of the *in situ* scans collected of the catalyst bed.

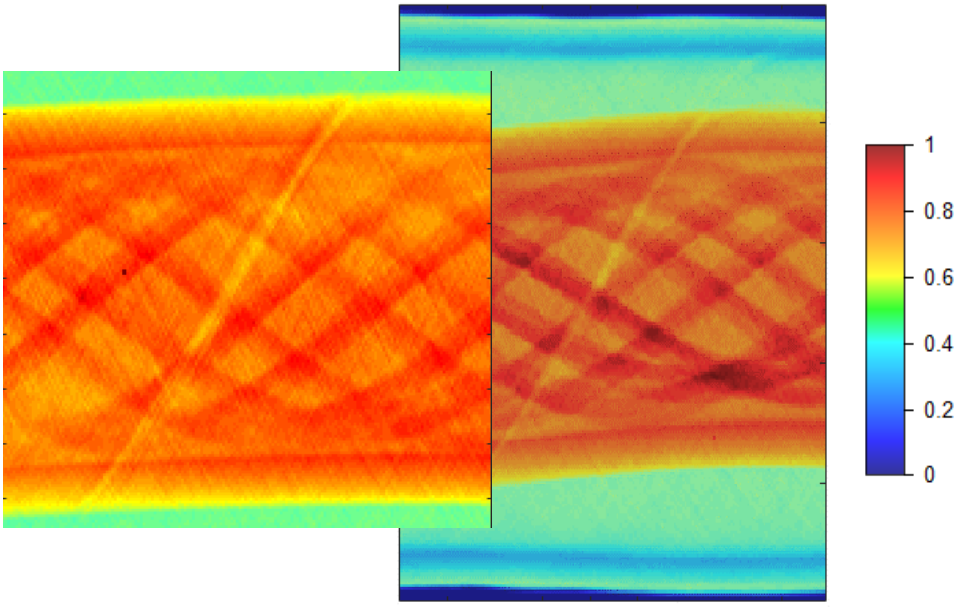

Figure 5-4 Illustration of equivalent sinograms measured with & without coverage of external reactor wall. Heatmap scale bar represents normalised relative summed diffraction intensity

By stitching the additional translation steps that measured the exterior reactor tube over the measurements collected of the catalyst bed, it allows the reconstructed CTs to include the entirety of the reactor volume. Figure 5-5 shows the comparison of a reconstructed CT without and with stitching the additional translation steps onto the sinogram prior to reconstruction.

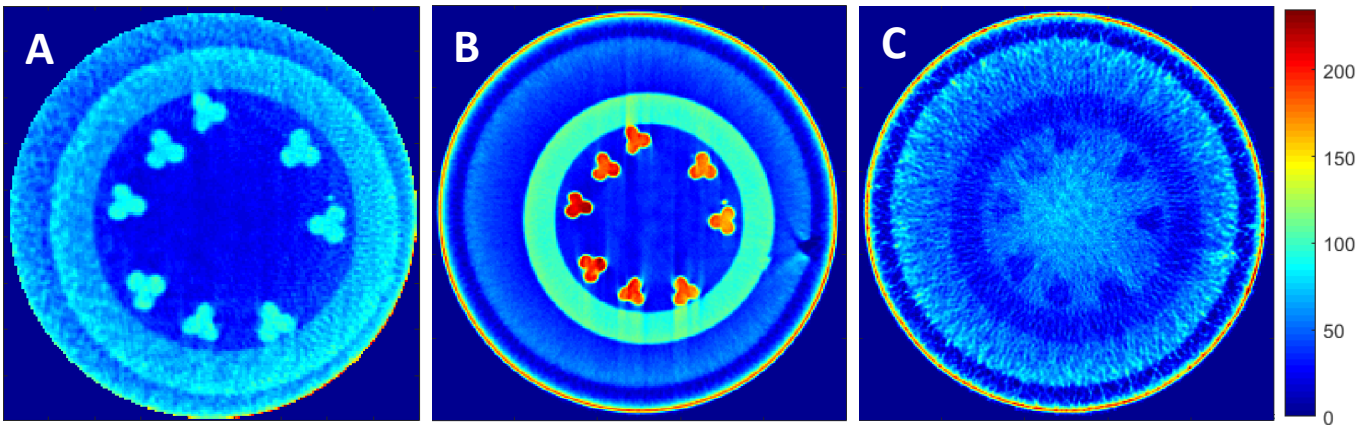

Figure 5-5 Comparison on CT reconstruction A) without, B) with stitching of wide-scan translation steps, and C) reactor diffraction contribution around 3.7° 2ϑ

While Figure 5-5 B shows that stitching is facilitating the reconstruction of the outer reactor tube, the entirety of the diffraction contribution is not being accurately reconstructed to the volume of the tube wall. Figure 5-5 C shows the CT intensity at 3.7° 2θ, the (111) reflection of the carbon steel structure identified as an austenite cubic structure[7] of the outer reactor tube. As shown, significant contribution is observed throughout the internal volume of the tube, however the intensity is diminished within the wall of the outer tube. The cause of the diffraction intensity being reconstructed incorrectly is thought to be due to the effect of parallax arising during the collection of the XRD-CT data. The variation of peak position of the reactor contribution within the measured diffraction patterns is causing the reconstruction algorithm to incorrectly place the diffracted contribution within the internal volume of the outer reactor tube, coinciding with the catalyst extrusions. Additionally, the high penetration depth required at the edges of the reactor tube is leading to significant absorption of the incident beam and diffraction contribution. This is causing the reconstruction algorithm to associate the inner volume of the walls of the reactor tube to be of lower contribution of the phase than reality.

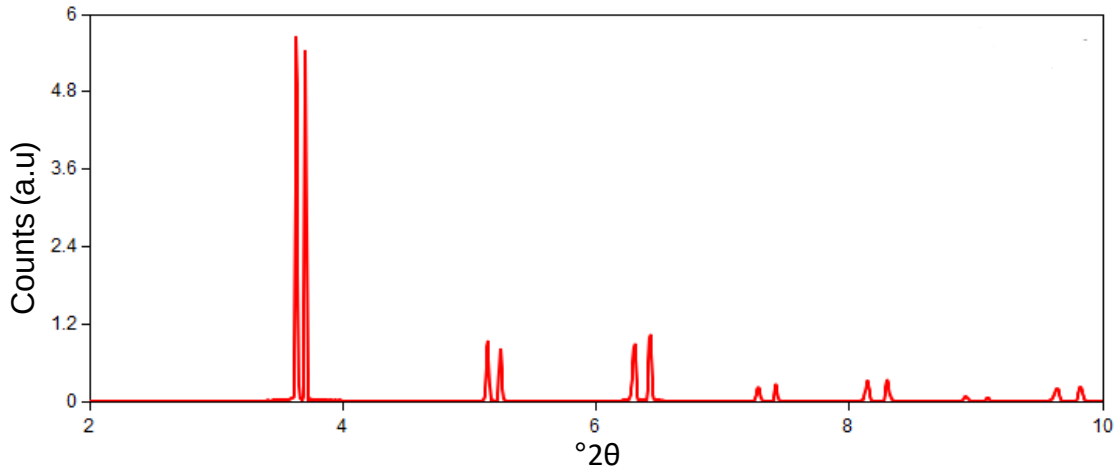

Figure 5-6 Example diffractogram of reactor contribution.

Figure 5-6 shows a diffractogram taken from the centre of an unprocessed sinogram, at a point with no contribution from the loaded catalysts. As shown, the diffracted peaks are split into doublets. This is due to the difference in the distance, 3/4”, of the front wall and the back wall of the reactor tube to the detector, as the X-ray beam passes through the reactor. As the

distance between the entrance and the exit of the X-ray beam varies as the reactor is translated through the X-ray beam, the filtered back projection algorithm used to reconstruct the sinograms into CTs cannot accurately reconstruct the parallaxed reactor wall contribution.

While the interference of the reactor diffraction contribution is limited to the regions where the diffraction peaks are present, these peaks overlap with the FCC cobalt peaks in the catalyst systems studied and so methods to remove or accurately reconstruct the reactor contribution have been attempted.

An alternative workflow to circumnavigate this issue is to subtract the reactor contribution via a blank scan, i.e a CT scan taken outside the catalyst bed. While the collected diffraction contribution will not be identical at a different part of the reactor, it may be similar enough to account for the majority of the contribution. During the experimental time, a scan was collected 1 cm above the measurement plane where no catalyst extrusions were present. Figure 5-7 A shows the reconstructed CT generated from a sinogram subtracted by the blank scan. While the outer reactor tube was aligned for the subtraction, the inner quartz tube is off axis, and so the subtraction is not aligned for the inner tube which represents as a crescent on either side of the reactor. As the diffraction contribution of the quartz inner tube does not meaningfully interact with the diffraction contribution of the catalyst extrusions, either spatially or in regards to °2θ.

While the overall intensity of the reactor contribution is reduced in the resulting CT and diffraction pattern, as shown in Figure 5-7 B an additional complication is introduced in that subtracting the blank contribution creates the potential for negative diffraction intensity. While the FBP algorithm can account for negatives in the reconstruction of the CT, there is no experimental potential for negative values in diffraction data.

While both methods of stitching and subtraction are effective in reducing the overlapping of reactor wall diffraction contribution with the catalyst extrusions, neither method is sufficiently effective to reduce the obscuring of the catalyst extrusions at the regions where diffraction peaks of the reactor wall are present. Due to the intensity of the reactor tube diffraction being roughly 100 fold that of the overlapping FCC cobalt phase per voxel, a high level of accuracy is required for any subtraction or masking of the contribution. For example, if the reactor diffraction was subtracted to an accuracy of 95 %, the 5 % error would be far

more significant than the remaining cobalt phase. This means that meaningful assignment of the FCC cobalt contribution cannot be achieved with the current strategies tried to accurately assign the reactor contribution to the correct location.

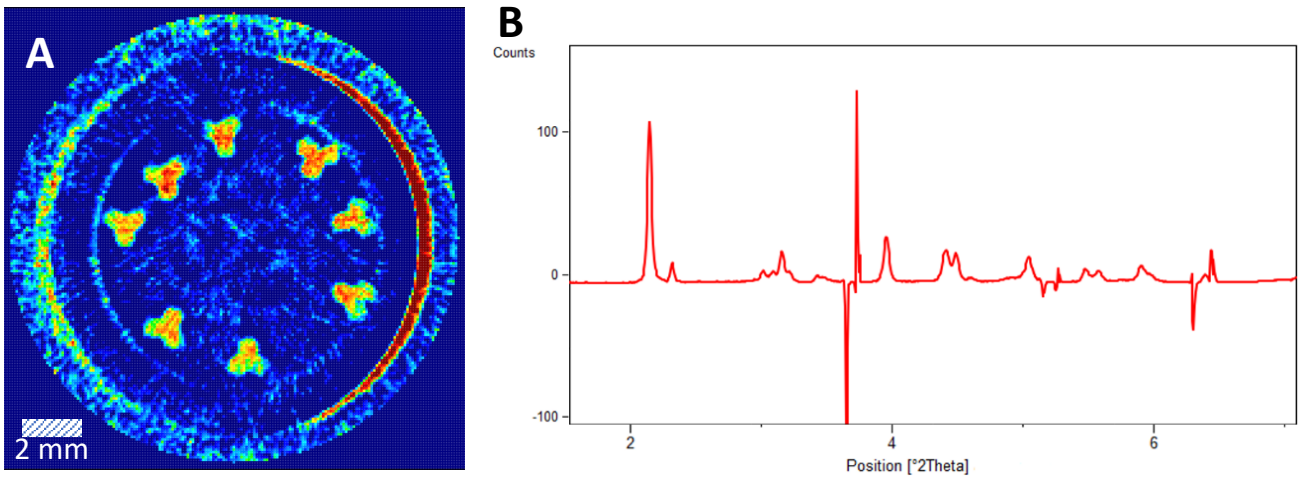

Figure 5-7 A) Reconstructed CT and B) diffraction pattern, from sinogram minus the blank scan.

Additionally, the parallax effect also impacts the diffraction data collected for the catalyst extrusions. While the extrusions do not exhibit the doublet behaviour of the reactor walls, they do experience a change in the distance to the diffraction detector as the reactor is rotated. This is due to the catalyst extrusions being ordered radially around the centre of rotation in the inner reactor wall. The effect is less significant than the parallax of the outer reactor walls, as the distance of the extrusions from the centre of rotation is significantly less than the outer walls of the reactor.

As the reactor is only rotated 180° during the collection of the XRD-CT data, this means that the effect of the changing detector distance varies depending on the starting location of the catalyst extrusion. For instance, if a catalyst extrusion is closest to the detector at 0° and furthest at 180° then the delta distance to the detector is double that of an extrusion that is closest to the detector at 90°.

This affects the collected diffraction data in two ways. First, as the average distance to the detector varies for each catalyst extrusion, the 2θ axis will be shifted slightly for each sample and will need to have the zero point corrected independently of each other. Second, as the delta distance is different for each sample, they will each experience slightly different broadening from this effect.

Both of these varying effects would be overcome by collecting the sinograms with the full 360° of rotation. In this instance, each extrusion would experience the full rotation and so the effect on zeroing would be averaged out, and while the broadening effect would still be present, the effect would be consistent for each sample assuming they shared the same distance from the centre of rotation, such as with the nominal positioning of the extrusions loaded in this experiment. With the experimental setup reported, the 1/16" gas stainless steel lines used for the inlet and outlet gas streams allowed for rotation of the setup across a range of 180° without undesired movement in the reaction cell, however attempts to rotate the cell a full 360° would consistently lead to the gas lines inputting undesired leverage on the reactor cell, causing it to shift in its mount. This would then move the positioning of the catalyst bed within the measurement plane of the beamline, leading to the measurement failing. An effective solution to this problem would be the addition of a slip ring to the reactor to allow the inlet and outlet gas lines to be connected, but separated from the rotation of the reactor cell. This would allow the section of the cell containing the catalyst bed to be independently rotated without the sections of the cell containing the gas connections moving.

Beyond the interference of the outer reactor tube with the CT reconstruction, the quality of the reconstructed diffraction patterns are good, with clearly defined and separated peaks. Figure 5-8 shows an example diffraction pattern from a reconstructed single 80 x 80 µm voxel of a catalyst extrusion prior to reduction. While the highlighted intense duplicate peaks of the reactor contribution become more broad and significant at high 2θ angles, they have only limited overlap below 6°.

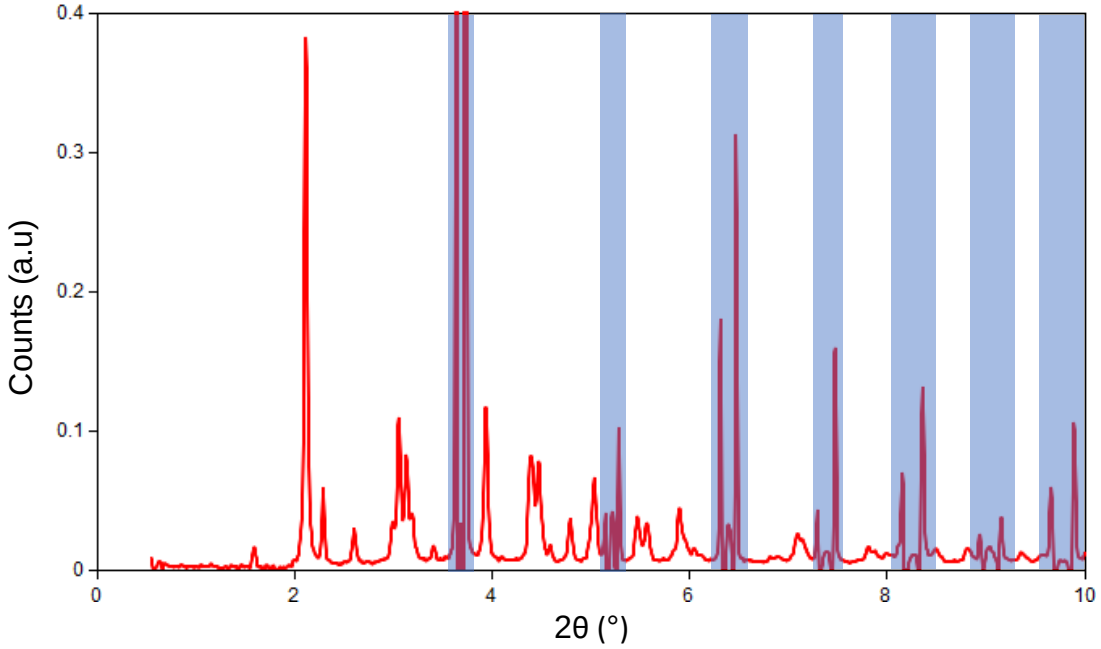

Figure 5-8 Example diffraction pattern from single reconstructed voxel with 2θ regions containing reactor contribution highlighted (blue regions). The reactor contribution is reconstructed as a doublet, and includes negative values between the peak maximums

Due to this, the refinement processing was limited to 6.25°. While this provides a sufficient number of reflections for profiling of the TiO_2 polymorphs, $Co_{(3-x)}Mn_{(x)}O_4$, CoO and cobalt HCP structures for reconstruction, it does cause significant interference with the cobalt FCC reconstruction as the major diffraction peak of the FCC structure overlaps with the reactor contribution around 3.6°. Two peaks remain within the refined range, at 4.2° and 5.95°. While the peak at 4.2° does not overlap significantly with other contributions, the peak at 5.95° does. Both peaks however are low intensity relative to the 3.6° peak.

5.3.3 In situ reduction

The catalyst series was scanned during reduction in hydrogen to investigate how the addition of varying levels of manganese to the catalyst extrusions affected the evolution of cobalt phases throughout activation. During the initial temperature ramp to 350 °C XRD-CT, 4 scans were measured between 100 and 350 °C. During the 12 h temperature hold, further scans were taken with the CTs reported in Figure 5-9 & 8 representing a scan for every 2 h period.

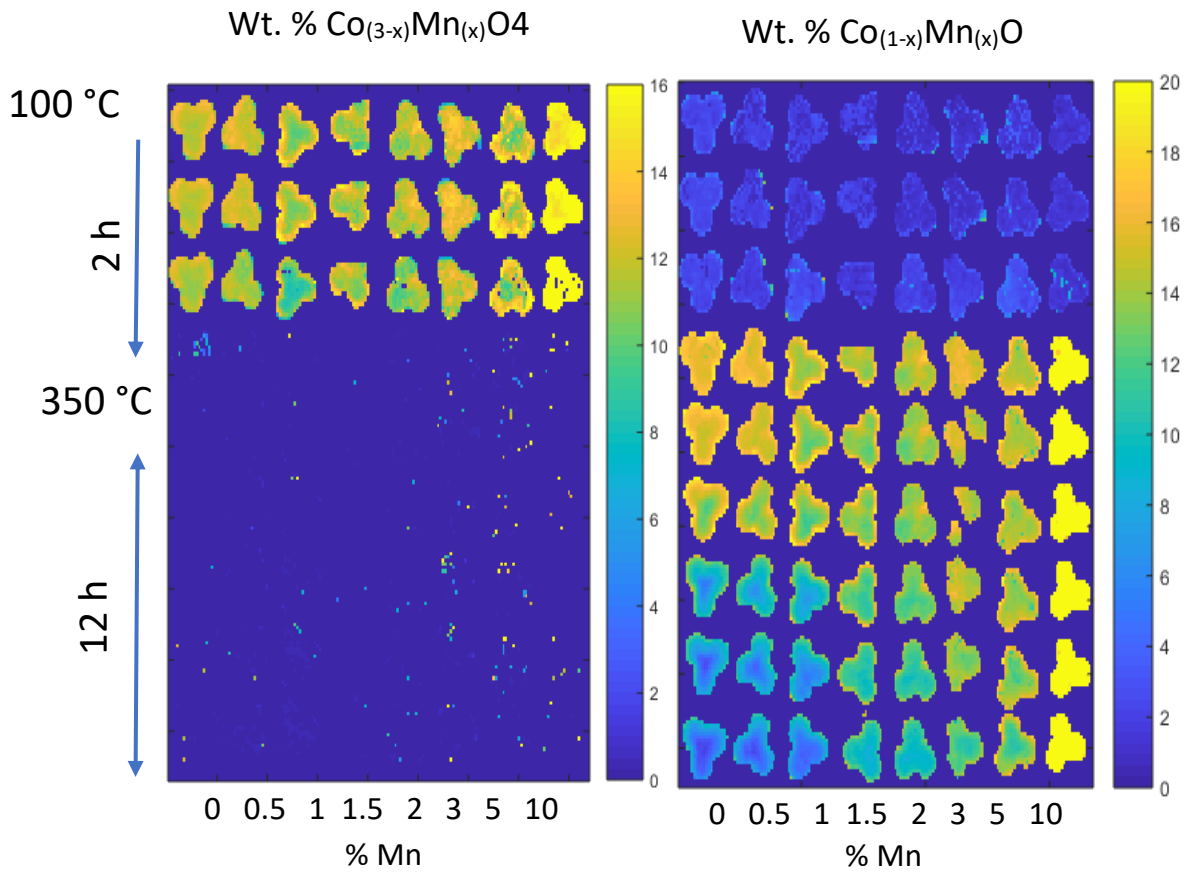

Figure 5-9 Heatmaps of refined wt. % loadings for oxide phases during catalyst activation. For each group of heatmaps, the vertical stacking corresponds to subsequent scans measured, and the horizontal stacking corresponds to increasing manganese content for 0, 0.5, 1, 1.5, 2, 3, 5 & 10 % Mn.

exemplar fit in Topas 6 is reported in Figure 8-12 in the appendix. Across the catalyst series, Figure 5-9 shows the reduction of the spinel cobalt-manganese phase is completed between the third and fourth scan, with no significant $Co_{(3-x)}Mn_{(x)}O_4$ diffraction detected within the fourth scan. While in general the fit of the spinel phase corresponds well to the extrusions, there are several outlier voxels that stand out both before and after the transition to the $Co_{(1-x)}Mn_{(x)}O$ phase. This is apparent by the random voxels with supposed $Co_{(3-x)}Mn_{(x)}O_4$ intensity

beyond scan 4. The inconsistent presence of these intensities between voxels suggest they are not representative and are instead noise arising due to a reconstruction artefact. The noise also appears to be more present for the extrusions containing 3, 5 and 10 % Mn.

Figure 5-10 shows the reconstruction artefact suspected to relate to the noise observed. The artefact is caused by the welded joint of the steel reactor tube, which is likely causing reconstruction artefacts due to large crystal grain size. This is not being reconstructed accurately and instead the diffraction contribution produces a starburst of intensity focused on one side of the reactor. The 3, 5 and 10 % Mn extrusions are loaded on the side of the reactor with the welded seam of the reactor tube, giving a potential explanation for the increase in noise for these extrusions relative to the rest of the series. The presence of these rogue voxels can easily be accounted for in the grouped data, as the voxels can easily be filtered out by their higher Rwp values. This means that this anomaly has no impact on the following reported results.

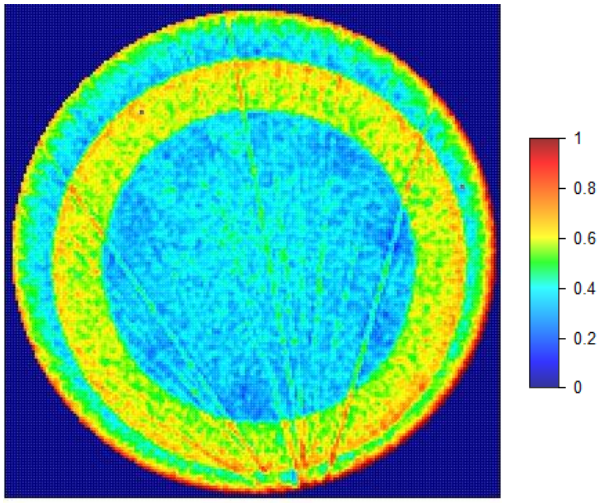

Figure 5-10 Visualisation of reconstruction artefact from reactor tube weld, with heatmap intensity representing normalised diffraction intensity at 3.7° 2θ

The heatmaps for $Co_{(1-x)}Mn_{(x)}O$ shown in Figure 5-9 correspond well with the expected evolution throughout reduction, with the appearance of the phase matching the disappearance of the spinel phase in scan 4. Throughout the temperature hold in subsequent scans, the intensity of the phase decreases significantly in the first half of the catalyst series,

with the phase remaining at high intensity at higher manganese levels. This trend corresponds both to observations made during the ambient pressure *in situ* reduction study .

At higher manganese loadings, a larger proportion of the $Co_{(1-x)}Mn_{(x)}O$ is manganese versus cobalt, which unlike cobalt is not expected to reduce fully to the metallic phase.[8][9] It is clear across the catalyst series from the wt. % of CoO that by the end of reduction the cobalt has not reduced in its entirety, as the wt. % loadings remaining are significantly higher than can be accounted for by the nominal manganese loadings alone. It is clear from these results that a proportion of the cobalt is not reduced to the metallic phases, and is instead retained within the 2+ oxide with the manganese dopant.

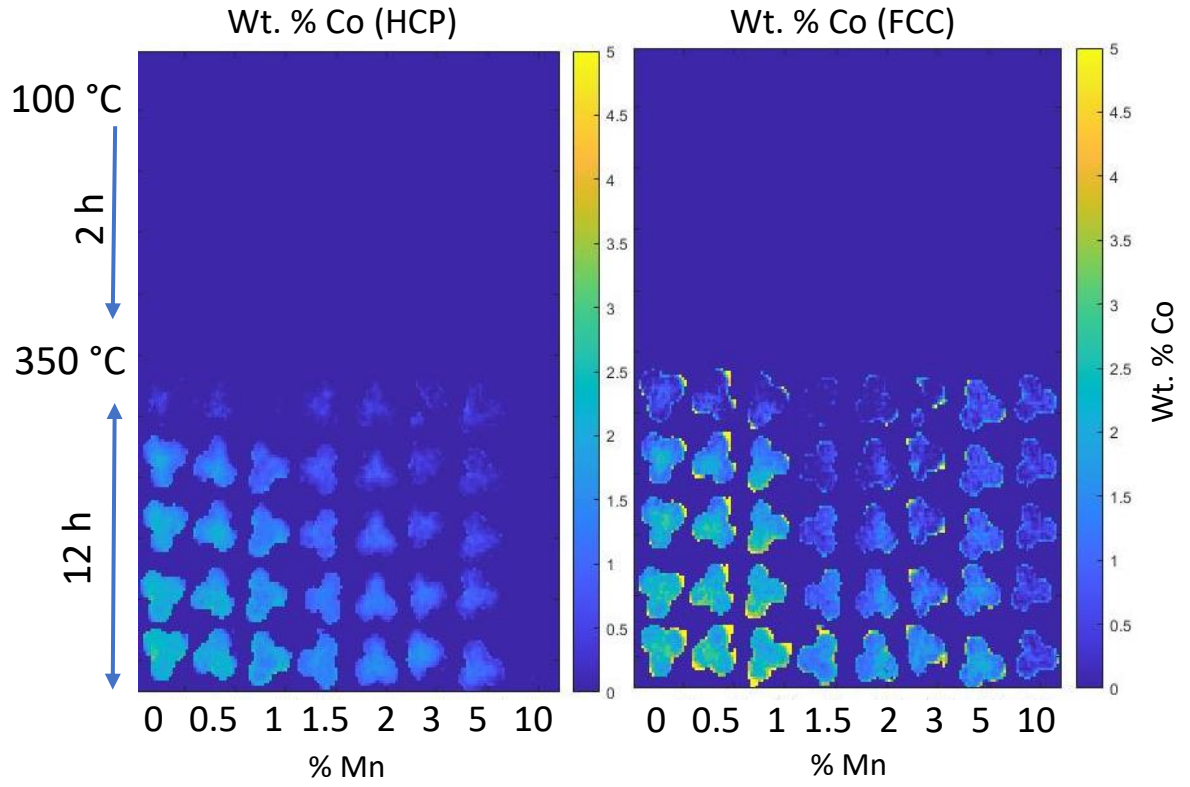

Figure 5-11 Heatmaps of refined wt. % loadings for cobalt metallic phases during catalyst activation

Figure 5-11 shows the heatmaps of refined cobalt metal, both HCP and FCC phases, throughout the catalyst activation. The HCP phase appears to be refining well, even at low loadings. The refined heatmaps show a gradual introduction of HCP phase throughout the series, with loading increasing in intensity between each scan measured. A notable exception is the catalyst with the highest doping, 10 % Mn ,which appears to show no presence of HCP cobalt metal by diffraction. The spatial distribution of HCP cobalt within the extrusions appears to be reasonably uniform towards the end of reduction, with neither the presence of

high intensity regions or obvious radial trends at low % Mn doping, however there are a number of regions across multiple extrusions that show consistently higher Co FCC loading. These high loading Co FCC voxels are located towards the exterior of the catalyst extrusions, where the intensity of the catalyst diffraction can be at its lowest, and where the refinement is most susceptible to misfitting of crystalline phases to contribution from the reactor. However, the gradual occurrence of this weight loading between subsequent scans suggests that it is a real effect.

As evidence for this, the Rwp, or goodness of fit, value can be considered as a valuable score to filter out voxels where the Rietveld refinement has not achieved an acceptable fit. Figure 5-12 shows the radial dependence of the Rwp value for each catalyst extrusion at the end of reduction, before any filtering has been applied. We can see that across the catalyst series, the goodness of fit value is largely independent of radial depth, with the exception of the exterior layer of the extrusion, where there is a marked increase. This is expected for two reasons. Firstly, the exterior voxels are comprised of varying ratios of both catalyst and empty space, leading to a decrease in diffracted intensity compared to the inner volume of the extrusions. This decrease in signal-to-noise leads to a worse fit. Secondly, as the intensity of the reactor contribution caused by the parallax is independent on catalyst depth, the ratio in intensity of the catalyst diffraction vs reactor contribution is less favourable at the exterior of the extrusions. This combination leads to the exterior of the extrusion being more susceptible to misfitting specifically of the cobalt FCC phase, which shares its crystalline structure with the cubic phase of the steel reactor tube with only a minor shift in unit cell size.

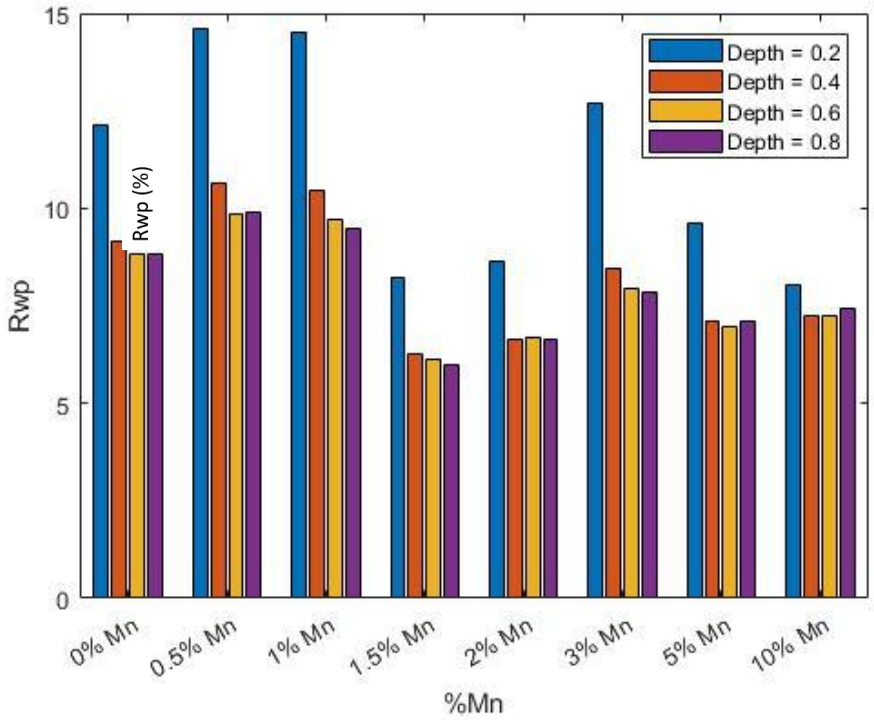

Figure 5-12 Radially batched Rwp for each catalyst extrusion at end of reduction, before filtering out high Rwp voxels.

As the Rwp value measures the goodness of fit of the Rietveld refinement, it is an appropriate metric to use as a filter for the removal of voxels where the refinement has not achieved an acceptable quality of fit. A threshold of > 15 was chosen as a reasonable value, as it allowed for the removal of the voxels where the cobalt FCC phase had been fit to the reactor contribution, while still being a reasonable distance away from the typical Rwp range of 7-10 in which the majority of refined voxels reside.

Figure 5-13 shows the radial distribution of the cobalt HCP and FCC phases across the catalyst series at the end of reduction, with Rwp filtering applied. We can see that for the cobalt FCC phase, even once the filtering is applied there is still a skew in FCC loading in the outer layer of the catalyst extrusion, across the series of extrusions. The trend in loading is unique to the FCC phase however, with the same trend not observed in the radial distribution of the HCP phase.

The radial distribution of the HCP cobalt phase shows some variation between different extrusions. Across some extrusions, predominantly with lower % Mn doping, the distribution of HCP cobalt is more uniform between radial depths. At higher loadings however, > 2 % Mn,

the distribution of HCP cobalt is weighted more towards the centre of the extrusions. From the anticipated loading of 10 % cobalt metal across the catalyst series, we can see that for each catalyst extrusion the total loading of FCC & HCP metallic phases falls short of this, with the undoped catalyst only measuring 5.7 % cobalt metal. This is however consistent with the observation of $Co_{(1-x)}Mn_{(x)}O$ wt. % still observed at the end of reduction, as shown in Figure 5-9.

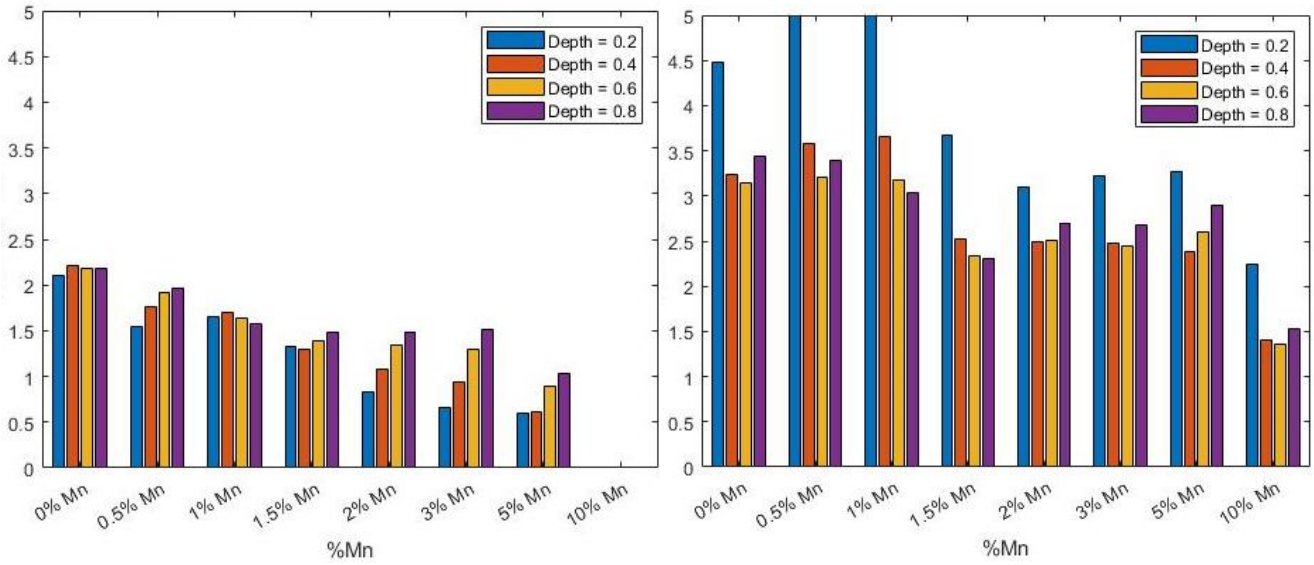

Figure 5-13 Radially batched refined wt. % of Cobalt HCP and Cobalt FCC for each catalyst extrusion, with Rwp filtering set to 15 %.

5.3.4 In situ Fischer-Tropsch synthesis

While the results of the catalyst activation suggest that the catalyst series was not reduced to the extent expected, the series was still operated and studied under representative FTS conditions. The catalysts were operated for 36 h at conditions, and the reported XRD-CT scans represent t = 1, 18 & 36 h on stream.

Figure 5-14 shows the heatmaps of $Co_{(1-x)}Mn_{(x)}O$ for each catalyst extrusion. Across the series, we can see a visible reduction in 2+ oxide contribution, in both the haloing around the exterior of catalyst extrusions, as well as the intensity within the inner body of the extrusions. This implies that further reduction of the catalyst is ongoing during operation, which is consistent with the continuing change observed at the end of the activation measurements. In the final scan, we can see that sections of some of the extrusions are missing. This is due to high Rwp values for these areas which have been removed by the Rwp filter. This is caused by minor shifts in the catalysts loading position throughout the experiment, with regions becoming overlapped with areas with higher reactor contribution.

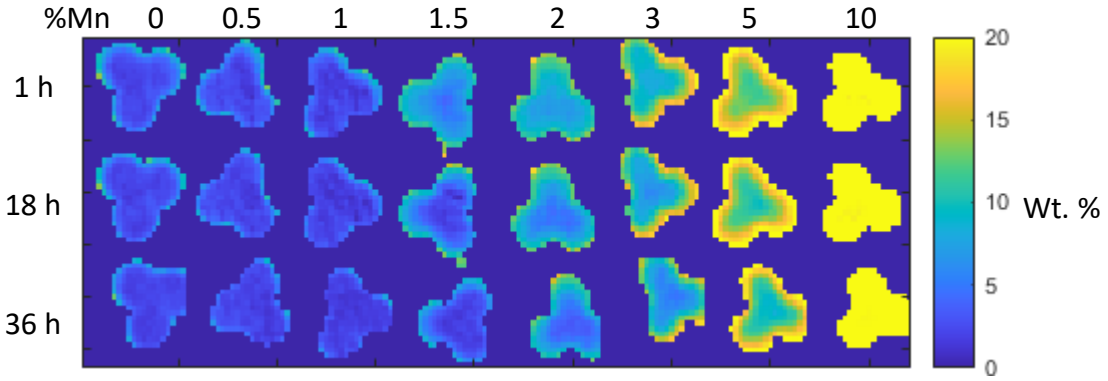

Figure 5-14 Heatmaps of refined wt. % of $Co_{(1-x)}Mn_{(x)}O$ at t = 1, 18 & 36 hours, for each catalyst extrusion.

Figure 5-15 shows the radially batched change in $Co_{(1-x)}Mn_{(x)}O$ wt. % loading between t = 1 h and t = 36 h. With the exception of the 10 % Mn catalyst, we can see a decrease in 2+ oxide content across the series. At 0 – 1 % Mn doping, this decrease is focused on the exterior of the catalyst where the loading decreases by 2.5 – 3 wt. %, compared to 0 — 1.5 wt. % in the catalyst interiors. At 1.5 wt. % Mn and above however, the reduction is more significant, and less focused on any particular radial depth within the extrusions.

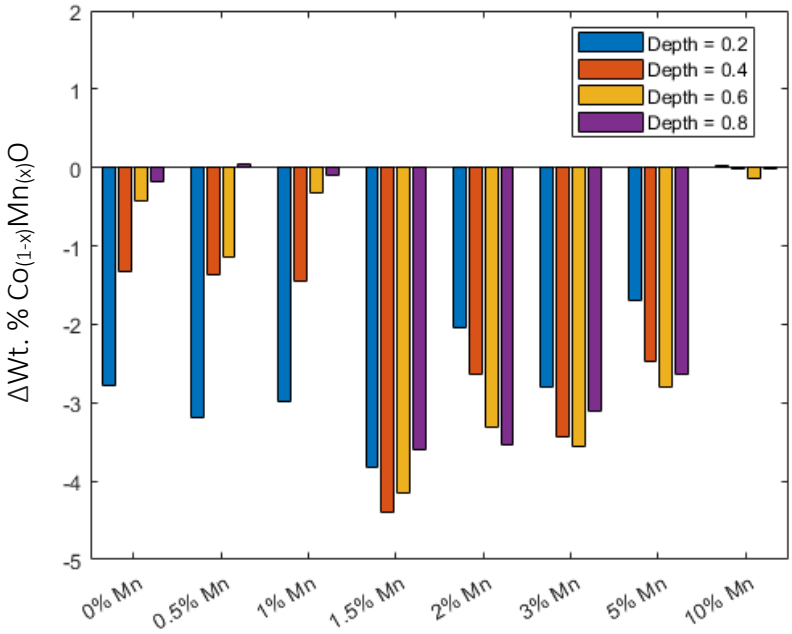

Figure 5-15 Radially grouped change in $Co_{(1-x)}Mn_{(x)}O$ wt. % loading between t = 1 h & t = 36 h, for each catalyst extrusion.

As the $Co_{(1-x)}Mn_{(x)}O$ is further reduced during FT operation, a corresponding increase in cobalt metal loading is observed. Figure 5-16 shows the heatmaps of the cobalt FCC & HCP wt. % phase for each extrusion. One of the standout changes throughout the heatmaps is the increase in FCC intensity within the interior of the extrusions between 1.5 and 5 wt. % Mn, representing an increase of 0.5 – 1 wt. %. Meanwhile the HCP heatmaps also suggest an increase in reduction, with a minor increase in wt. % appearing in the same extrusions. Additionally, the loading of FCC cobalt in the first scan appears to be higher than measured at the end of the catalyst activation, in Figure 5-11. This is especially apparent for the low doping catalysts, between 0 – 1 wt. % Mn, which appear to be significantly higher than both the rest of the series, and what was measured in the scan at the end of reduction. The remaining catalysts also show an increase of ~ 0.5 wt. % loading compared to the end of reduction.

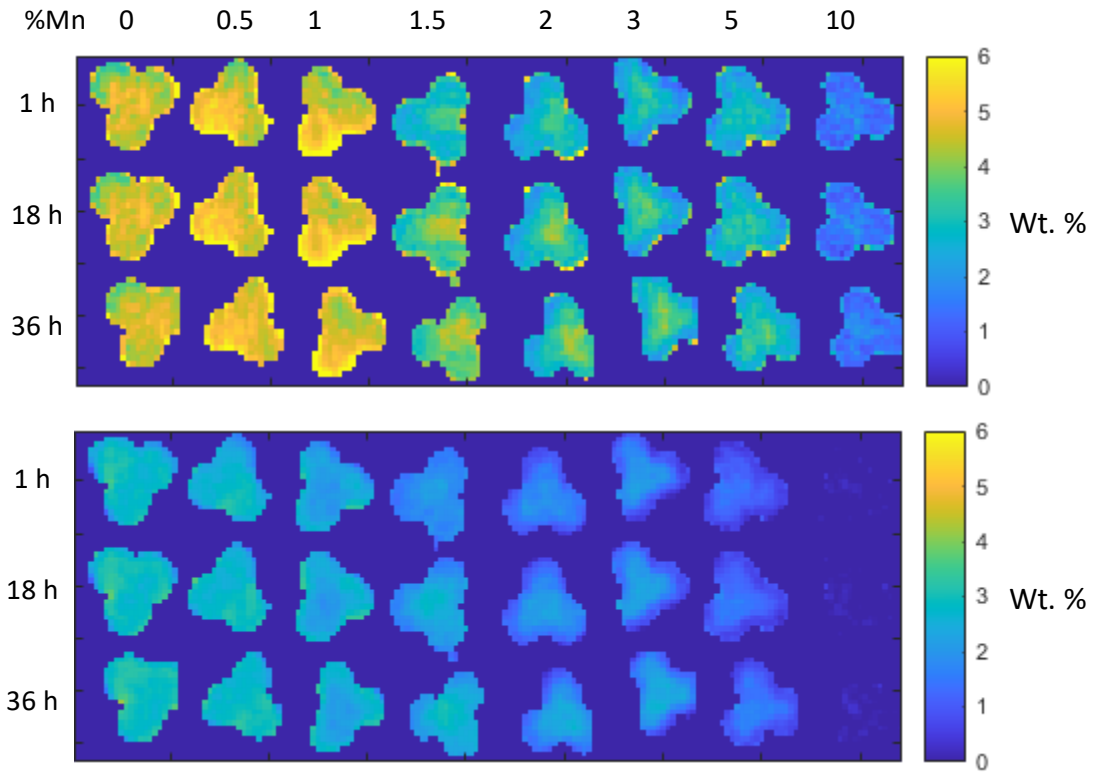

Figure 5-16 Heatmaps of refined wt. % of A) FCC cobalt and B) HCP cobalt at t = 1, 18 & 36 hours, for each catalyst extrusion.

Figure 5-17 shows the comparison of cobalt FCC & HCP radially distributed weight loading at the end of reduction, compared to the first scan under FT conditions. In general, we can see an increase in metal loading between the reduction and first FT scan, with the change becoming less significant with increasing manganese. This is consistent with the initial lower amount of reduced cobalt metal present in the catalysts due to the extent of reduction correlating to manganese loading. The extent of the increase for the HCP phase is less significant than the FCC phase, however this is consistent with the overall lower loading of this phase.

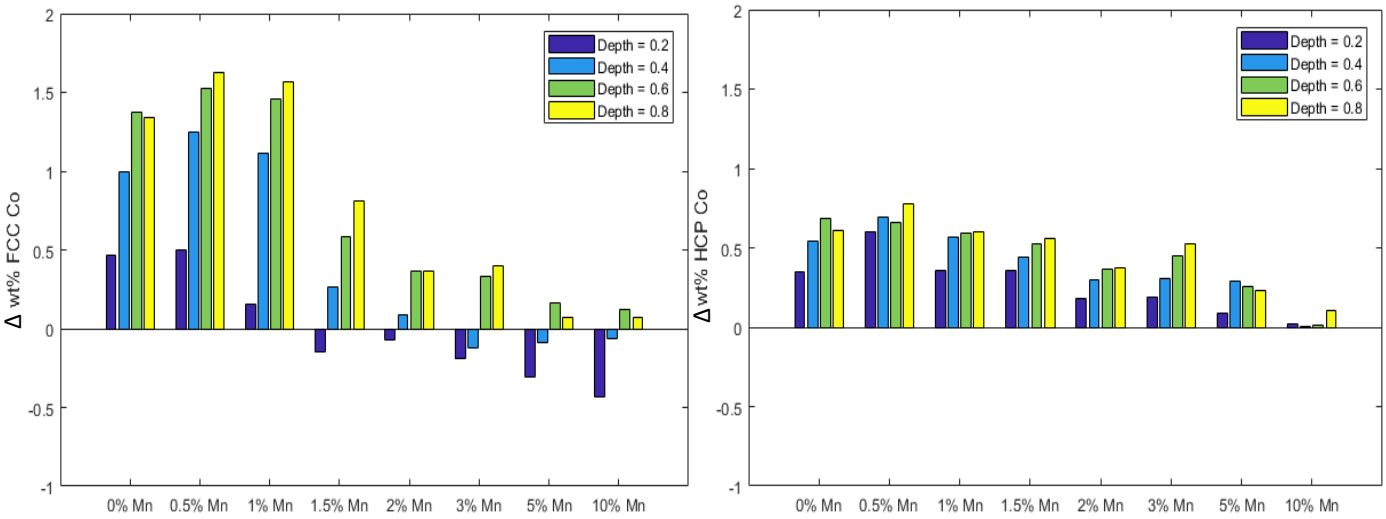

Figure 5-17 Radially grouped change in metal loading between end of reduction and start of FT, for FCC & HCP.

There are a number of possibilities for this increase, one of which is further reduction occurring during the ramping stages, after the last reduction scan was measured but before the first scan during ramping to Fischer-Tropsch conditions. Alternatively, the increase could be due to sintering of sub 5 nm particles rapidly sintering under syngas conditions to larger particles.[10] Initially, the smaller particles would be too small to contribute to the X-ray diffraction, causing an underestimation of phase loading. The sintering to larger particles would then allow this proportion of the phase to diffract, increasing the apparent loading.

Figure 5-18 shows the evolution of cobalt FCC and HCP during the FT operation. For the FCC phase we can see no significant variation in loading between the start and end of operation in the extrusions with 1 % Mn and below, however at 1.5 % Mn and above, we can see increases in FCC loading of up to 1 % Co throughout the reaction. The extent of this increase is reduced as the manganese loading is further increased, with negligible change observed in the 10 % Mn extrusion. The increases in FCC loading appear to be localised to the interior of the catalyst extrusions, and for each of the extrusions where an increase is seen, the change in loading measured at the exterior layer of the extrusion is negligible.

For the HCP phase, we can see a trend again divided by the 1 % Mn and below extrusions, which experience a significant increase in loading preferentially located towards the extrusion exteriors. Meanwhile for the 1.5 % Mn extrusion and higher, a more significant increase is observed with less preferential reduction relating to the radial depth. Additionally, no

significant change is observed at the 10 % Mn extrusion, which still shows no presence of HCP cobalt at the end of the catalysts' operation.

The changes observed in the cobalt metal loadings correlate well with the observations made in the changes of the $Co_{(1-x)}Mn_{(x)}O$ phase.

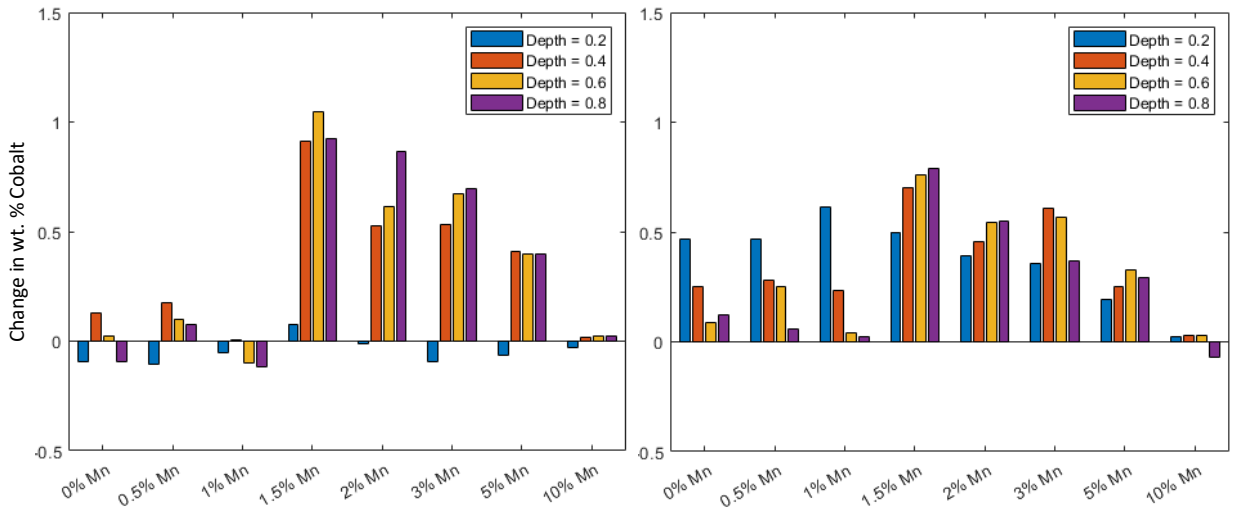

Figure 5-18 Radially grouped change in A) FCC cobalt and B) HCP cobalt wt. % loading between t = 1 h & t = 36 h, for each catalyst extrusion.

Other than the changes observed in the cobalt phases discussed, no other peaks were identified in the diffraction pattern at the end of operation under FT conditions that weren't present at the beginning. Paterson *et al.*[11] report the formation of bulk cobalt carbide measured by *in situ* XRD on the 5 % Mn extrusion under FT conditions of 10 bar, H_2:CO of 1.4. As the ratio of H_2:CO decreases towards the outlet of the reactor during FTS, this ratio represents a typical ratio around the middle of the catalyst bed. Study of the 1 % Mn however under the same *in situ* experiment found that even with a H_2:CO ratio as low as 0.6, the 1 % Mn did not indicate any presence of CoC_2 by XRD. As Pei *et al.*[12] report the ability of synthesised cobalt metal-carbide catalysts to be highly selective towards the production of linear alcohols during FT, detection of the formation of CoC_2 phase during reaction conditions would suggest a cause for the reported alcohol selectivity at high % Mn loadings.

In this work, the reaction was conducted at high GHSV, with a H_2:CO ratio of 2, to ensure each extrusion studied was representative of the same bed position no matter its activity, the reactor inlet. Given this, the lack of CoC_2 detected in even the high % Mn extrusions is not unexpected.

Figure 5-19 shows the summed diffraction patterns for the 5 % Mn extrusion at t = 1 & 36 h, with the equivalent comparisons for the remaining catalyst extrusions in Figure 8-13 through Figure 8-19. While the restructuring measured during operation at FTS conditions was minor throughout the catalyst series, it exemplifies the benefits of utilising Rietveld refinements to fit the collected data. With the limitations of parallax broadening and overlapping reactor contribution interfering with the diffraction data collected, meaningful changes are still quantifiable during the activation and operation of the catalyst series.

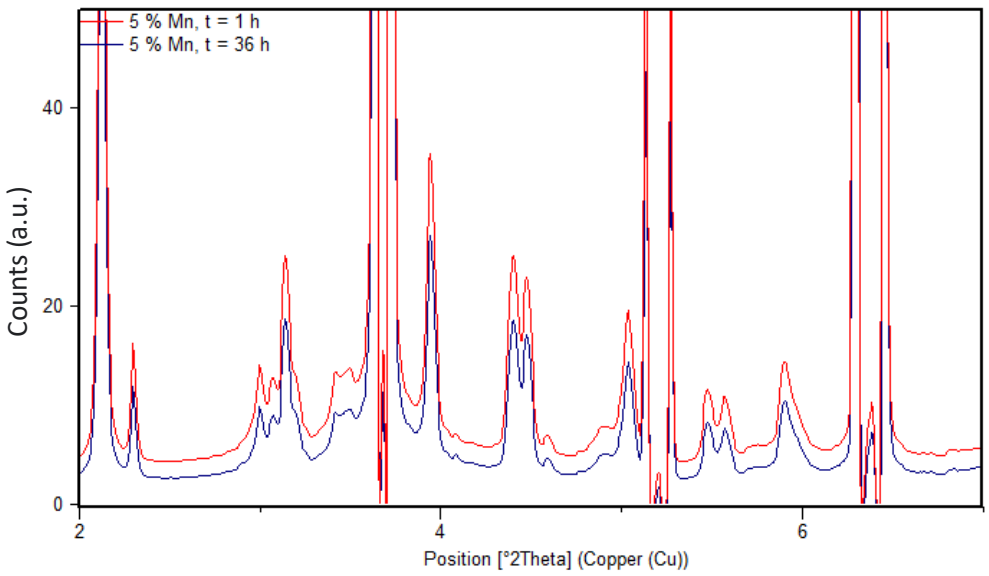

Figure 5-19 *Summed diffraction pattern of 5 % Mn catalyst at t = 1 h & t = 36 h.*

The challenges in processing the collected data arise largely due to the parallax effect caused by the large reactor cell diameter. The effect of both the reactor contribution being mis-represented by the FBP reconstruction, and the artificial broadening caused by the variance of reactor distance of the studied samples, has limited the potential of the Rietveld refinement due to the limitations that have been placed on the modelling to achieve a representative fit.

This issue can be rectified in future experiments by reducing the diameter of both the outer cell wall, and the distance the catalyst extrusions are loaded from the centre of rotation.

Additionally, if further reduction of the parallax effect was required, the distance of the 2D detector and X-ray energy could both be adjusted to minimise the variation in relative detector difference, which would reduce the artificial peak broadening caused by the parallax effect.

Regardless of the challenges caused by the parallax effect with the experimental setup used, the combination of the XRD-CT technique with an operando capable high pressure reaction cell has been shown to provide a high granularity of spatially resolved data regarding the evolution of crystalline structures within catalyst extrusions during operation.

5.4 Conclusion

A high pressure reaction cell has been successfully commissioned with a series of catalyst samples loaded simultaneously, and studied by XRD-CT during both catalyst activation and operation under representative conditions.

Various methods were attempted to minimise the effect of parallax on the data generated, caused by the large diameter of the reaction cell. Trivial adjustments can be made to future experimental work to reduce the scale of this issue.

The quality of diffraction data collected has been shown to be sufficient to produce highly granular phase wt. % data, allowing good insight into the spatially resolved evolution of crystalline phases within the reaction cell during operation.

The extent of manganese doping levels on the cobalt Fischer-Tropsch catalyst series studied has been shown to have an impact on the evolution of mixed Mn-Co phases during activation and operation at pressure. While the reaction was operated under representative FTS conditions for 36 h, further reduction of the oxide phases was observed. This suggests the intended extent of reduction during catalyst activation was not achieved within the timeframes operated.

5.5 References

1. N. E. Tsakoumis, M. Rønning, Ø. Borg, E. Rytter, and A. Holmen, *Catalysis Today*, 2010, ***154*(3-4)**, 162-182.
2. I. K. Van Ravenhorst, A. S. Hoffman, C. Vogt, A. Boubnov, N. Patra, R. Oord, and B. M. Weckhuysen, *ACS catalysis*, 2021, ***11*(5)**, 2956-2967.
3. S. Jacques et al., *Angewandte Chemie International Edition*, 2011, **50.43**, 10148-10152.
4. A. C. Kak and M. Slaney, Principles of Computerized Tomographic Imaging, Society for Industrial and Applied Mathematics, 2001.
5. H. M. Rietveld, *Journal of Applied Crystallography*, 1969, **2.2**, 65-71.
6. A. A. Coelho, *Journal of Applied Crystallography*, 2018, **51.1**, 210-218.
7. G. V. Jumov, *Metallurgical Transactions A*, 1976, ***7*(7)**, 999-1011.
8. F. Morales, F. M. F. De Groot, O. L. J. Gijzeman, A. Mens, O. Stephan and B. M. Weckhuysen, *Journal of Catalysis*, 2005, **230.2**, 301–308.
9. O. A. Bulavchenko, T. N. Afonasenko, A. V. Ivanchikova, V. Y. Murzin, A. M. Kremneva, A. A. Saraev and S. V. Tsybulya, *Inorganic Chemistry*, 2021, **60(21)**, 16518-16528.
10. H. Karaca, J. Hong, P. Fongarland, P. Roussel, A. Griboval-Constant, M. Lacroix and A. Y. Khodakov, *Chemical Communications*, 2010, ***46*(5)**, 788-790.
11. J. Paterson, M. Peacock, R. Purves, R. Partington, K. Sullivan, G. Sunley, and J. Wilson, *ChemCatChem*, 2018, ***10*(22)**, 5154-5163.
12. Y. P. Pei et al. *ACS Catalysis,* 2015, **5.6**, 3620-3624.

Chapter 6 - Manganese doped model catalyst systems for alcohol selective Fischer-Tropsch

6.1 Introduction

Interest in the FT reaction has increased over the last several decades due to more favourable economics, and more recently due to the interest in producing hydrocarbons from alternative and renewable sources. Industrial scale facilities currently produce fuels, oils and wax from feedstocks including gasified coal, natural gas, landfill gas and biomass. While the majority of the FT product are typically paraffins, olefins are also produced in substantial amounts. In addition, alcohols and carboxylic acids are also formed however typically not in large enough amounts to be economically separated into their own product streams.

Manganese is a frequently studied dopant in cobalt based FT catalysts. The addition on small quantities of Mn to Co-based FT catalysts has been found to lead to improvements in activity and long-chain product selectivity[1] due to its ability to improve the dispersion of the cobalt during catalyst synthesis, leading to improved activity, but also in model nanoparticle systems.[2] Recently, the addition of substantial quantities of Mn to a Cobalt FT catalyst has been found to substantially increase alcohol selectivity at FT reaction conditions.[3] The authors observed a dramatic increase in both olefin and alcohol selectivity with >3 wt. % Mn / 10 wt. % Co on TiO_2.

One of the challenges of studying oxide supported catalysts, is that there can be a wide distribution of environments in one sample. This can include a wide range of catalyst crystallite size, catalyst-dopant interactions, support environments etc. This can make identifying dopant-catalyst interactions difficult, as the range of local environments present can obscure the interactions that are responsible for any dopant effects observed. An alternative route to study fundamental aspects of catalysts is to study model catalyst systems, where the active component or precursor is prepared without the oxide support. This allows the variables of the active component to be tuned and characterised prior to supporting and testing. For example, Prieto *et al.*[4] produced model Co/ITQ-2 catalysts to study the effect of cobalt particle size in FT synthesis. The authors synthesised Co_3O_4 nanoparticles with varying

crystallite size distributions ranging from 6 – 12 nm means, and used them to study the dependence of turnover frequency with Co particle size.

In this work, we synthesise and characterise a series of model catalyst particles with varying catalyst-dopant interactions in an effort to isolate variables that may arise during traditional catalyst synthesis. By synthesising nanoparticles with specific catalyst-dopant orientations, we are able to closely control the level and interaction of the dopant with the oxide catalyst. Additionally, it allows the variations to be tailored by the synthesis while maintaining equivalence in other variables that may otherwise be adjusted inadvertently during synthesis via traditional methods.

To study the effect of manganese we produced mixed-oxide particles, surface coated particles and physical mixtures at varying doping levels, which could then be characterised prior to supporting and catalytic testing. A salt-mediated hydrothermal synthesis[5] was utilised to synthesise various nanoparticles, and tuned to alter the resulting order and composition. The hydrothermal synthesis has the added benefit of removing the opportunity of any surfactant to interfere with the surface of the particles, while the authors also identify that the reaction mediating sodium salt is not found in the synthesised particles, which would have the potential to act as a poison in FTS.[6]

The catalyst systems synthesised were characterised and supported before undergoing catalytic testing and DRIFTS CO absorption. Catalytic testing was complemented by off-line product analysis to quantify the alcohol selectivity of the liquid product streams.

6.2 Experimental

6.2.1 Catalyst Synthesis

To make the model catalyst systems, cobalt-manganese oxide nanoparticles were synthesised before being supported. The nanoparticle synthesis technique was varied to produce nanoparticles with different ratios of Co and Mn, as well as different structural orders.

The nanoparticle synthesis methods are based on an altered hydrothermal synthesis technique,[5] where metal nitrate salts were injected into a heated saturated $NaNO_2$ solution and stirred under airflow for several hours to oxidise into the spinel oxide phase. The experimental details were varied to produce particles with varying Co:Mn ratios.

For the reference Co_3O_4 nanoparticles (JP25), the experimental details were as follows. Sodium Nitrite (150 g) and Sodium Hydroxide (3.6 g) were dissolved in 100 ml of de-ionized water, and heated to 105 °C under reflux in a 3-necked round bottom flask under rapid stirring. Compressed air was bubbled into the stirred solution at ~100 ml/min via a needle. Once at a stable temperature, 20 ml of 3M cobalt nitrate solution was injected into the solution over 1 minute. The reaction was left stirring and bubbling at temperature for up to 48 hours, and during the first 24 hours NO_x evolution and a gradual shift in suspension colour to black was observed.

After 48 hours, the reaction was cooled to room temperature. The resulting solids were separated and purified via centrifuge, where each sample was washed and centrifuged 3 times in distilled water, followed by 3 times in 0.1M HCl, followed by 3 further times in distilled water. The purified material was dried overnight in an oven at 80 °C.

For the synthesis of equivalent Mn_3O_4 particles, the reaction was repeated with the cobalt nitrate salt substituted with manganese nitrate salt. To produce mixed spinel $Co_{(3-x)}Mn_{(x)}O_4$ nanoparticles, manganese nitrate was co-injected with cobalt nitrate at the desired ratio of the product. Table 6-1 shows the amount of nitrate salts used for each sample, and the ratio of Co:Mn.

Table 6-1 — Synthesis details of mixed spinel nanoparticles

Sample code	Co:Mn	Vol 3M Co-nitrate (ml)	Vol 3M Mn-nitrate (ml)	$NaNO_2$ (g)	NaOH (g)	H_2O (ml)
JP25	100:0	20	0	150	3.6	100
JP23	0:100	0	20	150	3.6	100
JP11	100:50	6.66	3.33	75	1.8	50
JP26	100:30	15.38	4.62	150	3.6	100
JP27	100:10	18.18	1.82	150	3.6	100

The reference Co_3O_4 particles were used to create Mn_3O_4 coated Co_3O_4 particles. This was achieved by dispersing a given mass of sample in ~10 ml of a dilute solution of manganese nitrate, drying the mixture via rotary evaporation and finally calcining the mixture at 250 °C for 4 h. Table 6-2 shows the quantities of material used to achieve each Co:Mn ratio. For the 100:30 Co:Mn sample, the manganese was introduced in three steps to limit agglomeration of the manganese salts prior to calcination.

Table 6-2 — Synthesis details of surface coated nanoparticles

Sample Code	Co:Mn	Mass Co_3O_4 / $Co_{(3-x)}Mn_{(x)}O_4$	Mass $Mn(NO_3)_2.6H_2O$
JP25A(1)	100:10	1.238	0.415
JP25A(2)	100:20	1.038	0.364
JP25A	100:30	0.811	0.309
JP25B	100:10	0.495	0.166
JP25C	100:5	0.519	0.087
JP25D	100:1	0.539	0.018

To support the synthesised particles, each system was mixed with a specific weight of dried P25 TiO_2, such that the loaded weight of Co after reduction of the oxide phases was 10 wt. % on TiO_2. This provided loaded catalysts with a consistent loading of cobalt relative to the catalyst support. Each set of particles were dispersed in 25 ml of de-ionized water via light sonication, and the P25 support was added followed by further sonication. The resulting slurry was dried to a free-flowing powder via rotary evaporation, before being calcined at 120 °C for 4 h.

6.2.2 Characterisation

STEM imaging was conducted on a JEOL ARM200CF at the Electron Physical Sciences Imaging Centre (ePSIC) at the Rutherford Appleton Laboratory.

TEM imaging and EDX mapping was conducted at the Research Complex at Harwell (RCaH) on a JEOL JEM 2100 EM.

To prepare samples for imaging by STEM and TEM, roughly 10 mg of sample was dispersed in ~ 2 ml of ethanol by sonication. A drop of the suspended sample was added to a holey carbon film on 300 mesh copper sample grid for imaging.

X-ray Diffraction measurements were taken on a Rigaku Miniflex 10-70° 2θ 1.54 Å Cu source, measured at 3°/min. Roughly 100 mg of each of the measured materials was finely ground and flattened on a sample holder for analysis. Rietveld refinements were conducted using the collected XRD diffraction patterns using Topas 6.

Quantitative XRF elemental analysis was conducted by diluting approximately 0.2 g of sample in 6.5 g of lithium tetraborate / lithium metaborate / lithium bromide at a ratio of 66.67 % : 32.83 % : 9,5 %. The diluted samples were fused at 1050 °C for 12 mins, and cast into a 32 mm glass bead for analysis.

XPS measurements were taken by XPS Harwell. For each sample, a monochromatic Al Kα (1486.7 eV) source was used. High resolution scans of the Co & Mn edges were typically taken in 3 sweeps of 300 steps, 0.1 eV step size and 239 ms dwell time. XPS spectra were charge corrected using adventitious carbon at 284.8 eV. XPS spectra were plotted and quantified using CasaXPS v2.3.25.

DRIFTS CO absorption experiments were conducted on an Agilent Carey 680 Fourier-Transformed Infrared Spectrometer, with a Harrick Praying Mantis cell. Samples were reduced in 20 ml/min 50% H_2 / He at 400 °C (10 °C / min) for 1 h, and cooled to 30 °C. For CO Absorptions, the sample cell was purged with He and a baseline collected. Sequential measurements were taken every 30 s for 5 mins while 10 ml/min of 10 % CO / He was dosed through the cell. For samples supported on P25, the samples were studied undiluted. For the unsupported nanoparticles, the samples were diluted in pre-dried KBr, at a ratio of 10:1 KBr:sample.

6.2.3 Catalyst Testing

Catalyst testing was conducted in a multi-tubular fixed bed reactor by Drochaid Research Services, St Andrews. Nominally, 600 mg of supported catalyst was diluted in 3 g on SiC (get details of SiC) before being loaded into a reactor tube. The loaded catalysts were reduced under pure 50 ml/min H_2 (5000 ml/gcat/h) at 300 °C and atmospheric pressure for a dwell of 12 hours, before being cooled to 130 °C. At 130 °C the reaction pressure was increased to 30 bar under Ar flow, and syngas was introduced (1.8:1 H_2:CO, 51 % Ar, 8800 ml/gcat/h). The temperature was ramped progressively to 170 °C (2 °C/min), 200 °C (1 °C/min), and finally 220 °C (0.2 °C/min). Typically for each set of tests, the temperature was increased to 230 °C, followed by 240 °C after ~24 h at each temperature.

During testing, online tail-gas analysis was conducted by GC every ~2 h. The reported metrics of % CO conversion, % CH_4 selectivity & % C5+ selectivity were determined from the results of the tail-gas analysis.

Post decommissioning the wax, liquid organic and aqueous products were collected for mass balancing and analysed by GC for organic content. Paraffin : olefin: alcohol selectivity was determined from the organic fraction of the liquid products.

6.3 Results & Discussion

6.3.1 Synthesis & Characterisation

6.3.1.1 XRD

To verify that the hydrothermal synthesis was creating the desired product, the purified black precipitate synthesised was investigated by X-ray Diffraction (XRD). Figure 6-1 shows the collected powder diffractogram for JP-25, the reference synthesised Co_3O_4 nanoparticles. The diffractogram suggests that the reaction cobalt has been successfully oxidised to the Co_3O_4 spinel phase,[7] and does not suggest the presence of any other crystalline phases in significant quantities, such as intermediate cobalt oxides / hydroxides or reaction salts such as sodium nitrite.

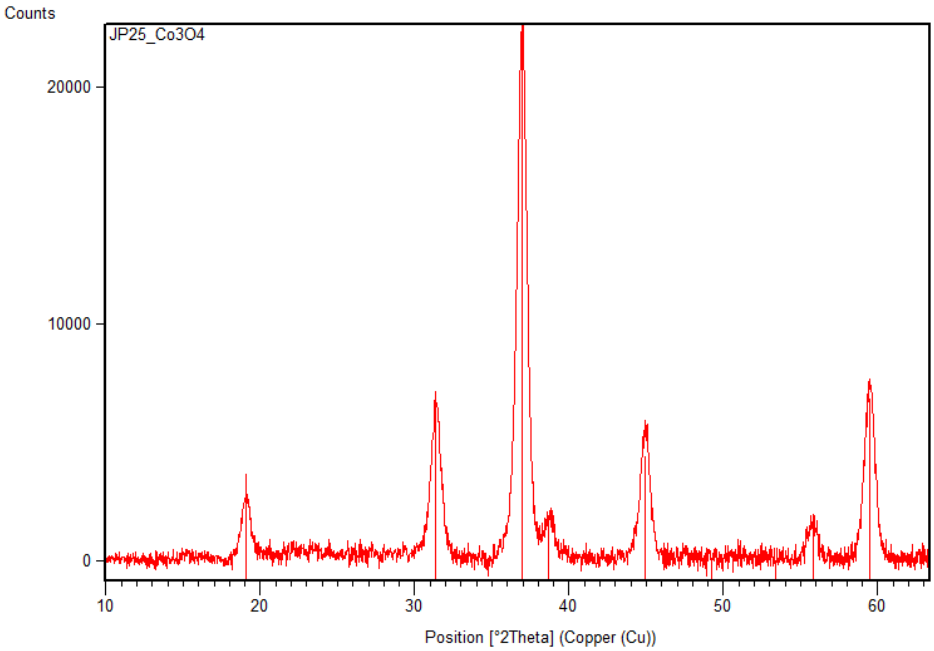

Figure 6-1 Background subtracted diffraction pattern of synthesised JP25, with Co_3O_4 reflections indexed.

Figure 6-2 shows the diffraction data collected from the Co-Mn co-injected samples. The diffraction patterns show only the presence of the spinel oxide phase. As the amount of Mn introduced during the synthesis is increased, if the Mn is incorporated into the spinel structure as desired then the expected response is an increase in lattice parameter. This is due to the more extensive integration of the larger Mn ion into the spinel oxide structure. From the diffraction measured, a shift in peak positions to a lower °2θ value is observed with increasing Mn doping. This is consistent with the expected lattice expansion as the manganese dopant is introduced to the structure of the base Co_3O_4 particles.

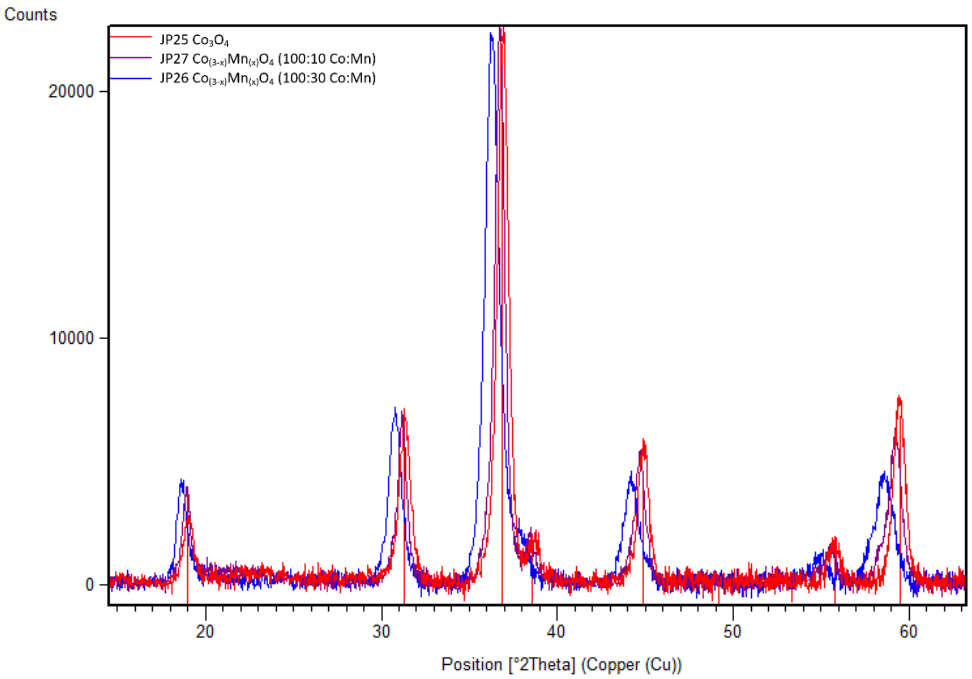

Figure 6-2 Background subtracted diffraction patterns of synthesised mixed-oxide particle series JP25 (Co_3O_4) , JP26 (100:30 Co:Mn) & JP27 (100:10 Co:Mn), with reflections indexed for Co_3O_4.

Table 6-3 – Rietveld refined parameters of mixed spinel nanoparticles

Sample	Co:Mn	Lattice Parameter (a)	% expansion	Crystallite size (nm)
JP25	-	8.078	-	19.2
JP27	100:10	8.096	0.22%	20.5
JP26	100:30	8.167	1.09%	15.7

The measured diffraction patterns for the mixed-oxide series of particles were Rietveld refined. The refinement lattice parameters and crystallite size of each mixed-oxide sample are reported in Table 6-3. As the amount of Mn injected into the reaction mixture is increased, we can see that the lattice parameter of the corresponding spinel product increases. As no other minor phases are detected within the diffraction pattern, this suggests that the addition of Mn introduced during the synthesis is successfully being incorporated into the spinel oxide structure.

Meera *et al.*[8] report the lattice parameters for $Co_{(3-x)}Mn_{(x)}O_4$ for $0.1 < x < 1$, and show a roughly linear increase in lattice parameter with increasing manganese content. Figure 6-3 shows the relationship reported between x and lattice parameter, along with the lattice parameters measured for the synthesised supported mixed-oxide particles. While we can see

the there is an increase in lattice parameter corresponding to the increase in manganese content, the increase is not as significant as the literature reference would suggest. If the entirety of the manganese being introduced into the reaction mixture is not being incorporated fully into the spinel mixed oxide phase, there are two alternatives. Firstly, the manganese salt may not be fully oxidised by the end of the reaction, leading to a lower ratio of Mn:Co in the synthesised material. Secondly, the manganese may partially be oxidising into discrete particles, or preferential location within the particles such as towards the exterior. A variation in the rate of oxidation between the cobalt and manganese salts may lead to a trend in Co:Mn throughout the depth of the synthesised nanoparticles.

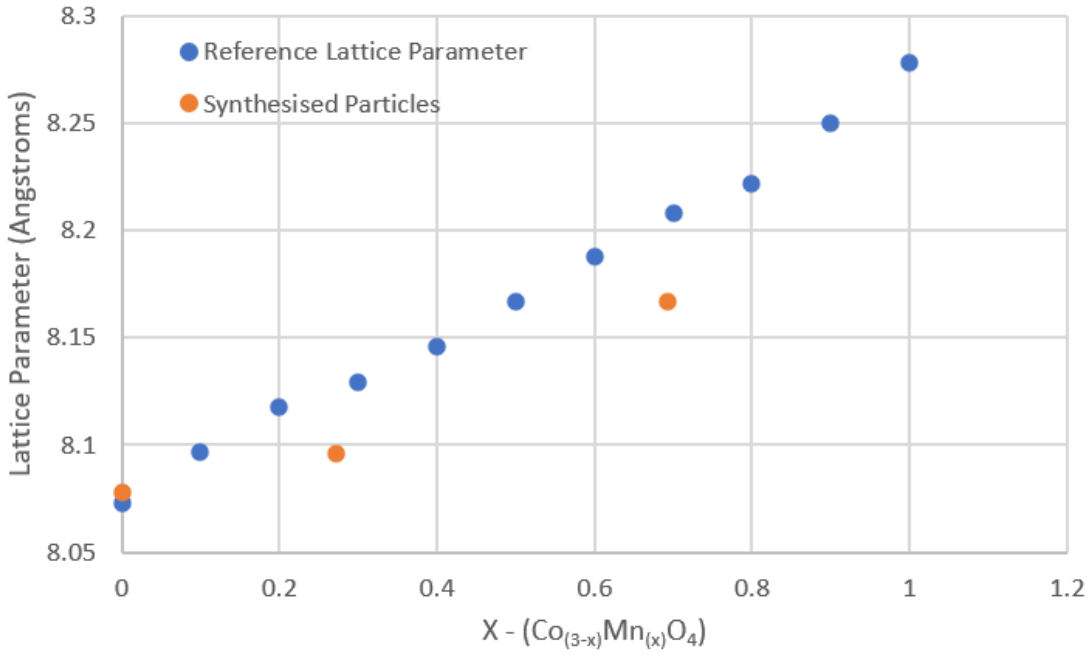

Figure 6-3 Lattice Parameter of $Co_{(3-x)}Mn_{(x)}O_4$ for varying x from reference literature adapted from Meera et al.[8], and synthesised mixed oxide nanoparticle series with varying Mn doping.

Figure 6-4 shows the diffraction patterns for the surface coated Co_3O_4 particles. Unlike the mixed oxide particles, we do not see any shift in spinel peak positions with increasing Mn loading on the particles' surface. There is also no presence of distinct Mn_3O_4 detected, or other crystalline phases. This suggests that the impregnation method of dosing Mn onto the surface of the Co_3O_4 particles is successful in forming a well distributed coverage.

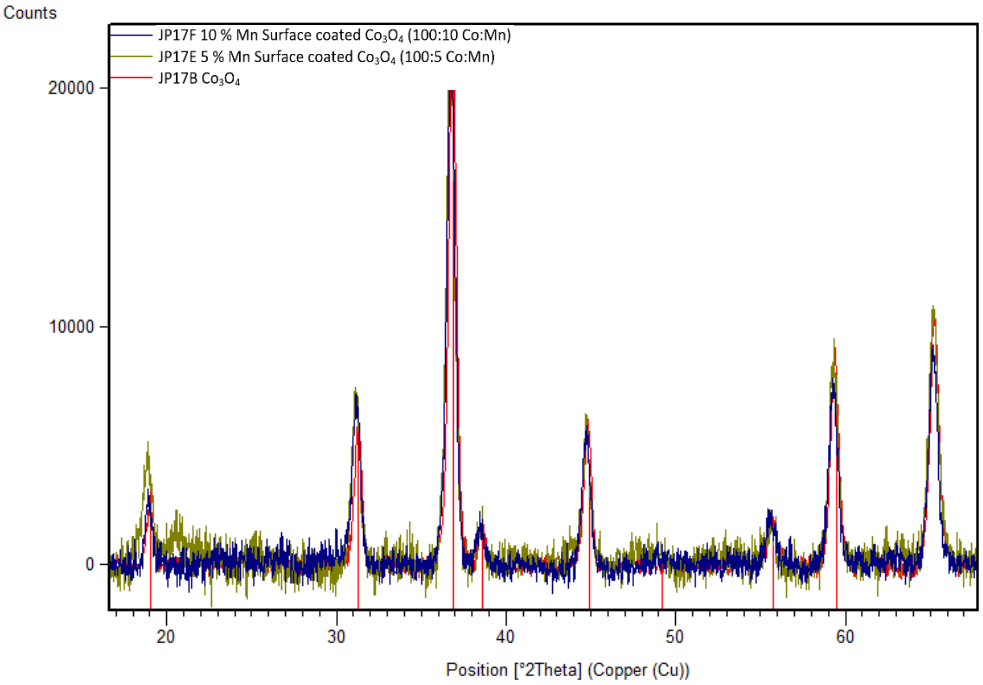

Figure 6-4 Background subtracted diffractograms of Mn surface coated Co_3O_4 particles, with Co_3O_4 reflections indexed (red).

Table 6-4 – Rietveld refined parameters of surface coated nanoparticles.

Sample	Co:Mn	Lattice Parameter (Å)	% expansion
JP17B	-	8.078	-
JP17E	100:5	8.071	-0.09%
JP17F	100:10	8.074	-0.05%

Table 6-4 shows the Rietveld refined parameters for a series of surface doped particles. As expected there is only minor variability between the results, with no observable trend. However, the series on unsupported particles only ranges up to 100:10 Co:Mn, and without significant enough quantities to be used beyond characterisation to verify the synthesis technique.

Table 6-5 shows the Rietveld refined parameters for a series of surface doped particles with have been supported on P25, TiO_2. In this series, the doping levels of Mn increase to a ratio of 100:30. Within this series, we still observe no meaningful variability or trend with increasing manganese levels doped onto the Co_3O_4 particles, either in the lattice parameter of the spinel structure or the presence of other manganese phases within the sample. This is consistent

with the aim, targeting the doping of manganese onto the surface of the cobalt oxide particles suggesting that it is being effectively achieved by the synthesis program.

Table 6-5 — Rietveld refined parameters for surface coated particles supported on TiO_2.

Sample	x	Lattice Parameter (Å)	% expansion
JP25	0	8.078	-
JP25D-1	100:1	8.081	0.04
JP25C-1	100:5	8.077	-0.01
JP25B-1	100:10	8.086	0.10
JP25A-1	100:30	8.084	0.07

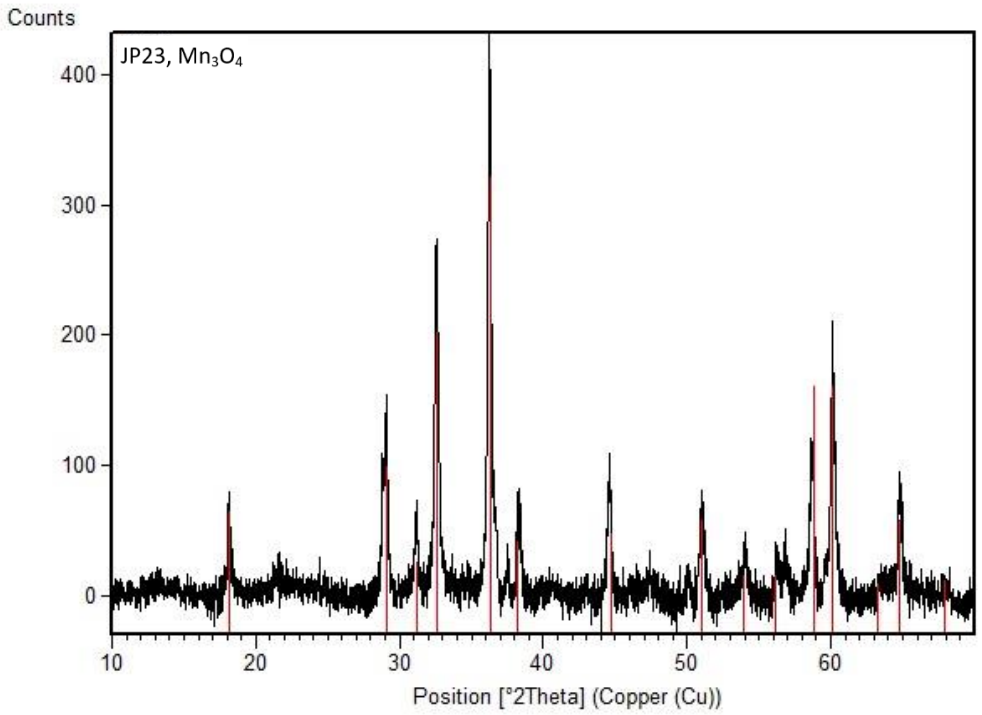

Figure 6-5 Background subtracted diffraction pattern of synthesised sample JP23, Mn_3O_4, with reflections of tetragonal spinel indexed (red).

Figure 6-5 shows the diffractogram of the hydrothermal synthesis with manganese in the absence of cobalt. The resulting brown solid was filtered and purified, and the measured diffraction pattern corresponds to tetragonal Mn_3O_4, Hausmannite.[9] The sample produced was used to produce catalysts with physical mixtures of Co_3O_4 / Mn_3O_4 supported particles.

6.3.1.2 Microscopy

To verify the successful synthesis of the desired Co_3O_4 nanoparticles, sample JP25 was imaged by high-resolution STEM. Figure 6-6 shows imaging of a cluster of synthesised particles, as well as a high resolution image of a single particle. The imaging of the sample show a cluster of particles with similar particle size ~20 nm described by XRD refinement. The high resolution image displays good alignment of the crystal lattice with the imaging plane. Measurement of the d-spacing between the lattice planes of the high resolution particle resulted in a value of 2.88 Å, which corresponds well to the d-spacing of the 220 plane of Fd-3m Cubic Co_3O_4, reported as 2.89 Å.[10]

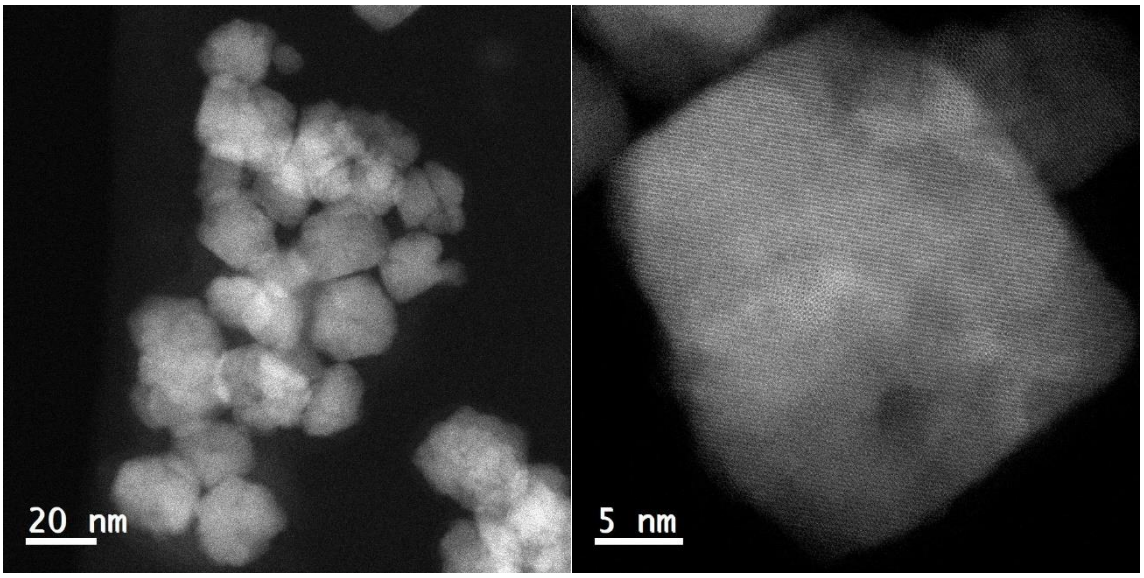

Figure 6-6 STEM imaging of JP25, Co_3O_4.

To understand how effectively the doped manganese is distributed in our Co_3O_4 particles for each doping method, STEM-EDX was used to map cobalt and manganese. Samples A, B, & C in Figure 6-7 show the distribution of manganese over the surface of the base Co_3O_4 particles at varying levels. The maps show that even at 1 % Mn (100:1, x = 0.03) on Co_3O_4, the coverage of Mn is reasonably uniform, and no hot spots are observed. This is consistent up to a surface coverage of 10 % Mn on Co_3O_4, as shown by sample C, where specifically the manganese distribution can be seen to disassociate with the cobalt distribution. Here we can see that the

void in cobalt distribution between the particles imaged by EDX is not present in the map of manganese, indicating that the manganese may be present at the interface of these particles.

Sample D shows the distribution of elements in the mixed oxide synthesis. For the particles imaged, we can see that Co and Mn follow the same distribution, suggesting that the synthesis method is producing a well distributed mixed spinel oxide.

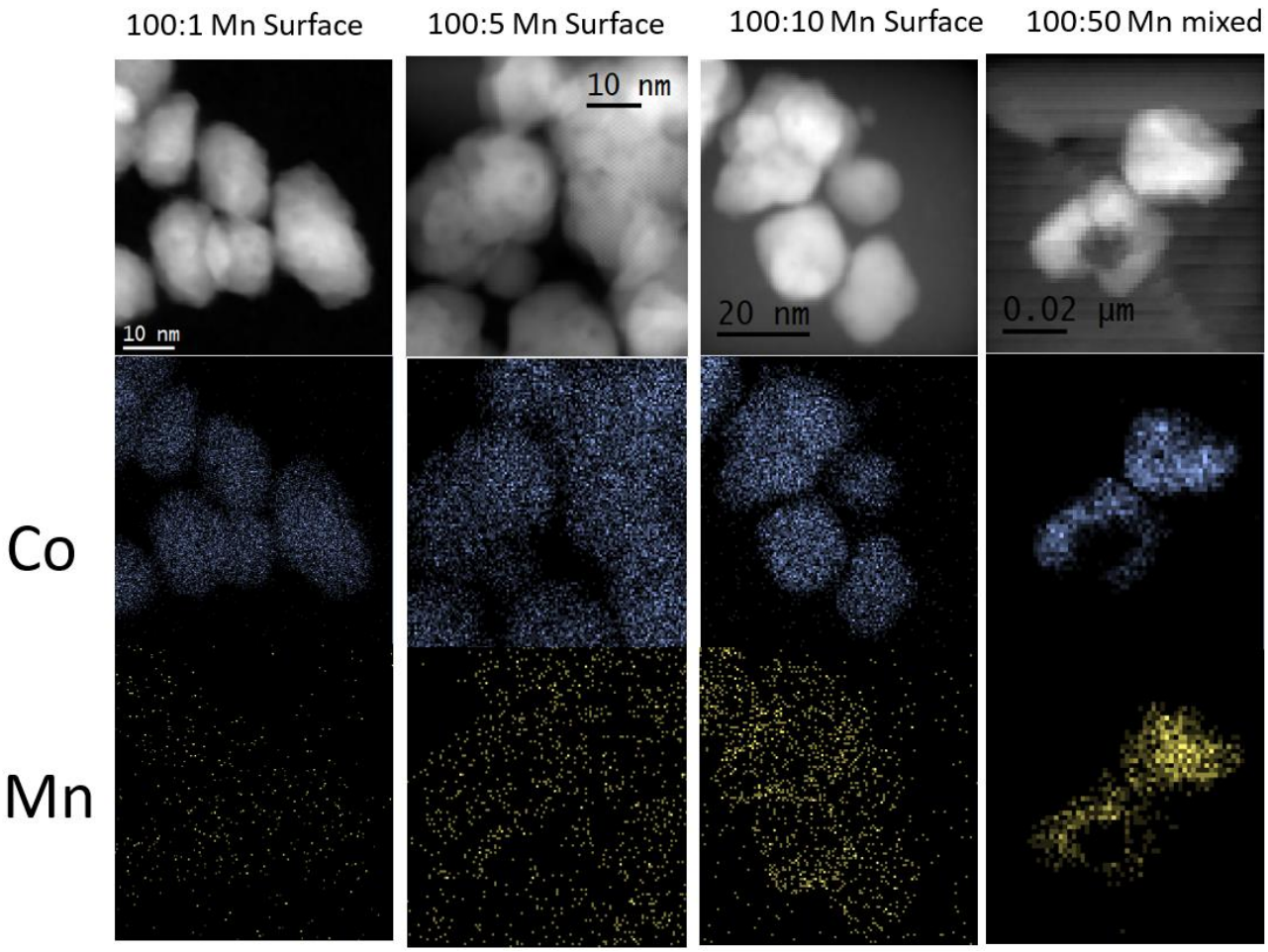

Figure 6-7 STEM images and Co, Mn elemental maps of a) JP25-D (100:1), b) JP25-C (100:5), c) JP25-B 100:10 surface doped Co:Mn, and d) JP11 100:50 mixed oxide Co:Mn particles.

Figure 6-8 shows the Ti K Series and Co K series EDX maps of JP25-1, the supported Co_3O_4 particles. The aim of this mapping is to understand how effectively the supporting method is in distributing the synthesised cobalt oxide particles on the titania support. The distribution of Ti and Co within the maps show similar distribution for each element, suggest that the experimental method for the supporting of the particles is effective in achieving a well-mixed system.

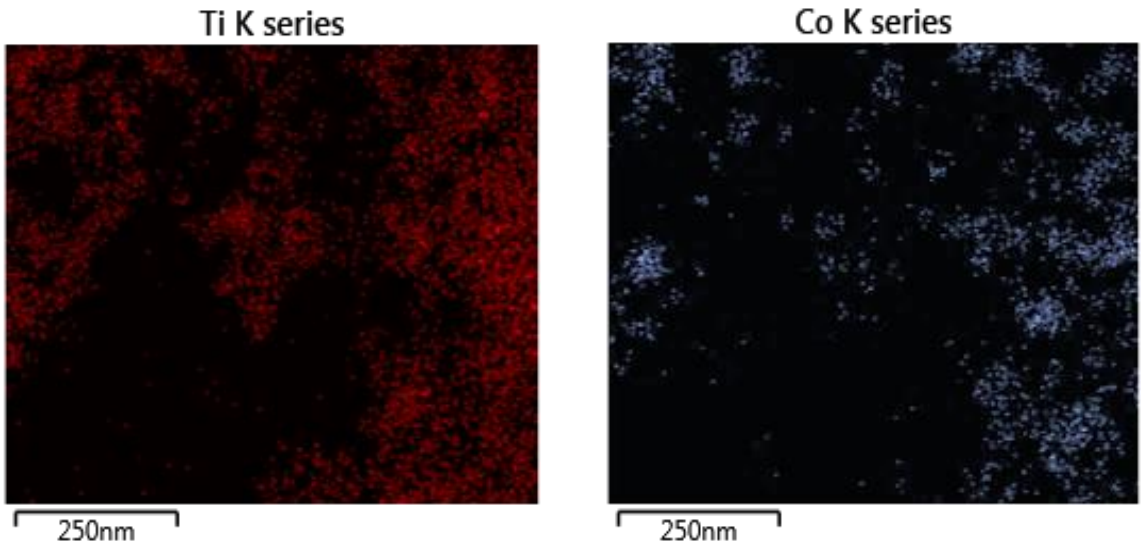

Figure 6-8 Ti and Co EDX maps of TiO_2 supported Co_3O_4 reference particles JP25.

6.3.1.3 XRF Elemental Analysis

Table 6-6 — Elemental XRF analysis results of tested supported catalyst series

Sample	Composition	Wt. % Co Expected**	Wt. % Co Measured	Wt. % Mn Expected**	Wt. % Mn Measured
JP25-1	Undoped	9.74	9.0	0.00	0.01
JP25D-1	Surface	9.74	9.4	0.10	0.13
JP25C-1	Surface	9.74	9.2	0.49	0.66
JP25B-1	Surface	9.73	9.0	0.97	0.90
JP25A-1	Surface	9.72	8.9	2.92	2.62
JP27-1	mixed oxide	9.73	9.3	0.97	0.83
JP26-1	mixed oxide	9.72	8.8	2.92	2.28
JP11-1*	mixed oxide	9.71	-	4.85	-
JP23-2*	Mixtures	9.72	-	2.92	-
JP23-1	Mixtures	9.73	9.6	0.97	0.89

*Not enough sample
** Nominal loadings in oxide catalysts

Table 6-6 shows the results of the XRF elemental analysis conducted on the catalyst series tested. For the majority of samples tested, the measured loading of cobalt and manganese are close to the expected loadings, with any deficit observed appearing reasonably consistent for each element, suggesting that the desired ratios are still present. Two exceptions would be JP25C-1, which appears to contain a higher Mn:Co than expected, and JP26-1, which appears to be manganese deficient. With both these catalysts however, they both maintain

their usefulness within their respective series' even though they diverge from their nominal loadings.

6.3.1.4 XANES

XANES measurements were conducted to understand if the manganese environment in the synthesised supported catalysts varies with the synthesis method or manganese loading. Figure 6-9 shows the normalised XANES spectra collected for 1, 3 & 5 % Mn mixed oxide supported catalysts, as well as the 3 % Mn physical mixture catalyst.

The manganese present in the 3 % physical mixture catalyst was identified as Mn_3O_4 by XRD, and the spectra stands out from the spectra measured for the series of mixed oxide catalysts in multiple regions. Firstly, the pre-edge section of the spectra is slightly more intense in compared to the mixed oxide systems. Secondly, there is a minor energy shift of 1 eV of the K-edge. Finally, the intensity of the edge peak is diminished for the Mn_3O_4 sample compared to the mixed oxide series. Bulavchenko *et al.*[21] report the XANES spectra for the Mn K-edge for a series of $Co_{(3-x)}Mn_{(x)}O_4$ samples with x incrementing from 0.1 – 2.7 across 8 samples. With increasing values of x, or Mn levels, they report a decrease in energy of the K-edge absorption, in addition to the intensity of the peak maximum. In the samples reported in Figure 6-9 we see this energy shift of the K-edge for the mixed oxide systems, however only a variation in intensity for the 1 % mixed oxide system is observed compared to the high doping levels, with the 3 & 5 % Mn samples displaying virtually identical spectra.

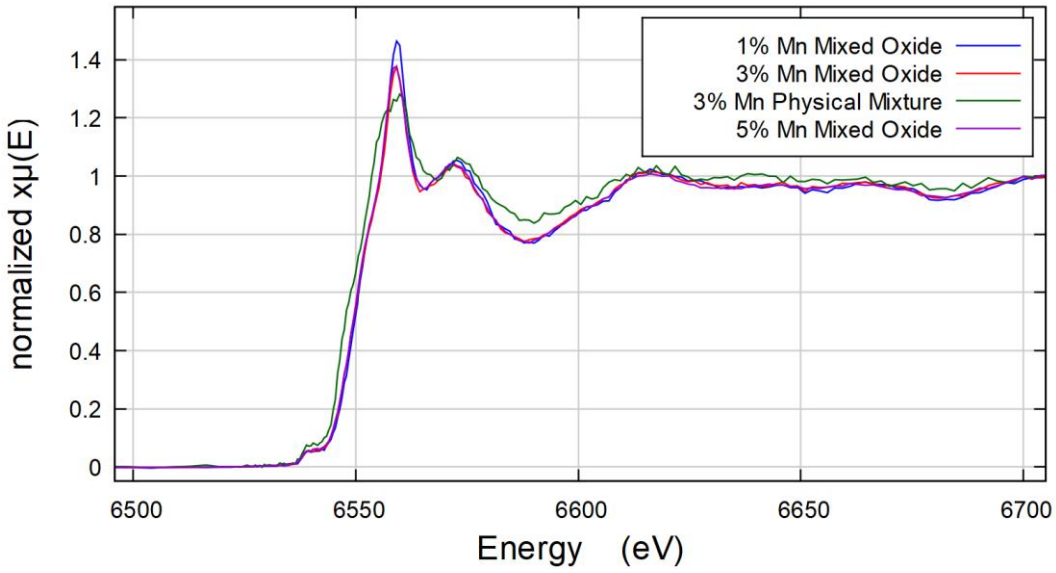

Figure 6-9 XANES Spectra of Mn K-edge for 1, 3 & 5 % Mn Mixed oxide catalyst series, and 3 % physical mixture catalyst.

In Figure 6-10, the XANES spectra of the 3 % mixed oxide, surface doped and physical mixture catalysts are compared at the Mn K-edge. While the surface doped sample displays significantly worse data quality, we can see it roughly conforms to the mixed oxide system. The notable exception to this is at the pre-edge, where the surface doped sample appears to correspond more to the profile of the physical mixture catalyst. The high noise in this region however makes meaningful comparison challenging.

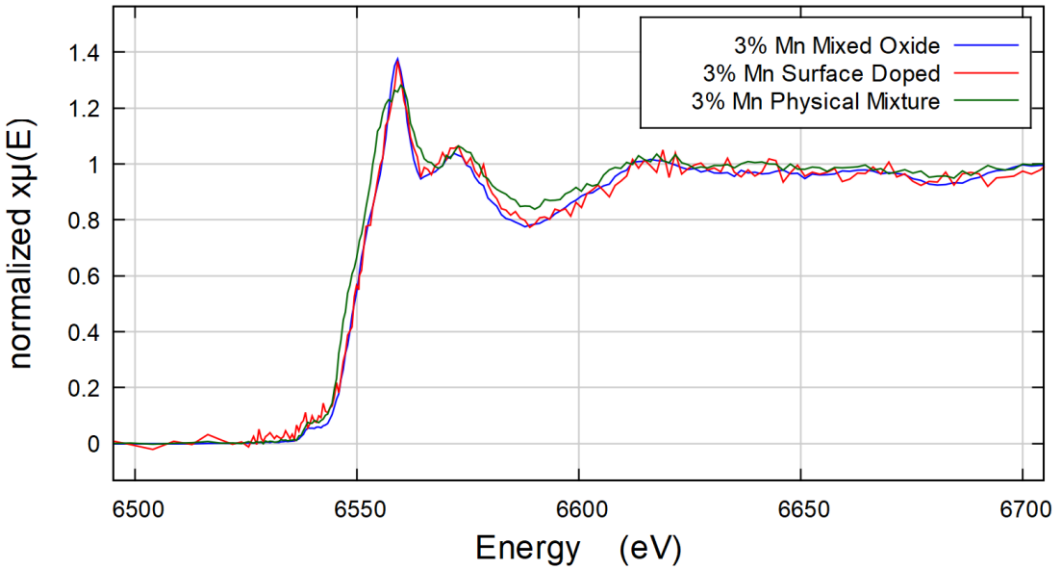

Figure 6-10 XANES Spectra of Mn K-edge for 3% Mn mixed oxide, surface doped & physical mixture catalysts.

Since the data quality collected are not high, linear combination was not attempted in order to estimate the proportion of the two oxide components, however spectra collected for both

the mixed oxide and surface doped series suggest the manganese state in each is different to the synthesised Mn_3O_4.

6.3.1.5 XPS

To further investigate the potential of interaction between the doped manganese and cobalt in the synthesised particles, a small number of samples were studied by XPS. As the binding energies measured by XPS are affected by the local chemical environment of the atoms, any variation identified between doping methods or loadings may be indicative of the effectiveness of the synthesis goals. The Co 2p transitions for the measured samples are shown in Figure 6-11. The synthesised Co_3O_4 species shows reasonable consistency in peak position with the synthesised 100:10 Co:Mn mixed oxide species, while there is a minor shift in binding energy for the sample with higher manganese content of 100:30 Co:Mn.

For the Co_3O_4 and 100:10 Co:Mn mixed oxide samples, the peak positions of 780.0 & 795.25 eV correspond well to the reported binding energies for $2p_{3/2}$ and $2p_{1/2}$ respectively for Co_3O_4.[11] Meanwhile, a shift to higher binding energy for the 100:30 mixed oxide sample, to 780.5 & 796.25 eV is observed.

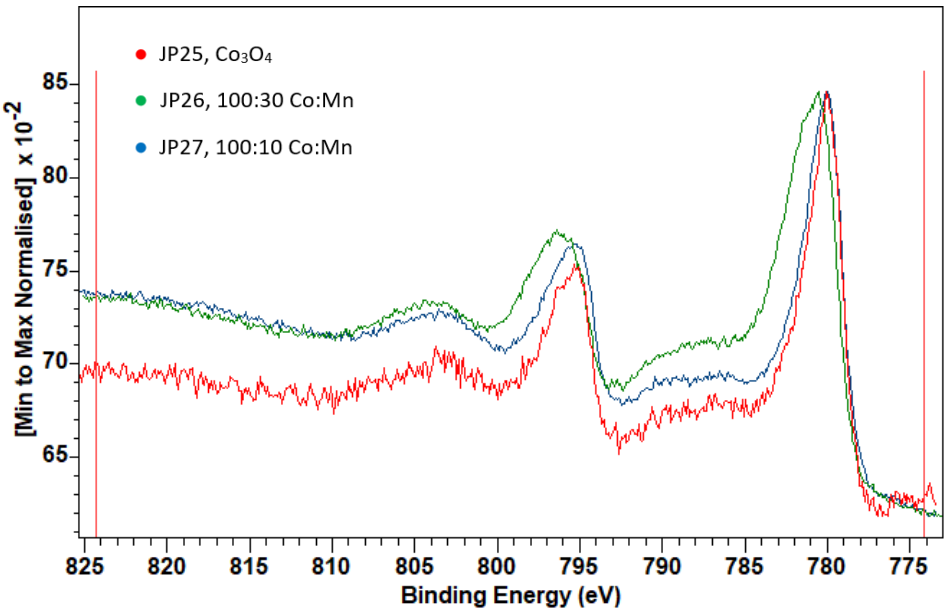

Figure 6-11 XPS spectra of JP25 (Co_3O_4), JP26 (100:30 mixed oxide) & JP27 (100:10 mixed oxide) at the Co 2p region.

Figure 6-12 shows the XPS spectra for JP23 (Mn_3O_4), JP26 (100:30 mixed oxide) & JP27 (100:10 mixed oxide) for the Mn 2p transitions. For the synthesised Mn_3O_4, the peak positions of 641.5

eV & 653.25 eV correspond to the reported binding energies for $2p_{3/2}$ and $2p_{1/2}$ respectively for Mn_3O_4.[22] While a minor shift in peak position is observed for the mixed oxide samples, the biggest change in the profile is for the 100:10 mixed oxide sample where a broadening of the binding energy towards higher energies is observed. This shift suggests an increase in the ratio of Mn^{3+} present within the sample, suggesting the potential preferential occupation of the manganese within the octahedral sites of the spinel structure at this lower % Mn loading. [12]

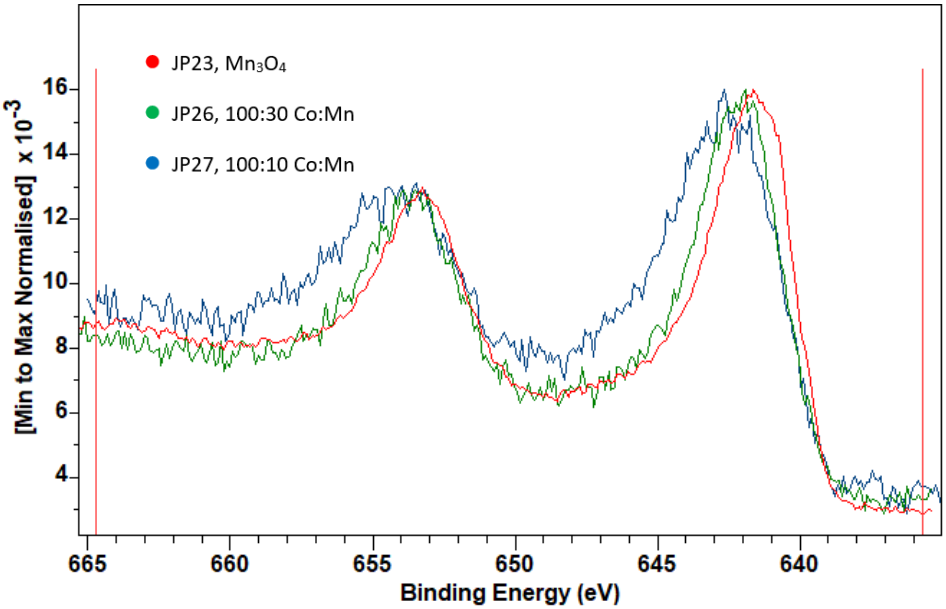

Figure 6-12 XPS spectra of JP23 (Mn_3O_4), JP26 (100:30 mixed oxide) & JP27 (100:10 mixed oxide) at the Mn 2p region.

Table 6-7 shows the relative quantification of Co and Mn by fitting of high resolution XPS measurements taken in the 2p regions for each element. The two samples studied, JP25A (100:30 Surface doped) & JP26 (100:30 mixed oxide) have nominally the same ratio of Co:Mn, 100:30. As XPS is a surface sensitive technique rather than a bulk measurement, we would expect to see the calculated loadings to be dependent on the order of the metals within the synthesised nanoparticles. The quantification of 83.7 % Mn at the surface of JP25A suggests the manganese is effectively distributed over the surface of the cobalt, and obscuring the majority of the cobalt content from quantification with only 16.3 % being measured. Meanwhile, the mixed oxide 100:30 sample (JP26) shows good consistency with the nominal loadings, with the measured 24.3 % Mn closely corresponding to the nominal loading of 23.1 %.

Table 6-7 – Relative Quantification of Co and Mn phases by fitting of XPS results.

Sample	Doping Method	Co:Mn	% Co	% Mn
JP25A	Surface doped	100:30	16.3	83.7
JP26	Mixed oxide	100:30	75.7	24.3

6.3.1.6 Characterisation Summary

The combination of the characterisation results collected suggest that we are effectively producing the desired catalyst systems, including mixed spinel Co-Mn oxide and surface coated Mn oxide on Co oxide at various Co-Mn ratios. Additionally, the conversion of the synthesis to produce Mn_3O_4 also appears to be successful. XRD results suggest that we are producing mixed spinel oxides, with STEM-EDX showing homogeneous distributions of Co and Mn within these particles. XPS also suggests that the manganese is incorporated into the body of the particles structure with quantification fits measured at the particles surface correlating well with nominal loading.

Surface coated particles have been synthesised and do not show any lattice expansion by XRD. This suggests that the added Mn oxide is distributed over the surface of the Co_3O_4 particles rather than forming discreet Mn-oxide particles. STEM-EDX appears to show high dispersion of Mn over the Co_3O_4 particles, even at very low dosing levels (100:1 Co:Mn), with evidence of Mn present in the interstitials between particles clustered during imaging. Quantitative XPS analysis shows the loading of manganese to be far in excess of cobalt relative to the nominal loading, suggesting the manganese coating is effectively obscuring the majority of the cobalt contribution to the surface sensitive technique.

A method has been developed to effectively disperse the synthesised particles onto a catalyst support in preparation for catalytic testing, which has been verified by TEM-EDX. Quantitative XRF has been conducted on the supported samples to allow for catalytic testing metrics to be compared against actual metal loadings rather than nominal, and the Co:Mn ranges have been measured to confirm they are close to the expected regions.

6.3.2 Catalytic Testing

Catalytic testing was conducted on the supported catalyst series under FTS conditions. The focus of this testing was to understand how the manganese doping levels, as we as the doping method, would affect the catalyst performance and selectivity during FTS.

Figure 6-13 shows the % CO conversion and alcohol selectivity measured in the organic liquid products, of the surface coated catalyst series. As we can see, even the lowest loading of Mn onto the surface of the cobalt oxide particles leads to a significant drop in CO conversion, which remains lower than the reference throughout the series. This is not unexpected, as the manganese added has the potential to cover the reduced cobalt surface and block catalytic sites from the gas phase reactants. Additionally, as this series was synthesised from a shared base of synthesised Co_3O_4 particles, JP25, any change in activity cannot be explained by an initial variation in crystallite size of the catalyst prior to reduction. While the lowest doping level does not appear to show a shift in % CH_4 or % C5+ produced, above 0.5 % Mn there is a meaningful increase in % CH4 selectivity, from 12.3 to 21 %. Across the series, we can see an increase in alcohol selectivity over the reference catalyst, with selectivities ranging from 5 – 10 % for 1 % Mn and below. For the highest loaded sample however, a significant jump in alcohol selectivity to 35 % is observed. Interestingly for the 3 % Mn catalyst, a lower CH_4 selectivity is observed compared to the rest of the series. While the lower % C5+ selectivity has not returned to the levels measured for the undoped sample, an explanation for this is the significantly reduced conversion.

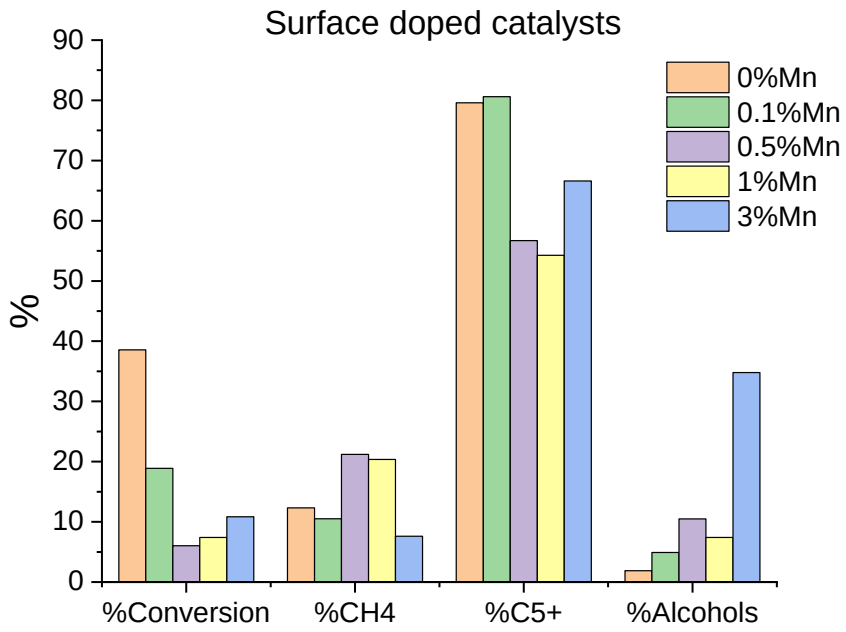

Figure 6-13 Summary of catalytic testing results of surface doped model catalysts at 240 °C.

In addition to the surface-doped samples, the mixed oxide catalyst samples were also tested. Figure 6-14 shows the results from this catalyst series. As before, we can see that a significant jump in alcohol selectivity is observed at 3 % Mn, which is measured at ~30 % for both the 3 and 5 % Mn catalysts. However, at 1 % Mn and lower the selectivity remains relatively unchanged in relation to the reference sample. While the mixed-oxide catalyst series does show a drop in conversion throughout compared to the un-doped catalyst, the drop is less significant than that observed by the surface coated samples, as well as being more variable. Unlike the surface doped catalyst series, the mixed-oxide series is produced from particles which were synthesised separately. The variability in crystallite size of the synthesised particles is a likely major contributing factor in the variation in activity between different loading levels. The % CH_4 selectivity is also less affected by the addition of Mn in the mixed-oxide series than the surface coated samples, though we can see a steady decrease in methane selectivity from 0.5 to 5 % Mn, the 5 % Mn catalyst achieving only 5 % CH_4 compared to 12.3 % for the undoped catalyst at the same temperature. Again, similar to the surface doped catalyst series, we can see that at higher manganese loadings, methane selectivity is improved compared to the undoped reference, a corresponding increase in C5+ selectivity is

not observed. In this case however, the conversions observed are much closer together and so the effect cannot be explained by lower activity alone.

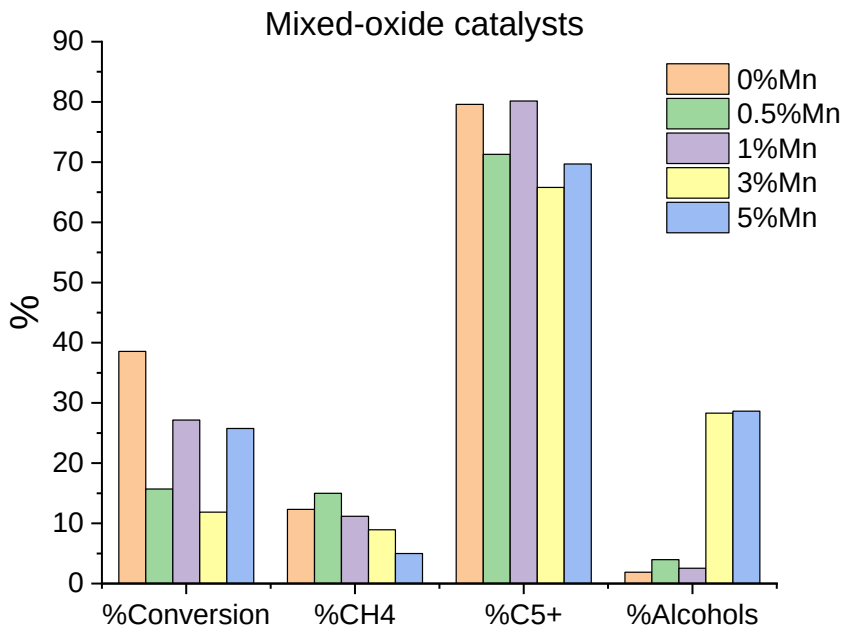

Figure 6-14 *Summary of catalytic testing results of mixed-oxide model catalysts at 240 °C.*

A final set of catalysts were tested, where a mixture of separate Co_3O_4 and Mn_3O_4 particles were loaded on to the same support at loadings of 10 % Co/ 1 % Mn and 10 % Co/ 3 % Mn. Figure 6-15 shows the results of the testing of these samples. For both doping levels tested, the alcohol selectivity remains unchanged relative to the catalyst reference. The lack of alcohol selectivity in the 3 % Mn sample is not consistent with the selectivity observed in the 3 % Mn mixed oxide or surface doped samples. This suggests that a close interaction is required between the active cobalt and manganese dopant for the effect in alcohol selectivity to be produced. Additionally, the performance of the 3 % Mn sample is significantly higher than the reference and the 1 % Mn sample, in regard to CO conversion, % CH_4 & % C5+ selectivity.

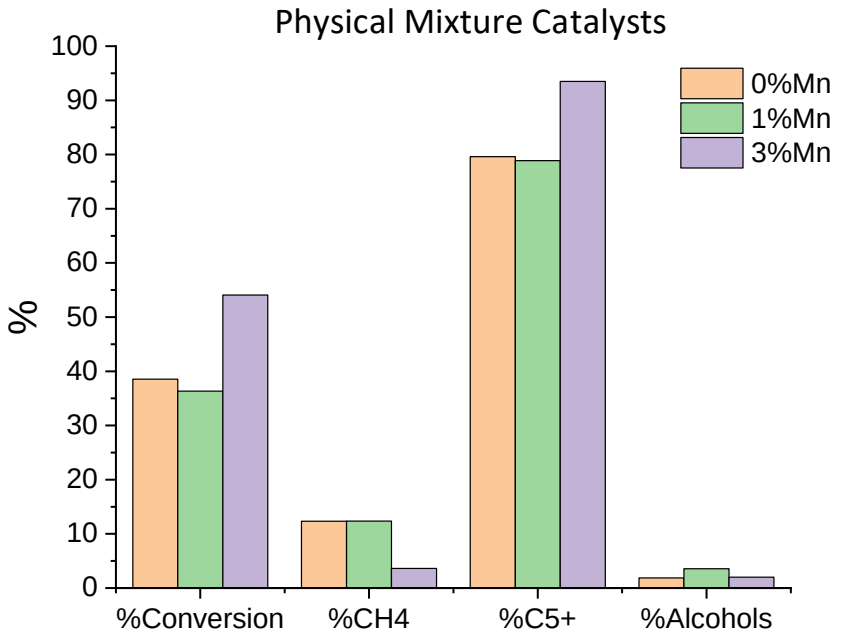

Figure 6-15 Summary of catalytic testing results of physical mixture model catalysts at 230 °C.

Paterson *et al*. [3] report a significant increase in alcohol selectivity with manganese doping ≥3 % on 10 % Co/TiO_2. The reported catalysts were synthesised via co-impregnation of cobalt and manganese precursor salts and characterisation show the metals form a mixed oxide in the synthesised catalyst. For the model catalysts studied, a similar increase in alcohol selectivity is observed in catalysts with ≥3 % Mn. In the mixed oxide model series, no increase in alcohol selectivity is observed up to 1 % Mn, which is in contrast to the surface coated series which exhibits an increase at low loadings, though not proportional to the amount of manganese present. The difference in behaviour between these two series implies that there is a dependence of exposed surface area of the manganese species with alcohol selectivity. This suggests the manganese phase is directly involved with the gas phase of the reaction, rather than simply imparting electronic effects onto the active cobalt metal.

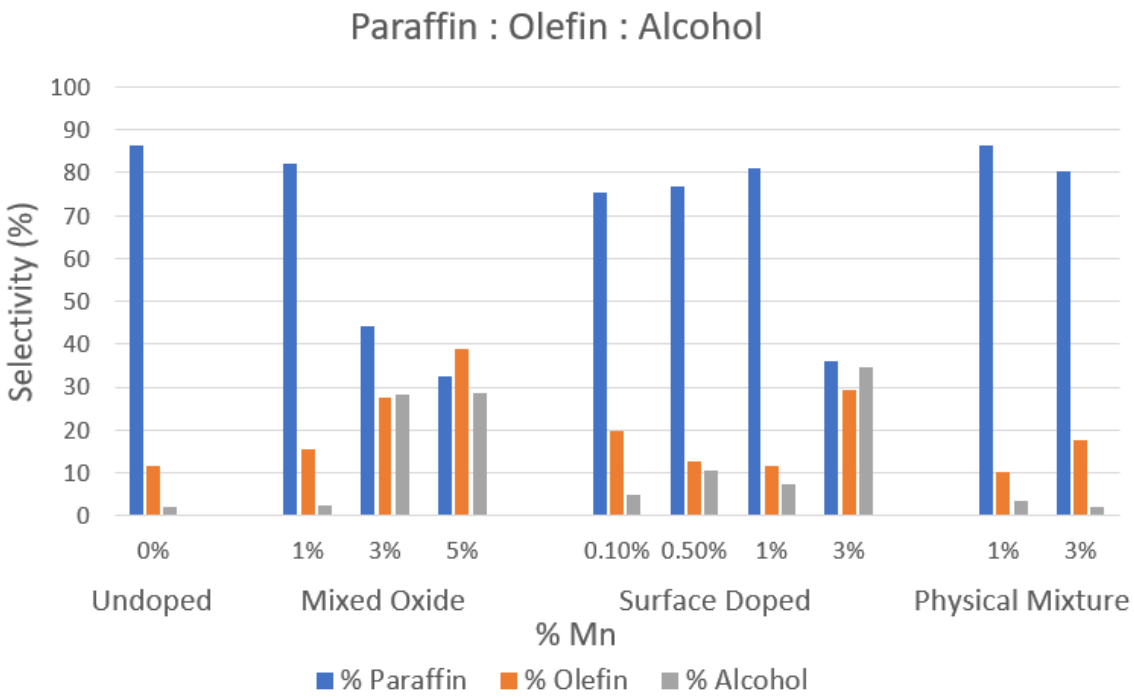

Figure 6-16 Paraffin : Olefin : Alcohol selectivities for each catalyst series tested.

The ratio of paraffins : olefins : alcohols produced by each catalyst tested is shown in Figure 6-16. Overall, we can see that catalysts displaying high levels of alcohol selectivity also have higher olefin selectivity. This is consistent with the catalysts studied by Paterson *et al.*,[3] who report similar correlation between high alcohol selectivity and olefin selectivity.

Meanwhile, minor increases in olefin production are observed at lower Mn doping levels without a corresponding increase in alcohol selectivity. The relationship between increased olefin production and Mn doping is expected, with Mn being reported[23] to be effective in increasing olefin selectivity from 10 to 30 % with 1 % Mn doping.

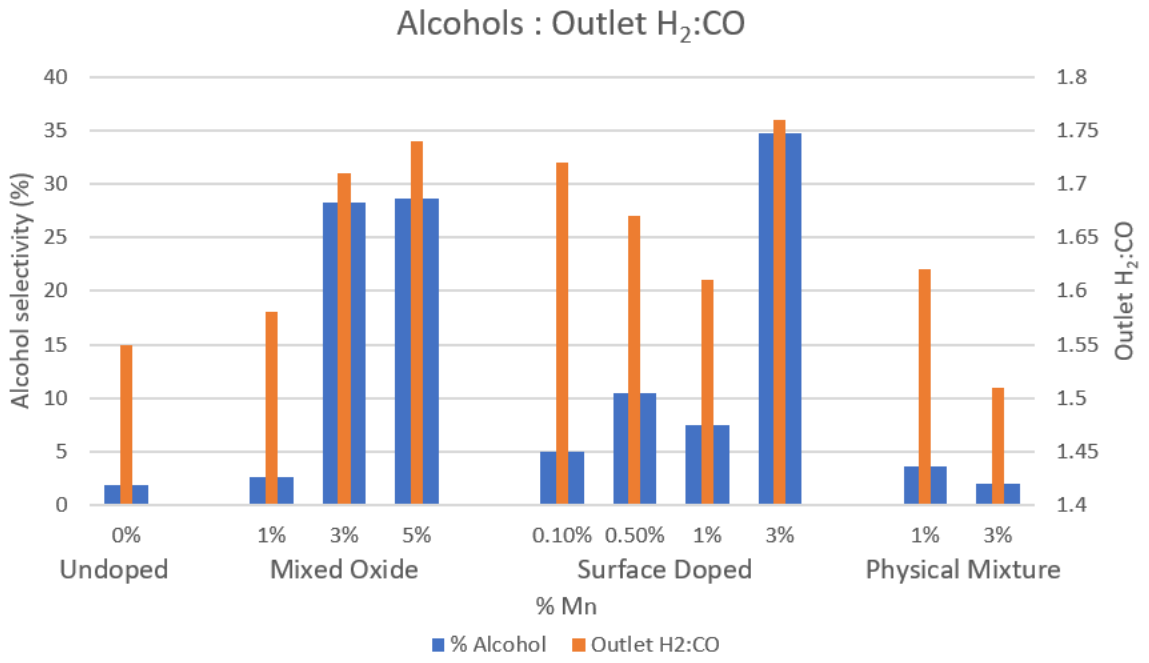

Figure 6-17 Alcohol selectivity (primary axis) and outlet H_2:CO (secondary axis) for each catalyst series tested.

Figure 6-17 shows the relationship between alcohol selectivity and the outlet H_2:CO. Given that the inlet H_2:CO is nominally 1.81, the outlet H_2:CO is expected to be lower than this across the tested catalysts. The value at the reactor outlet is dependent on the consumption ratio of the tested catalyst and the conversion rate, however the H_2:CO is also influenced by WGS activity. In the catalysts with high alcohol selectivity, we can see the outlet H_2:CO is consistently high, above 1.7.

The model catalyst samples studied are supported on P25, a non-porous support. As such the localised H_2:CO experienced by the active catalyst is not expected to vary due to gas diffusion or mass transfer limitations of the synthesised products, as you might expect in highly porous catalyst supports.

Paterson *et al*.[3] report the evolution of bulk cobalt metal to cobalt carbide at a H_2:CO of 1.4 and lower on 5 % Mn, 10 % Co/TiO_2 by *in situ* XRD. Across the model catalyst series tested, we can see that the highly alcohol selective catalysts all display an outlet H_2:CO of >1.7. This suggests that a low H_2:CO at the outlet is not a requirement for high alcohol selectivity in these catalysts, and that the formation of bulk CoC_2 may not be necessary. The

As the range of conversions within the series of catalysts tested is wide, a more representative comparison between the samples is to look at the H_2:CO consumption ratio, as shown in

Figure 6-18. As the WGS is also responsible for varying the H_2:CO ratio, the % CO_2 selectivity is also shown, however CO_2 can also be formed during carbon monoxide disassociation.

We can see a significant dependence of % CO_2 selectivity in the high manganese catalysts in both the mixed oxide and surface coated series, however the % CO_2 selectivity remains at the baseline for the 3 % Mn physical mixtures catalyst. This suggests that it is not the manganese species itself that is responsible for the % CO_2 selectivity, but rather the cobalt modified by the presence of local manganese.

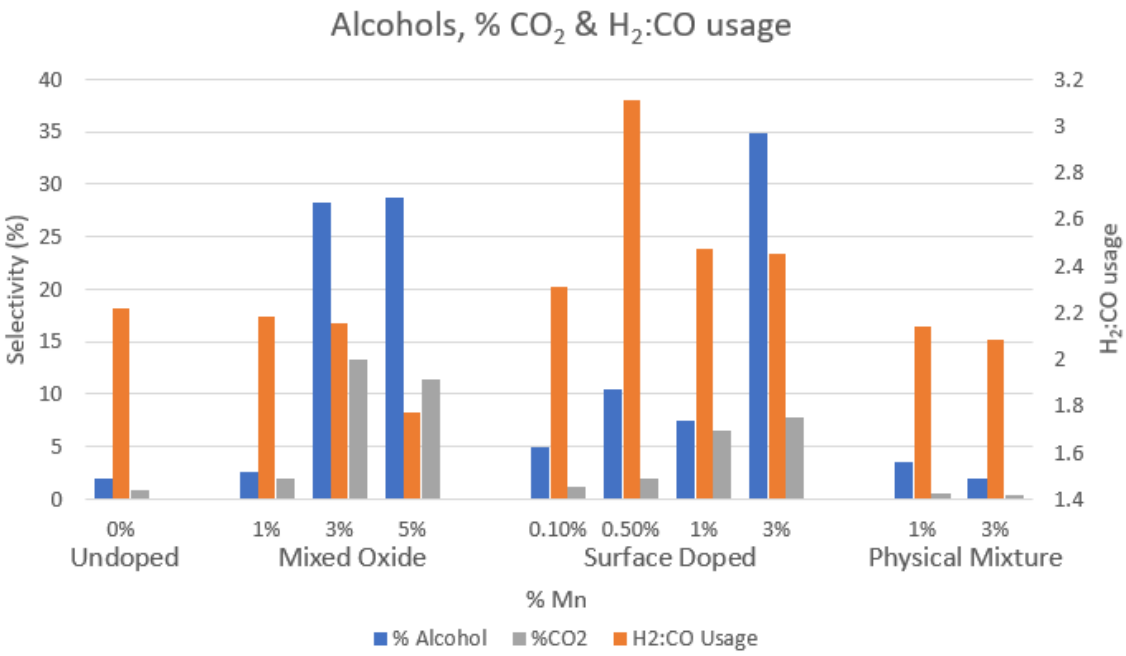

Figure 6-18 Alcohol selectivity, CO_2 selectivity (primary axis) and H_2:CO consumption (secondary axis) for each catalyst series tested.

The catalysts that display high alcohol selectivity also display the highest % CO_2 selectivity. The apparent H_2:CO consumption is less consistent though, with the usage ratio swinging both lower and higher than the reference undoped catalyst.

Higher CO_2 selectivity resulting from the WGS will lead to the production of H_2, creating an apparent decrease in the H_2:CO consumption. However, the formation of CO_2 via CO dissociation will also lead to both higher CO_2 selectivity and a lower H_2:CO due to the consumption of CO without H_2.

6.3.3 Activity comparison

The activity of each catalyst per gram of cobalt was calculated using the cobalt loadings measured by elemental XRF. Figure 6-19 shows the activity of each catalyst series tested.

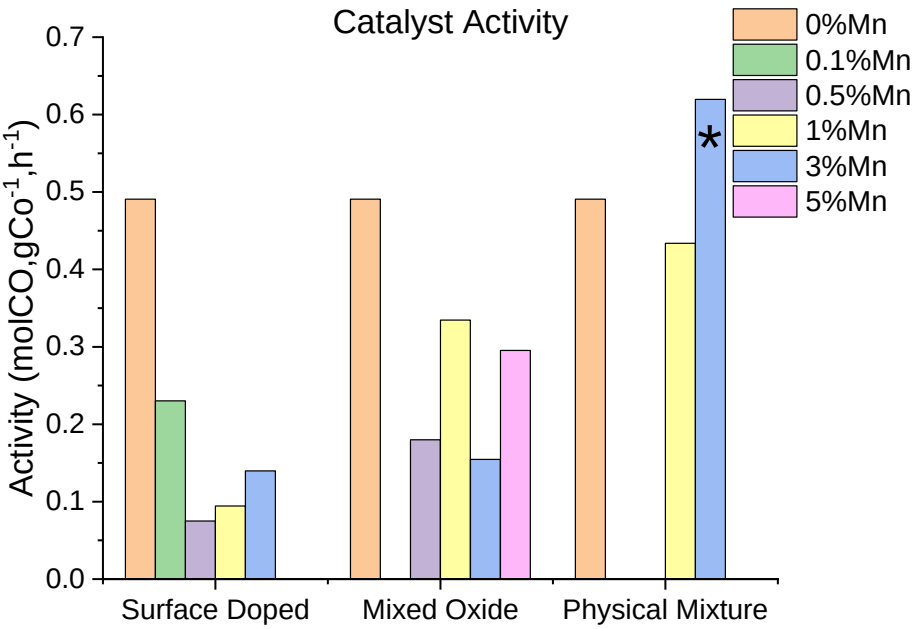

*Figure 6-19 Activity of each catalyst series tested per g cobalt at 240 °C (*230 °C).*

The trends observed in the % CO conversion results are not changed by the translation of the data to activity per unit of cobalt. For the surface doped particles the drop in activity, even at low levels of Mn, can be explained by the expected blocking of surface cobalt sites in the activated catalyst by the manganese dopant. This effect appears to be diminished as the manganese level is increased in the 3 % sample.

For the mixed oxide samples, each catalyst shows a significant reduction in activity in comparison to the undoped particles. Unlike the surface doped series however, the mixed oxide series do not share a consistent particle size of the spinel oxide as they were synthesised separately, so the activity results have not been deconvoluted from the effect of crystallite size, or metal surface area, on activity.

The 3 % Mn catalyst in the physical mixture series is the only catalyst tested that outperforms the reference catalyst. The difference is more significant than it appears in Figure 6-19, as the 3 % Mn sample is operating at a temperature 10 °C lower than the rest of the catalyst series.

Figure 6-20 shows the CO conversion data for the physical mixture series. As shown, the conversion of the 3 % Mn catalyst increases over time at 230 °C, climbing from ~38 to ~55 % over a span of 3 days at 230 °C. This suggests that there is a significant amount of restructuring occurring within this sample. This observation was unique to the 3 % Mn physical mixture, and progressively increasing conversion was not observed in any other of the model catalyst systems discussed. The most common explanation for a steady increase in CO conversion is due to further reduction of cobalt oxide during the FT reaction, due to only partial reduction occurring during the activation procedure. This explanation appears insufficient to explain this observation however, as the Co_3O_4 particles supported in this catalyst are identical to those in the reference catalyst. Additionally, the 3 % Mn physical mixture catalyst shows an improvement in initial conversion at 220 °C of ~23 %, compared to ~14 % in the reference Co_3O_4 catalyst, with this gap increasing during the lifetime of the run.

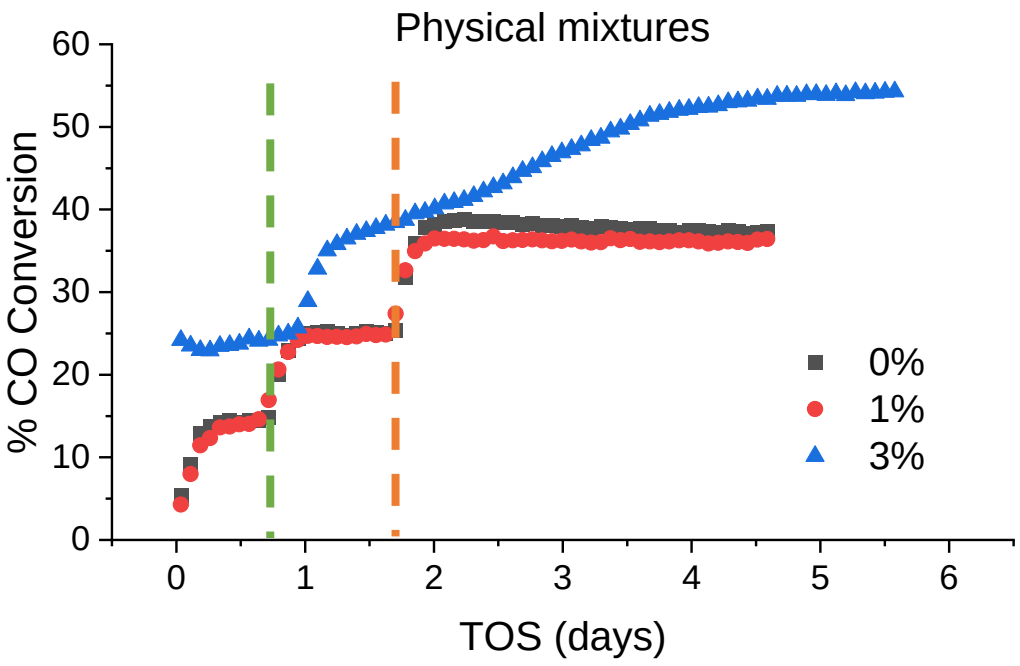

Figure 6-20 Activity profile of physical mixture model catalysts throughout testing, with temperature increases from 220 – 230 °C (green dashed line) for each catalyst, and temperature increase from 230 – 240 °C (orange dashed line) for 0 and 1 % Mn catalysts only.

While the addition of separate Mn_3O_4 particles to the 3% physical mixture catalyst appears to have no effect on the alcohol selectivity, as well as the increased activity there is an increase

in % C5+ selectivity to 93.5 %, and corresponding decrease in % CH_4 selectivity to 3.62 %, which is remarkably low for a cobalt FT catalyst at these temperature ranges.[13][14][15]

6.3.4 DRIFTS CO Absorption

In an effort to understand how varying the doping interaction of the manganese on cobalt affects the catalyst, DRIFTS has been utilised to investigate the absorption of CO on the activated catalysts. Figure 6-21 shows the absorption of CO on the supported mixed oxide catalyst series after reduction. The profile shows several peaks in addition to the gas phase CO, as well as a large depression on the introduction of CO between 1000 – 3400 cm^{-1}.

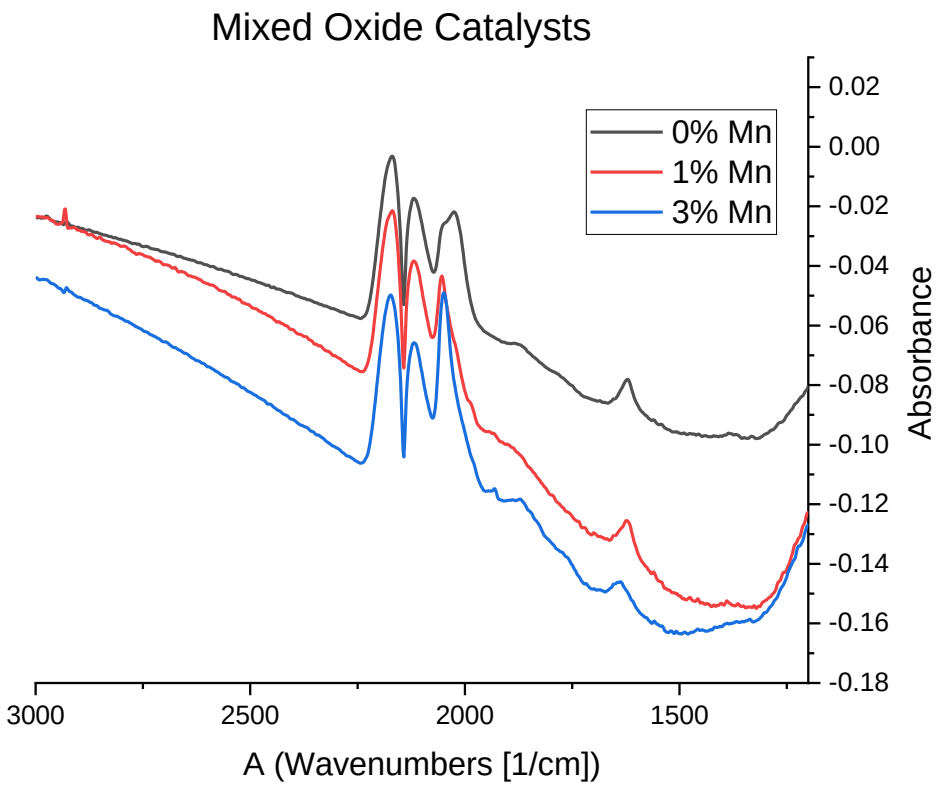

Figure 6-21 DRIFTS spectra for CO absorption on supported mixed oxide catalyst series.

On subtracting the gas phase CO as well as the depression, as shown in Figure 6-22, we can see three distinct regions present. The first region in Figure 6-22 is in the range of 1975 – 2075 cm^{-1}, and correlates with linearly bonded CO.[16] For each sample, we can see what appears to be multiple overlapping peaks, due to the shoulders and asymmetry present. While the

shape and maximum of the peak varies between samples, there is no consistent trend with varying manganese levels.

From 1700 – 1950 cm^{-1} we can see a broad contribution, which is expected to represent bridge absorbed CO.[17][18] The intensity of this band appears to be somewhat proportional to the linearly bonded CO. Though there is no significant shift or trend observed between samples in the peak position of the band, this may be obscured due to the breadth of the band as well as the multitude of peaks around the contribution. Finally, in the 1500 - 1700 cm^{-1} carbonate region,[19] we can see each catalyst displays a single peak. The 0 and 1 % Mn catalyst share a position of 1620 cm^{-1} for this peak, while the 3 % Mn catalyst displays a shift to 1637 cm^{-1}.

In an effort to better understand the absorption environment, the absorption of CO on the catalyst support and reduced model catalyst particles were measured independently.

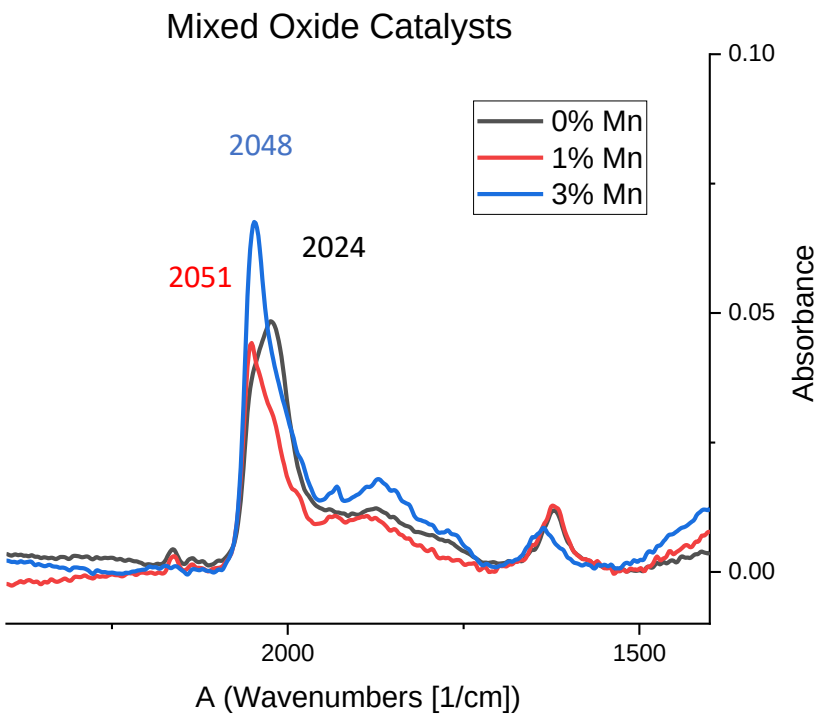

Figure 6-22 DRIFTS spectra with baseline correction and gas phase CO subtraction of supported mixed oxide catalyst series.

CO absorption was measured on the bare P25 catalyst support. Figure 6-23 shows that the catalyst support is able to absorb linearly bonded CO at 2055 cm^{-1} as well as a shoulder at 2020 cm^{-1}, similarly to the supported catalysts. However, there is no response for bridge

bonded CO in the 1850 cm^{-1} range. Additionally, two peaks are present in the carbonate region at 1685 & 1620 cm^{-1}. While the major peak at 1620 cm^{-1} matches observations made in the mixed oxide catalyst, the 1685 cm^{-1} peak is not observed in the supported mixed oxide catalysts. The presence of CO absorption on the bare support makes the assignment of absorbed CO on the supported catalysts a challenge, as the contributions cannot be easily deconvoluted between the support surface and catalyst metal surface.

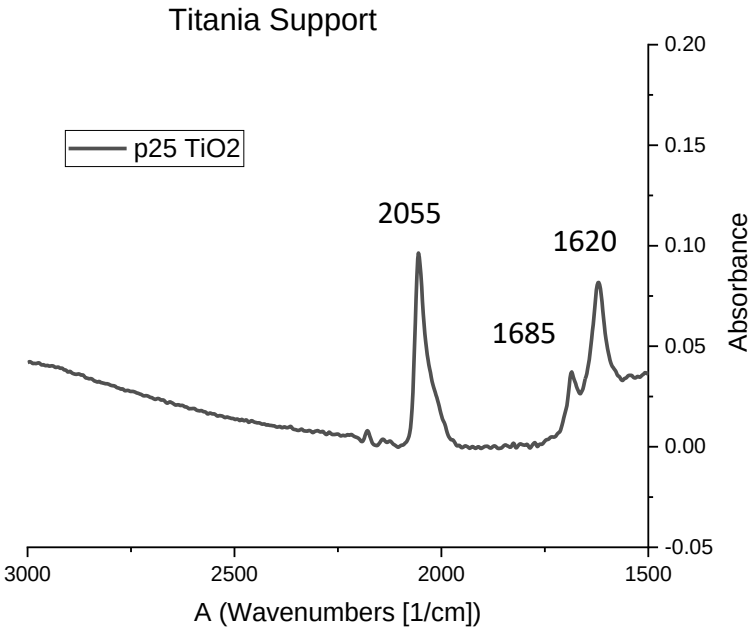

Figure 6-23 DRIFTS spectrum with baseline correction and gas phase CO subtraction of CO absorption on P25 TiO_2.

An advantage of using model catalyst systems in this study, is that we can look at the synthesised particles independently of the support. Figure 6-24 shows the absorption profile of CO on the unsupported mixed oxide particles after reduction. A very different profile is measured compared to the supported catalysts, with only one absorption peak present at 1775 — 1800 cm^{-1}. The difference in peak position is minimal between the 100:10 and 100:30 Co:Mn particles, however the peaks are significantly shifted to a lower wavenumber compared to the undoped particles. The reduced cobalt peak is centred at 1792 cm^{-1}, however the 100:10 and 100:30 manganese doped particles are centred at 1769 cm^{-1} and 1763 cm^{-1} respectively. This suggests that the reduced cobalt particles are being affected by the electron withdrawing nature of the manganese oxide present in close interaction, causing a stronger

absorption interaction from the CO. The minimal difference between the spectra for the 1 and 3 % Mn equivalent samples, which display different alcohol selectivities during catalyst testing when supported on P25, suggest the need to study the supported catalysts if there is any dependence on catalyst selectivity with CO absorption on the reduced catalysts.

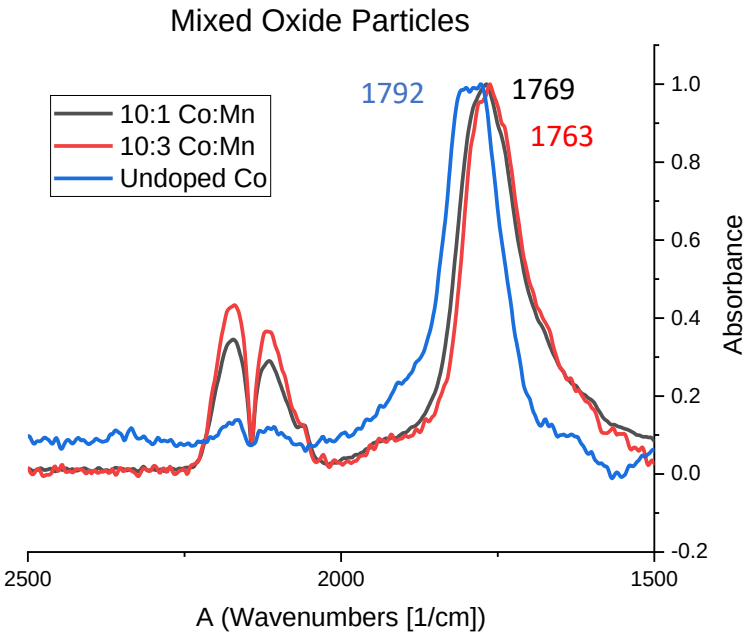

Figure 6-24 Normalised DRIFTS spectra of normalised CO absorption on unsupported mixed oxide model particles.

The absorption of CO on the surface doped model catalyst series was also measured, the results of which are shown in Figure 6-25, however the intensity of the resulting absorption was greatly reduced in this series in comparison to the other catalysts studied. The resulting spectra for the 0.1, 0.5 and 1 % Mn show similar peaks, with overlapping positions and only minor variations in ratios. The 3 % Mn sample does show the presence of additional peaks in the carbonate region 1400 – 1700 cm^{-1}, as well as a more pronounced peak in the bridge bonded CO region around 1900 cm^{-1}, relative to the linearly bonded CO absorption peak. While the higher % Mn catalysts displayed a higher CO_2 selectivity during operation, the 3 % Mn displayed a similar selectivity to the 1 % Mn surfaced doped sample. Given this, no trend can be determined between the absorption spectra within the carbonate region and the CO_2 selectivity observed during catalyst testing.

Unlike with the mixed oxide series, the manganese loading in the surface coated series appears to have no effect on the maximum peak position of the linearly bonded CO consistently at 2055 cm^{-1}, likely represented by linearly absorbed CO on P25. While a shoulder to this peak is observed in two of the measurements, it is present in the 0.1 and 3 % Mn catalyst samples, representing the two extreme ends of the doping levels.

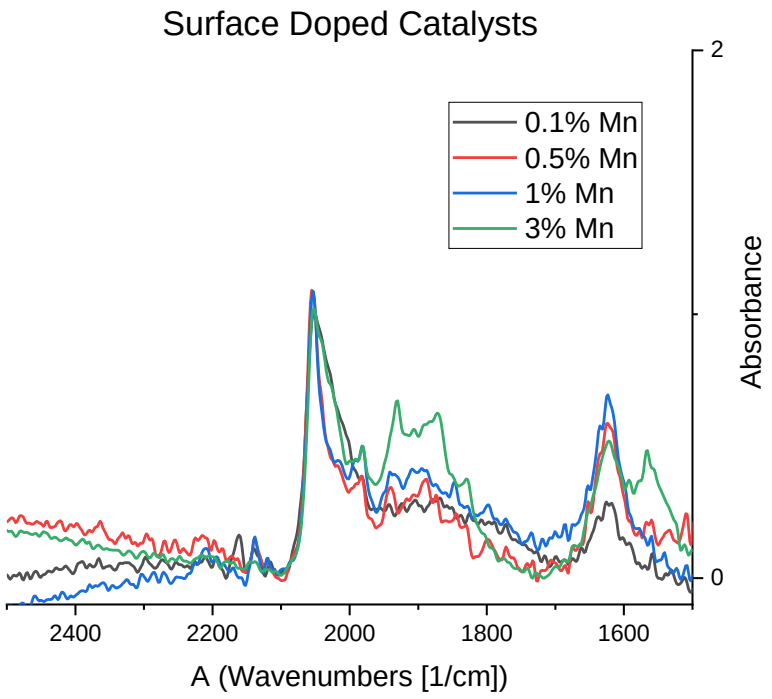

Figure 6-25 Normalised DRIFTS spectra with baseline correction and gas phase CO subtraction of normalised CO absorption on supported surface doped catalyst series.

The composition of the catalysts measured in Figure 6-26 are nominally the same, with each catalyst having 3 % Mn loading. While the surface coated and mixed oxide catalysts exhibited high alcohol selectivity, the physical mixture catalyst did not, and so it provides a potentially useful comparison of catalysts with the same composition, but different physical interactions between the cobalt and the dopant. The surface coated system displays a significantly different spectra compared to the physical mixture, with both increased contribution in the bridge bonded region, and an additional peak present at ~1560 cm^{-1} in the carbonate region. This is not consistent however in the mixed oxide system, whose spectra much more closely resembles that of the physical mixture sample. Consistent between the surface coated and mixed oxide system is the shape of the 2050 cm^{-1} peak, with its long right-hand tail off

resembling that present in the spectra of P25 shown in Figure 6-23. The physical mixture sample however has a much more rounded peak which resembles more the peak present in Figure 6-22 for the undoped catalyst.

Although the two alcohol selective catalysts studied show dramatically different spectra, they both share an increased contribution of bridge bonded CO across the 1800-2000 cm^{-1} region, though the intensity of this absorption region is clearly not proportional to the alcohol selectivity results measured for these catalysts.

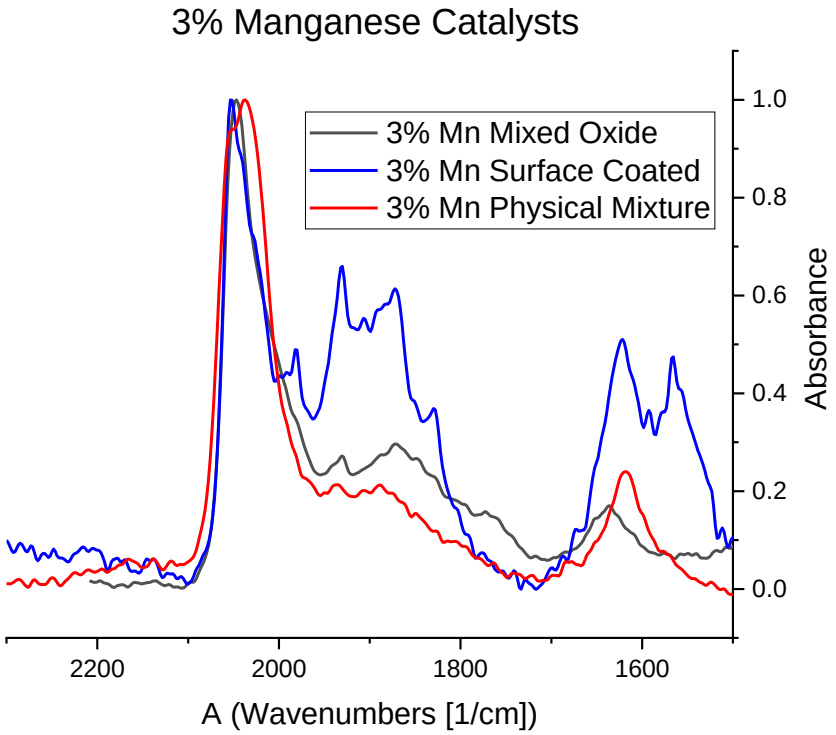

Figure 6-26 Normalised DRIFTS spectra with baseline correction and gas phase CO subtraction of supported 3 % Mn catalysts with varying interaction methods.

While overall the DRIFTS measurements show that the presence of manganese is altering the absorption of CO onto the surface of both the supported catalyst systems and unsupported model particles, a strong correlation could not be identified between peak presence or position with the selectivity of alcohols during Fischer-Tropsch. Measurement of the samples with and without the support was found to have an effect on the absorption of CO, however the bare support itself was found to absorb CO in significant quantities in the same region as the cobalt, potentially obscuring details of the absorption.

Research by Morales *et al.*[20] is published on DRIFTS CO absorption on catalysts with similar composition, being 0 - 3 % Mn doping on 8 % Co/P25 TiO_2. The synthesis technique employs sequential addition, not simultaneous, of the metals and so while the composition is similar, the interaction between cobalt and the manganese dopant is not a direct comparison. Morales *et al*. identify a significant reduction in CO absorption with increasing manganese doping, particularly in the bridging CO region. The results collected in this work are not consistent with the observations reported, however the effect of the support absorption of CO may have less of a contribution in catalysts with a more traditional synthesis due to the expected better coverage of cobalt over the surface of the support. Additionally, the difficulties observed in measuring CO absorption on surface doped catalyst are consistent with the significant reduction in catalyst activity measured during catalytic testing.

6.4 Conclusions

A series of model catalyst systems have been developed to study the correlation of manganese doping amount and interaction with alcohol selectivity in cobalt Fischer-Tropsch catalysts. A salt-mediated hydrothermal synthesis was used to produce Co_3O_4, Mn_3O_4, Co-Mn mixed oxide and Mn coated Co_3O_4 particles at varying doping levels, which were then supported on P25 TiO_2. XRD, XPS and STEM-EDX were used to verify whether the synthesis methodology was effective in producing the desired systems.

Catalytic testing of these doped model catalysts showed the mixed oxide and surface coated particles to be highly selective towards alcohols at and above 3 % Mn, or 100:30 Co:Mn. The surface doped series showed slight improvements in alcohol selectivity at lower Mn levels, though at the expense of a significant loss in activity, which was less significant in the mixed oxide catalysts. The presence of high alcohol selectivity was found to correlate with high CO_2 selectivity, however the source of this selectivity via WGS and CO dissociation could not be deconvoluted. While the highly alcohol selective catalysts all displayed high outlet H_2:CO >1.7 due to the relatively low activity, the consumption rates varied, ranging from 1.77 to 2.47.

Testing of physical mixtures of Co_3O_4 and Mn_3O_4 particles indicated no effect of Mn levels on alcohol selectivity at the levels tested, however the 3 % Mn catalyst curiously displayed a significant gradual increase in activity throughout the 5 days of testing, suggesting that the presence of discreet Mn particles allowed the active cobalt to evolve or restructure during testing which led to a doubling of activity relative to the reference catalyst at the same target temperature.

DRIFTS experiments were conducted in an effort to understand how the absorption of CO on the surface of the active catalyst was altered by the presence of Mn, and whether any observations in CO absorption correlated to the differences observed during catalyst testing. While some variation was observed between spectra in both supported and unsupported systems, these could not be correlated with the alcohol selectivity measured during catalyst testing. The contribution of the bare support complicated the interpretation of the CO absorption results, and although the spectra of the unsupported particles showed the effect of the introduction of Mn in absorption, it did not appear to be proportional to the amount

of Mn incorporated. No observations made could conclusively be identified exclusively in catalysts that display high alcohol selectivity.

6.5 References

1. F. Morales, F. M. F. De Groot, O. L. J. Gijzeman, A. Mens, O. Stephan and B. M. Weckhuysen, *Journal of Catalysis*, 2005, **230.2**, 301–308.
2. S. Werner, G. R. Johnson, A. T. Bell, *ChemCatChem*, 2014, **6.10**, 2881-2888.
3. J. Paterson, M. Peacock, R. Purves, R. Partington, K. Sullivan, G. Sunley, and J. Wilson, *ChemCatChem*, 2018, ***10*(22)**, 5154-5163.
4. G. Prieto, A. Martínez, P. Concepción, and R. Moreno-Tost, *Journal of Catalysis*, 2009, **266.1**, 129-144.
5. J. Pritchard, L. Morris, D. Walsh, S. Sadasivan, H. Ménard, R. M. Bellabarba, M. T. Weller and R. P. Tooze, *Catalysis Letters*, 2018, ***148*(1)**, 235-245.
6. Ø. Borg, S. Eri, E. A. Blekkan, S. Storsæter, H. Wigum, E. Rytter and A. Holmen, *Journal of Catalysis*, 2007, **248(1)**, 89-100.
7. S. Hendricks, *Berichte der Deutschen Chemischen Gesellschaft,* 1928, **61**, 2153
8. Meera *et al.*, *International Journal of Physical, Chemical & Mathematical Sciences*, 2014, **3**, 1.
9. J. D. Hanawalt, H. W. Rinn and L. K. Frevel, *Industrial & Engineering Chemistry Analytical Edition*, 1938, **10(9)**, 457-512.
10. X. Liu and C. T. Prewitt, *Physics and Chemistry of Minerals*, 1990, **17(2)**, 168-172.
11. X. Yan, *Synthesis and Electrocatalytic Properties of Structure Engineered First-Row Transition Metal Derivatives, 2018* (Doctoral dissertation, University of Missouri--Kansas City).
12. A. N. Naveen and S. Selladurai, Physica B: Condensed Matter, 2015, **457**, 251-262.
13. R. M. De Deugd, F. Kapteijn and J. A. Moulijn, *Catalysis Today*, 2003, ***79***, 495-501.
14. J. Yang, W. Ma, D. Chen, A. Holmen, B. H. Davis, *Applied Catalysis A: General*, 2014, ***470***, 250-260.
15. Z. Liu, G. Jia, C. Zhao and Y. Xing, *Fuel*, 2021, ***288***, 119572.
16. V. B. Kazansky, A. V. Zaitsev, V. Y. Borovkov and A. L. Lapidus, *Applied Catalysis*, 1988, **40**, 17-25.
17. A. A. Davydov and N. Coville, *Russian Chemical Bulletin*, 1995, ***44*(10)**, 1866-1871.
18. N. Sheppard, Vibrations of Monatomic and Diatomic Ligands in Metal Clusters and Complexes—Analogies with Vibrations of Adsorbed Species on Metals. In *Vibrational Spectroscopy of Adsorbates*, 1980, 165-177, Springer.
19. L. F. Liao, C. F. Lien, D. L. Shieh, M. T. Chen and J. L. Lin, *The Journal of Physical Chemistry B*, 2002, ***106*(43)**, 11240-11245.
20. F. Morales, E. de Smit, F. M. de Groot, T. Visser and B. M. Weckhuysen, *Journal of Catalysis*, 2007, **246.1**, 91-99.
21. O. A. Bulavchenko, T. N. Afonasenko, A. V. Ivanchikova, V. Y. Murzin, A. M. Kremneva, A. A. Saraev and S. V. Tsybulya, *Inorganic Chemistry,* 2021, **60(21)**, 16518-16528.
22. G. C. Allen, S. J. Harris, J. A. Jutson and J. M. Dyke, *Applied Surface Science*, 1989, ***37*(1)**, 111-134.
23. D. Schröder, J. Thiessen, A. Jess and J. Scholz, *Catalysis Science & Technology*, 2020, **10(2)**, 475-483.

Chapter 7 - Summary and Conclusions

The aim of this project was to investigate the relationship between alcohol selectivity & manganese doping levels in Co Fischer-Tropsch catalysts. The main way this was achieved was by the study of a series of Mn doped cobalt catalyst extrusions by *in situ* XRD-CT, during catalyst activation and operation. The series studied was previously reported to display significant alcohol selectivity during FTS at Mn doping levels above 3 %.[1] Additionally, a series of corresponding model catalyst samples were developed and tested to correlate specific Co-Mn interactions and loadings with alcohol selectivity during FTS.

Initial work on this project focused on the in situ study of the catalyst extrusion series by XRD-CT at ambient pressure. The catalysts were studied during both hydrogen activation and reaction under pseudo-FT conditions. To maximise the number of samples that could be investigated, the catalyst extrusions were loaded into the same reaction cell and studied simultaneously. The spatially resolved nature of the measurement technique used allowed for the contributions from the individual extrusions to be investigated separately. To maximise the insight into the diffraction data collected, Rietveld refinements were conducted using the spatially resolved diffraction data.[2] This provided quantitative phase information of the phases present during catalyst activation and operation.

It was found that due to the reasonable homogeneity of the catalyst extrusions, that a manual Rietveld refinement of the total summed diffraction contribution across a cropped extrusion could be used as a basis to refine the individual voxels within that crop. This allowed for the production of heatmaps of the refined metrics, including wt. % loadings and lattice parameters. Additionally, the refined parameters were grouped by a function of the distance of the voxel from the exterior surface of the catalyst extrusion. This allowed insight into the dependence of radial depth on the phases present within the extrusions, and how they evolve depending on their radial location.

From the experiment conducted, it was found that at high manganese loadings of 5 & 10 % Mn a significant proportion of the cobalt was retained in a mixed $Co_{(1-x)}Mn_{(x)}O$ phase at the end of hydrogen activation, at conditions that led to the complete reduction of cobalt at 1 % Mn and below. While the cobalt is expected to reduce fully to cobalt metal during catalyst activation, the manganese dopant is expected to progress only as far as MnO.[3][4] In the 0.5

and 1 % Mn extrusions, the cobalt oxides were found to be fully reduced however at the low loadings no diffraction contribution was detected for the manganese dopant at the end of the hydrogen reduction. At all doping levels, manganese was detected exclusively in the mixed oxide phases with cobalt, and no distinct manganese oxide phases were detected. The spatially resolved diffraction data provided the observation of preferential reduction of the cobalt oxide species at the exterior of the catalyst extrusions, progressing to the interior.

After catalyst activation, the experiment was run briefly under pseudo-FT conditions, with similar gas composition and temperature as FTS, however at atmospheric pressure due to reactor constraints. During the 3 h operation under pseudo-FT conditions, no significant changes were observed in the diffraction profile for any of the studied catalysts. While Rietveld refined wt. % loadings of the cobalt metals suggested a minor 0.2 % decrease in absolute metal loading, there was no indication of any additional phases at the end of the 3 h operation.

A hypothesis as to the mechanism by which higher Mn loadings leads to high alcohol selectivity within this catalyst series, is via the formation of cobalt carbide. Paterson *et al*. [1] report the formation of bulk CoC_2 by *in situ* XRD in a 5 % Mn / 10 % Co / TiO_2 catalyst under FT conditions. The H_2:CO feed was decreased from 1.8, representing the reactor inlet, to 1.4, representing the middle of a fixed bed, and observed the formation of bulk CoC_2 in a 5 % Mn catalyst over the span of ~15 h, but not in an equivalent 1 % Mn catalyst. The H_2:CO was dropped as low as 0.6, and the 1 % Mn catalyst still displayed no bulk carbide formation.

Pei *et al*.[5] report the ability of Co-CoC_2 catalysts to display high alcohol selectivity during FTS. They suggest this occurs due to preferential non-dissociative absorption of CO at the Co-CoC_2 interface, allowing the alcohol group to be added preferentially during chain growth. DFT calculations performed showed an increase in the activation energy for the dissociation of CO over the CoC_2 sites compared to the Co sites, suggesting a preference for the retention of the CO bond during absorption.

While no formation of cobalt carbide was detected under the pseudo-FT conditions, the time frame of ~15 h observed by Paterson *et al.*, combined with the ambient pressure of the XRD-CT experiment suggest that it would be unlikely to occur.

In an effort to study the catalyst extrusion series under conditions more representative of FTS, a cell was designed to allow for high pressure operation during XRD-CT measurements. The cell is analogous to the design of the quartz cell used for ambient studies, however designed with stock Swagelok parts to allow for easy modification. Initial commissioning tests of the cell were unsuccessful, as it was found that the large grain size of the stainless steel outer tube was leading to bright spots triggering the safety limits of the detector. An alternative steel tube was used in place as it was found to have good powder diffraction rings. A 3/4" (~19 mm) tube was used for the outer tube of the reactor to allow for a large catalyst bed volume.

A comparative experiment was conducted using the high pressure cell with a larger range of catalyst extrusions. Eight samples were loaded simultaneously in the 12 mm inner reactor tube, and the catalysts were hydrogen activated at 10 bar, followed by operation under FT conditions at 25 bar for 36 h. Upon reconstruction of the collected data, it was found that the reactor contribution was not correctly being attributed to the location of the reactor tube. This occurred due to the parallax effect, of having the large diameter tube leading to a significant variation in distance to the detector. This created an apparent shift in 2θ value of the reactor wall depending on what angle of rotation the XRD line scan was measured from. This resulted in the diffraction contribution not correctly reconstructing and instead overlapping with the diffraction contribution of the catalyst extrusions.

Due to the exponentially more intense diffraction of the dense reactor wall vs the catalyst extrusions, this overpowered the diffraction contribution in the overlapping regions in the diffractogram. This overlap mainly affected the cobalt metal FCC phase, which only the (200) reflection remained unobscured due to the reactor contribution.

Attempts to remove the reactor contribution were unsuccessful. For example, a blank scan on the reactor tube was taken above the catalyst bed. The collected sinogram was then subtracted from the sinogram of the scan collected within the catalyst bed, in an attempt to remove the reactor contribution prior to CT reconstruction. This was unsuccessful however, and lead to other issues with the data. Instead, the regions with reactor contribution were excluded from the conducted Rietveld refinements, and the cobalt metal FCC phase refined on just one peak.

Compared to the experiment conducted at ambient pressure, it was found that the hydrogen activation at 10 bar led to a decrease in the degree of reduction for the catalyst series at 350 °C, even with an increased hold time. Furthermore once introduced to FT conditions, the extent of reduction increased over the following 36 h, with both a decrease in oxide weight loading observed, as well as a corresponding increase in cobalt metal loadings. An experimental cause for the observed degree of reduction could not be determined.

Throughout the 36 h of operation under FT conditions, no additional phases were detected by XRD-CT in any of the catalyst extrusions studied. The operational conditions were selected to mimic the inlet of the reactor, and as such has a high GHSV and H_2:CO of 2. At these high partial pressures of H_2 the formation of bulk CoC_2 is unlikely. If CoC_2 was formed on the surface of the cobalt particles, it would not be detectable by diffraction.

The capability to perform simultaneous studies of multiple samples by XRD-CT under *operando* conditions has been shown, including the refinement of the collected diffraction data to provide quantitative phase wt. % loadings and lattice parameters.

During *in situ* study of the catalyst extrusion series at both ambient and high pressure, the presence of manganese was only detected in the form of mixed Mn-Co oxides, either as the spinel $Co_{(3-x)}Mn_{(x)}O_4$ in the early stages of reduction, and predominantly as $Co_{(1-x)}Mn_{(x)}O$ in the latter and during FTS.

To attempt to simplify the potential environments present within the supported catalysts, a series of model catalyst systems were developed. The aim of these model samples was to provide a comparable set of catalysts with varying manganese content in specific orientations relative to cobalt. This included the generation of three different systems. 1) A series of Co-Mn mixed-oxide nanoparticles with varying Mn content, 2) a series of Co_3O_4 nanoparticles with varying Mn-oxide surface coating, and 3) A series of physical mixtures of Co_3O_4 and Mn-$_3O_4$.

These nanoparticle systems were successfully synthesised and characterised prior to being supported on P25 TiO_2. By synthesising the systems out with the support, it allows for control of variables that are convoluted during traditional catalyst synthesis, such as crystallite size. The basis of the synthesis method revolved around a salt-mediated hydrothermal synthesis of Co_3O_4.[6] The synthesised Co_3O_4 nanoparticles were impregnated with Mn-nitrate and

calcined to produce Mn coated Co_3O_4 particles with various doping levels. The salt-mediated synthesis was modified by co-reacting cobalt and manganese salts to produce mixed spinel $Co_{(3-x)}Mn_{(x)}O_4$ particles. Finally, Mn_3O_4 particles were formed by substituting entirely the cobalt reaction salts for manganese in the salt-mediated synthesis. The final set of model samples was produced by mixing the synthesised Mn_3O_4 with Co_3O_4 at the desired ratios.

The synthesised particles were characterised prior to supporting on P25 TiO_2, to verify the intended Mn-Co interaction and doping level was achieved. The various series produced were catalytically tested to determine their alcohol selectivity. Significant alcohol selectivity was observed above 3 % Mn loading of the mixed oxide and surface coated particles, however not from the 3 % Mn physical mixture sample. These observations are consistent with those reported by Paterson *et al.*[1] on the traditionally synthesised catalysts including an equivalent physical mixture catalyst. A corresponding relationship was observed with the olefin selectivity in the model catalysts tested,

CO absorption DRIFTS were conducted on the model catalyst systems to understand how the varying interactions and doping levels affect the absorption of CO onto the surface of the activated catalysts. Morales *et al.*[4] report CO absorption DRIFTS on FT catalysts with similar nominal composition. They report the addition of manganese leads to a decrease in wavenumber for linearly bonded CO, therefore a weakening of the CO bond. Additionally, they see a decrease in bridge bonded CO, with the remaining also shifted to a lower wavenumber. In this work, the manganese dopant in the mixed oxide systems led to an increase in wavenumber for the peak position of the linearly bonded CO compared to the undoped sample. It was found that the spectra of the supported catalyst matched closely to that measured on the bare P25 TiO_2 support. CO absorption measured on the unsupported reduced mixed oxide particles indicated the Mn dopant causing a stronger interaction between Co and CO, compared to the undoped particles, however this was largely independent of the doping level.

DRIFTS measurements on the surface doped catalyst series were found to be significantly lower quality compared to the mixed oxide series. This is consistent with the blocking of surface cobalt sites, leading to overall lower absorption. Little difference was observed between the varying doping levels of the surface doped series, with the exception of the 3 %

Mn sample which showed an increased ratio of bridge bonded CO vs linear, as well as an additional peak present in the carbonyl region.

The addition of Mn above 3 % on 10 % Co / TiO_2 has been shown to result in high alcohol selectivity in model catalyst systems where Mn and Co are closely interacted, consistent with reported selectivities for traditionally synthesised catalysts via co-impregnation calcination. DRIFTS results from model catalyst systems has shown the addition of Mn leads to stronger absorption of CO in unsupported mixed oxide particles, though shift is comparable between 1 and 3 % Mn in mixed oxide particles. This suggests a higher surface coverage of CO, which could outcompete H_2, leading to a lower rate of hydrogenation during catalysis.

The higher selectivity of alcohols observed has been shown to correlate with higher olefin selectivity in the model catalyst systems. The presence of MnO in proximity to the enables the removal of electron density from cobalt metal due to the Lewis acidity of the Mn^{2+}.[7] This removal of electron density from the cobalt metal would be expected to lead to stronger absorbed CO, which is seen in the DRIFTS measurements of the unsupported mixed oxide particles. This stronger interaction of CO towards the active surface could lead to an increased preference of absorbed CO vs H_2 during FTS. Decreased hydrogen availability could lead to an overall decreased activity, as well as the favouring the selectivity of unhydrogenated olefins. Both these observations are seen with the introduction of manganese at low levels, even before the observed threshold for alcohol selectivity.

Given the reported selectivity of Co-CoC_2 catalysts towards alcohols during FTS, the likelihood of CoC_2 formation being responsible for the observed alcohol selectivity appears strong. In this work the model catalyst systems show the requirement for close interaction of the active cobalt metal and manganese oxide during FTS for the high alcohol selectivity to be observed. The formation of cobalt carbide shown by Paterson *et al*.[1] in the presence of MnO suggests a likely link towards alcohol selectivity.

During study of the catalyst extrusion series by XRD-CT, the manganese dopant was detected exclusively in mixed oxides with cobalt. The lack of distinct Mn phases detected suggests high dispersion of the dopant is being achieved, with no isolated MnO phase detected. A proportion of the cobalt was found to be retained in the $Co_{(1-x)}Mn_{(x)}O$ mixed oxide at the end of reduction under the activation procedure used at both atmospheric pressure and 10 bar.

At no point during XRD-CT measurements was cobalt carbide detected, however to detect the phase by diffraction cobalt carbide would need to form bulk particles. If cobalt carbide was forming on the surface of the catalyst particles, this would not be detected by diffraction. Additionally, if cobalt was forming bulk CoC_2, a response in activity would be expected.

7.1 Further work

There are a small number of complimentary experiments that were planned but could not be conducted due to various reasons.

While the DRIFTS experiments were conducted for CO absorption on the model catalyst series, additional absorptions of H_2/CO gas mixtures were planned but not conducted due to instrumental and time constraints. The effect of co-absorption of both reactant gases compared to CO alone may provide additional insight into the electronic effect of MnO during operation.

During the development of the model catalyst systems, attempts were made to synthesise Mn core / Co shell particles. The aim of these particles was to attempt to isolate the electronic effect of the manganese without introducing the dopant phase to the reaction atmosphere. While progress was made to synthesise particles with this order via sequential injection of reaction salts into the salt-mediated synthesis, the synthesis could not be verified in time for catalytic testing to occur. The isolation of the electronic promotor effects of MnO may provide valuable insight into the olefin and alcohol selectivity observations made thus far.

Recent in group developments involving the use of machine learning look promising in the use of correcting for the parallax of large body objects during CT measurements. If successful, the method would allow for more complete processing of the collected data, in addition to providing a solution for future experiments where the use of large multi-sample reactors may be desired for optimal throughput.

7.2 References

1. J. Paterson, M. Peacock, R. Purves, R. Partington, K. Sullivan, G. Sunley, and J. Wilson, *ChemCatChem*, 2018, ***10*(22)**, 5154-5163.
2. H. M. Rietveld, *Journal of Applied Crystallography,* 1969, **2.2**, 65-71.
3. O. A. Bulavchenko, T. N. Afonasenko, A. V. Ivanchikova, V. Y. Murzin, A. M. Kremneva, A. A. Saraev and S. V. Tsybulya, *Inorganic Chemistry,* 2021, **60(21)**, 16518-16528.
4. F. Morales, E. de Smit, F. M. de Groot, T. Visser and B. M. Weckhuysen, *Journal of Catalysis*, 2007, **246.1**, 91-99.
5. Y. P. Pei et al., *ACS Catalysis*, 2015, **5.6**, 3620-3624.
6. J. Pritchard, L. Morris, D. Walsh, S. Sadasivan, H. Ménard, R. M. Bellabarba, M. T. Weller and R. P. Tooze, *Catalysis Letters*, 2018, ***148*(1)**, 235-245.
7. Y. Marcus, *Ion Properties*, 1997, CRC Press.

Author Contribution Statement

The author would like to acknowledge the following contributions for work conducted as part of this project:

Drochaid Research Services & BP, for the catalytic testing of model catalyst systems.

BP, for supplying the series of manganese doped cobalt FT trilobed extrusions studied by XRD-CT.

BP, for conducting quantitative XRF on model catalyst samples.

Monik Panchal, for his assistance collecting TEM imagery during the development of model catalyst systems.

Mark Isaacs & Harwell XPS, for the measurement of XPS spectra for model catalyst particles.

Chapter 8 Appendices

Appendix for Chapter 4 – Ambient pressure XRD-CT study of Mn doped catalyst extrusion series

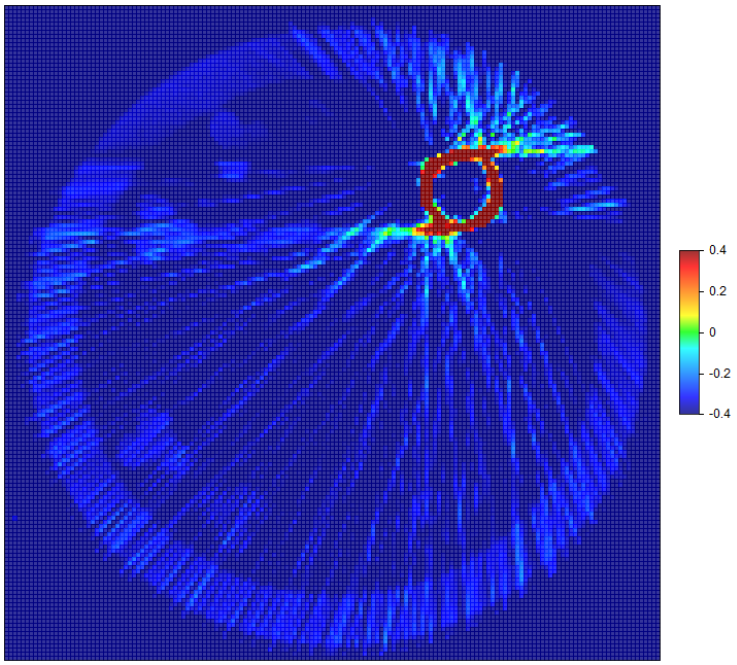

Figure 8-1 – CT Example of reconstruction artefact caused by outer casing of thermocouple. Large grain size leading to incorrect reconstruction, with diffraction contribution from 310 Stainless steel FCC structure overlapping with internal reactor volume, including regions containing catalyst extrusion.

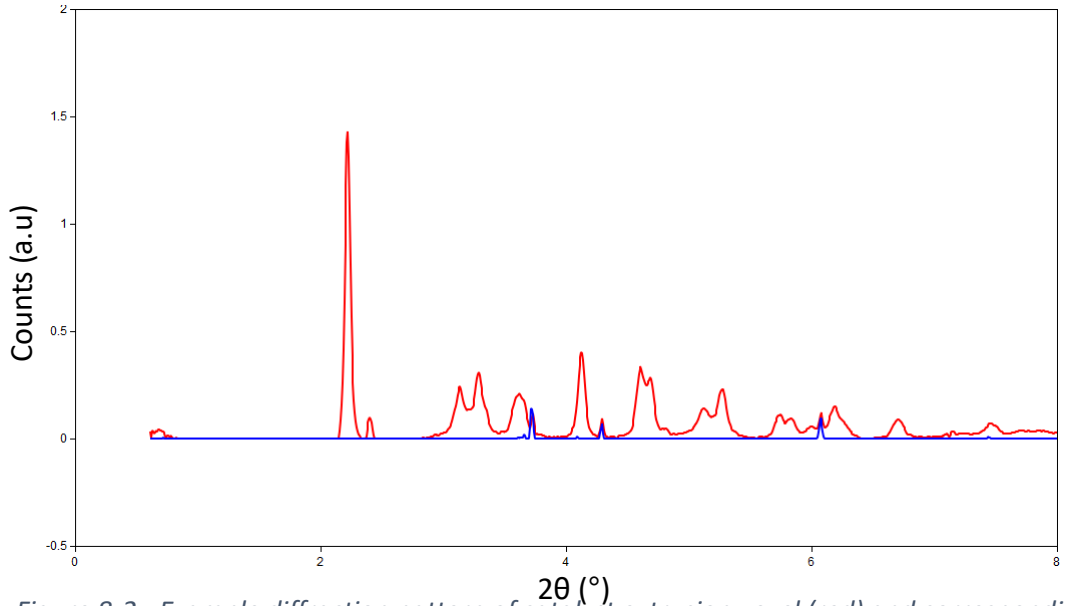

Figure 8-2 - Example diffraction pattern of catalyst extrusion voxel (red) and corresponding diffraction pattern of reactor diffraction contribution artefact (blue).

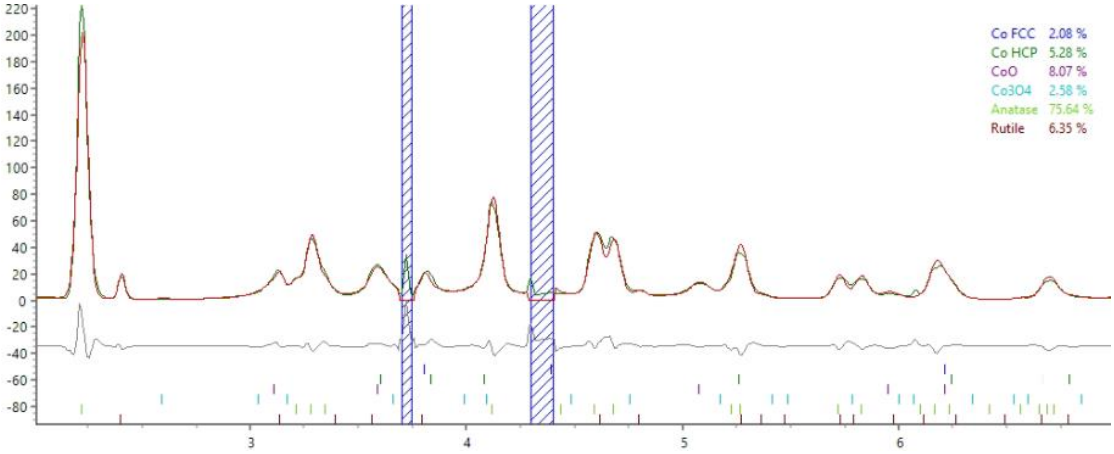

Figure 8-3 Example Rietveld refinement fit in Topas 6 for single voxel of 10% Mn extrusion at end of reduction.

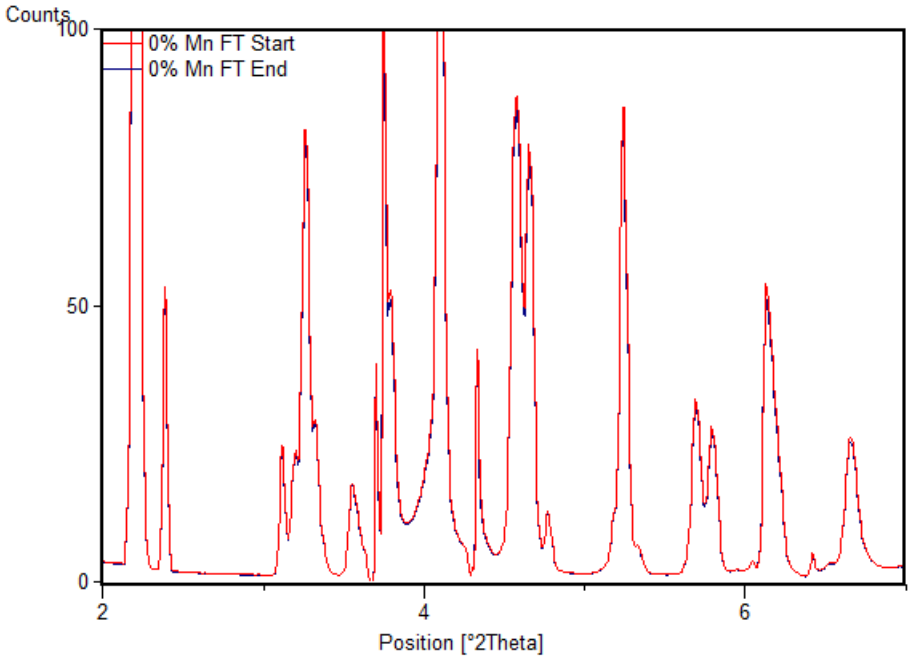

Figure 8-4 – Summed X-ray diffraction patterns of 0% Mn catalyst at start (red) & end (blue) of FT conditions.

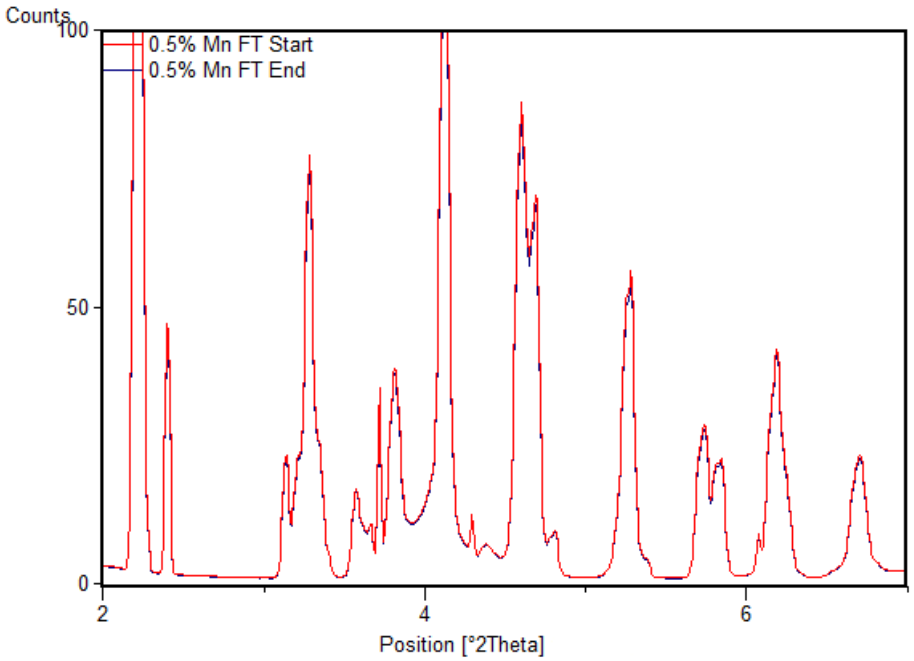

Figure 8-5 – Summed X-ray diffraction patterns of 0.5% Mn catalyst at start (red) & end (blue) of FT conditions.

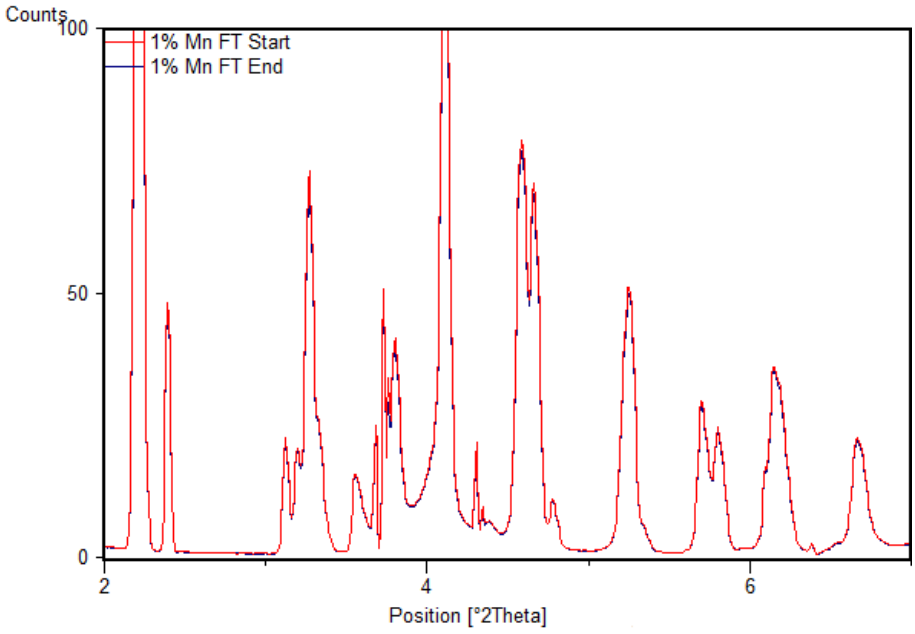

Figure 8-6 - Summed X-ray diffraction patterns of 1% Mn catalyst at start (red) & end (blue) of FT conditions.

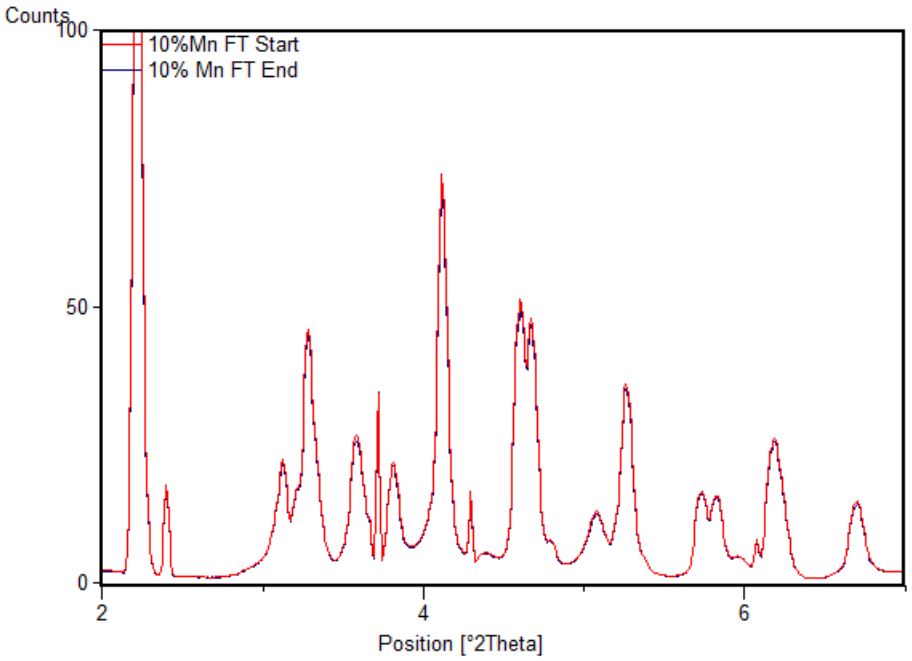

Figure 8-7 - Summed X-ray diffraction patterns of 10% Mn catalyst at start (red) & end (blue) of FT conditions.

Example Input parameter file for Rietveld refinement in Topas 6

The following is an example of the constructed Rietveld refinement file used for the spatially resolved refinements in Topas 6:

Figure 8-8 Example input parameter file used for Rietveld refinements in Topas 6.

```
r_wp 17.8376647 r_exp 23.2555225 r_p 11.9452003 r_wp_dash 18.9004845 r_p_dash 12.7876655 r_exp_dash 24.641154
weighted_Durbin_Watson 0.190415425 gof 0.767029193
iters 100
chi2_convergence_criteria 0.001
xdd activerefinement.xy
        x_calculation_step = Yobs_dx_at(Xo); convolution_step 4
        bkg @ 1.28499178` -0.449515237` 0.288058652` -0.328118446` 0.352119007` 0.0969820248`
        lam ymin_on_ymax 0.0001 la 1.0 lo wl 0.1353627` lh 0.1
        LP_Factor( 90)
        ''Variable_Divergence_Intensity
        Zero_Error(zero, 0.00096`)
        Specimen_Displacement(height,-0.00549`)
        start_X 2
        finish_X 7
        exclude 3.7 3.8
        exclude 4.3 4.4
                str
                phase_name "Co FCC"
                weight_percent percent_fcc 2.802`
                a !fcca 3.540257`
                b !fcca 3.540257`
                c !fcca 3.540257`
                al 90.
                be 90.
                ga 90.
                volume 44.372`
                space_group "Fm-3m"
                site Co0 x 0 y 0 z 0 occ Co 1 beq 0
                scale scalefcc 4.19297307e-008`
                r_bragg 70.8996564
                LVol_FWHM_CS_G_L(1, 8.96717`, 0.89, 8.49885`, csgcfcc, 9.55464`, cslcfcc, 10000.00000`_LIMIT_MIN_0.3)
                ''TCHZ_Peak_Type(pku, 0.00039,pkv, -0.00221,pkw, -0.00146,!pkz, 0.0000,pky, 0.00957,!pkx, 0.0000)
                ''Simple_Axial_Model(axial,10)
```

```
                Phase_Density_g_on_cm3( 8.82196`)
                prm !kf 0.89
                prm !lvolc_fwhm_fcc =kf/Voigt_FWHM_from_CS(csgcfcc, cslcfcc);
        str
                phase_name "Co HCP"
                weight_percent percent_hcp  6.063`
                a !hcpa  2.514540`
                b !hcpa  2.514540`
                c !hcpb  3.980936`
                al 90.
                be 90.
                ga 120.
                volume  21.799`
                space_group "P63/mmc"
                site Co0   x =1/3;     y =2/3;      z 0.25       occ Co 1       beq 0
                scale scalehcp  3.69412481e-007`
                r_bragg  8.09204497
                LVol_FWHM_CS_G_L(1, 3.62718`, 0.89, 3.67693`, csgchcp, 4.49317`, cslchcp, 27.77198`)
                ''TCHZ_Peak_Type(pku, 0.00039,pkv, -0.00221,pkw, -0.00146,!pkz, 0.0000,pky, 0.00957,!pkx, 0.0000)
                ''Simple_Axial_Model(axial,10)
                Phase_Density_g_on_cm3( 8.97856`)
                prm !kf 0.89
                prm !lvolc_fwhm_hcp =kf/Voigt_FWHM_from_CS(csgchcp, cslchcp);
        str
                phase_name "CoO"
                weight_percent percent_CoO  0.287`
                space_group "Fm-3m"
                al 90
                be 90
                ga 90
                a lpf  4.334990`
                b lpf  4.334990`
                c lpf  4.334990`
                volume  81.464`
                site O1    x 0.5        y 0.5        z 0.5        occ O-2  1       beq 0
                site Co1   x 0          y 0          z 0          occ Co+2 1       beq 0
                scale scaleCoO  1.8378973e-009`
                r_bragg  19.3711846
                LVol_FWHM_CS_G_L(1, 16.49753`, 0.89, 15.64111`, !csgcCoO, 17.59255`, !cslcCoO, 10000.00000`_LIMIT_MIN_0.3)
                ''TCHZ_Peak_Type(pku, 0.00039,pkv, -0.00221,pkw, -0.00146,!pkz, 0.0000,pky, 0.00957,!pkx, 0.0000)
                ''Simple_Axial_Model(axial,10)
                Phase_Density_g_on_cm3( 6.10964`)
    prm !kf 0.89
    prm !lvolc_fwhm_CoO =kf/Voigt_FWHM_from_CS(csgcCoO, cslcCoO);
        str
                phase_name "Co3O4"
                weight_percent percent_Co3O4  0.000`
                a lpa  8.099580
                b lpa  8.099580
                c lpa  8.099580
                al 90.
                be 90.
                ga 90.
                volume  531.358
                space_group "F-43m"
                site Co1   x 0          y 0          z 0          occ Co+2 1.      beq 0.3
                site Co2   x 0.25       y 0.25       z 0.25       occ Co+2 1.      beq 0.3
                site Co3   x 0.625      y 0.625      z 0.625      occ Co+3 1.      beq 0.3
                site O1    x !xc1  0.37590    y !xc1  0.37590    z !xc1  0.37590    occ O-2  1       beq 0.3
                site O2    x !xc2 -0.12590    y !xc2 -0.12590    z !xc2 -0.12590    occ O-2  1       beq 0.3
                scale scaleCo3O4  1.00000034e-015`_LIMIT_MIN_1e-015
                r_bragg  7.49880973
                LVol_FWHM_CS_G_L(1,   1.53540`,   0.89,   1.45475`,   !csgcCo3O4,   1.63475`_LIMIT_MIN_0.3,   !cslcCo3O4,
7648.11076`_LIMIT_MIN_0.3)
                Phase_Density_g_on_cm3( 6.02009)
    prm !kf 0.89
    prm !lvolc_fwhm_Co3O4 =kf/Voigt_FWHM_from_CS(csgcCo3O4, cslcCo3O4);
        str
                phase_name "Anatase"
                weight_percent percent_anatase  81.295`
                a !lpd  3.786578
```

```
                    b !lpd  3.786578
                    c !lpe  9.510527
                    al 90.
                    be 90.
                    ga 90.
                    volume  136.364
                    space_group "I41/amdS"
                    site Ti1    x 0          y 0          z 0          occ Ti+4  1  beq   0.39
                    site O1     x 0          y 0          z !xa1  0.20886     occ O-2  1  beq  0.61
                    scale scaleana  2.92131055e-007`
                    r_bragg  4.18156616
                    LVol_FWHM_CS_G_L(1,         16.81975`,         0.89,         16.01692`,         !csgcana,         18.11957`,         !cslcana,
1527.58498`_LIMIT_MAX_335.792323)
                    Phase_Density_g_on_cm3( 3.89020)
          str
                    phase_name "Rutile"
                    weight_percent percent_rutile  9.553`
                    a !lpb  4.598411
                    b !lpb  4.598411
                    c !lpc  2.961121
                    al 90
                    be 90
                    ga 90
                    space_group "P42/mnm"
                    site O1    x !xr1  0.29844     y !xr1  0.29844     z 0.000000     occ O    1.000000   beq 0.500033637
                    site TI1   x 0.000000     y 0.000000     z 0.000000     occ Ti   1.000000   beq 0.500033637
                    scale scalerut  1.49527074e-007`
                    r_bragg  7.79091426
                    LVol_FWHM_CS_G_L(1, 27.19038`, 0.89, 25.79114`, !csgcrut, 29.02850`, !cslcrut, 10000.00000`_LIMIT_MIN_0.3)
                    Phase_Density_g_on_cm3( 4.23612)
for strs {
                    TCHZ_Peak_Type(!pku,-0.27401`,!pkv,     -0.01183`,     !pkw,          0.00022`,!pkz,     0.00000,!pky,     0.13292`,!pkx,
0.00010_LIMIT_MIN_0.0001)
                    Finger_et_al(   0.09307`,    0.25936`)
}
out "Bulkresults.txt" append
Out(Get (r_wp), " %11.5f")
Out(scaleana, " %11.15f", " %11.15f")
Out(percent_anatase, " %11.5f", " %11.5f")
Out(csgcana, " %11.5f", " %11.5f")
Out(cslcana, " %11.5f", " %11.5f")
Out(scalerut, " %11.15f", " %11.15f")
Out(percent_rutile, " %11.5f", " %11.5f")
Out(csgcrut, " %11.5f", " %11.5f")
Out(cslcrut, " %11.5f", " %11.5f")
Out(scaleCo3O4, " %11.15f", " %11.15f")
Out(percent_Co3O4, " %11.5f", " %11.5f")
Out(csgcCo3O4, " %11.5f", " %11.5f")
Out(cslcCo3O4, " %11.5f", " %11.5f")
Out(scaleCoO, " %11.15f", " %11.15f")
Out(percent_CoO, " %11.5f", " %11.5f")
Out(csgcCoO, " %11.5f", " %11.5f")
Out(cslcCoO, " %11.5f", " %11.5f")
Out(scalefcc, " %11.15f", " %11.15f")
Out(percent_fcc, " %11.5f", " %11.5f")
Out(csgcfcc, " %11.5f", " %11.5f")
Out(cslcfcc, " %11.5f", " %11.5f")
Out(scalehcp, " %11.15f", " %11.15f")
Out(percent_hcp, " %11.5f", " %11.5f")
Out(csgchcp, " %11.5f", " %11.5f")
Out(cslchcp, " %11.5f", " %11.5f")
Out(lpa,  " %11.5f", " %11.5f")
Out(lpf, " %11.5f", " %11.5f")
Out(hcpa, " %11.5f", " %11.5f")
Out(hcpb, " %11.5f", " %11.5f")
Out(fcca, " %11.5f", " %11.5f")
Out(lvolc_fwhm_Co3O4, " %11.5f", " %11.5f")
Out(lvolc_fwhm_CoO, " %11.5f", " %11.5f")
Out(lvolc_fwhm_hcp, " %11.5f", " %11.5f")
Out(lvolc_fwhm_fcc, " %11.5f", " %11.5f\n")
```

Data Processing Code for XRD-CT

The following scripts were used to automate the bulk Rietveld refinements and collate and categorise the resulting refinement parameters. The scripts were processed in Matlab 2017 and the refinements conducted using Topas 6.

Processing of Spatially resolved Rietveld Refinement and Refinement map key

Figure 8-9 Refinement and refkey script. This script was used to process the cropped CT array of extrusion diffraction data for Rietveld refinement. The cropped array contains a series of 23x23 crops with increasing manganese & scan number on the axes. The doping level and scan number of each crop is identified, to correlate it with a specific input parameter file. The input parameter file for the refinement is shared for each voxel within a CT crop. Prior to a voxel being refined, selection criteria is applied to ensure diffraction contribution from the catalyst is present in that voxel, and that empty space is not being refined. The RefKey is a map of which voxels were refined, such that the output data can be spatially reconstructed.

```
%import two-theta values
tth = importdata('tthFeb.asc');
%create blank refinement array key
refkey = zeros(size(stackedCT,1),size(stackedCT,2));
%loop refinement for each doping level
doplevels = 5;
for i = 1:doplevels
    if i == 1
            dopant = '0%';
    end
    if i == 2
            dopant = '0,5%';
    end
    if i == 3
            dopant = '1%';
    end
    if i == 4
            dopant = '5%';
    end
    if i == 5
            dopant = '10%';
    end
%loop for each scan and cut crop for scan x extrusion for crop size of 23x23
numscans = 15;
for j = 1:numscans;
    Extrusion = strcat('FebRed', num2str(j), '_', dopant);
    activecrop = stackedCT([((j-1)*23+1):(j*23)], [((i-1)*23+1):(i*23)], [1:2038]);

    %image is cropped, select each voxel within crop
   a = 1
for ii = 1:size(activecrop, 1);
        for jj = 1:size(activecrop, 2);
            signal = activecrop(ii, jj, :);
            signal = [signal(:)];
            x = tth;
            y = signal;
            %check if voxel contribution adheres to selection criterea
            if (sum(y) > 30) && (max(y) > 1);

            % 1 = refined voxel = true
            refkey(ii+(23*(j-1)), jj+(23*(i-1))) = 1;
            xy = [x,y];

            %export voxel diffraction pattern for .inp file
            save('activerefinement.xy', 'xy', '-ascii');
            %hold to ensure file saved prior to refinement cmd
```

```
            pause(0.1);

            wdir = 'C:\Users\anorg\Documents\JPTopaz\BatchFiles\';
            extr = [wdir Extrusion '_riet_01'];
            cmd = sprintf('C:\\Topas6\\tc.exe "%s" ', extr);
            system(cmd)
            else
                % -1 = refined voxel false
                refkey(ii+(23*(j-1)), jj+(23*(i-1))) = -1;
            end
            a = a + 1
        end
end
end
end
refkeyname = 'refkey.mat';
save(refkeyname, 'refkey');
```

Import Refined Parameters

Figure 8-10 Import Refined Parameters Script. This script is designed to rearrange the imported bulk results of a refined dataset into a 2D array. The refined data and refinement key are used to remap each refined voxel to their 2D coordinate. The 3rd dimension of the array are the various Rietveld refinement parameters exported from the input parameter files at the end of each refinement.

```
rowy = 1;
%create blank array for refinement metrics
refinedarray = zeros(size(refkey, 1), size(refkey, 2), 67);
refineddata(isnan(refineddata)) = 0;
%loop for crops of size 23x23 voxels
for j = 1:(size(refkey, 2))/23;
for i = 1:(size(refkey, 1))/23;
   for ii = 1:23
       for jj = 1:23
    %for each voxel in crop, if refkey = 1 then refinement = true, and
    %import next row of refinement results into that voxel, move to next
    %row
    if refkey(ii+(i-1)*23, jj+(j-1)*23) == 1;
       refinedarray(ii+(i-1)*23, jj+(j-1)*23,[1:size(refineddata, 2)]) =
refineddata(rowy, [1:size(refineddata, 2)]);
       rowy = rowy + 1;
    end
    end
end
end
end

imax = size(refinedarray, 1);
jmax = size(refinedarray, 2);
%Rwp filter out voxels with Rwp > 15
for i = 1:imax
    for j = 1:jmax
        if refinedarray(i, j, 1) > 15;
            refinedarray(i, j, :) = 0;
           refkey(i, j, :) = 0;
        end
    end
end
%Refined parameter maps
rwp  = refinedarray([1:imax], [1:jmax], [1:1]);
anatasescale  = refinedarray([1:imax], [1:jmax], [2:2]);
anataseweight  = refinedarray([1:imax], [1:jmax], [4:4]);
rutilescale  = refinedarray([1:imax], [1:jmax], [10:10]);
rutileweight  = refinedarray([1:imax], [1:jmax], [12:12]);
co3o4scale  = refinedarray([1:imax], [1:jmax], [18:18]);
```

```
co3o4weight  = refinedarray([1:imax], [1:jmax], [20:20]);
co3o4size = refinedarray([1:imax], [1:jmax], [60:60]);
cooscale  = refinedarray([1:imax], [1:jmax], [26:26]);
cooweight  = refinedarray([1:imax], [1:jmax], [28:28]);
coosize = refinedarray([1:imax], [1:jmax], [62:62]);
fccscale  = refinedarray([1:imax], [1:jmax], [34:34]);
fccweight  = refinedarray([1:imax], [1:jmax], [36:36]);
fccsize = refinedarray([1:imax], [1:jmax], [68:68]);
hcpscfle  = refinedarray([1:imax], [1:jmax], [42:42]);
hcpweight  = refinedarray([1:imax], [1:jmax], [44:44]);
hcpsize = refinedarray([1:imax], [1:jmax], [66:66]);
coolat = refinedarray([1:imax], [1:jmax], [52:52]);
co3o4lat = refinedarray([1:imax], [1:jmax], [50:50]);
fcclat = refinedarray([1:imax], [1:jmax], [58:58]);
hcplat = refinedarray([1:imax], [1:jmax], [54:54]);
metalweight = refinedarray([1:imax], [1:jmax], [44:44]) + refinedarray([1:imax],
[1:jmax], [36:36]);
metalratio = rdivide(fccweight, hcpweight);
```

Radial Batching

Figure 8-11 Radial Batching - This script filters each extrusion from the refinement key, and for each voxel gives a corresponding integer value for radial depth, from 1 at the catalyst exterior up to 4 at the catalyst interior.The refined values are then squeezed into a single average at each radial depth value, for each extrusion within the dataset.

```
RadiusRefkey = zeros(size(refkey, 1), size(refkey, 2), 2);

RadiusRefkey(:, :, 1) = refkey(:, :);

for k = 1:10;
    %checks each voxel adjacent to (i,j). If an adjacent voxel is empty
    %(i.e 0) then must be exterior layer for depth k
for i = 1:size(RadiusRefkey, 1)-1;
for j = 1:size(RadiusRefkey, 2)-1;

    if RadiusRefkey(i, j, 1) == 1;
       if RadiusRefkey(i+1, j, 1) == -1;
           RadiusRefkey(i, j, 2) = k;

       elseif RadiusRefkey(i-1, j, 1) == -1;
           RadiusRefkey(i, j, 2) = k;

       elseif RadiusRefkey(i, j+1, 1) == -1;
           RadiusRefkey(i, j, 2) = k;

       elseif RadiusRefkey(i, j-1, 1) == -1;
           RadiusRefkey(i, j, 2) = k;

       elseif RadiusRefkey(i+1, j+1, 1) == -1;
           RadiusRefkey(i, j, 2) = k;

       elseif RadiusRefkey(i+1, j-1, 1) == -1;
           RadiusRefkey(i, j, 2) = k;

       elseif RadiusRefkey(i-1, j+1, 1) == -1;
           RadiusRefkey(i, j, 2) = k;

       elseif RadiusRefkey(i-1, j-1, 1) == -1;
           RadiusRefkey(i, j, 2) = k;
       end
    end
end
```

```
end
%if voxel marked with current loop depth k, set layer 1 to 0 to behave as
%new exterior
for i = 1:size(RadiusRefkey, 1);
for j = 1:size(RadiusRefkey, 2);
    if RadiusRefkey(i, j, 2) == k;
        RadiusRefkey(i, j, 1) = -1;
    end
end
end
end
radiusarray = zeros(size(RadiusRefkey, 1), size(RadiusRefkey, 2),
size(refinedarray, 3), 6);
%Squeeze each extrusion at each radius depth into single average value
for k = 1:6;
    for i = 1:14;
        for j = 1:5;
            sum = zeros(1, 1, size(refinedarray, 3));
            count = 0;
            for ii = 1:23;
                for jj = 1:23;
                   if RadiusRefkey(ii+(i-1)*23, jj+(j-1)*23, 2) == k;
                       sum(1, 1, :) = sum(1, 1, :) + refinedarray(ii+(i-1)*23,
jj+(j-1)*23, :);
                       count = count + 1;
                   end
                end
            end
            sum(1, 1, :) = sum(1, 1, :)/count;
            radiusarray(i, j, :, k) = sum(1, 1, :);
        end
    end
end
```

Appendix for Chapter 5 – High pressure XRD-CT study of Mn doped catalyst extrusion series

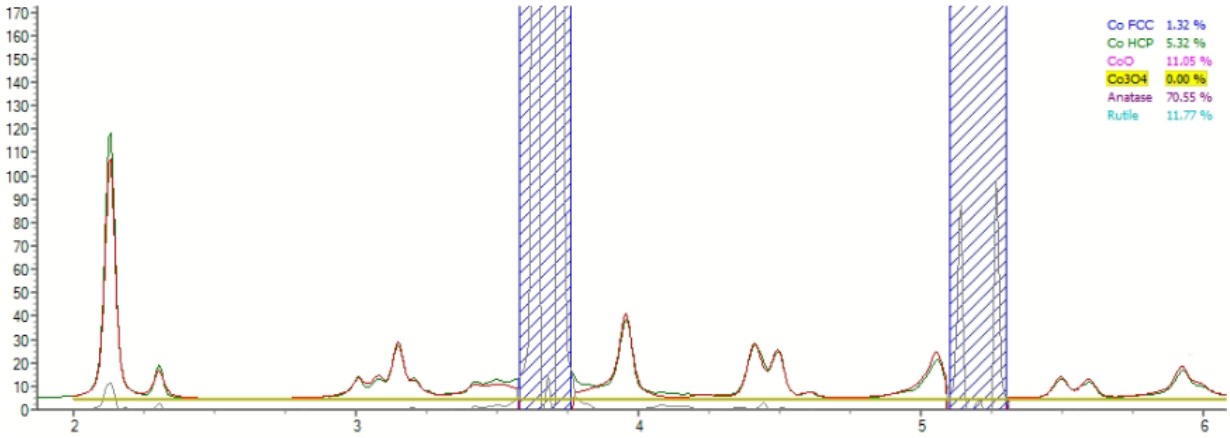

Figure 8-12 - Example Rietveld refinement fit for single voxel of 10% Mn extrusion at end of reduction.

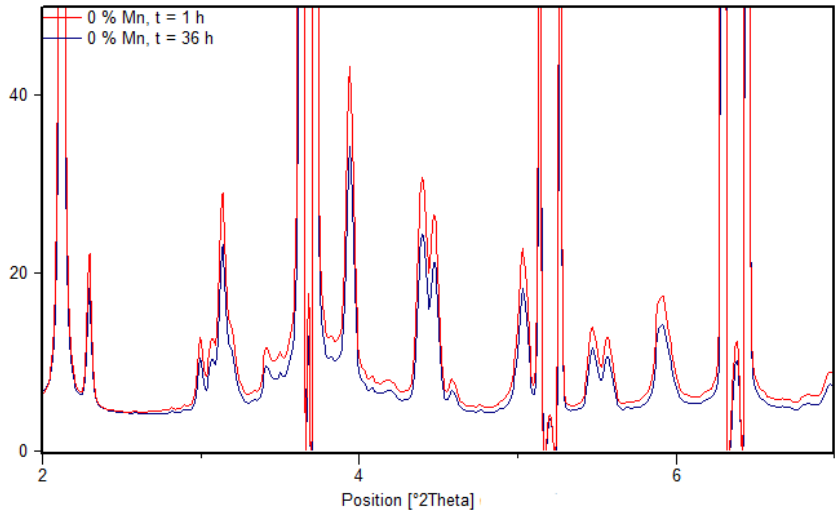

Figure 8-13 Summed diffraction pattern for 0 % Mn catalyst at t = 1 h & t = 36 h.

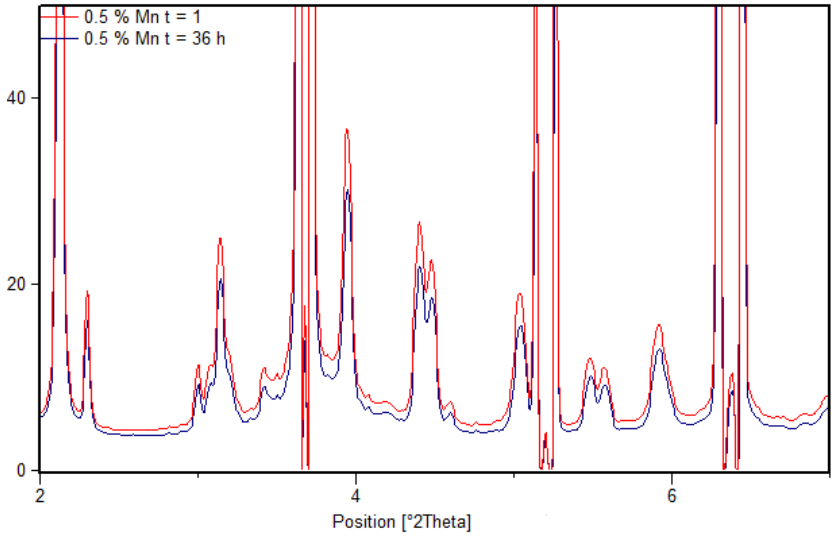

Figure 8-14 Summed diffraction pattern for 0.5 % Mn catalyst at t = 1 h & t = 36 h.

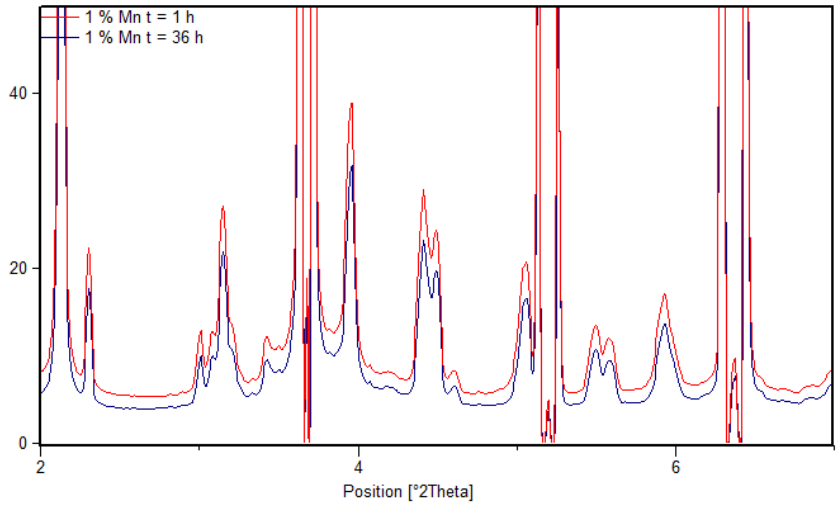

Figure 8-15 Summed diffraction pattern for 1 % Mn catalyst at t = 1 h & t = 36 h.

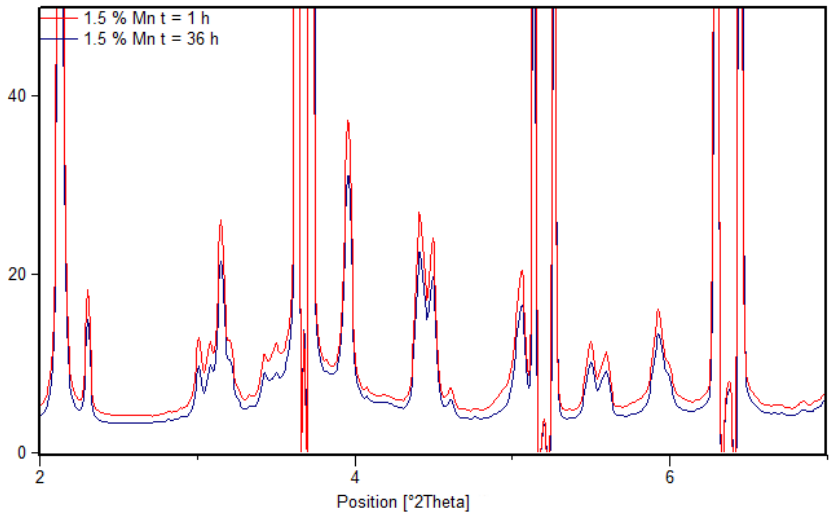

Figure 8-16 Summed diffraction pattern for 1.5 % Mn catalyst at t = 1 h & t = 36 h.

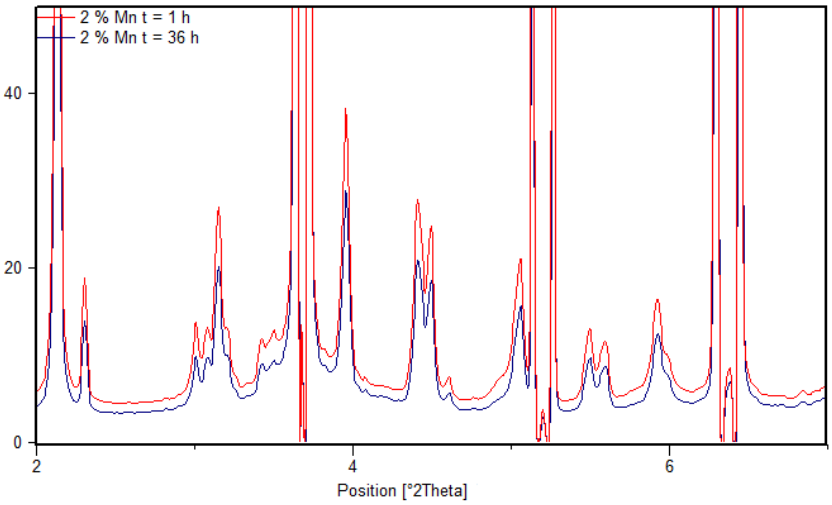

Figure 8-17 Summed diffraction pattern for 2 % Mn catalyst at t = 1 h & t = 36 h.

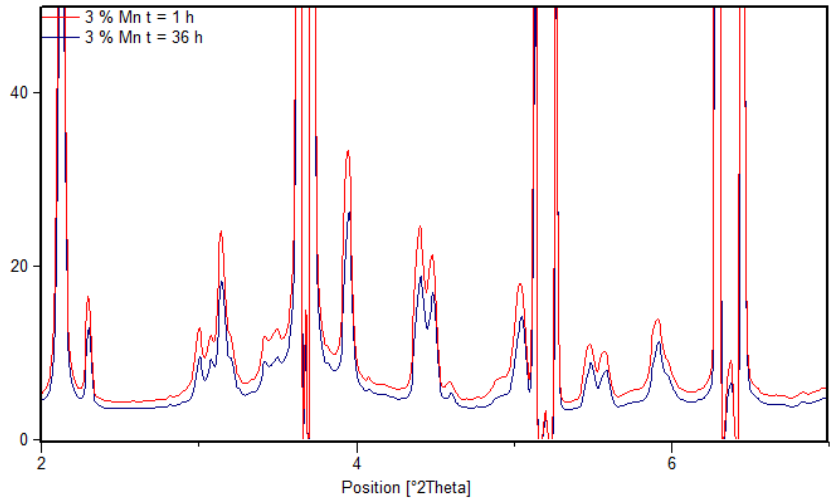

Figure 8-18 Summed diffraction pattern for 3 % Mn catalyst at t = 1 h & t = 36 h.

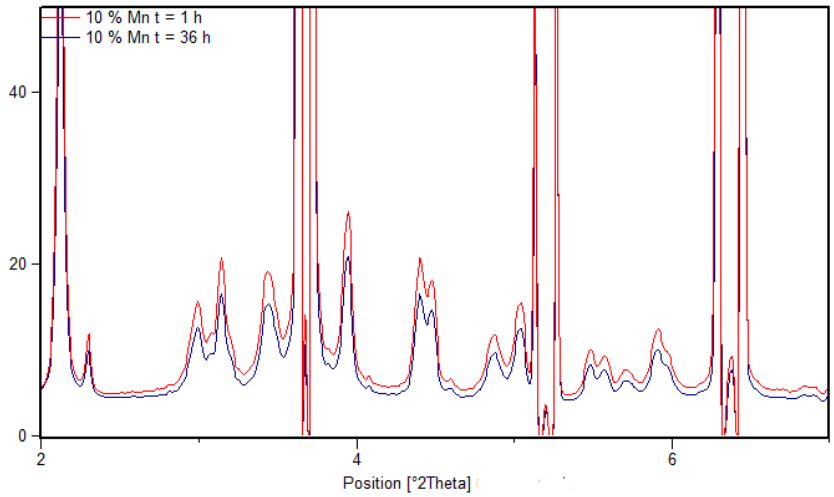

Figure 8-19 Summed diffraction pattern for 10 % Mn catalyst at t = 1 h & t = 36 h.

Appendix for Chapter 6 – Manganese doped model catalyst systems for alcohol selective Fischer-Tropsch

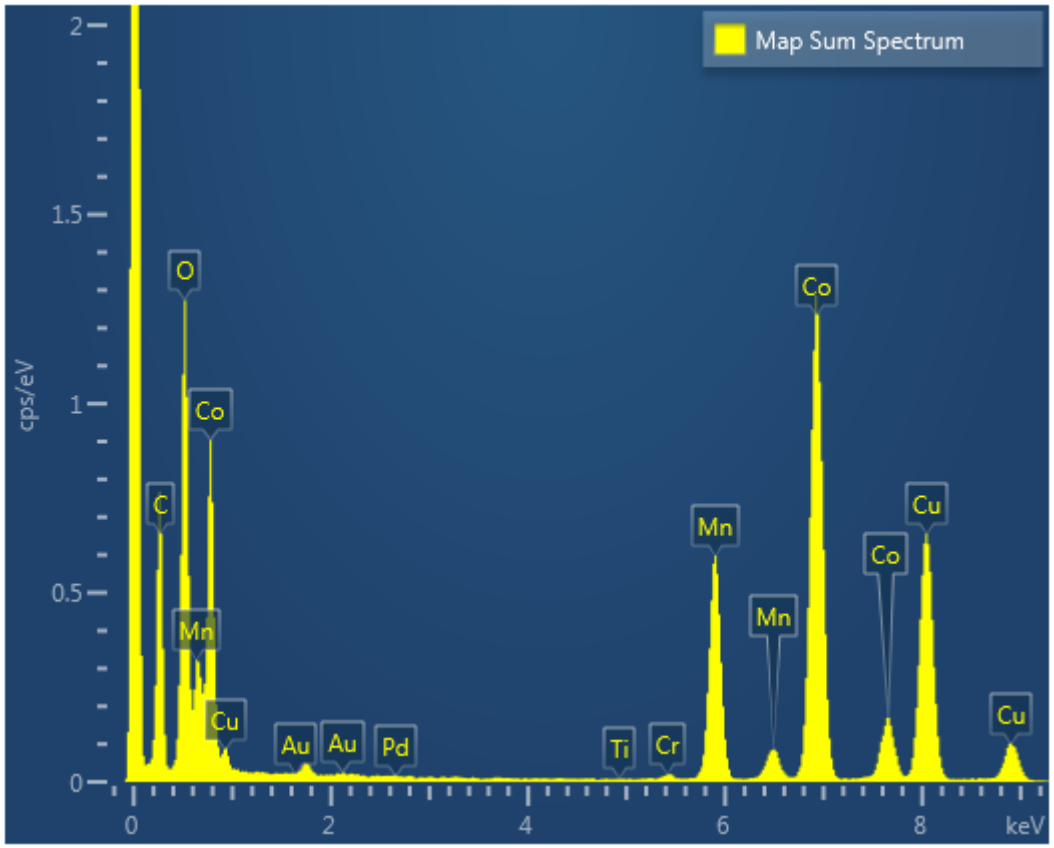

Figure 8-20 - EDX spectrum of JP11, 100:50 mixed oxide nanoparticles.

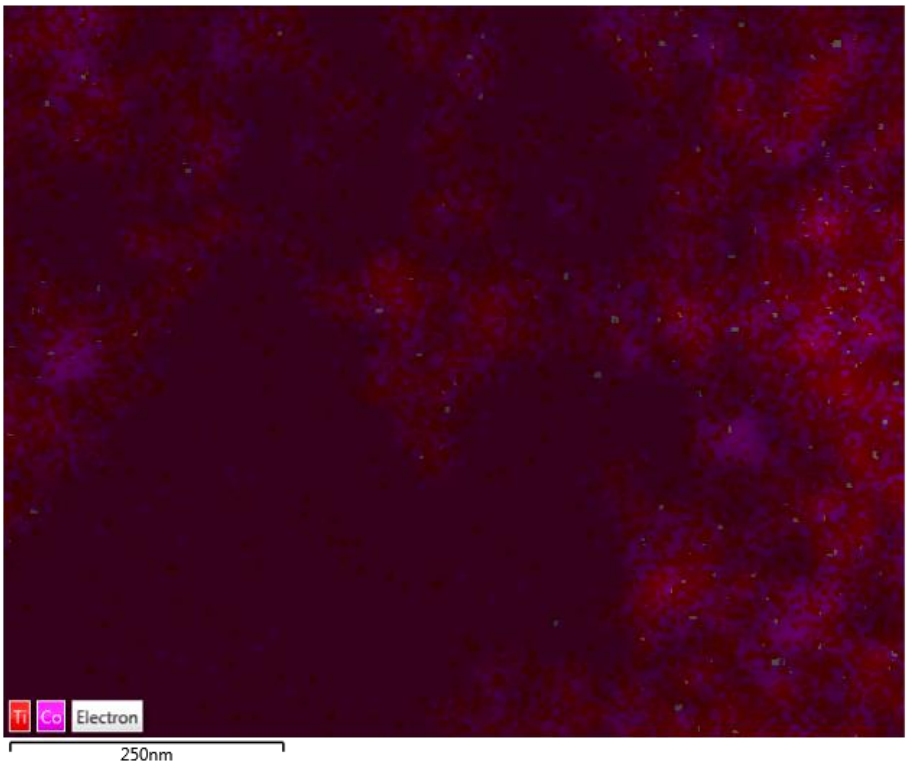

Figure 8-21 - EDX Layered Image of JP17-1, supported Co_3O_4 dispersed in P25 TiO_2.